UNIVERSITÉ DE MONTRÉAL

ANALYSIS OF SUB-CORTICAL MORPHOLOGY IN BENIGN EPILEPSY WITH CENTROTEMPORAL SPIKES

MAHSA SHAKERI
DÉPARTEMENT DE GÉNIE INFORMATIQUE ET GÉNIE LOGICIEL
ÉCOLE POLYTECHNIQUE DE MONTRÉAL

THÈSE PRÉSENTÉE EN VUE DE L'OBTENTION
DU DIPLÔME DE PHILOSOPHIÆ DOCTOR
(GÉNIE INFORMATIQUE)
DÉCEMBRE 2016

UNIVERSITÉ DE MONTRÉAL

ÉCOLE POLYTECHNIQUE DE MONTRÉAL

Cette thèse intitulée :

ANALYSIS OF SUB-CORTICAL MORPHOLOGY IN BENIGN EPILEPSY WITH CENTROTEMPORAL SPIKES

présentée par : SHAKERI Mahsa
en vue de l'obtention du diplôme de : Philosophiæ Doctor
a été dûment acceptée par le jury d'examen constitué de :

M. PAL Christopher J., Ph. D., président
M. KADOURY Samuel, Ph. D., membre et directeur de recherche
Mme LIPPÉ Sarah, Ph. D., membre et codirectrice de recherche
M. CHAKRAVATY Mallar, Ph. D., membre
M. DUCHESNE Simon, Ph. D., membre externe

DEDICATION

To My Loving Parents
To Hani, whose love has motivated
and inspired me to succeed in my life...

ACKNOWLEDGEMENTS

I would like to express my deep and sincere gratitude to my director, Samuel Kadoury, who gave me the chance to pursue my dreams and fulfill my curiosities.

I would like to greatly thank my codirector, Sarah Lippé, who guided me throughout my phd with her patience, and great supports.

During my PhD study, I also had the privilege to collaborate with INRIA CVN laboratory, at CentraleSupelec, France in a stunning team led by Nikos Paragios, who trusted me, gave me an insightful eye on research, and introduced me to great researchers.

I would like to convey my gratitude to all members of my Ph.D. committee for accepting to be a jury member.

I am deeply thankful to all my friends and colleagues at the MEDICAL laboratory of the department of Computer and Software Engineering for all their help and support.

I would like to thank my friends and and colleagues at the NED laboratory of the department of Neuropsychology for their support and guidance.

My special gratitude goes to my parents for their support, encouragement, love, and patience during my scientific studies.

And finally, my deepest and warmest thanks to Hani, my beloved husband, for dreaming with me and for being a constant source of encouragement and inspiration.

RÉSUMÉ

Au Canada, l'épilepsie affecte environ 3 à 6 enfants par 1000 âgés de 0 à 15 ans dans la population globale. Quinze à 25 % de ces enfants ont une épilepsie bénigne avec des pointes centrotemporelles (BECTS), ce qui fait de BECTS le syndrome épileptique focal de l'enfant bénin le plus fréquent. Initialement, BECTS était considéré comme bénin parmi les autres épilepsies car il était généralement rapporté que les capacités cognitives ont été préservées ou ramenées à la normale pendant la rémission. Cependant, certaines études ont trouvé des déficits cognitifs et comportementaux, qui peuvent bien persister même après la rémission. Compte tenu des différences neurocognitives chez les enfants atteints de BECTS et de témoins normaux, la question est de savoir si des variations morphométriques subtiles dans les structures cérébrales sont également présentes chez ces patients et si elles expliquent des variations dans les performence cognitifs. En fait, malgré les preuves accumulées d'une étiologie neurodéveloppementale dans le BECTS, peu est connu sur les altérations structurelles sous-jacentes. À cet égard, la proposition de méthodes avancées en neuroimagerie permettrait d'évaluer quantitativement les variations de la morphologie cérébrale associées à ce trouble neurologique. En outre, l'étude du développement morphologique du cerveau et sa relation avec la cognition peut aider à élucider la base neuroanatomique des déficits cognitifs. Le but de cette thèse est donc de fournir un ensemble d'outils pour analyser les variations morphologiques sous-corticales subtiles provoquées par différentes maladies, telles que l'épilepsie bénigne avec des pointes centrotemporelles.

La méthodologie adoptée dans cette thèse a conduit à trois objectifs de recherche spécifiques. La première étape vise à développer un nouveau cadre automatisé pour segmenter les structures sous-corticales sur les images à resonance magnètique (IRM). La deuxième étape vise à concevoir une nouvelle approche basée sur la correspondance spectrale pour capturer précisément la variabilité de forme chez les sujets épileptiques. La troisième étape conduit à une analyse de la relation entre les changements morphologiques du cerveau et les indices cognitifs.

La première contribution vise plus spécifiquement la segmentation automatique des structures sous-corticales dans un processus de co-recalage et de co-segmentation multi-atlas. Contrairement aux approches standards de segmentation multi-atlas, la méthode proposée obtient la segmentation finale en utilisant un recalage en fonction de la population, tandis que les connaissances à prior basés sur les réseaux neuronaux par convolution (CNNs) sont incorporées dans la formulation d'énergie en tant que représentation d'image discriminative.

Ainsi, cette méthode exploite des représentations apprises plus sophistiquées pour conduire le processus de co-recalage. De plus, étant donné un ensemble de volumes cibles, la méthode proposée calcule les probabilités de segmentation individuellement, puis segmente tous les volumes simultanément. Par conséquent, le fardeau de fournir un sous-ensemble de vérité connue approprié pour effectuer la segmentation multi-atlas est évité. Des résultats prometteurs démontrent le potentiel de notre méthode sur deux ensembles de données, contenant des annotations de structures sous-corticales. L'importance des estimations fiables des annotations est également mise en évidence, ce qui motive l'utilisation de réseaux neuronaux profonds pour remplacer les annotations de vérité connue en co-recalage avec une perte de performance minimale.

La deuxième contribution vise à saisir la variabilité de forme entre deux populations de surfaces en utilisant une analyse morphologique multijoints. La méthode proposée exploite la représentation spectrale pour établir des correspondances de surface, puisque l'appariement est plus simple dans le domaine spectral plutôt que dans l'espace euclidien conventionnel. Le cadre proposé intègre la concordance spectrale à courbure moyenne dans un plateforme d'analyse de formes sous-corticales multijoints. L'analyse expérimentale sur des données cliniques a montré que les différences de groupe extraites étaient similaires avec les résultats dans d'autres études cliniques, tandis que les sorties d'analyse de forme ont été créées d'une manière à réduire le temps de calcul.

Enfin, la troisième contribution établit l'association entre les altérations morphologiques sous-corticales chez les enfants atteints d'épilepsie bénigne et les indices cognitifs. Cette étude permet de détecter les changements du putamen et du noyau caudé chez les enfants atteints de BECTS gauche, droit ou bilatéral. De plus, l 'association des différences volumétriques structurelles et des différences de forme avec la cognition a été étudiée. Les résultats confirment les altérations de la forme du putamen et du noyau caudé chez les enfants atteints de BECTS. De plus, nos résultats suggèrent que la variation de la forme sous-corticale affecte les fonctions cognitives. Cette étude démontre que les altérations de la forme et leur relation avec la cognition dépendent du côté de la focalisation de l'épilepsie.

Ce projet nous a permis d'étudier si de nouvelles méthodes permettraient de traiter automatiquement les informations de neuro-imagerie chez les enfants atteints de BECTS et de détecter des variations morphologiques subtiles dans leurs structures sous-corticales. De plus, les résultats obtenus dans le cadre de cette thèse nous ont permis de conclure qu'il existe une association entre les variations morphologiques et la cognition par rapport au côté de la focalisation de la crise épileptique.

ABSTRACT

In Canada, epilepsy affects approximately 3 to 6 children per 1000 aged from 0 to 15 years in the overall population. Fifteen to 25% of these children have benign epilepsy with centrotemporal spikes (BECTS), making BECTS the most common benign childhood focal epileptic syndrome. Initially, BECTS was considered as benign among other epilepsies since it was generally reported that cognitive abilities were preserved or brought back to normal during remission. However, some studies have found cognitive and behavioral deficits, which may well persist even after remission. Given neurocognitive differences among children with BECTS and normal controls, the question is whether subtle morphometric variations in brain structures are also present in these patients, and whether they explain variations in cognitive indices. In fact, despite the accumulating evidence of a neurodevelopmental etiology in BECTS, little is known about underlying structural alterations. In this respect, proposing advanced neuroimaging methods will allow for quantitative assessment of variations in brain morphology associated with this neurological disorder. In addition, studying the brain morphological development and its relationship with cognition may help elucidate the neuroanatomical basis of cognitive deficits. Therefore, the focus of this thesis is to provide a set of tools for analyzing the subtle sub-cortical morphological alterations in different diseases, such as benign epilepsy with centrotemporal spikes.

The methodology adopted in this thesis led to addressing three specific research objectives. The first step develops a new automated framework for segmenting subcortical structures on MR images. The second step designs a new approach based on spectral correspondence to precisely capture shape variability in epileptic individuals. The third step finds the association between brain morphological changes and cognitive indices.

The first contribution aims more specifically at automatic segmentation of sub-cortical structures in a groupwise multi-atlas coregistration and cosegmentation process. Contrary to the standard multi-atlas segmentation approaches, the proposed method obtains the final segmentation using a population-wise registration, while Convolutional Neural Network (CNN)-based priors are incorporated in the energy formulation as a discriminative image representation. Thus, this method exploits more sophisticated learned representations to drive the coregistration process. Furthermore, given a set of target volumes the developed method computes the segmentation probabilities individually, and then segments all the volumes simultaneously. Therefore, the burden of providing an appropriate ground truth subset to perform multi-atlas segmentation is removed. Promising results demonstrate the potential of

our method on two different datasets, containing annotations of sub-cortical structures. The importance of reliable label estimations is also highlighted, motivating the use of deep neural nets to replace ground truth annotations in coregistration with minimal loss in performance.

The second contribution intends to capture shape variability between two population of surfaces using groupwise morphological analysis. The proposed method exploits spectral representation for establishing surface correspondences, since matching is simpler in the spectral domain rather than in the conventional Euclidean space. The designed framework integrates mean curvature-based spectral matching in to a groupwise subcortical shape analysis pipeline. Experimental analysis on real clinical dataset showed that the extracted group differences were in parallel with the findings in other clinical studies, while the shape analysis outputs were created in a computational efficient manner.

Finally, the third contribution establishes the association between sub-cortical morphological alterations in children with benign epilepsy and cognitive indices. This study detects putamen and caudate changes in children with left, right, or bilateral BECTS to age and gender matched healthy individuals. In addition, the association of structural volumetric and shape differences with cognition is investigated. The findings confirm putamen and caudate shape alterations in children with BECTS. Also, our results suggest that variation in sub-cortical shape affects cognitive functions. More importantly, this study demonstrates that shape alterations and their relation with cognition depend on the side of epilepsy focus.

This project enabled us to investigate whether new methods would allow to automatically process neuroimaging information from children afflicted with BECTS and detect subtle morphological variations in their sub-cortical structures. In addition, the results obtained in this thesis allowed us to conclude the existence of the association between morphological variations and cognition with respect to the side of seizure focus.

TABLE OF CONTENTS

LIST OF TABLES

LIST OF FIGURES

LIST OF SYMBOLS AND ABBREVIATIONS

BECTS	Benign Epilepsy with Centrotemporal Spikes
RE	Rolandic Epilepsy
MRI	Magnetic Resonance Imaging
CAD	Computer Aided Detection
EEG	Electroencephalography
CTS	Centrotemporal Spikes
GM	Gray Matter
WM	White matter
CSF	Cerebrospinal Fluid
VBM	Voxel-Based Morphometry
DBM	Deformable-Based Model
PDM	Point Disrtibution Mode
SVM	Support Vector Machine
CNN	Convolutional Neural Networks
MLP	Multi-layer Perceptron
VAE	Variational Auto-Encoder

LIST OF APPENDIXES

CHAPTER 1 INTRODUCTION

Benign epilepsy with centrotemporal spikes (BECTS) is one of the most common childhood epilepsy syndromes (Kramer et al., 1998; Wirrell and Hamiwka, 2006), which occurs in children aged from three to 13 years old (Panayiotopoulos et al., 2008). Initially, BECTS was considered as benign, but recently some studies have found cognitive and behavioral deficits (Weglage et al., 1997; Metz-Lutz and Filippini, 2006), which could affect the quality of life of these children (Malfait, 2011).

Despite the various studies on neurodevelopmental etiology in BECTS, no research study has assessed the underlying structural shape alterations and its relation with cognition in this disease. Recent advancements in the neuroimaging have enabled developing reliable frameworks for investigating neuroanatomical alterations in sub-cortical brain organs. For this purpose, first the boundary of each sub-cortical structure should be delineated using a segmentation approach, then a shape analysis process is required to detect the location of morphological alterations. The detected alterations can be further analyzed to reveal the relation between structural morphology in BECTS and cognitive impairments.

Manual segmentation of sub-cortical structures on Magnetic Resonance (MR) images is considered as gold standard. However, manual delineation of structures is costly and requires trained experts. Therefore, automatically segmenting structures has become of special interest. In recent years, various automatic segmentation methods have been proposed in the literature. Nonetheless, the accuracy of these approaches is still far from the gold standard. Among available segmentation techniques, multi-atlas segmentation approaches have been shown to be amongst the most powerful ones (Iglesias and Sabuncu, 2015). These methods use a dataset of MR atlases with their corresponding ground truth labels to find the segmentation of an unseen target image. The problem is that these approaches still require manual annotations on atlas images. In this thesis, a multi atlas segmentation algorithm is proposed that removes the burden of selecting an appropriate ground truth subset. The proposed coregistration and cosegmentation approach uses prior probability maps in the energy formulation of the registration process to segment multiple unseen images at the same time. Here, the priors are computed using two classifiers, Convolutional Neural Networks (CNN) and Random Forests. Contrary to the standard multi-atlas segmentation approaches, which usually segment one target image at a time, the proposed method performs the segmentation in a groupwise manner.

Once the sub-cortical structures are segmented, the location of alterations can be identified

using a shape analysis process. Among morphological analysis approaches, surface-based methods have become more popular because of their ability to represent local shape deformities. However, the main challenge in these methods is that these approaches are sensitive to the surface correspondences established across a population of meshes for the purpose of groupwise shape analysis. Recently, spectral matching approach has been proposed (Lombaert et al., 2013a,b) for mapping surface meshes in a computational efficient manner. In this thesis, the spectral matching algorithm is employed in a groupwise shape analysis pipeline, designed for the population-wise comparison between two groups of subcortical structures. In order to improve the surface matching accuracy, we incorporate the mean curvature information as an additional features in the spectral matching process.

The proposed groupwise shape analysis framework is applied on BECTS participants to extract the location of morphological alterations. Contrary to the previous studies that combined participants with different sides of seizure focus (Garcia-Ramos et al., 2015a; Kim et al., 2014), our experiments are conducted with respect to the location of epilepsy focus, to reveal the role of epilepsy lateralization on sub-cortical morphometry. In addition, the association between subcortical alterations and cognitive indices is studied, to verify whether sub-cortical morphometric alterations explain variations in cognition.

Therefore, this thesis precisely develops new methods for morphological analysis of subcortical structures in BECTS. The next sections provide the main contributions and an overview of the organization of the manuscript.

1.1 Thesis contributions

This thesis is in the field of biomedical imaging and summarizes the development of a brain morphological analysis framework, which are applied to the study of BECTS. The main contributions of this work can be summarized as follows :

— Presenting a data-driven coregistration and cosegmentation framework for automatic segmentation of sub-cortical structures on MR images. The proposed approach integrates the learned semantic segmentations, defined by convolutional neural networks (CNN), as priors into the energy formulation to boost the spatial transformation estimation in the registration process. Therefore, instead of only using the appearance features the developed method exploits the sophisticated learned probability maps to drive the coregistration process. Contrary to the standard multi-atlas segmentation approaches, which segment one target image at a time, our method considers a target set of images to be segmented and registered at the same time. Thus, in the case of large datasets, the burden of selecting an appropriate ground truth subset to perform

multi-atlas segmentation is removed ; one simply has to compute the probability masks on the input volumes (Chapter 5).

— Proposing a statistical shape analysis tool based on spectral matching to detect groupwise morphological changes across population of 3D surfaces. The spectral matching approach is integrated into a groupwise shape analysis framework, designed for the population-wise comparison between two groups of subcortical structures. The mean curvature feature is used as additional information in the spectral matching process in order to increase the surface matching accuracy. The proposed framework allows for the detection, localization, and quantification of statistically significant morphological alterations in brain subcortical structures in a computational efficient manner (Chapter 6).

— Establishing a relationship between sub-cortical morphometry and neuropsychological findings in children with benign epilepsy with centrotemporal spikes (BECTS) (Chapter 7). Previous research studies have not assessed the underlying structural shape alterations and its relation with cognition in this neurological disorder. In this study, MR imaging and statistical morphological analysis is used to detect morphological changes in children with left, right, or bilateral BECTS to age and gender matched healthy individuals. In addition, the association of morphological alterations with neuropsychological performance is investigated.

1.2 Thesis structure

This thesis is composed of nine chapters. Following this introduction, Chapter 2 provides background information that is necessary for reading this thesis. Chapter 3 presents a critical review of the literatures and a summary of the state of the art on segmentation, shape analysis, and previous findings on benign epilepsy with centrotemporal spikes. The research problem, objectives and hypothesis, along with the general methodology are described in Chapter 4. The main body of this thesis is presented as three research publications which are included in Chapter 5 to Chapter 7. The first two papers has been published and the last one has been submitted for publication. The organization of the chapters is as follows :

The Chapter 5 presents the first article entitled "Prior-based Coregistration and Cosegmentation" accepted by the International Conference on Medical Image Computing and Computer Assisted Intervention (MICCAI 2016). This paper presents a coregistration and cosegmentation approach of 3D MRI data guided by semantic label likelihoods, obtained from a deep convolutional neural network (CNN).

The Chapter 6 presents the secondary article entitled "Statistical shape analysis of subcortical structures using spectral matching" published by the journal of Computerized Medical Imaging and Graphics. This paper presents a new groupwise shape analysis framework for subcortical surfaces based on spectral matching theory, in order to detect regional morphological alterations of subcortical structures from patients with neurological conditions.

The Chapter 7 presents the third article entitled "Sub-cortical brain morphometry and its relationship with cognition in rolandic epilepsy" submitted to the journal of Epilepsy Research. This paper presents a study on sub-cortical morphological alterations in benign epilepsy with centrotemporal spikes (BECTS) in children with left, right, or bilateral hemispheric focus. In addition, the link between sub-cortical morphometry and neuropsychological performance are assessed.

In Chapter 8, the general objectives of the thesis and its benefits to the neuroimaging community are briefly discussed. Finally, Chapter 9 summarizes the findings, limitations, and main recommendations for future work.

CHAPTER 2 BACKGROUND

In this chapter, the background information related to the research project is proposed. First, the anatomy of the brain will be explained, followed by a brief description of the anatomy of each sub-cortical structure. Then, benign childhood epilepsy with centrotemporal spikes and its characteristics will be described. The final section will present the available computer aided diagnosis systems, which contribute to the study of epilepsy.

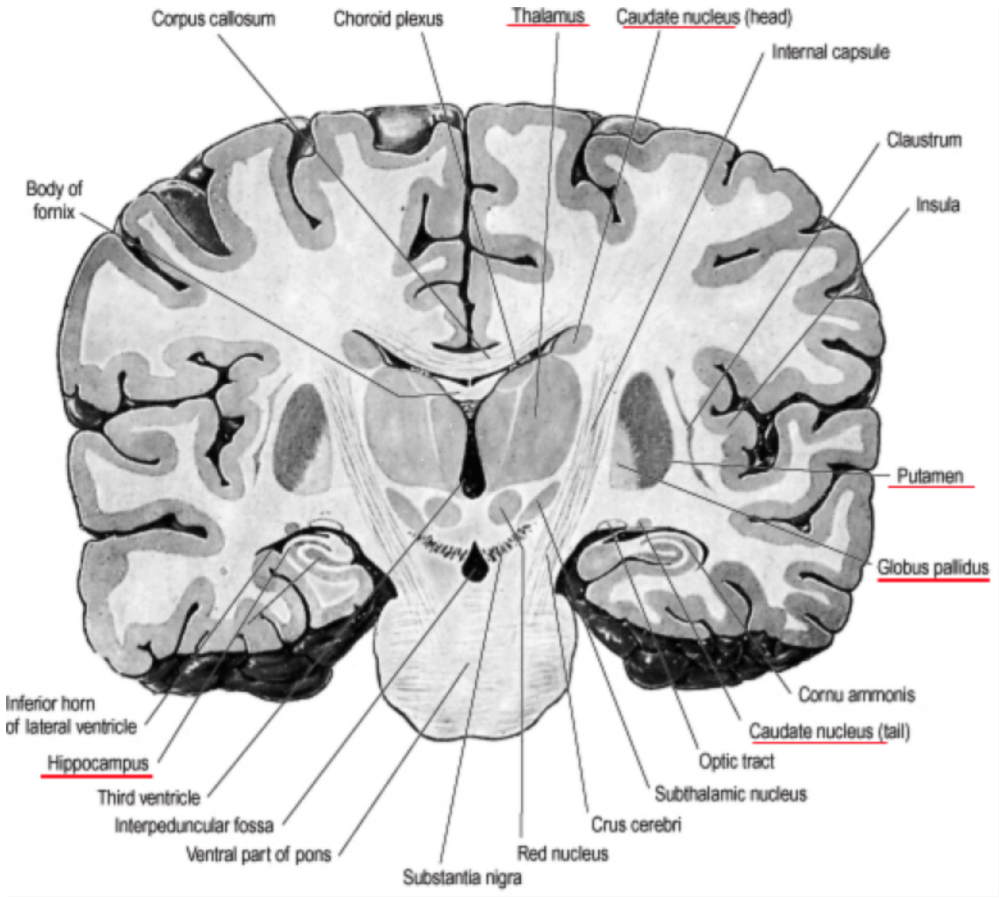

Figure 2.1 The brain in coronal view. Sub-cortical structures are underlined in red (Standring, 2016).

2.1 Anatomy of the brain

The human brain consists of two major tissue components : white (WM) and gray matter (GM), and the brain floats in a clear bodily fluid, which is called the cerebrospinal fluid (CSF). The cortex is a gray matter layer that covers the outer brain surface, over the white

matter tracts in the brain. The white matter comprises the connective pathways between the various processing regions. The sub-cortical structures are groups of grey matter organs within the brain that are not included as part of the cortex. Figure 2.1 shows the location of sub-cortical structures in a brain. Figure 2.2 illustrates the $3D$ view of different sub-cortical structures.

The anatomy of sub-cortical structures is described in the following paragraphs.

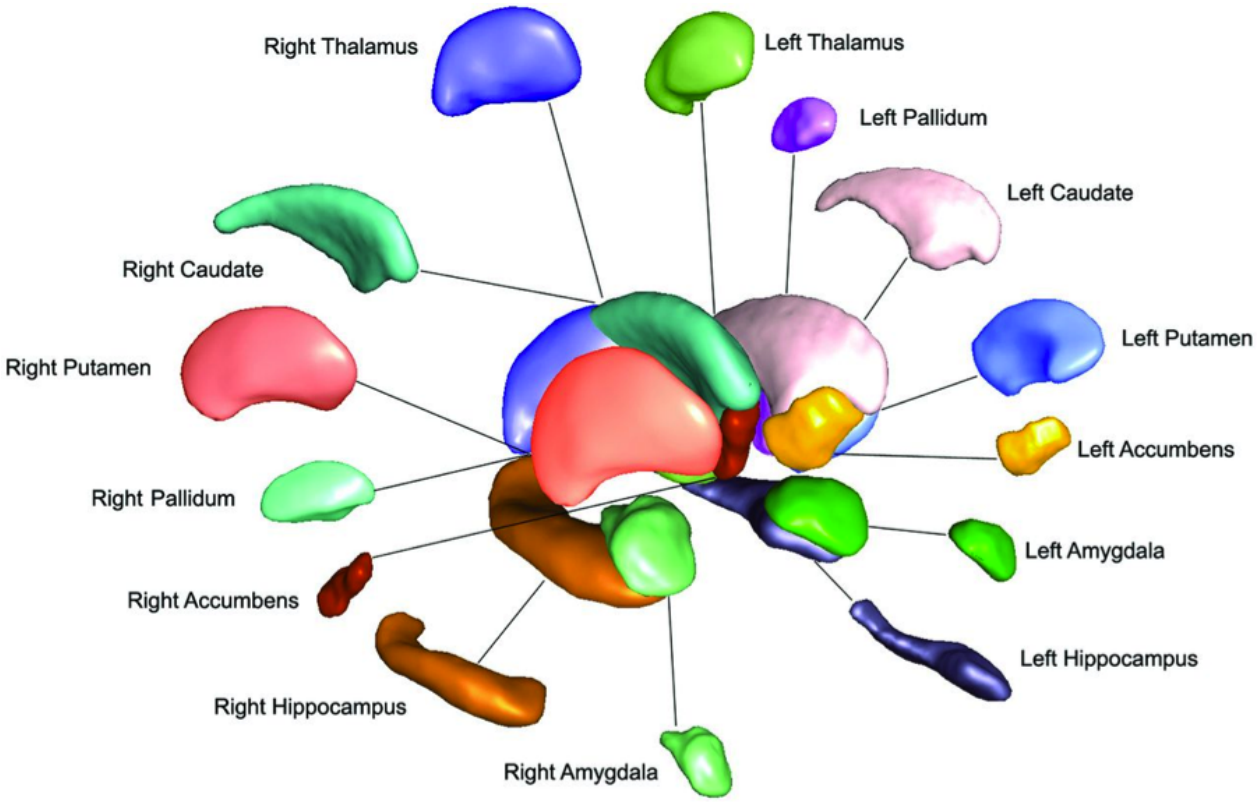

Figure 2.2 3D view of left and right deep gray matter structures (Patenaude et al., 2011a).

The Thalamus

The thalamus is a large egg-shaped nuclear mass, which is located in both hemispheres at the midline. The two thalami are separated medially by the third ventricle. The thalamus may be thought of as a relay station for the brain, since it serves as a communication hub between various regions of the brain (Standring, 2016).

The Basal Ganglia

The basal ganglia are a group of nuclei, which are located in the medial temporal lobe, above the thalamus and connected to the cerebral cortex. Typically, the basal ganglia include the caudate nucleus, putamen, pallidum, and nucleus accumbens. The basic functions of these nuclei deal with cognition, learning, and motor control and activities. The basal ganglia are also associated with learning and memory processes, such as motor skills. Damage to the basal ganglia has been linked to dysfunctional learning of motor and perceptual-motor skills (Standring, 2016).

The Hippocampus

The hippocampus is a small grey matter (GM) structure that resides symmetrically in the medial temporal lobes of both hemispheres of the brain (Standring, 2016). The hippocampus can be subdivided into an anterior section, a medial section, and a posterior section, commonly referred to as the head, body, and tail, respectively. The hippocampus is responsible for carrying out complex behaviour tasks such as declarative and representative memory processing. It is often related to loss of memory in patients with Alzheimer's disease.

The Amygdala

The amygdala is located in the medial temporal lobe. It has a rounded shape and is situated anterior and superior to the hippocampus. The amygdala and hippocampus are two primary structures that comprise the limbic system. The limbic system is largely involved with emotional responses as well as transforming short-term memories to long-term memories (Standring, 2016).

2.2 Benign childhood epilepsy with centrotemporal spikes (BECTS)

BECTS (also called rolandic epilepsy) is an age-dependant syndrome. The peak frequency of onset in 75% of the cases (Panayiotopoulos, 2005) occurs in children aged from three to 13 years old, with a 1.5 male predominance (Panayiotopoulos, 2005) and it is resolved by mid-adolescence (Sarco et al., 2011).

Epileptic seizures in BECTS are caused by the "hyperexcitability of the somatosensory or somatomotor system" of a system of neurons in one hemisphere (Capovilla et al., 2009). The focal seizure can sometimes lead to a generalized tonic-clonic seizure (Chan and Lee, 2011). Seizures are typically brief, increasing during sleep and drowsiness, lasting in general from 1

to 3 minutes (Panayiotopoulos, 2005).

The diagnosis of BECTS can be strongly suspected by the distinctive seizure semiology in addition to the age of onset and nocturnal predominance (Shields and Snead, 2009). A diagnosis can be confirmed by electroencephalography (EEG). The EEG in BECTS children is distinctive, showing centrotemporal spike (CTS) discharges with a horizontal dipole that is negative in the centrotemporal area and positive in the frontal area (Shields and Snead, 2009).

With regards to the aetiologies of RE, the underlying cause of this disease remain largely unknown, although a genetic basis is postulated in the majority of affected RE individuals (Reinthaler et al., 2014). Genomic variation at $16p11.2$ was found in 1.3% of RE, and the 16p11.2 duplication represented a significant genetic risk factor for children with BECTS (Reinthaler et al., 2014) . An autosomal dominant inheritance of the EEG trait centrotemporal spikes has been found in a few studies (Heijbel et al., 1975; Bali et al., 2007), while several other studies reported a complex mode of inheritance (Vears et al., 2012). Linkage studies identified loci for centrotemporal spikes on $15q14$ and $11p13$ (Neubauer et al., 1998; Strug et al., 2009). In addition, fine mapping CTS revealed an association between CTS and the $ELP4$ gene, but causative mutations have not yet been identified (Strug et al., 2009).

Initially, BECTS was considered as benign among other epilepsies, since it was generally reported that cognitive abilities were preserved or brought back to normal during remission (Lindgren et al., 2004; Verrotti et al., 2002). However, the relationship between the neuropsychological disorder and the pediatric epilepsy is well established, with up to a 50% prevalence of learning difficulties (Sarco et al., 2011). Recently, more and more studies on BECTS show the presence of cognitive and behavioral deficits. Researches studying BECTS often report general deficits (Danielsson and Petermann, 2009) in IQ (Weglage et al., 1997), sleep (Piccinelli et al., 2008), mood and behavioral disabilities (Sarco et al., 2011; Verrotti et al., 2002), impaired quality of life (Connolly et al., 2006), fine motor dysfunction (Perkins et al., 2008), and social behaviour problems (Genizi et al., 2012). Similar results were obtained in studies investigating a larger population of patients diagnosed with BECTS (Northcott et al., 2005, 2007). According to the studies, these cognitive deficits may be resolved or may well persist during remission. Moreover, in BECTS, the earlier in life the onset and the higher the number of seizures occur, the greater the probability of developing specific learning impairments is (Piccinelli et al., 2008).

2.3 Computer aided detection in epilepsy

Advances in medical imaging technology and computer science have greatly enhanced interpretation of medical images, and contributed to early diagnosis of different neuropathologies. The development of Computer Aided detection (CAD) systems to assist physicians in making better decisions has been an area of high interest in recent years. CAD systems aim to provide a computer output used as a second opinion in order to assist physicians in the detection of abnormalities, quantification of disease progress and alternate diagnosis of lesions. Modern structural and functional brain imaging methodologies have made a great impact in the diagnosis and management of epilepsies (Panayiotopoulos, 2005). Here, we introduce the two common techniques (i.e., electroencephalography (EEG) and magnetic resonance imaging (MRI)), which are used to obtain a proper diagnosis of epilepsy in individuals with seizures.

Electroencephalography (EEG)

Electroencephalography (EEG) (Schomer and Lopes da Silva, 2010) is the measurement of the electrical activity of the brain by recording from electrodes placed on the scalp. The resulting traces are known as an electroencephalogram (EEG) and represent an electrical signal from a large number of neurons. EEGs are frequently used in experimentation because the process is non-invasive to the research subject. The EEG is capable of detecting changes in electrical activity in the brain on a millisecond-level. EEG is the main diagnostic tool for epilepsy and it can be used for gross localization of epileptogenic area. EEG is one of the few techniques available that has such high temporal resolution. However, it has poor spatial resolution in comparison to other imaging techniques. The BECTS EEG shows centrotemporal spike-wave discharges. It is important to perform a wake-sleep EEG on these children because the spike-wave discharges are activated as the patient enters the sleep phase (Shields and Snead, 2009).

Magnetic resonance imaging (MRI)

Magnetic resonance imaging (MRI) (Panayiotopoulos, 2005) is a non-invasive imaging technique that provides high-resolution images of soft tissues. After a patient lies in an MRI scanner, the scanner creates a strong magnetic field around the body. The protons in the body line up in the same direction. Then the short bursts of radio waves are sent, knocking the protons out of alignment. When the radio waves are turned off, the protons realign and in doing so send out radio signals, which are picked up by receivers. The protons in different

types of tissue realign at different speeds and produce distinct signals. Thus, these signals provide information about tissue types.

MRI scanners use magnetic fields, radio waves, and field gradients to generate images of the body tissues. The protocol for the MRI acquisition process must be set up to produce the appropriate spatial characteristics for a specific clinical procedure. This includes factors, such as the number of slices, slice orientation, and the structure within each individual slice. Multiple MRI sequences exist and each sequence has numerous variations. For instance, there are image acquisition techniques such as spin-echo and gradient echo, and images can be acquired one at a time or in a volumetric manner. T1-weighted imaging is one of the fundamental MR imaging sequences, in which gray matter is relatively darker than white matter. T1 image is useful for assessing the cerebral cortex and identifying fatty tissue. T2-weighted imaging is another fundamental MR imaging sequences, where white matter appears darker than gray matter. T2 contrast is useful for detecting edema, revealing white matter lesions. Each of MRI scan variations has their strengths and weaknesses, and determining the optimal imaging strategy may vary by institution, as well as by disease process. In general, the magnetic resonance imaging scans allow in vivo visualization of structural alterations in epileptic patients. The sensitivity for detecting subtle abnormalities could be increased by improvements in scanner hardware, acquisition sequences and post-acquisition processes.

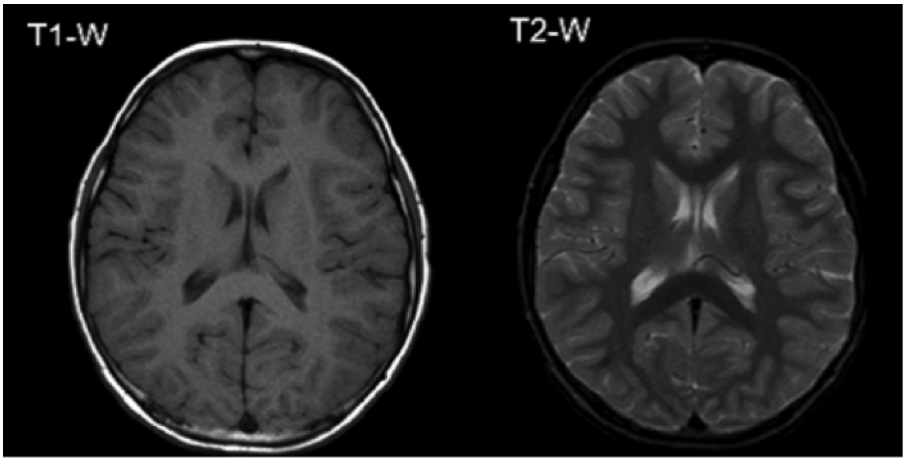

Figure 2.3 T1- and T2- weighted MRI scans.

2.4 Summary

In summary, in a child with epileptic seizures, a recording of brainwave activity using EEG and an MRI of the brain are usually used to obtain a proper diagnosis. In special circumstances, when medication fails to control seizures or the side effects become intolerable,

surgical intervention may be used. Hence, different medical imaging approaches would help localize the side of epilepsy and detect the specific location of brain region that generates seizures. Besides, medical analysis approaches could be combined with advanced techniques in computer science to enhance interpretation of medical images, and contribute to the diagnosis of neurological disorders.

CHAPTER 3 CRITICAL LITERATURE REVIEW

3.1 Segmentation of magnetic resonance images

The goal of brain structure segmentation in MR images is to define the boundaries of a specific neuroanatomical region, so that it could provide informative characteristic of structures, which could assist physicians in the detection of abnormalities and quantification of disease progress. Segmentation is a crucial step in a medical image analysis pipeline, since its quality affects the accuracy of the subsequent analysis. Furthermore, brain structure segmentation in MR images is a challenging task, due to the fact that the intensity distributions of different structures show considerable overlap and some boundaries are not visible on MR images. Therefore, sub-cortical segmentation methods cannot rely on intensity information alone. They need a priori knowledge to separate the structure of interest from the background.

Before applying a segmentation algorithm on a brain MR image, several preprocessing steps might be necessary. One preliminary step for many segmentation algorithms is skull stripping or brain extraction process. In this pre-processing step, skull, fat, and dura mater are removed from the MR image. The skull stripping process can be performed manually or automatically. The two common automatic skull stripping tools are Brain Extraction Tool (BET) (Smith et al., 2004), and Robust Learning-Based Brain Extraction (ROBEX) (Iglesias et al., 2011) algorithm.

Intensity inhomogeneity correction is another pre-processing step that is usually performed before applying a segmentation algorithm. Intensity inhomogeneity in MRI is typically caused by the imperfections of the image acquisition process, such as B1 inhomogeneity, receive coil non-uniformity, or static field inhomogeneity (Vovk et al., 2007). The N4 algorithm proposed in (Tustison et al., 2010) corrects intensity inhomogeneity on MR images and has been implemented in the software package of Medical Image Processing Analysis and Visualization(MIPAV) [1]. Histogram matching is another preprocessing step, which is usually required in segmentation algorithms based on multiple images. Histogram based intensity normalization ensures homogeneity of corresponding tissue type intensities between the images. This process has also been implemented in MIPAV software package.

Once all the required preprocessing steps are performed on a MR image, a segmentation approach can be applied to define the boundary of sub-cortical structures. The current brain structure segmentation literature can be divided into three categories with respect to the level

1. http ://mipav.cit.nih.gov/

of human involvement : manual segmentation, semi-automatic segmentation, and automatic segmentation.

Manual segmentation is usually performed by trained experts, following certain protocols defining regions of interest (ROIs). The anatomical knowledge of the expert contributes to the segmentation when the boundaries of the structures are difficult to detect because of the low tissue contrast between different structures. Although expert delineated segmentations are considered as the ground truth, in practice, manual approaches are subjected to both intra- and inter-rater variability (Nugent et al., 2013). Moreover, manually tracing the structures of interest by experts is a tedious task, which can be time consuming and expensive. This can make manual segmentation impractical and inefficient, especially when large cohorts of healthy and diseased population are involved.

Semi-automatic and automatic methods have been developed to reduce the subjectivity in the manual segmentation, and to increase the efficiency and reproducibility. In semi-automatic methods, prior knowledge is introduced by a human operator who identifies landmarks, seed points, or bounding boxes (Chupin et al., 2007; Shen et al., 2002; Ghanei et al., 1998). However, in automatic methods, the segmentation protocol is fully automated, and there is no demand of interaction with the user (Konrad et al., 2009). In order to validate the accuracy of an automatic segmentation approach compared to a ground truth annotation (manual segmentation), different metrics can be used. For instance, Dice coefficient (Dice, 1945) estimates the amount of volume overlap between the automatically segmented structure (A) and the corresponding manually annotated one (B) :

$$Dice(A, B) = 2\left|\frac{A \cap B}{|A| + |B|}\right| \tag{3.1}$$

Dice coefficient ranges between [0, 1] and is equal to 1 when the two segmentations of A and B are completely similar. Contour mean distance (CMD) [2] is another metric that computes the average vertex-by-vertex Euclidean distance between the automatic annotation A and the ground truth labeling B in 3D. Hausdorff distance (HD)[2] measures the maximum 3D distance between A and B. Hausdorff distance metric has high sensitivity to positional differences between two segmentations, while Dice and contour mean distance calculate the average similarity between two segmentations and ignore tiny over-segmentation error that might occur in an automatic segmentation process.

The current fully automatic brain structure segmentation literature can roughly be divided

2. http ://plastimatch.org/plastimatch.html

into five categories based on the type of additional knowledge that they incorporate : voxel classification, deformable models, shape and appearance models, atlas-based segmentation, and deep learning based approaches. In the following sections these paradigms will be briefly introduced.

3.1.1 Voxel classification-based approaches

Voxel classification-based methods segment brain structures voxel-by-voxel based on spatial and appearance information. To segment an unlabeled target image, manually labeled example images in a feature space are used to train a voxel classifier and find the decision boundaries that best separate different structures. After training, the classifier is applied to the unlabeled target images by mapping them in the feature space and labeling them according to the decision boundary. The available classification based segmentation methods vary in terms of the type of features used and the approach applied to derive the decision boundary.

Arzhaeva et al. (Arzhaeva et al., 2007) presented a supervised voxel classification method for segmentation of the caudate nucleus from brain MRI images. They used general spatial and local structure features extracted from image voxels together with a k-nearest neighbor classifier. Although the method performed well on the test data originating from the same population as the training images, it failed on data with different intensity ranges. Powell et al. (Powell et al., 2009) employed features, including probability information, spatial location, and intensities of voxels and their direct neighbours to delineate the subcortical nuclei and the cerebellum (See Figure 3.1). They compared the performance of two different machine learning algorithms, artificial neural networks (ANN) and support vector machines (SVM). Some reliable segmentation results were achieved using both applied methods. Morra et al. (Morra et al., 2010) and Maglietta et al. (Maglietta et al., 2016) segmented the hippocampus using thousands of features and a boosting algorithm(e.g., ADABoost or RUSBoost). Their experiments showed that RUSBoost gave the best results in terms of evaluation metrics and agreed well with human raters.

An important point in voxel classification based approaches is that, using more features improves the classifier's ability to model the structure's appearance and location. However, it also tends to increase the complexity of the decision boundary, which increases the risk of overtraining. One can decrease this risk by increasing the number of examples, constraining the complexity of the decision boundary, or decreasing the number of features by removing those that are not very relevant for the classification accuracy.

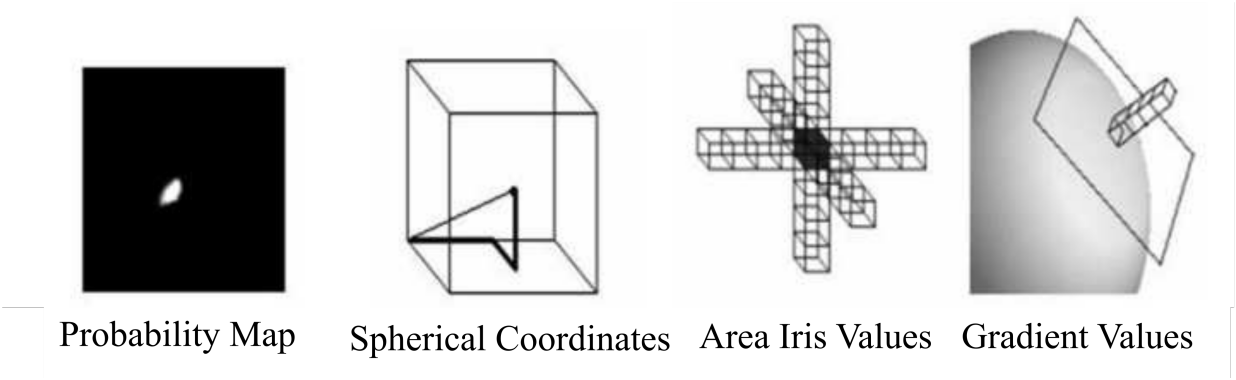

Figure 3.1 An example of an input feature vector including probability information, spherical coordinates, area iris values, signal intensity along the image gradient (Powell et al., 2009).

3.1.2 Deformable model methods

Deformable model methods iteratively deform the boundaries of an initial shape to find the true border of the target structure while minimizing an energy function. These methods use the boundary forces from the gradient image to warp a shape structure to the edges of the structure (See Figure 3.2). The model can be improved by integrating prior anatomical knowledge, like shape orientation or landmarks (Pitiot et al., 2004).

A group of deformable model based methods constrained the deformable surface to evolve within the range of normal shape variations, in order to prevent unreasonable shape deformation. Ghanei et al. (Ghanei et al., 1998), attempted to incorporate the statistical shape information using a deformable balloon model. Keleman et al. (Kelemen et al., 1999) used the mean shape of healthy subjects in the initial step and used PCA to guide the deformation direction. The problem of using prior information based on healthy subjects is that in the presence of anatomical variants, segmentation method may fall into local minima.

Apart from these parametric models, recently non-parametric models using level-set formulation have been used for this problem (Tsai et al., 2003; Yang and Duncan, 2004). These models enable more flexible deformations against morphological and topological variations. However these non-parametric models do not allow for point-wise inter subject correspondences, which complicates local sampling to capture texture and shape characteristics within separate regional compartments (Yang and Duncan, 2004).

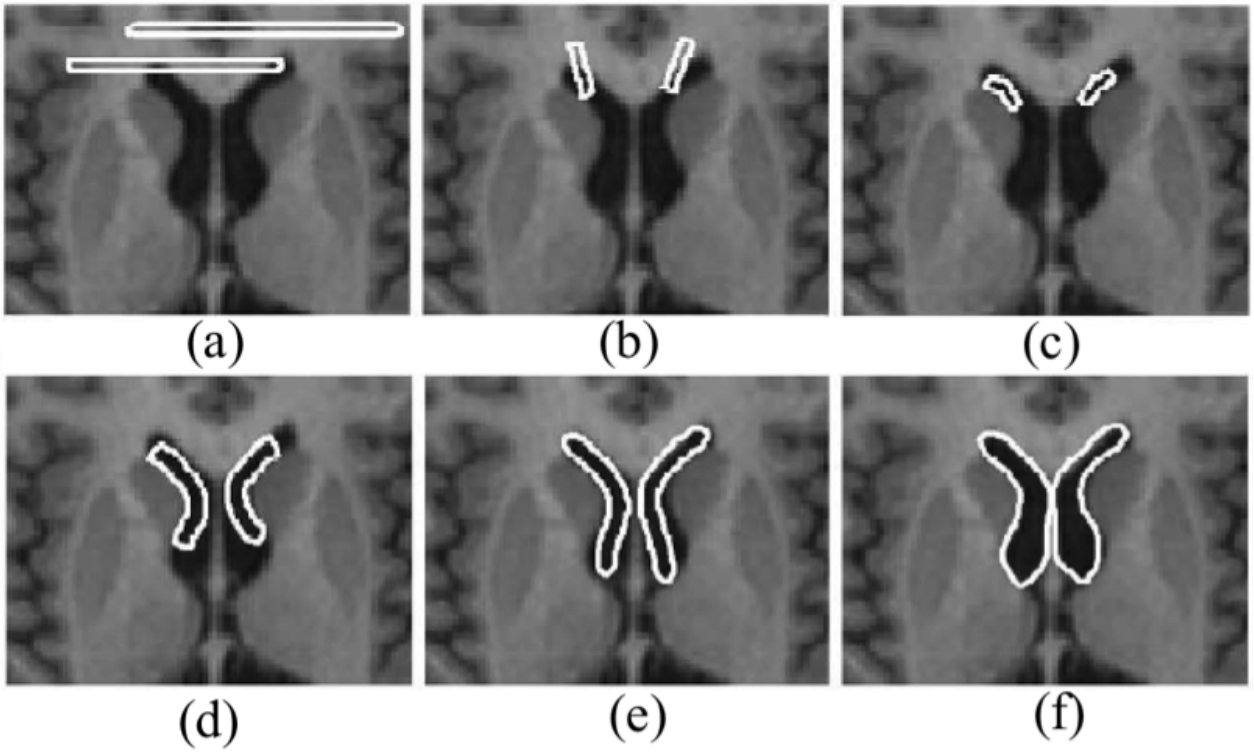

Figure 3.2 Automatic MR image segmentation of lateral ventricle by deformable model. (a) initial contours ; (b-e) intermediate results of contour deformation ; (f) final result (McInerney et al., 2002).

3.1.3 Shape and appearance based methods

The Active Shape Model (ASM) is an automated segmentation method that has been widely used in medical image segmentation over the past two decades (Cootes et al., 1995) (See Figure 3.3). The ASM introduced the notion of using a Point Distribution Model (PDM) to model shape of each structure, where a shape is represented by a surface, which is composed of a set of connected vertices. Constructing a statistical shape model basically consists of extracting the mean shape and a number of modes of variation from a collection of training samples. Images are segmented using the model built from the training data, which specifies the range of likely shapes.

Active Appearance Model (AAM) is an extension of the ASM framework that incorporates intensity and texture information in addition to the shape structure of the landmarks (Cootes et al., 1998). The AAM relates the shape and intensity models with each other using a weighting matrix estimated from the training set. Fitting shapes to unseen images is done by minimizing the square of residual differences between predicted intensities and obser-

ved image intensities. Many variants of this basic formulation have been presented in the literature (Heimann and Meinzer, 2009).

Székely et al. (Székely et al., 1996) and Kelemen et al. (Kelemen et al., 1999) employed spherical harmonic mapping for each training shape rather than using a PDM. The elastic deformation of the model is used to match the local intensity profile to a prior shape subspace learned from the training set. The technique has been applied to automatically segment the left and right hippocampus, thalamus, putamen, and globus pallidus from volumetric magnetic resonance scans taken from schizophrenia studies. Staib and Duncan (Staib and Duncan, 1996) employed Fourier surfaces (an extension of the classical 1D and 2D Fourier transforms) to describe shapes of several different topologies. They used the conjugate gradient (CG) algorithm to fit the statistical shape model to new data. The method was applied to synthetic images and $3D$ medical images of the heart and brain (e.g. caudate).

Shen et al. (Shen et al., 2001, 2002) employed local affine transformations, modulated by a Gaussian envelop function, to adjust the deformable model. The proposed model has the ability to weight different parts of the model differently during the search process. These techniques have been used to segment boundaries of the ventricles, the caudate nucleus, the lenticular nucleus, and hippocampus from volumetric MR images. Duchesne et al. (Duchesne et al., 2002) proposed an appearance based method, which incorporates analysis of dense 3D deformation fields from a nonlinear registration algorithm into the framework of appearance-based segmentation.

Pizer et al. (Pizer et al., 2003) presented a medial model with a coarse-to-fine representation which consisted of a collection of points on the centerlines and vectors pointing from there towards the boundary. This approach had a special deformation scheme, where the entire Statistical Shape Model (SSM) was first fitted globally in a hierarchical procedure. Then individual subfigures and subsequently the medial atoms are adjusted (all using a conjugate gradient optimizer). The method was applied to segment the hippocampus from MR images.

A different approach to increase model flexibility is to divide the SSM into several, independently modeled parts. The rationale behind this is that smaller parts exhibit less variation, which can be captured with fewer training samples than the variation for the full shape. Zhao et al. (Zhao et al., 2005) presented a scheme based on mesh partitioning, in which each part of the mesh is modeled separately, but parameters for the individual parts are connected by curves in a combined shape space. The authors claim that limiting these curves to similar patterns as encountered in the training set helps to prevent invalid shapes of the SSM. The method applied to MR images of the left thalamus and left hippocampus. Nain et al. (Nain et al., 2007) presented a novel multi-scale shape representation based on the spherical wavelet

transform. This methodology found independent shape variation processes at multiple scales. They applied the algorithm to two different brain structures, the caudate nucleus and the hippocampus, in the study of schizophrenia. Hu et al. combined a level-set method to model the brain structures and their variation with active appearance modeling to generate images that are used to drive the segmentation (Hu and Collins, 2007). This algorithm incorporated multi-modality images to improve the segmentation performance.

Patenaude et al. (Patenaude et al., 2011a) proposed a segmentation tool (FSL-FISRT), which uses a Bayesian probabilistic approach. The shape and appearance models in FIRST are constructed from a library of manually segmented images. The manual labels are parameterized as surface meshes and then modeled as a point distribution. Using the learned models, FIRST searches through shape deformations that are linear combinations of the modes of variation to find the most probable shape instance given the observed intensities from the input image.

The most important difference between the proposed methods in the field of active shape models is the flexibility of the parameterization. In an ASM approach, a general model with many degrees of freedom can describe a complex boundary, but requires more labeled examples to represent the potential shape variations.

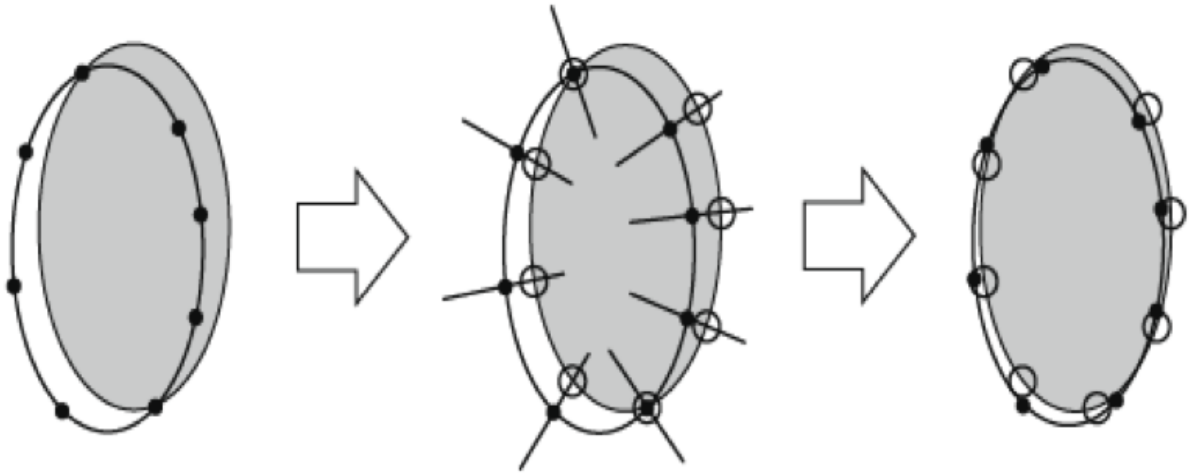

Figure 3.3 One iteration of an ASM search : At the beginning, the model is located at the lower left of the true position. Local appearance models for all landmarks are evaluated. Finally, model parameters are updated to minimize the squared distances to the found best positions (Heimann and Meinzer, 2009).

3.1.4 Atlas-based methods

In atlas-based segmentation approaches, additional knowledge is introduced through an atlas image, in which an expert has labeled the brain structures of interest. The atlas is first nonlinearly registered to the target image, and the resulting transformation is then used to deform the atlas labels to the coordinate system of the target image. Atlas-based segmentation approaches reported in the literature differ in the type of deformations that is applied. Registration methods based on elastic (Miller et al., 1993; Losifescu et al., 1997; Christensen and Johnson, 2001), fluid (Hogan et al., 2000; Crum et al., 2001), and optical flow (Baillard et al., 2001; Dawant et al., 1999; Hartmann et al., 1999) have been involved in matching the image with the atlas.

Collins et al. presented a framework (Collins et al., 1995; Collins and Evans, 1997) denoted as ANIMAL, which is an iterative procedure that estimates a 3D deformation field that matches a source to a target volume. In this approach, first, the deformations required to match blurred versions of the source and target data are estimated. Then, this deformation field is upsampled and used as input to the next iteration, where the blurring is reduced and the estimation of the deformation field is refined. Khan et al. (Khan et al., 2008) combined the probabilistic-based FreeSurfer labeling method with the Large Deformation Diffeomorphic Metric Mapping (LDDMM) (Beg et al., 2005) to search for optimal nonlinear transformation between the image and the atlas. In another study, an appearance model method has been used to guide the deformation (Duchesne et al., 2002; Klemencic et al., 2004). Avants et al. (Avants et al., 2008, 2010) developed a symmetric image normalization method (SyN) for maximizing the cross-correlation within the space of diffeomorphic maps between a source and an atlas image. (Ardekani et al., 2005) presented a high-dimensional non-parametric automatic registration toolbox (ART), which has been used in atlas based segmentation in (Klein et al., 2009). Klein et al. (Klein et al., 2009) provided a comprehensive evaluation of the accuracy of atlas-based brain structure segmentation with several different publicly available registration methods. SyN (Avants et al., 2008, 2010) and ART (Ardekani et al., 2005) registration techniques were the only methods that attained top rank for all tests in that large-scale evaluation of brain image registration methods.

As mentioned above, in atlas-based segmentation methods, image information is transferred from the labeled atlas to subjects through non-rigid image registration. Since the image registration algorithms are inherently related to the anatomical similarity between atlas and subject, an atlas that is anatomically similar to a subject would result in better performance for the segmentation. However, if the anatomy of the atlas is very different from the target, the accuracy of the segmentation tends to decrease. Therefore, the choice of atlas has a

vital impact on the accuracy of the final segmentation. To cope with this problem, a group of studies have demonstrated the use of an optimal atlas in a number of cortical and sub-cortical segmentation applications (Avants et al., 2010; Wu et al., 2007).

Another way to resolve this issue is the iterative registration of multiple manually labeled training images into a common space (Joshi et al., 2004). The resulting deformations are then applied to both the training images and their manual labels. The result of this process would be a smooth image (atlas) and a probability map, which represents the average anatomical variation of the training population. This average atlas, along with the probability maps can then be used to segment an un-labeled target image (Gouttard et al., 2007; Hammers et al., 2003). In this regard, the FreeSurfer software package (Fischl et al., 2002) uses a probabilistic atlas of anatomical and tissue classes along with spatial constraints for class labels encoded using a Markov random field model to segment the entire brain.

Another possible solution to increase the atlas-based segmentation accuracy is to use a multi-atlas segmentation strategy, in which several atlases are registered to the target image and the deformed labels are combined to generate the final segmentation (Heckemann et al., 2006; Rohlfing et al., 2004) (See Figure 3.4). In this context, using a multi-atlas approach increases the accuracy and robustness of the segmentation, since the anatomical variability is represented more accurately compared to a single atlas based method. In addition, if a large number of atlases are available, results could even further be improved by selecting a subset of atlases that are very similar to the target (Aljabar et al., 2009; Wolz et al., 2010; Shen et al., 2010; Zikic et al., 2014). In a study by Chakravarty et al. (Chakravarty et al., 2013) new automatically generated atlases were created from a single labeled brain and the resulting atlases were used in a multi-atlas segmentation framework. However, this approach has the disadvantage that segmentation mistakes reinforce themselves. An extensive review of multi-atlas segmentation methods can be found in (Iglesias and Sabuncu, 2015).

One imperative point in multi-atlas segmentation is how to combine the labels from initial atlases to generate the final segmentation. Voxel-wise majority voting is a basic method that has been proposed as a label fusion strategy (Heckemann et al., 2006). A more sophisticated approach is weighted voting strategies that uses global (Artaechevarria et al., 2009), local (Isgum et al., 2009; Sabuncu et al., 2010; Wang et al., 2011), semi-local (Sabuncu et al., 2010; Wang et al., 2013), and non-local (Coupé et al., 2012) intensity similarity metrics. These methods have demonstrated consistent improvement in segmentation accuracy (Artaechevarria et al., 2009; Sabuncu et al., 2010). In contrast to ad-hoc weighted voting, statistical fusion strategies have been proposed, which involves simultaneous truth and performance level estimation (STAPLE) (Warfield et al., 2004). This method estimates the performance

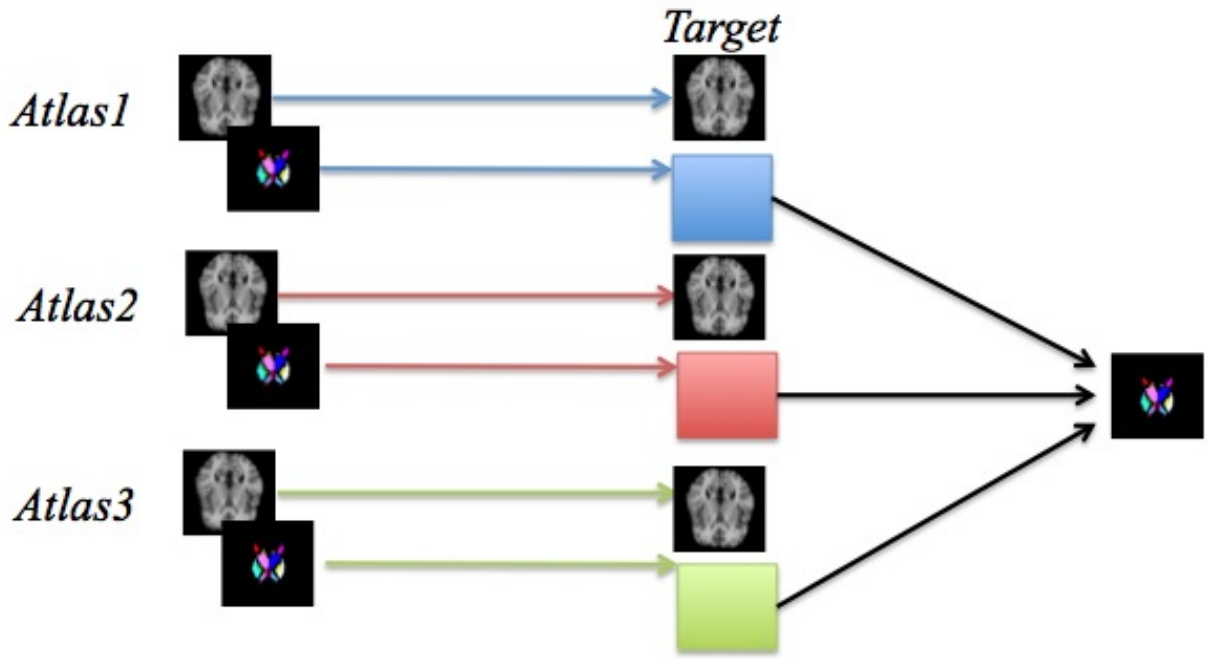

Figure 3.4 Schematic illustration of a standard multi-atlas segmentation. A set of atlas anatomical images $\{Atlas1, Atlas2, Atlas3\}$ are registered to the *target* image. The resulting transformations are used to transform the corresponding atlas segmentations to the *target*. The transformed segmentations are then combined to create an estimate of the *target* image segmentation

level of the atlases using an expectation-maximization (EM) algorithm. Non-Local STAPLE (NLS) (Asman and Landman, 2013) is an extended version of STAPLE, which reformulates the STAPLE framework from a non-local means perspective in order to learn what label an atlas would have observed, given perfect correspondence.

In general, using a single atlas has less computational complexity than performing a multi atlas segmentation. However, segmentation based on a single atlas might be less accurate than multi atlas segmentation approaches, since in multi-atlas methods each atlas could represent the anatomical variation of a separate population of subjects.

3.1.5 Deep learning-based methods

Deep neural networks can be considered as complex and highly non-linear mathematical functions which parameters are learned to transfer the input observed variables to the output variables. In the past few years, deep learning techniques, have shown outstanding results for feature extraction in many computer vision applications (Krizhevsky et al., 2012a; Chen

and Lin, 2014). Contrary to traditional machine learning techniques based on hand-crafted features or shallow networks, deep learning methods automatically learn hierarchies of relevant features directly from the raw inputs (Bengio, 2009). Recently, stacked autoencoder (SAE) (Hinton and Salakhutdinov, 2006) have been widely applied in medical applications such as multiple organ detection (Shin et al., 2013), brain tissue segmentation (Zhao et al., 2016), hippocampus segmentation in infants (Guo et al., 2014), and nuclei regions extraction Xu et al. (2016). A SAE is composed of two processes (Hinton and Salakhutdinov, 2006). First, an encoding process learns the parameters to map the input vector to a low-resolution latent representation. Second, a decoding stage regenerates the input vector from the latent representation.

Convolutional Neural Networks (CNNs) is another deep learning approach, which have helped set new performance records for many computer vision tasks, such as object detection, texture recognition and object semantic segmentation (Krizhevsky et al., 2012a). CNNs applies a series of convolution/pooling/subsampling operations to learn deep feature representations (Krizhevsky et al., 2012a). Zhang et al. (Zhang et al., 2015) used CNNs for brain image segmentation of three tissue types (WM, GM, and CSF) in MR images of 6-8 month-old infants. This method was based on 2D patches extracted from T1-weighted, T2-weighted and fractional anisotropy images. In another study on T1-weighted MR images, De Brébisson et al. (Brébisson and Montana, 2015) segmented 134 brain regions using a multiple parallel networks of 2D patches in orthogonal planes, a 3D patch , and distance to a previous segmentation step. Moeskops et al. (Moeskops et al., 2016) presented a multi-scale approach to segment brain structures of patients in different age groups. The method used multiple patch sizes and multiple convolution kernel sizes to acquire multi-scale information about each voxel. The method attained good results on eight tissue classes, with Dice similarity coefficients averaging between 0.82 to 0.91 on five different datasets.

In the majority of works in medical imaging domain, use of a deep network has shown to produce either similar or superior results compared to the state-of-the-art (Tajbakhsh et al., 2016). However, some major concerns still remain. Since neural networks architectures usually require large amount of data to train the network, there is a need to provide large datasets for each medical tasks. Another issue is about providing a strong input representation of medical images (e.g., $2D$ vs. $3D$, patches vs. whole images).

3.2 Shape analysis on sub-cortical structures

Quantifying morphological characteristics of brain structures is an important and challenging problem in medical image analysis. The development of sophisticated mathematical and

algorithmic methods for extracting and modeling brain structures allows for more accurate findings in medical studies, and the discovery of potential biomarkers for disease diagnosis. Early morphological studies on the brain structures were based on volumetric analysis, which had the advantage of simplicity (Shi et al., 2009; Hastings et al., 2004). However, structural changes at specific locations were not accurately detected using volumetric frameworks. Thus, shape analysis has emerged as a way of evaluating morphology location in the brain anatomy. Several works have been proposed for shape analysis in the literature, which can be classified into three categories : voxel-based, deformation-based, and surface-based analysis. We will present these categories in the following sections.

3.2.1 Voxel-based morphometry

Voxel-based morphometry (VBM) (Ashburner and Friston, 2000) has been used to assess structural abnormalities in various types of brain disorders, since it enables the automatic identification of regional changes in the amount of white matter (WM) and gray matter (GM) without a priori region of interest (Wilke et al., 2004). After applying preprocessing steps, such as non-uniformity correction and linear spatial normalization, an automated classifier is performed on MR images to categorize voxel intensities into GM, WM, or cerebrospinal fluid (CSF). An isotropic Gaussian kernel is applied to generate tissue density estimates at each voxel. The density estimates are used for statistical inference in order to assess differences of GM, WM, and CSF's tissue concentration among subjects. A set of major modifications have been applied to generalize the method for detection of changes in small regions. The detection process included an optimization method based on the integration of tissue specific templates, as well as a modulation process that adjusted tissue density estimates with Jacobian determinants computed in the nonlinear registration (Good et al., 2001).

Some studies have reported inconsistency between the detected atrophy by VBM and the one found by an expert manually (Kim, 2012). The inconsistent results and lower sensitivity of VBM may be explained by several factors. First, the size of the smoothing kernel might be large, making the detection of volume variation in smaller regions unlikely. Second, inaccurate spatial normalization in VBM approach could misplace the location of volume changes. Third, tissue density computation in VBM is highly dependent on accurate tissue segmentation (Kim, 2012).

3.2.2 Deformation-based morphometry

Deformation-based morphometry (DBM) methods evaluate the information contained within the deformation vector field generated by a non-linear warping of an individual MR image to a template (Chung et al., 2001). In DBM, the gradients (Jacobian) of the deformation field is used to identify volumetric structural differences. Figure 3.5 shows the use of DBM approach in a longitudinal study. DBM techniques have been applied to many brain image analysis studies to assess morphological changes related to disorders (Chung et al., 2001; Brambati et al., 2009). In contrast to VBM, DBM approaches do not need segmentation of a priori region of interest. However, due to the isotropic gaussian kernel-based smoothing process, DBM suffers from the same limitations as VBM and has low sensitivity in detecting abnormalities in small sub-cortical regions.

3.2.3 Surface-based approaches

In contrast to the voxel-based and deformation based approaches, surface-based techniques are able to examine highly localized morphological differences between groups, while preserving point-wise correspondences across subjects (Gerig et al., 2001a).

One type of surface-based method is based on medial surface descriptions, which allows for the quantification of local positional changes by assessing morphological variation of the skeleton extracted from a given structure (Bouix et al., 2005). Since this approach relies on coarse-scale sampling, it may not be sensitive enough to assess high dimensional features.

In addition to these methods, spherical harmonics were used in combination with Point Distribution Models (PDM) to discover structural differences across a population (Shen et al., 2003; Styner et al., 2006a). In an approach presented by Styner et al. (Styner et al., 2006a), namely SPHARM-PDM, a set of binary segmentations of a single brain structure, such as the hippocampus or caudate were first converted into a corresponding spherical harmonic description (See Figure 3.6). Then, the correspondence problem was solved by the alignment of the spherical parametrization using a first order ellipsoid. In this method, the spherical description of surface meshes was sampled into triangulated surfaces via a icosahedron subdivision. These surfaces were then spatially aligned using rigid Procrustes alignment. Although these methods have enabled the reliable assessment of local shape variation, they need to establish correspondence on simplified spherical models of surfaces, which is restricted to surfaces with spherical topology and is highly time-consuming.

We can conclude that among different shape analysis approaches in the literature, surface-based approaches enable the most reliable evaluation of regional alteration in brain struc-

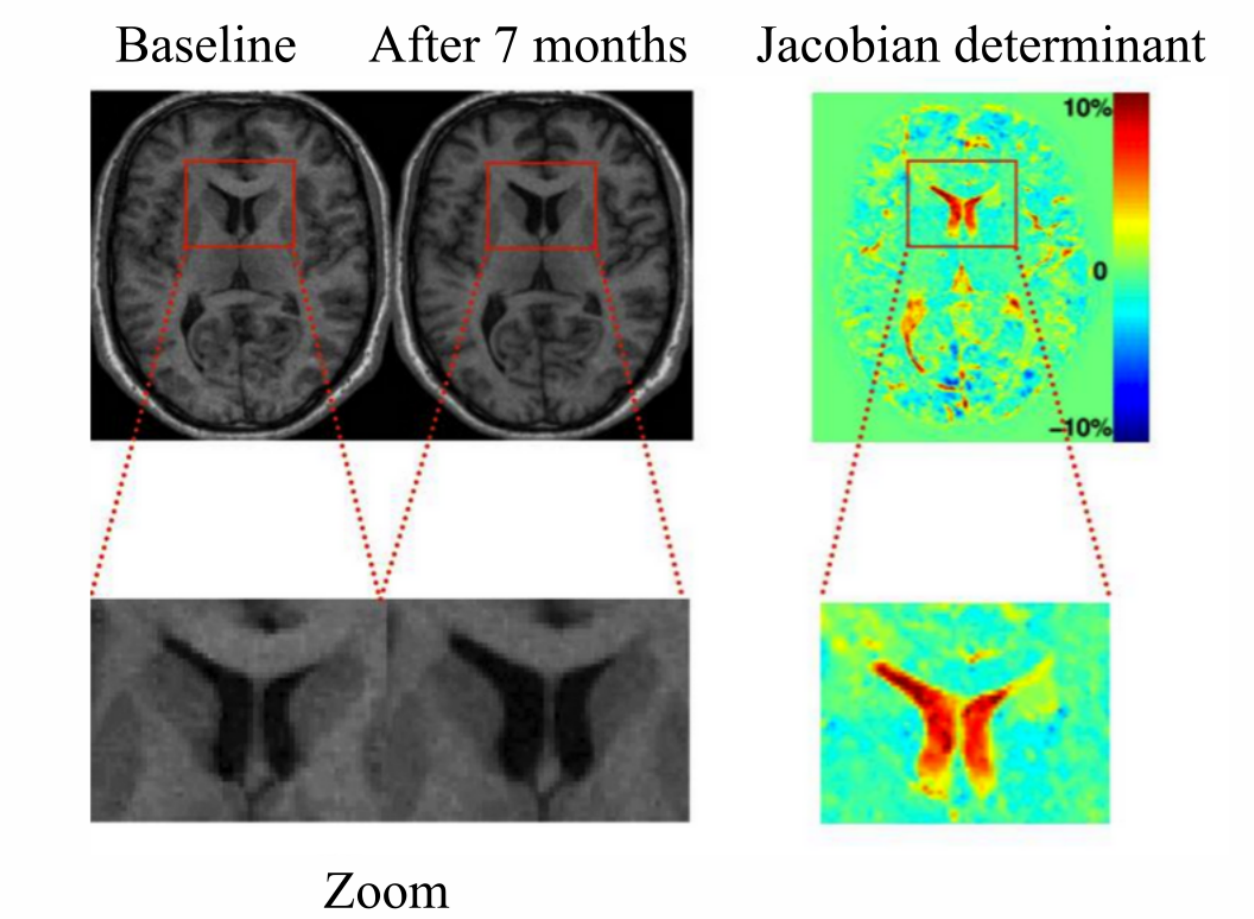

Figure 3.5 The principle of deformation-based morphometry (DBM). Two T1 images of a patient with schizophrenia are shown at his first episode and after 7 months. DBM warps the second scan to the baseline scan. The differences between two images are encoded in the deformations. Volume changes is calculated by computing of the Jacobian determinant (Mietchen and Gaser, 2009).

tures. However, these surface-based frameworks depend on establishing vertex correspondences across subjects, which are prone to inter-subject variability and are more adapted to sphere-like shapes.

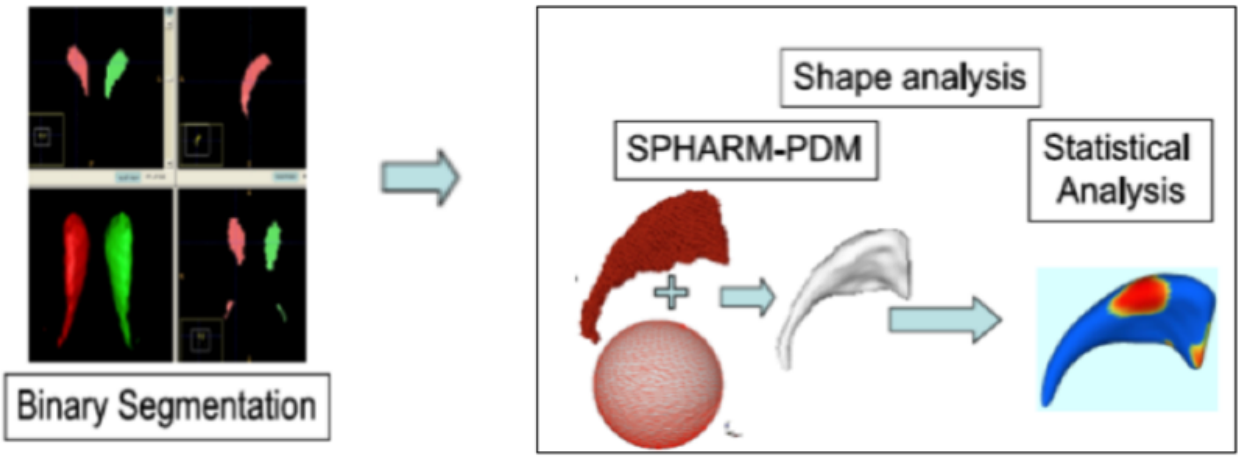

Figure 3.6 SPHARM-PDM based shape analysis. First, binary segmentations are converted to surface meshes. Then, the meshes are parameterized using a spherical harmonic description and point distribution models (SPHARM-PDM). Finally, statistical differences between surface meshes are computed to indicate the local shape variations (Styner et al., 2006a).

3.3 Benign childhood epilepsy

3.3.1 Cognitive impairments

BECTS is a self-limited childhood focal epilepsy associated with subtle cognitive impairments (Vannest et al., 2015). Examples of these cognitive deficits include attention, executive function, and memory dysfunction (Connolly et al., 2006; Danielsson and Petermann, 2009; Genizi et al., 2012; Northcott et al., 2005, 2007; Perkins et al., 2008; Piccinelli et al., 2008; Sarco et al., 2011; Verrotti et al., 2002; Weglage et al., 1997), which are likely responsible for poorer educational outcomes and behavioural problems (Pinton et al., 2006; Völkl-Kernstock et al., 2009). Hermann et al. (Hermann et al., 2006) found that regardless of epilepsy syndrome, children with new-onset epilepsy scored more poorly than controls across cognitive domains. Garcia-Ramos et al. (Garcia-Ramos et al., 2015b) also reported cognitive deficits in children with new-onset BECTS, which remained consistent over two years. Although children with BECTS typically no longer have seizures or centrotemporal spikes by the time they reach adulthood, language impairments have been shown to persist even when children with BECTS were in remission for 1-8 years (Monjauze et al., 2005, 2011). On the contrary, Volkl-Kernstock et al. (Völkl-Kernstock et al., 2009) found that problems with aggressive behaviour, attention problems, and anxiety/depression had resolved one year after remission. This shows that long-term follow-up studies on cognitive assessments of children with BECTS

are required to clarify the presence of cognitive and behavioural problems after remission.

A number of studies have focused on the relationship between the frequency and lateralization of centrotemporal spikes (CTS) on cognitive and behavioural outcomes in BECTS. A few studies suggested an association between CTS and poorer cognitive outcomes (Riva et al., 2007; Piccinelli et al., 2008), however other studies did not confirm this result (Goldberg-Stern et al., 2010; Jurkevičienė et al., 2012; Liasis et al., 2006). Moreover, Overvliet et al. (Overvliet et al., 2011) reported that a proportion of children with BECTS had speech and language therapy before they were diagnosed with rolandic epilepsy. This suggests that language difficulties may well precede spikes and/ or seizures. Therefore, it remains unclear whether Rolandic epilepsy (or the nocturnal epileptiform activity) causes the language impairments or whether the Rolandic epilepsy and the language impairments are both symptoms of an underlying syndrome (Overvliet et al., 2011). Literacy and language deficits might be part of an inherited set of impairments that accompany rolandic epilepsy, and which may be associated with delayed neural maturation (Doose et al., 1997).

3.3.2 Neuroanatomical alterations

Different studies have assessed the neuroanatomical alterations in BECTS. In (Sheth et al., 1997), the authors reported a cortical dysplasia perpendicular to the Sylvian fissure and ipsilateral to the spike lateralization in an eight year old girl with rolandic epilepsy. MRI-assisted EEG dipole analysis indicated that the discharges originated from the Sylvian fissure and not from the cortical dysplasia. Sarkis et al. (Sarkis et al., 2010) investigated the brains of children with benign focal epileptiform discharges. Half of those patients (45 cases) also had seizures consistent with benign epilepsy with centrotemporal spikes (BECTS). They reported the existence of abnormalities in 27% (12 cases) of children with BECTS (hippocampal atrophy, abnormal cortical development, Chiari malformation). Lundberg et al. (1999) found hippocampal abnormalities ipsilateral to the spike lateralization in six patients out of 18 children with BECTS. In their study, the MR images were reviewed by an experienced neuroradiologist, however no control group were included. Another study by Gelisse et al. (2003) on 71 patients with BECTS demonstrated ventricular enlargement and hippocampal atrophy in 14% of subjects. These detected abnormalities were not consistently ipsilateral to the spike lateralization. In Gelisse et al.'s study, only CT imaging was available for most of the subjects and no healthy group was included for comparison purposes. Boxerman and colleagues (Boxerman et al., 2007) performed a case-control study comparing the MRIs of 25 patients with rolandic epilepsy to 25 controls with migraines. Some structural abnormalities were found in 52% of rolandic epilepsy cases, but they were not statistically significant. All

these studies lacked a sufficient control group, due to including control participants with other pathologies, e.g., migraines Boxerman et al. (2007) or not using any control cohort Lundberg et al. (1999); Gelisse et al. (2003).

Kanemura et al. (Kanemura et al., 2011) studied the growth of the frontal and prefrontal lobe in seven children with BECTS with/without cognitive impairments and behavioural problems. They assessed the volume changes on MR images and evaluated correlations between prefrontal lobe growth and active seizure duration compared to 11 normal controls. Abnormalities in growth of the frontal and prefrontal lobes were found in some of the cases. In addition, prefrontal-to-frontal lobe volume ratio increased serially in some children with BECTS (5 cases) similarly to controls, but was stagnant or decreased in others (2 cases). Prefrontal growth also revealed more rapid recovery in one BECTS patient with shorter active seizure period. Thus, the authors reported that longer active seizure period with frequent spike-waves coupled with the occurrence of frequent seizures may be associated with prefrontal lobe growth abnormalities, which relates to neuropsychological problems. In (Pardoe et al., 2013), a Voxel-Based Morphometry (VBM) analysis indicated increased bilateral grey matter volume in the superior frontal gyrus, insula and right inferior frontal gyrus regions in BECTS compared to healthy controls. In this study, Pardoe and colleagues reported that the magnitude of gray matter volume increase and cortical thickening in BECTS lessened with age.

In a study on children with bilateral BECTS and healthy controls (Lin et al., 2012), Lin and colleagues found putamen hypertrophy in children with bilateral BECTS. Moreover, shape analysis showed dorsoventral elongation of the left caudate and bilateral putamen, with subnuclei expansion in ventral and dorsal striatum. They indicated that larger putamen volumes were linked to better cognitive performances in executive function tests. However, they focused on children with bilateral BECTS, and no experiment was conducted on children with left or right hemispheric seizure location. Kim et al. (Kim et al., 2015) compared MR images of 20 newly diagnosed BECTS to 20 age-matched healthy controls. According to their analysis, children with BECTS showed significantly thicker right superior frontal, superior temporal, middle temporal, and left pars triangularis cortices. Also, voxel-based morphometric analysis detected significantly larger cortical gray matter volumes of the right precuneus, left orbitofrontal, pars orbitalis, precentral gyri, and bilateral putamen and the amygdala of children with BCECTS compared to normal controls. Kim et al. combined children with different sides of epilepsy focus in one group, without considering the epilepsy localization. Garcia-Ramos et al. (Garcia-Ramos et al., 2015b) performed a longitudinal study comparing 24 children with new-onset BECTS and 41 age- and gender-matched healthy controls. They reported left and right putamen volume enlargement persisting over two years in BECTS compared to

healthy individuals. Baseline neuroimaging revealed thinner cortex in BECTS compared to controls in frontal, temporal, and occipital regions. Longitudinally, healthy controls showed widespread cortical thinning in both hemispheres, while BECTS individuals showed sparse regions of both cortical thinning and thickening. Also, baseline cognitive abnormalities associated with BECTS persisted over 2 years. Garcia-Ramos et al.'s analysis was based on volumetric measurements and the side of epilepsy focus was not considered in their work. Lou et al. (Luo et al., 2015) performed a Voxel-Based Morphometry (VBM) analysis on 21 BECTS and 20 healthy participants. They reported increased GM volume in the bilateral putamen and fronto-temporo-parietal cortex in patients with BECTS compared to healthy controls. Lou et al. also did not evaluate the effect of the epilepsy lateralization on their analysis.

In summary, structural alterations are found at the onset of the disorder, and the structural abnormalities are persistent over the years (Garcia-Ramos et al., 2015b). This may be related to the long term existence of cognitive impairments before and after the diagnosis (Overvliet, 2011). Therefore, the structural alterations may be associated with cognitive impairments, also genetic and heredity may be involved in rolandic epilepsy.

3.4 Summary

In this chapter, we reviewed the literature and the current state-of-the-art methods in different areas of relevant application to the proposed research project.

First, various available image segmentation approaches have been presented and their advantages and disadvantages were mentioned. Secondly, a summary of the different shape analysis methods, along with their limitations were presented. Thirdly, a review of the available studies on BECTS was performed to introduce the concepts and highlight the existing methods' limitations.

In this review, we have observed that one of the main challenges in medical imaging studies was applying an accurate automatic image segmentation technique. On one hand, manual labeling is the gold standard, although it requires trained experts and is time-consuming. On the other hand, according to recent evaluations, the performance of the state-of-the-art automatic segmentation methods is still far from manual labeling. In regard to morphological analysis, we have noticed that surface-based approaches have enabled the most reliable evaluation of regional alteration in brain. However, the main challenge in surface-based frameworks is to establish precise alignment of structures across subjects, which is prone to inter-subject variability.

We also have observed that different studies in the field of benign childhood epilepsy reported the existence of neuroanatomical abnormalities in children with BECTS, which might be associated to some cognitive difficulties. Among the existing studies, a great number of them either included control participants with other neuropathologies or used no control group in their analysis. In addition, among the rest of the published literature, few studies analyzed subcortical shape alterations in BECTS and no work assessed the relationships between these morphological abnormalities and cognition.

In general, we can conclude that despite the development of various approaches in the field of brain abnormalities detection, there are still some limitations and challenges that need to be addressed in future studies on neuroanatomical alterations in children with BECTS. In order to propose an automatic morphological analysis framework in BECTS, several components in computer vision and shape modeling will be used. These components include, an image segmentation technique, a 3D morphological analysis algorithm, and a methodology to assess the association between morphological alterations and cognition.

CHAPTER 4 PROBLEM, HYPOTHESIS, OBJECTIVES, AND GENERAL METHOD

4.1 Problem Statement

Studying sub-cortical brain regions in benign epilepsy with centrotemporal spikes (BECTS) requires designing an accurate brain segmentation technique and a precise groupwise structural shape analysis framework. After detecting possible structural alterations in BECTS, the next step is to reveal the relationship between the extracted changes and cognition.

Image segmentation is a crucial step in medical imaging studies, since the quality of this process affects the accuracy of subsequent analysis. Manually segmenting sub-cortical regions is the most accurate technique, however it is time-consuming and requires trained experts. Therefore, the aim is to automate this process. Furthermore, standard segmentation approaches usually segment one target image at a time, while it is more preferable to have a framework that can handle segmenting multiple images simultaneously (cosegmentation). In addition, multi-atlas segmentation methods typically rely on precise ground truth annotations, while removing the burden of selecting an appropriate ground truth subset is of special interest. Thus, the first research question is formulated as : **Is it possible to design an automatic multi-atlas cosegmentation framework, which is accurate enough to detect the boundary of sub-cortical structures with limited dependency on ground truth annotations ?**

The main challenges in surface based groupwise shape analysis approaches are to extract 3D meshes, define the point-to-point correspondences across surface meshes, and perform groupwise comparisons. The precision of the surface extraction and the matching process affects the accuracy of the detected alteration in brain structures. Therefore, the second question arises : **How to extract sub-cortical surfaces and establish matching across meshes in order to detect the morphological alterations among the studied populations with better accuracy ?**

Cognitive deficits have been reported in children with BECTS, which may affect the children's quality of life. Despite the accumulating evidence of cognitive studies in BECTS, little is known about underlying structural alterations in these patients with different epilepsy focus. Given neurocognitive differences among children with BECTS and normal controls, the final question is : **Are morphometric variations in brain structures present in BECTS patients, do they explain variations in cognitive functions, and does the**

localization of epilepsy have a role in the structure to cognition link in BECTS ?

4.2 Hypothesis

Considering the explained problem in previous section, the following hypothesis can be formulated :

Hypothesis 1 : An automatic segmentation algorithm can be designed so that it can simultaneously perform prior-based cosegmentation of sub-cortical structures on multiple MR images.

Hypothesis 2 : An accurate automatic groupwise shape analysis can be proposed that can contribute to the study of subcortical shape variations.

Hypothesis 3 : Neuroanatomical alterations are present in children with BECTS with respect to normal controls and there is a relationship between structural alterations and cognition in this pathology.

4.3 Objectives

The general goal of this thesis is to design a framework for the morphological analysis of subcortical structures in children with benign epilepsy with centrotemporal spikes (BECTS). The main target is fulfilled in the following three specific objectives.

Objective 1 : Developing an automatic segmentation technique of sub-cortical structures on T1-weighted MR images.

One of the main challenges in any anatomical alteration study is to detect the boundary of a structure of interest by applying an accurate segmentation strategy. In this project, a groupwise coregistration and cosegmentation process is proposed, which enables us to segment multiple images at the same time. In this approach Convolutional Neural Network (CNN)-based priors are integrated to the energy formulation to boost the spatial transformation estimation process (**paper 1**). In another work, a classifier based on Fully Convolutional Neural Network (F-CNN) is developed to segment brain sub-cortical structures (**Appendix A**). In this method the output of the F-CNN is used as potentials of a Markov Random Field (MRF).

Objective 2 : Designing a framework for matching $3D$ sub-cortical surface meshes and investigating the group-wise structural differences between two populations of surfaces, i.e.,

healthy and pathological subjects.

Surface-based morphological analysis is challenging, since it requires establishing a reliable point-to-point correspondences across surface meshes. In addition, surface matching is often a compromise between accuracy and fast computational time. Therefore, the use of spectral representations in matching $3D$ structures can be beneficial in that regard, which have the advantages of being largely invariant to changes in poses and being computationally efficient in establishing surface correspondences. In this research, a spectral matching approach is employed in a group-wise shape analysis framework, designed for the population-wise comparison between two groups of subcortical structures. A preliminary framework of this approach (**Appendix B**) uses the spherical representations of input meshes. An extended and fully validated version of the framework (**paper 2**) applies a curvature-based mesh smoothing, integrates mean curvature feature into the matching process, and performs a statistical permutation-based analysis to detect the significant groupwise shape differences. Furthermore, the extracted spectral shape representation of surfaces is employed in two automatic classification applications in distinguishing healthy subjects from pathological individuals (**Appendix C** and **D**).

Objective 3 : Applying a technique to find the association between brain morphological changes in children with BECTS and cognition.

Benign epilepsy with centrotemporal spikes (BECTS) is associated with cognitive impairments in children. These cognitive impairments may be linked to the underlying structural alteration. The objective is to investigate the sub-cortical structures morphology that is potentially responsible for cognitive deficits or compensatory phenomenon in BECTS. In addition, the aim is to understand the role of the side of epilepsy on the structure to cognition link in left vs. right vs. bilateral BECTS. The proposed approach in **paper 3** extracts putamen and caudate shape variations from two populations of BECTS and normal controls. Then, investigates the association between morphological alterations and cognition considering epilepsy lateralization in BECTS cohort.

4.4 General methodology

In this research, a set of frameworks is proposed for a study on sub-cortical morphometry in children with benign epilepsy with centrotemporal spikes (BECTS). Our proposed methodology consists of three main blocks : (1) Automatic segmentation of sub-cortical structures ;

(2) Statistical groupwise shape analysis ; and (3) Study of sub-cortical morphometry and its association with cognition. An overview of the proposed framework is shown in Figure 4.1. The methodological structure of this thesis is illustrated in Figure 4.2.

The first objective of this project is to design an automatic segmentation of sub-cortical structures on MR images using a coregistration and cosegmentation process. This method incorporates segmentation priors, learned by a Convolutional Neural Network (CNN) classifier, in to the energy formulation of the deformable registration. In this way, the accuracy of the registration between source and target is improved. This approach is presented in (Chapter 5) (Shakeri et al., 2016a). In another approach, which is presented in Appendixvolume Sup (Shakeri et al., 2016b) a classifier is designed based on Fully Convolutional Neural Network (F-CNN) to segment brain sub-cortical structures on 3D MR images . In this method the output of the F-CNN is used as potentials of a Markov Random Field (MRF) to further refine the CNN output and impose spatial volumetric homogeneity to the CNN priors. These methods allow us to segment sub-cortical structures of both BECTS and healthy individuals with a promising accuracy.

The second objective is to extract 3D surface meshes from segmented sub-cortical structures and apply statistical groupwise shape analysis across population of healthy and pathological surfaces. This method employs spectral surface matching approach to establish point-to-point correspondences across population of surfaces. A preliminary version of our groupwise shape analysis approach is presented in Appendix B (Shakeri et al., 2014), which uses the spherical representations of input surfaces. The extended version of the approach is proposed in Chapter 6 (Shakeri et al., 2016c), which exploits a curvature-based surface smoothing, incorporates mean curvature feature into the spectral matching process to improve the matching accuracy, and applies a statistical permutation-based analysis to detect the significant local shape differences across populations. The extracted spectral shape representation of surfaces are used in two classification applications. One approach, trains a discriminant manifold based on Grassmannian kernels to maximize the class separability between matched $3D$ surfaces of healthy and pathological subjects. Then, a SVM classification technique is applied to define the decision boundary between classes. The method is tested on classification of subjects with Alzheimer's disease, mild cognitive impairment, and healthy controls (Appendix C) (Shakeri et al., 2015). In another work, a deep learning variational auto-encoder network is applied on the spectral signature of the matched mesh models to learn its low dimensional feature representation. A multi-layer perceptrons (MLP) using softmax activation function is simultaneously trained to classify subjects with Alzheimer's disease from healthy controls (Appendix D) (Shakeri et al., 2016d).

The third objective is to investigate the brain morphological alterations in children with BECTS and reveal the association of the detected morphometry with cognitive functions. This study considers the epilepsy lateralization in all analysis. This work, presented in Chapter 7, enables us to understand the underlying neurodevelopmental alterations in children with BECTS, that could be associated with cognitive functions.

The different steps of the project as well as the obtained results are presented in the form of papers in Chapter 5 (**scientific objective 1**), Chapter 6 (**scientific objective 2**), and Chapter 7 (**scientific objective 3**). Finally, the discussion, conclusion, and recommendations are presented in Chapter 8 and Chapter 9.

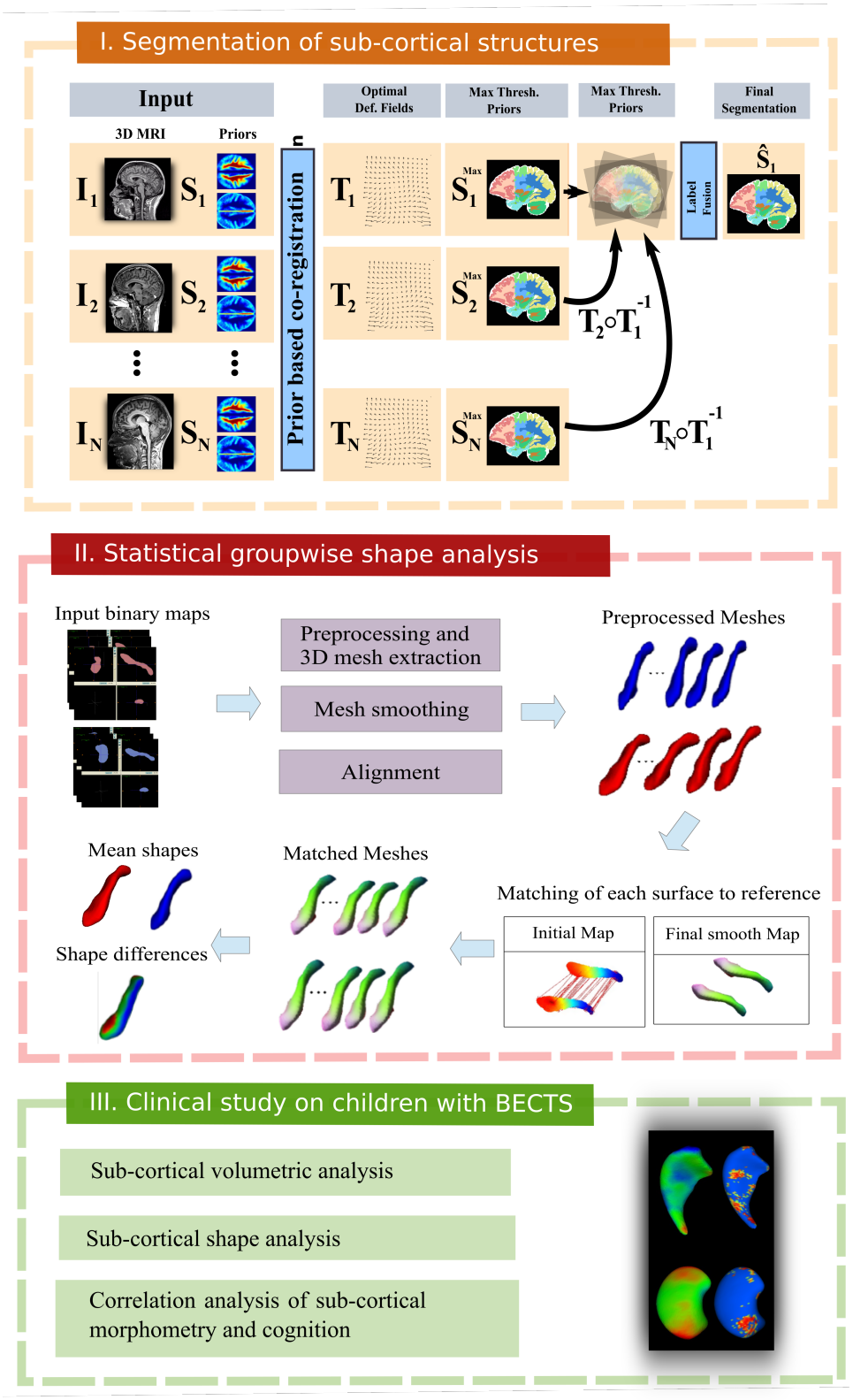

Figure 4.1 Proposed framework. (1) Segmentation : The input is a group of MR images. The output is the segmentation maps of sub-cortical structures. (2) Morphological analysis : The input is a dataset including segmentation maps of patients and normal controls. The output is morphological distances between two groups of subjects. (3) Correlation assessment : The input is morphological alterations detected by shape analysis framework, and the output is the association between sub-cortical morphometry and cognitive performance.

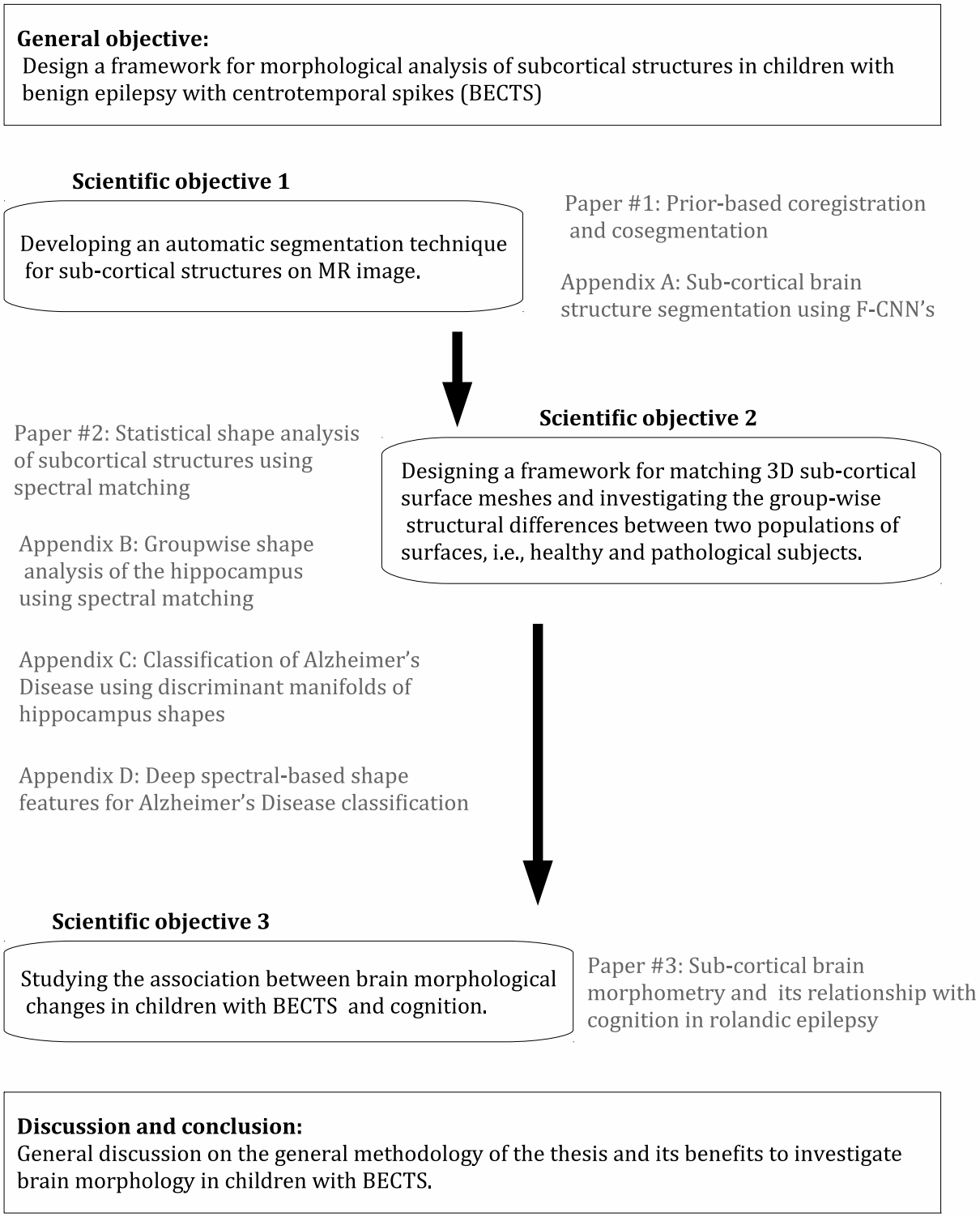

Figure 4.2 Methodological organization of the thesis.

CHAPTER 5 ARTICLE 1 : PRIOR-BASED COREGISTRATION AND COSEGMENTATION

Contribution of the first author in preparation and writing this paper is evaluated as 80%. This article has been accepted in the 19th International Conference on Medical Image Computing and Computer Assisted Intervention (MICCAI 2016) held in Athens, Greece, in October 2016.

Remarks : This works presents an automatic coregistration and cosegmentation framework which enables us to segment MR images. This approach integrates Convolutional Neural Network (CNN)-based priors to the energy formulation of the deformable registration to improve cosegmentation accuracy.

We evaluate our approach on two brain image datasets : IBSR and RE. The Internet Brain Segmentation Repository (IBSR) dataset (Rohlfing, 2012a) contains 18 labeled T1-weighted MR images of size $256 \times 256 \times 128$ with slice thickness of $1.3mm$. We specifically use the skull stripped version of the dataset provided in (Rohlfing, 2012a). The dataset is also supplied with manual expert segmentations of sub-cortical volumes. In this work, we use the set of 16 primarily subcortical annotations, including left and right lateral ventricle, thalamus, caudate, putamen, pallidum, hippocampus, amygdala, and accumbens.

The Rolandic Epilepsy (RE) dataset which contains 17 children with epilepsy and 18 matched healthy individuals. T1-weighted magnetic resonance images (MRI) scans were performed by a 3 T scanner (Philips Acheiva) with a resolution of $256 \times 256 \times 160$ and slice thickness of $1mm$. The left and right putamen structures were manually annotated by an expert. The skull-stripping was performed using ROBEX tool (Iglesias et al., 2011).

For both datasets, we performed the standard preprocessing of intensity normalization, and histogram matching using Medical Image Processing, Analysis, and Visualization tool (MIPAV version 1.0) [1]. For histogram adaptation, we performed matching to the histogram of the first image in each dataset as reference.

For validation, we consider the manual segmentations available on each dataset as ground truth, and estimate how close our automatic segmentation result is to the ground truth annotations. Dice coefficient (Dice, 1945) is reported, which indicates the amount of volume overlap between the automatically segmented structures and the corresponding manually annotated ones. In addition, Contour mean distance (CMD) [2] and Hausdorff distance (HD)[2] are

1. http ://mipav.cit.nih.gov/
2. http ://plastimatch.org/plastimatch.html

also calculated as the average and maximum distance between ground truth and automatic segmentation, respectively.

Experimental evaluations on two datasets in Section 5.4 demonstrate the importance of reliable segmentation priors. The results show that the label likelihoods extracted with a deep CNN outperform alternative methods and can replace ground truth annotations in coregistration process. Other experiments presented in Appendix E, shows the promising results of the proposed co-registration and co-segmentation algorithm compared to the two publicly available state-of-the-art automatic segmentation tools, i.e., Freesurfer (Fischl et al., 2002) and FSL-FIRST (Patenaude et al., 2011a).

Prior-based Coregistration and Cosegmentation

Mahsa Shakeri[2,4], Enzo Ferrante[1], Stavros Tsogkas[1], Sarah Lippe[3,4],
Samuel Kadoury[2,4], Iasonas Kokkinos[1], Nikos Paragios[1]

[1]CVN, CentraleSupelec-Inria, Universite Paris-Saclay, France,
[2] Polytechnique Montreal, Canada
[3]University of Montreal, Canada,
[4] CHU Sainte-Justine Research Center, Montreal, Canada

5.1 Abstract

We propose a modular and scalable framework for dense coregistration and cosegmentation with two key characteristics : first, we substitute ground truth data with the semantic map output of a classifier ; second, we combine this output with population deformable registration to improve both alignment and segmentation. Our approach deforms all volumes towards

consensus, taking into account image similarities and label consistency. Our pipeline can incorporate any classifier and similarity metric. Results on two datasets, containing annotations of challenging brain structures, demonstrate the potential of our method.

Keywords coregistration, cosegmentation, discrete optimization, priors.

5.2 Introduction

In recent years, multi-atlas segmentation (MAS) has become a widely used image segmentation technique for biomedical applications (Iglesias and Sabuncu, 2015). It uses an annotated dataset of atlases (images with their corresponding ground truth labels) to segment a target image. The atlases are first registered to the target ; then the deformed segmentation masks are fused, generating the final mask for the target. Such an approach suffers from two limitations : i) the need of accurate annotations ; ii) the sequential/independent nature of the mapping between the atlases and the target image.

In this work we propose a coregistration and cosegmentation framework that optimally aligns and segments a *set* of input volumes. We adopt the standard graph-based deformable registration framework of Glocker et al. (Glocker et al., 2011). Our novel energy formulation incorporates discriminative information produced by alternative classifiers, trained to differentiate between different cortical structures. We stress the fact that our method is different than typical MAS : the final segmentations are obtained after population registration, while the probabilistic segmentations delivered by our classifiers are used as a discriminative image representation that helps to improve registration performance. Therefore our approach is able to deal with the bias introduced from inaccurate segmentations while at the same time it exploits knowledge of the entire dataset simultaneously. Previous works on groupwise registration and segmentation of MR images have relied on image similarites (Bhatia et al., 2004), or shape and texture models (Tsai et al., 2004; Babalola and Cootes, 2006). The works that are most similar to ours are (Heckemann et al., 2010), (Alchatzidis et al., 2014) and (Parisot et al., 2012). They use probabilistic priors obtained with a pre-trained classifier to improve segmentation and registration. However, rather than performing prior- and intensity-based registration steps independently, as in (Heckemann et al., 2010), we consider both types of data at the same time in a single, compound matching criterion. Furthermore, in (Alchatzidis et al., 2014) and (Parisot et al., 2012) segmentation variables are explicitly modeled, whereas we only model registration variables, thus reducing the number of parameters to be estimated. More importantly, these works aim at segmenting a single target image ; contrary to that, we consider a target *population* of images to be segmented and registered simultaneously.

Our method infers the segmentations of the unseen images on-the-fly using learned classifiers, and incorporates this information in the energy formulation. As our experimental results in Section 5.4 demonstrate, our method has considerable advantages over standard MAS as well. Firstly, given a set of target volumes, MAS would repeatedly register a set of ground truth masks and perform label fusion individually for each target. Contrary to that, we compute the segmentation probabilities once, and then segment all the volumes simultaneously. If numerous ground truth masks are to be used for the registration step, our method leads to substantial computational gains, as complexity depends only on the number of volumes we want to segment. Secondly, in the case of large datasets, the burden of selecting an appropriate ground truth subset to perform MAS more efficiently is removed ; one simply has to compute the probability masks on the input volumes. Thirdly, in typical MAS only appearance features are used to compute the deformation fields between source and target. We go one step further, exploiting more sophisticated, learned representations to drive the coregistration process. These features are computed for all volumes involved, and are directly related to the desired final output. We validate the effectiveness of our approach on the task of segmenting challenging sub-cortical structures in two different brain imaging datasets.

5.3 Problem formulation using segmentation priors

We formulate our coregistration and cosegmentation algorithm as an energy minimization problem. The input is a set of 3D images $\mathcal{I} = \{I_1, I_2, \ldots, I_N\}, \quad I_i : \Omega \subset \mathbb{R}^3 \rightarrow \mathbb{R}$, and their corresponding segmentation likelihoods $\mathcal{S} = \{S_1, S_2, \ldots, S_N\}$ associated to the possible segmentation classes $c \in \mathcal{C} = \{0, \ldots, C\}$ as $S_i : \Omega \times \mathcal{C} \rightarrow [0, 1]$. Label zero (0) corresponds to the background. The output is the final multi-label segmentation masks $\hat{\mathcal{S}} = \left\{\hat{S}_1, \hat{S}_2, ..., \hat{S}_N\right\}$ together with the deformation fields $\hat{\mathcal{M}} = \left\{\hat{T}_1, \hat{T}_2, ..., \hat{T}_N\right\}$ that warp every image to a common coordinate space through an operation $I \circ \hat{T}$. In addition, let $\delta_{\mathcal{X}}$ be a function that measures similarity between inputs that lie in some domain $\mathcal{X}$. The objective function we want to minimize is

$$E(\mathcal{M}; \mathcal{I}, \mathcal{S}) = E_I\left(\mathcal{M}; \mathcal{I}\right) + E_S\left(\mathcal{M}; \mathcal{S}\right) + E_R\left(\mathcal{M}\right). \tag{5.1}$$

The first two terms seek agreement on the appearance of equivalent voxels and deformed priors respectively, across all volumes of the registered population :

$$E_I(\mathcal{M}; \mathcal{I}) = \sum_{x \in \Omega} \delta_{\mathcal{I}}(I_1 \circ T_1(x), I_2 \circ T_2(x), \ldots, I_N \circ T_N(x)), \tag{5.2}$$

$$E_S(\mathcal{M}; \mathcal{S}) = \sum_{c \in \mathcal{C}} \sum_{x \in \Omega} \delta_{\mathcal{S}}(S_1 \circ T_1(x, c), S_2 \circ T_2(x, c), \ldots, S_N \circ T_N(x, c)). \tag{5.3}$$

Here, $\delta_{\mathcal{I}}$ and $\delta_{\mathcal{S}}$ can be viewed as generalizations of the pairwise similarity, so as to account for multiple inputs. The deformation fields are applied on the probability map of each label separately and in the end we sum over all possible semantic labels $c \in \mathcal{C}$. The last term, E_R, imposes geometric or anatomical constraints on the deformation fields, e.g. smoothness. Different types of regularizers $\mathcal{R}$ can be used, usually chosen as convex functions of the gradient of the deformation field. We describe our choice of $\delta_{\mathcal{I}}$, $\delta_{\mathcal{S}}$ and $\mathcal{R}$ in Section 5.3.2. We apply $\mathcal{R}$ to each deformation field T_i independently :

$$E_R(\mathcal{M}) = \sum_{i=1}^{N} \sum_{x \in \Omega} \mathcal{R}(T_i(x)). \tag{5.4}$$

By minimizing the energy defined in Equation 5.1 with respect to $\mathcal{M}$, we can obtain the optimal deformation fields $\hat{\mathcal{M}} = \text{argmin}_{\mathcal{M}} E(\mathcal{M}; \mathcal{I}, \mathcal{S})$. The high-order terms that appear in E_I and E_S are hard to optimize and diminish the guarantees to obtain the globally optimal solution. As a remedy we propose the two-step procedure adopted from (Sotiras et al., 2009). Instead of considering all the deformation fields at the same time, we estimate the deformation field T_k of a single image, keeping all other images ($i \neq k$) fixed. This process is iterated for $i = 1, 2, \ldots, N$, and is reminiscent of the α-expansion algorithm (Boykov et al., 2001) : we start with an initial solution (in our case, the identity deformation fields) and iteratively move towards the optimal deformation fields that minimize E.

Once the optimal deformation fields $\hat{\mathcal{M}}$ have been estimated, we can build the final segmentation masks $\hat{\mathcal{S}}$. We first warp all segmentation priors in $\mathcal{S}$ to the common frame of reference, generating the deformed segmentation masks $S_i \circ \hat{T}_i$. Then, given a target volume I_k whose final segmentation we want to estimate, we back-project all warped segmentation masks $S_i \circ \hat{T}_i$ from the common frame, to the coordinate space of I_k using the inverse deformation field T_k^{-1}. This method is modular with respect to the fusion strategy. We use a simple majority voting, assigning to every voxel the class $c \in \{0, \ldots, C\}$ with the highest number of votes after back-projection.

5.3.1 Iterative Algorithm

We now rewrite Equation 5.1 as an iterative process. E_I^t, E_S^t and E_R^t consider a single deformation field T_k at a time t and are computed as

$$E_I^{t+1}(T_k^t;\mathcal{I}) = \sum_{i=0,i\neq k}^{N}\sum_{x\in\Omega}\delta_{\mathcal{I}}(I_i^t, I_k^t\circ T_k^t(x)) \tag{5.5}$$

$$E_S^{t+1}(T_k^t;\mathcal{S}) = \sum_{i=0,i\neq k}^{N}\sum_{c\in\mathcal{C}}\sum_{x\in\Omega}\delta_{\mathcal{S}}(S_i^t, S_k^t\circ T_k^t(x,c)) \tag{5.6}$$

$$E_R^{t+1}(T_k^t) = (N-1)\sum_{x\in\Omega}\mathcal{R}(T_k^t(x)). \tag{5.7}$$

I^t, S^t, T^t, denote the current image, segmentation and deformation field respectively, after applying the updates at iterations $1, 2, \ldots, t$. The regularization term is scaled by $(N-1)$ for normalization purposes. This iterative process is repeated until convergence. After all images have been aligned in a common reference frame, majority voting produces the final segmentation masks. For clarity, in the remaining of the text we drop the dependence on t. A step-by-step description of the procedure is given in Algorithm 1.

5.3.2 Discrete Formulation

We formulate non-rigid registration between two images I_i, I_k as a discrete energy minimization problem. Following (Rueckert et al., 1999), we parametrize the deformation fields T_k as a linear combination of $K \ll |\Omega|$ control points that form a regular 3D grid. We define a first order discrete MRF by superimposing an undirected graph $G = (V, U)$ on an image, with V and U denoting the graph nodes and edges respectively. Nodes are interpreted as random variables that model displacements $\mathbf{d}_p \in \mathbb{R}^3$ of the control points, while edges encode the interaction between these variables, in a 6-way neighborhood U_p.

Given a labeling $L = \{l_1, l_2, \ldots, l_K\} = \{\mathbf{d}_1, \mathbf{d}_2, \ldots, \mathbf{d}_K\}$, that assigns a label (displacement vector) to every node p in the MRF, the energy function becomes

$$E_{\text{MRF}}(L;G) = \sum_{p\in V} g_p(l_p) + \lambda \sum_{(p,q)\in U_p} f_{pq}(l_p, l_q), \quad \text{where} \tag{5.9}$$

$$g_p(l_p) = g_p(\mathbf{d}_p) = \sum_{x\in\Omega_p}\delta_{\mathcal{I}}(I_i, I_k\circ T_k^{\mathbf{d}_p}(x)) + \beta\sum_{c\in\mathcal{C}}\sum_{x\in\Omega_p}\delta_{\mathcal{S}}(S_i, S_k\circ T_k^{\mathbf{d}_p}(x,c)).$$

The unary term g_p is a combination of terms E_I, E_S that encode appearance and segmentation likelihood agreement. In practice, control points have a limited spatial support, therefore p receives contributions only from pixels inside a region Ω_p (e.g. patch) around it. $T_k^{\mathbf{d}_p}$ is the

Algorithm 1 Iterative Coregistration-Cosegmentation algorithm

procedure ICS($\mathcal{I} = \{I_1, I_2, \ldots, I_N\}$, $\mathcal{S} = \{S_1, S_2, \ldots, S_N\}$)
  Initialize the deformation fields $\left\{\hat{T}_1, \hat{T}_2, ..., \hat{T}_N\right\}$ as null (identity) deformation fields
  repeat
    repeat
      Sample an image $I_k \in \mathcal{I}$ without replacement
      Register I_k to all images in $\mathcal{I} \setminus \{I_k\}$, optimizing E :

$$\ddot{T}_k = \underset{T_k}{\operatorname{argmin}}\, E_I(T_k; \mathcal{I}) + E_S(T_k; \mathcal{S}) + E_R(T_k) \tag{5.8}$$

      Deform image and corresponding segmentation : $I_k \leftarrow I_k \circ \ddot{T}_k,\ S_k \leftarrow S_k \circ \ddot{T}_k$
      Update deformation field $\hat{T}_k \leftarrow \hat{T}_k \circ \ddot{T}_k$
    until all images have been chosen once
  until All T remain unchanged or the maximum of iterations is reached
  for each image $I_k \in \mathcal{I}$ **do**
    for each segmentation prior $S_i \in \mathcal{S}$ **do**
      Deform S_i to the native space of I_k : $S'_i = S_i \circ \hat{T}_k^{-1}$
    end for
    Apply label fusion (e.g., *Majority Voting*) on $\{S'_i\}_{i\in\{1,\ldots,N\}}$ to obtain $\hat{S}_k$
  end for
  Output : $\hat{\mathcal{M}} = \left\{\hat{T}_1, \hat{T}_2, ..., \hat{T}_N\right\}$ and $\hat{\mathcal{S}} = \left\{\hat{S}_1, \hat{S}_2, ..., \hat{S}_N\right\}$
end procedure

transformation induced by applying the displacement vector $\mathbf{d}_p$ on the control point p. The β coefficient determines the influence of segmentation priors on the optimization problem and λ is a scaling factor. In our experiments we set $\lambda = 5, \beta = 100$ using cross-validation. As $\delta_{\mathcal{I}}$ we use the sum of absolute difference (SAD), while $\delta_{\mathcal{S}}$ computes the Hamming distance on the segmentation maps obtained after assigning the semantic class with highest probability to each pixel. The pairwise term $f_{pq}(l_p, l_q) = f_{pq}(\mathbf{d}_p, \mathbf{d}_q) = ||\mathbf{d}_p - \mathbf{d}_q||$ is a discrete approximation of the gradient of the spatial transformation and acts as the regularizer $\mathcal{R}$ in Equation 5.4.

To infer the best labeling, we employ Fast-PD (Komodakis et al., 2008), an efficient move-making discrete optimization method based on linear programming relaxation, that has shown promising results when applied to multi-label problems with similar types of energies.

5.4 Experiments

We evaluate the performance of our approach on the task of subcortical brain structure segmentation on two MRI datasets, IBSR (Rohlfing, 2012a) (18 subjects, slice tickness of 1.3mm) and a Rolandic Epilepsy (RE) study (35 subjects, slice tickness of 1mm). In our experiments we use two types of classifiers to estimate segmentation maps, which are then used to guide the registration : convolutional neural networks (CNNs) (Shakeri et al., 2016b) and random forests (RFs) (Alchatzidis et al., 2014). For a description on the CNN architecture, training methodology and RE dataset, we refer to Appendix A.We focus on a subset of 16 subcortical structures, including left and right lateral ventricle, thalamus, caudate, putamen, pallidum, hippocampus, amygdala, and accumbens. Below we list the variants compared in our experiments.

Coreg+CNN and Coreg+RF : We use the terms Coreg+CNN and Coreg+RF to refer to the variants of our method that use CNN and RF priors respectively. We generate the CNN and RF priors using the methods described in Appendix A and (Alchatzidis et al., 2014) respectively.

CNN and RF : To further demonstrate the effect of using the iterative coregistration on top of CNN/RF priors, we report segmentation results based on the CNN/RF probability maps without coregistration. In this setting, given a CNN/RF prior, the segmentation class of every voxel is simply chosen as the class with the highest probability.

Pairwise : As a baseline, we implement the standard MAS based on pairwise registration. All atlases are independently registered to the target image as in (Glocker et al., 2011) ; then the ground truth annotations are fused to generate the final segmentation using majority voting. The use of the actual ground truth annotations offers a clear advantage with respect to Coreg+CNN and Coreg+RF, that use the *estimated* segmentation probability maps instead. Still, Coreg+CNN achieves better performance as shown in in Figures 5.1,A.2.

Coreg+GT (Oracle) : The merit of our approach is that it allows us to guide the coregistration process using probability maps as a surrogate for ground truth annotations, which are not always available. In order to assess the maximum potential of our method, we implemented an *oracle* that provides us with an upper-bound to its performance. The oracle makes use of the ground truth segmentation masks for all 3D volumes, except for the target image, for which we keep the probability maps computed by the CNN.

We summarize the results of our experiments in Figures 5.1-A.2. We compare performance using three different metrics : i) average Dice coefficient (DC) ; ii)Hausdorff distance (HD) ; iii) contour mean distance (CMD). Our results show that Coreg+CNN achieves higher segmentation accuracy compared to both Coreg+RF and the pairwise segmentation baseline. Respectively, the segmentations obtained using only the CNN classifier output (without any registration process) are much more accurate than the ones from random forests. Unsurprisingly, Coreg+GT outperforms all other variants. Nonetheless, performance of Coreg+CNN is close to Coreg+GT in most cases, also illustrated visually in Figure 5.3. This evidence solidifies our original claim, that reliable priors can act as a practical substitute for golden standard annotations in multi-atlas segmentation.

Another important observation is that our coregistration and cosegmentation framework significantly improves results of less accurate priors (e.g. the ones produced by RF), especially in terms of Hausdorff and contour mean distance. Such priors can be learned from weak annotations that are produced very efficiently compared to precise segmentation masks (e.g. bounding boxes) and still deliver acceptable results.

5.5 Conclusions

In this paper we have proposed a novel method for cosegmentation and coregistration of multi-volume data, guided by semantic label likelihoods. Our approach has the following characteristics : i) infers deformations that are anatomically plausible ; ii) establishes visual consistencies between all volumes according to any metric ; iii) enforces segmentation consistencies among all volumes according to the predicted likelihoods. Experimental evaluation on a standard, publicly available benchmark, as well as on an additional clinical dataset, demonstrates the effectiveness of our approach. Our experiments also show the value of reliable segmentation priors. Label likelihoods extracted with a deep CNN outperform alternative methods and can replace ground truth annotations in coregistration with minimal loss in performance.

Future research directions include studying the gains of combining different metrics per class and using them as content-adaptive potentials in the energy function. Explicitly modeling high-order interactions and simultaneously recovering all deformations with one-shot optimization are also of great theoretical and practical interest. Finally, an important future goal is testing the proposed method on a clinical problem where coregistration and cosegmentation are important, such as adaptive radiotherapy.

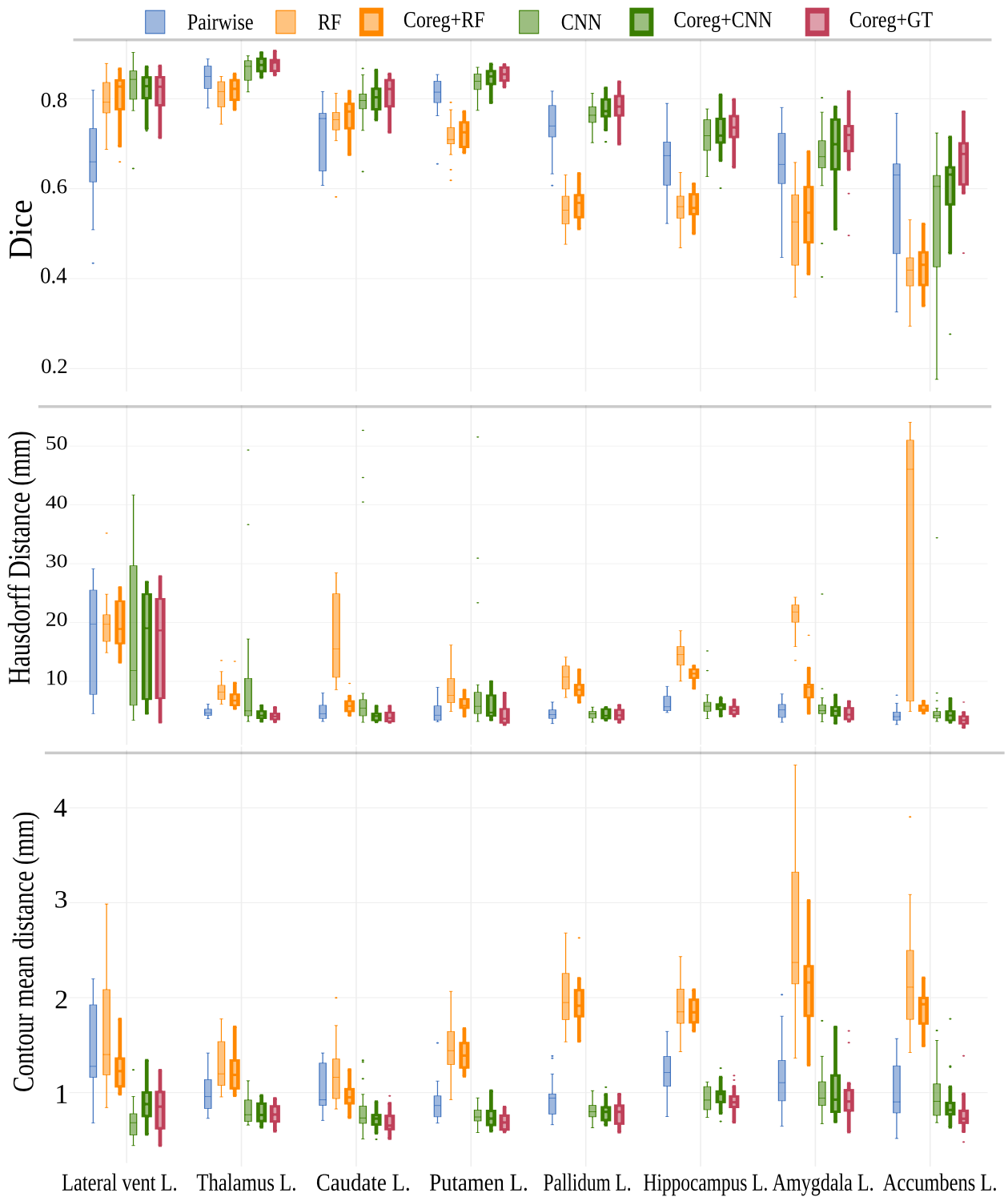

Figure 5.1 Box plots for average Dice coefficient (DC), Hausdorff distance (HD) and contour mean distance (CMD) for left side subcortical structures in IBSR (best viewed in color). **DC :** higher = better. **HD/CMD :** lower = better. Results for the right-side are included in Appendix E.

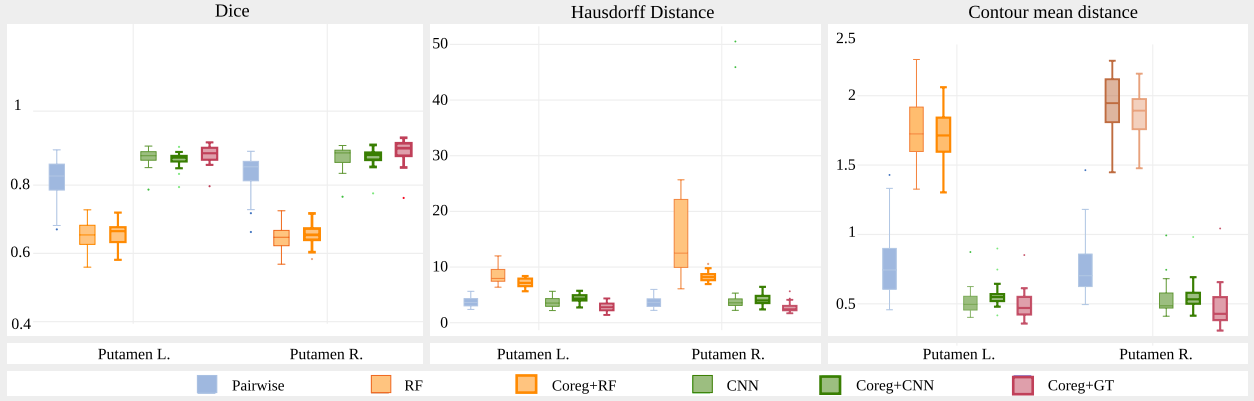

Figure 5.2 Box plots for average Dice coefficient (DC), Hausdorff distance (HD), and contour mean distance (CMD)for the left and right putamen in the RE dataset (best viewed in color). **DC :** higher = better. **HD/CMD :** lower = better. Coreg+CNN results approach the performance of the oracle.

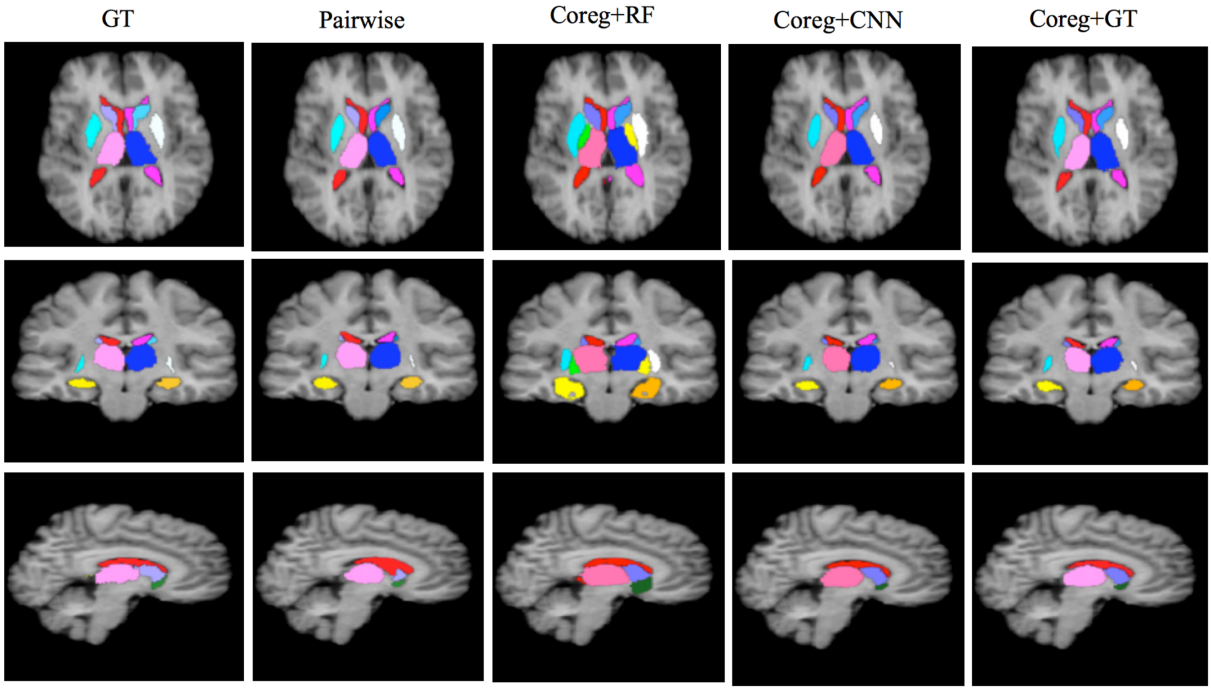

Figure 5.3 Segmentation results in three different views. Coreg+CNN can be used as a reliable substitute for ground truth annotations in multi-atlas coregistration and cosegmentation (view in color).

CHAPTER 6 ARTICLE 2 : STATISTICAL SHAPE ANALYSIS OF SUBCORTICAL STRUCTURES USING SPECTRAL MATCHING

Contribution of the first author in preparation and writing this paper is evaluated as 90%. This article has been published by the journal of Computerized Medical Imaging and Graphics on March 2016.

Remarks : This paper presents a groupwise shape analysis framework designed for the population-wise comparison between two groups of subcortical structures. The proposed method employs spectral surface matching approach to establish point-to-point correspondences across population of surfaces. Experiments revealed that the proposed approach could detect the location of morphological differences similar to state-of-the-art algorithms, but with a lower computational cost.

Statistical shape analysis of sub-cortical structures using spectral matching

Mahsa Shakeri[a,b], Herve Lombaert[c], Alexandre N. Datta[d], Nadine Oser[d], Laurent Létourneau-Guillon[e], Laurence Vincent Lapointe[f], Florence Martin[f], Domitille Malfait[b,f], Alan Tucholka[b,g], Sarah Lippé[b,f], Samuel Kadoury[a,b], Alzheimer's Disease Neuroimaging Initiative

[a] Polytechnique Montreal, Department of Computer and Software Engineering, Centre-ville, Montreal, QC, Canada H3C 3A7

[b]Sainte-Justine Hospital, Research Center, 3175 Cote-Sainte-Catherine Rd., Montreal, QC, Canada H3T 1C5

[c]Inria Sophia-Antipolis Méditerranée, Asclepios Team, 06902 Sophia-Antipolis, France

[d] University of Basel Children's Hospital, Basel, Switzerland

[e] Notre-Dame Hospital, Department of Radiology, Montreal, QC, Canada H2L 4M1

[f] University of Montreal, Department of Psychology, Montreal, QC, Canada H3C 3J7

[g] Barcelona Beta Brain Research Center, Pasqual Maragall Foundation, Barcelona, Spain

6.1 Abstract

Studying morphological changes of subcortical structures often predicate neurodevelopmental and neurodegenerative diseases, such as Alzheimer's disease and schizophrenia. Hence, methods for quantifying morphological variations in the brain anatomy, including groupwise shape analyses, are becoming increasingly important for studying neurological disorders. In this paper, a novel groupwise shape analysis approach is proposed to detect regional morphological alterations in subcortical structures between two study groups, e.g., healthy and pathological subjects. The proposed scheme extracts smoothed triangulated surface meshes from segmented binary maps, and establishes reliable point-to-point correspondences among the population of surfaces using a spectral matching method. Mean curvature features are incorporated in the matching process, in order to increase the accuracy of the established surface correspondence. The mean shapes are created as the geometric mean of all surfaces in each group, and a distance map between these shapes is used to characterize the morphological changes between the two study groups. The resulting distance map is further analyzed to check for statistically significant differences between two populations. The performance of the proposed framework is evaluated on two separate subcortical structures (hippocampus and putamen). Furthermore, the proposed methodology is validated in a clinical application for detecting abnormal subcortical shape variations in Alzheimer's disease. Experimental results show that the proposed method is comparable to state-of-the-art algorithms, has less computational cost, and is more sensitive to small morphological variations in patients with neuropathologies.

Keywords sub-cortical morphology, groupwise shape analysis, spectral matching, Alzheimer's disease.

6.2 Introduction

Quantifying groupwise neuroanatomical shape differences has become an important topic in neuroscience as well as in neuroimaging studies, since brain morphometry has been hypothesized to be linked to various neurological disorders (Nitzken et al., 2014). Recent advances in medical image analysis have led to several morphological studies on different pathologies including schizophrenia (Styner et al., 2004) and Alzheimer's disease (Shi et al., 2009). Early studies on brain morphology were based on volumetric analysis, which had the advantage of simplicity (Hastings et al., 2004; Shi et al., 2009). However, these methods lacked regional shape information, which are potentially important for neurological identification. Thus,

shape analysis has emerged as an alternative of evaluating morphology location and magnitude in the brain anatomy, in order to detect the neuroanatomical changes in specific regions of a single structure.

Several works have proposed groupwise shape analysis approaches based on creating a template image and estimating the deformation field between each individual image and the template (Allassonnière, 2007; Marsland and Twining, 2004; Rueckert et al., 2003). These methods non-rigidly register each image to a specific template, and evaluate the information contained within the deformation field to detect the location and magnitude of shape changes. In deformation-based approaches the template creation and the choice of the registration technique has a critical impact on the quality of the shape analysis results (Gao et al., 2014). Indeed, deformable registration remains a challenging problem, particularly in smaller regions such as subcortical structures, which requires a high level of accuracy to precisely match sub-fields.

Another approach for shape analysis is based on medial surface representations (Joshi et al., 2002; Bouix et al., 2005; Styner et al., 2003; Terriberry et al., 2007). These methods provide a compact parameterization of a volumetric object by extracting the 3D skeleton of a shape. The local positional changes are then quantified by assessing morphological variations of the skeleton across a population of shapes. The medial surface representation has been applied to various subcortical structures including the cross sectional images of the corpus callosum (Joshi et al., 2002) and hippocampus/amygdala complex (Styner et al., 2003), caudate (Terriberry et al., 2007), and lateral ventricle (Styner et al., 2005), in order to evaluate changes in patients diagnosed with schizophrenia. Since medial representation relies on a coarse-scale sampling of the structure of interest, it may be insensitive to small-scale shape differences, which might be present in a studied population (Styner et al., 2004).

In addition to the above-mentioned methods, several works have proposed surface parameterization based approaches, in which a parameterization of a shape is performed on a simple domain such as a sphere. One such approach is the spherical harmonics (SPHARM) method by Styner et al. (Styner et al., 2006a), which is used in combination with Point Distribution Models (PDM) to discover structural differences across a populations. In this approach, which is called SPHARM-PDM, shapes first represented by binary segmentations are converted into a corresponding spherical harmonic description. Then, the correspondence problem is solved by the alignment of the spherical parameterization using a first order ellipsoid. In this method, the spherical description of surface meshes is sampled into triangulated surfaces using icosahedron subdivision. These surfaces are then spatially aligned using rigid Procrustes alignment.

The SPHARM-PDM method has been applied in various clinical applications, such as for studying shape variations of the hippocampus (Styner et al., 2004) and lateral ventricles (Styner et al., 2005) in schizophrenia, and analyzing caudate morphological changes (Ong et al., 2012) in bipolar disorder. Although SPHARM-PDM enabled the reliable assessment of local shape variation across populations, it requires to establish correspondence on simplified spherical models of surfaces, which is restricted to surfaces with spherical topology (Paniaguaa et al., 2012; Cates et al., 2009). In order to overcome this limitation, combining SPHARM-PDM with an entropy-based particle system correspondence model has been proposed in (Paniaguaa et al., 2012). Furthermore, Cates et al. (Cates et al., 2009) proposed to model the shape as sets of particles, where the particles are distributed on the surfaces of the shapes by optimizing an entropy-based energy function. According to a recent evaluation in (Gao et al., 2014), this method was not able to find the location of group differences in some cases.

Chung et al. (Chung et al., 2010) proposed weighted-SPHARM, which expresses surface data as a weighted linear combination of spherical harmonics. The weighted-SPHARM method generalizes the traditional SPHARM representation as a special case. This method reduces ringing artifacts observed with the SPHARM representation especially for the high frequency components (Chung et al., 2010). However, it is applicable for a limited class of shapes and is only able to detect the sufficiently large shape difference across populations. SPHARM-MAT (SPHARM Modeling and Analysis Toolkit) is another shape analysis method, which creates parametric surface models using spherical harmonics (Shen et al., 2009). This approach is similar to SPHARM-PDM framework (Styner et al., 2006a) but applies different spherical parameterization and shape alignment process (Shen et al., 2009). A comparison between the two spherical harmonics-based methods showed that SPHARM-PDM could capture the shape differences more accurately rather than SPHARM-MAT (Gao et al., 2014)

In general, despite the development of various approaches in the field of group-wise shape analysis, there are still some limitations and challenges that need to be addressed. For instance, the morphometry framework should be robust to different shape topologies and shape segmentation approaches, while from a computational perspective, the total population-wise shape analysis process should be determined in an efficient time manner, in order to be feasibly implemented as a clinical diagnostic tool.

One of the main challenges in a surface-based groupwise shape analysis approach is to establish reliable one-to-one correspondences among the population of surfaces. Among various surface matching algorithms in the literature, the recent spectral matching approach proposed in (Lombaert et al., 2013a,b) have shown promising results, which enables mapping brain cortical surfaces in a computational efficient manner. To the best of our knowledge, no

studies have been based on spectral matching theory directly for groupwise shape analysis. In this paper, we employ the spectral matching approach in a groupwise shape analysis pipeline, designed for the population-wise comparison between two groups of subcortical structures. In the proposed framework, the mean curvature feature is used as feature information in the spectral matching process in order to increase the surface matching accuracy. This work presents a complete pipeline that allows the detection, localization, and quantification of statistically significant morphological differences in different subcortical brain structures across various populations.

The main contribution of this paper is to propose a robust and reliable spectral-based shape analysis framework using curvature features for analyzing simple (e.g., putamen) and complex (e.g., hippocampus) subcortical structures. Furthermore, in contrast to the above-mentioned methods, the suggested framework can perform population-wise shape analysis in a computational efficient fashion and integrates the spectral matching approach with a groupwise shape analysis framework. This paper is the first work that integrates spectral matching in to a groupwise subcortical shape analysis pipeline and incorporates curvature features to increase the surface matching accuracy (methodological contribution). Experimental analysis on real clinical datasets show that the extracted group differences is similar to the findings of other clinical studies (clinical contribution). This work would represent a significant forward for providing an alternative for future clinical studies on sub-cortical brain structures.

The proposed shape analysis framework processes two groups of segmented binary images from neuroimaging data (e.g., MRI) as input. After converting the images into triangulated surface meshes and applying the curvature flow smoothing process, the surface correspondence is established between two populations using the spectral matching approach. The mean curvature features are incorporated in the spectral matching process to improve the accuracy of the resulting surface correspondence. Then, two mean shapes for each group are created as the geometric mean of all surfaces, and the distance map between the two mean shapes is computed. To verify for statistically significant differences between two populations, a non-parametric permutation testing scheme (Pantazis et al., 2004) is applied, followed an FDR correction (Styner et al., 2006a) for multiple comparisons. The evaluation of the proposed shape analysis framework is performed on three separate neuroanatomical datasets, and group differences across populations are detected by point-to-point correspondences. The output of these analyses is compared to a state-of-the-art method used for group-wise analysis of anatomical shapes, namely SPHARM-PDM.

A preliminary version of the proposed method has been presented in (Shakeri et al., 2014), but was dependent of spherical representations of input shapes, integrated a point-based shape

matching method, and with limited validation. The present paper provides the detailed explanation of the methodology and offers the following major contributions : (i) a curvature-based surface smoothing is employed to smoothen extracted 3D surfaces, which has less computational requirements compared to the spherical-based smoothing method used inShakeri et al. (2014) ; (ii) mean curvature feature was added into the spectral matching process to increase the surface matching accuracy ; (iii) a statistical permutation-based analysis is applied to detect the significant shape differences across populations ; (iv) the evaluation of the proposed pipeline is performed on an increased number of clinical datasets with more samples. The remainder of this paper is organized as follows. In Section D.2, the methodology is presented, including the overview of the framework, the spectral surface matching approach, and the detailed description of the proposed population-wise shape analysis framework. The quantitative evaluation of the shape analysis method is provided in Section 6.4. Section 6.5 presents a discussion on the results obtained from different neuroimaging datasets, followed by a conclusion in Section D.4.

6.3 Materials and Methods

6.3.1 Framework overview

In this section, an overview of the proposed group-wise shape analysis pipeline is presented (Figure 6.1). The inputs of the proposed framework are two sets of segmented binary maps of a particular structure of interest from medical images, obtained either manually or automatically. The output of the proposed pipeline is the extracted local and global shape differences between two sets.

In the first step, the segmented binary maps are processed to the same image orientation and isotropic voxel sizes, and then converted into 3D triangulated surfaces using the marching cube algorithm (Lorensen and Cline, 1987). A smoothing process is subsequently applied on each surface in order to remove surface noise. Then, a reference surface is defined in an iterative process, and all triangulated surfaces are aligned to this reference using a rigid registration algorithm. In order to establish the point-to-point correspondences across all surfaces, each mesh is matched to a selected reference surface using the spectral matching algorithm. The vertices of all surfaces are rearranged to create the new reconstructed meshes with consistent vertex ordering. This enables to create a mean shape of each study group, and detect any morphological variations between two groups. A distance map between two mean shapes is computed to capture the local group differences across populations. Moreover, average and maximum distances, as well as Dice volume overlap are calculated to indicate

the global group differences between two study groups.

Surface spectral matching

This section presents the theoretical framework of computing the spectral matching between two surfaces in the spectral domain. The matching between two surfaces $\mathcal{S}_1$ and $\mathcal{S}_2$ is conducted in a two-step process (Figure 6.2.a and Figure 6.2.b). In the first step, an initial map is calculated between the two surfaces (Lombaert et al., 2013a). This initial map is then used in the second step to establish a smooth map between the two meshes (Lombaert et al., 2013b).

For each surface mesh $\mathcal{S}_i\,(i \in \{1,2\})$ composed of the set of vertices $\mathcal{V}_i$ and edges $\mathcal{E}_i$ (neighboring points in mesh faces), the corresponding graph $\mathcal{G}_i = \{\mathcal{V}_i, \mathcal{E}_i\}$ is built. Then, the weighted adjacency matrix $\mathcal{W}_i$ is created based on a distance between connected vertices and the graph Laplacian matrix $\mathcal{L}_i$ (Grady and Polimeni, 2010) is defined as :

$$\mathcal{L}_i = G_i\,(\mathcal{D}_i - \mathcal{W}_i)\,. \tag{6.1}$$

where $\mathcal{D}_i$ is a diagonal matrix with elements given by the degree of vertices. $\mathcal{G}_i$ is another diagonal matrix, which could be considered as $\mathcal{G}_i = \mathcal{D}_i^{-1}$ or any other (positive valued) vertex weights (Lombaert et al., 2013a, 2011). The eigendecomposition of the Laplacian matrix $\mathcal{L}_i$ computes the eigenvalues and the associated eigenmodes. The spectrum (spectral representation) $\tilde{\mathcal{S}}_i$ is defined as the first k eigenmodes associated with the non-zero eigenvalues.

Once the spectrums $\tilde{\mathcal{S}}_1$ and $\tilde{\mathcal{S}}_2$ are computed, the reordering and sign adjustment (Lombaert et al., 2013a) process are performed and the resulting spectrums are aligned using the Coherent Point Drift (CPD) method (Myronenko et al., 2009a). Then, the correspondence map c between two surfaces $\mathcal{S}_1$ and $\mathcal{S}_2$ is established with a simple nearest-neighbor search in the spectral domain. An overview of the procedure to find the correspondence map c is shown in Figure 6.2.a.

Given the initial map c between two surfaces, the final map φ (smooth match) is obtained according to Figure 6.2.b. In this procedure, an association graph $\mathcal{G}_a = \{\mathcal{V}_{1,2}, \mathcal{E}_{1,2,c}\}$ composed of the set of vertices and edges of $\mathcal{S}_1$ and $\mathcal{S}_2$ with the initial links c between the two surface meshes is created. Then, the Laplacian matrix is created as $\mathcal{L}_a = G_a\,(\mathcal{D}_a - \mathcal{W}_a)$, where $\mathcal{W}_a$, G_a, $\mathcal{D}_a$ could be defined in the similar way as Equation 6.1. The eigendecomposition of the Laplacian matrix $\mathcal{L}_a$ produces a shared set of eigenvectors that enables a direct mapping $\varphi_{1\to2}$ between two meshes (See (Lombaert et al., 2013b) for more details).

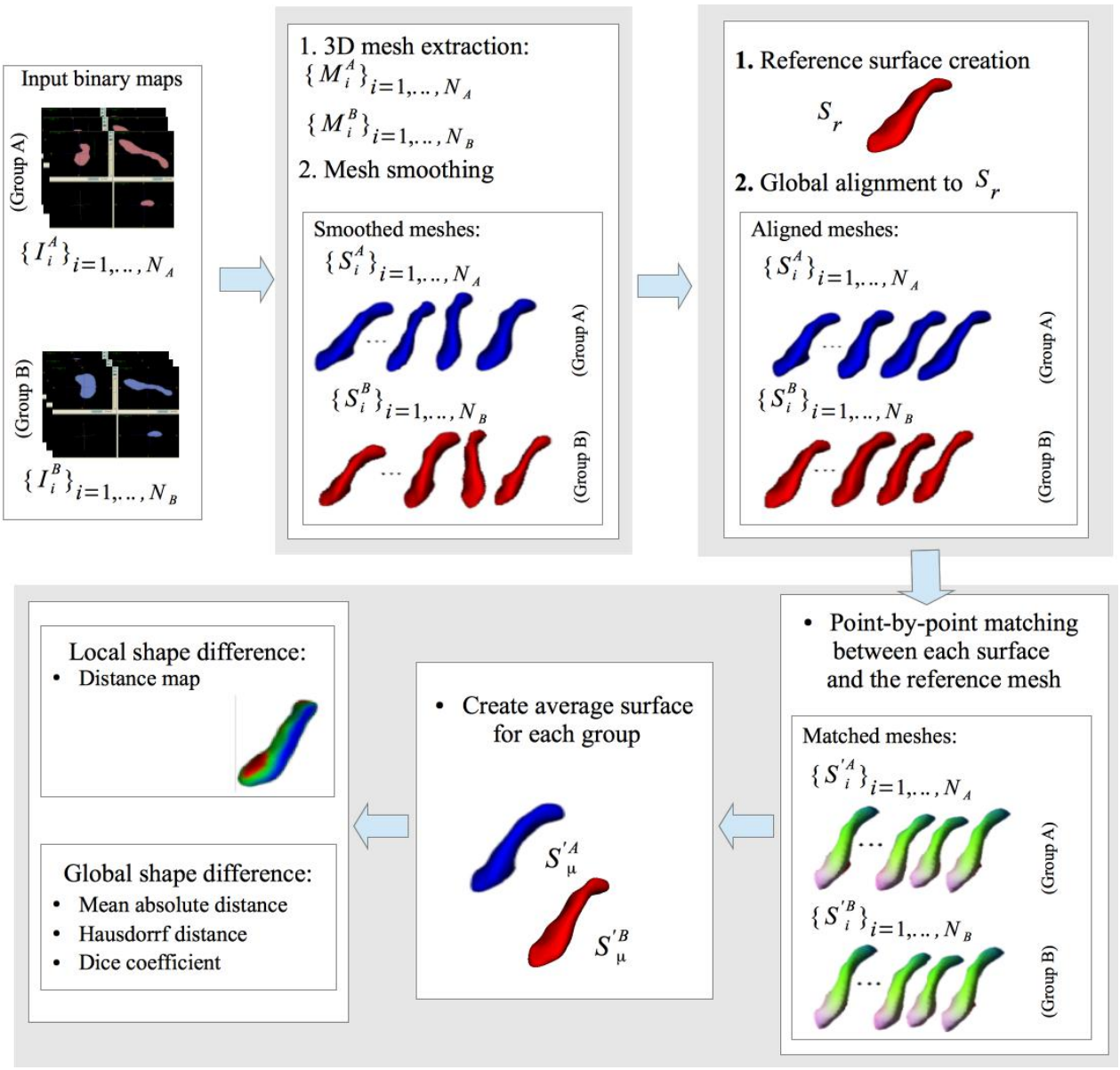

Figure 6.1 Shape analysis pipeline based on spectral decomposition between two groups of subjects ($\left\{I_i^A\right\}_{i=1,\ldots,N_A}$ and $\left\{I_i^B\right\}_{i=1,\ldots,N_B}$, where N_A and N_B are the number of samples in each set). Once 3D triangulated surfaces $\left\{\mathcal{M}_i^A\right\}_{i=1,\ldots,N_A}$ and $\left\{\mathcal{M}_i^B\right\}_{i=1,\ldots,N_B}$ are extracted, a mesh smoothing process is performed to create surfaces $\left\{\mathcal{S}_i^A\right\}_{i=1,\ldots,N_A}$ and $\left\{\mathcal{S}_i^B\right\}_{i=1,\ldots,N_B}$. Then, the reference surface $\mathcal{S}_r$ is created and all surface meshes are aligned to the reference. The point-to-point matching between all surfaces is computed using the spectral matching algorithm to generate the surfaces $\left\{\mathcal{S}'^A_i\right\}_{i=1,\ldots,N_A}$ and $\left\{\mathcal{S}'^B_i\right\}_{i=1,\ldots,N_B}$. Finally, the mean surfaces $\mathcal{S}'^A_\mu$ and $\mathcal{S}'^B_\mu$ are created and local and global shape differences are computed.

According to (Lombaert et al., 2013a, 2011), considering higher node weights in the graph $\mathcal{G}_a$ could improve the spectral matching precision between two surfaces. This could be achieved by adding extra features on node weights G_a (Lombaert et al., 2013a, 2011). In this paper, we propose to use the mean curvature (Cohen-Steiner and Morvan, 2003) as an additional feature, due to it's ability to represent the pointwise characteristic within a surface. In fact, the exponential of the mean curvature is added to the node weights in the Laplacian graph $\mathcal{L}_a$ to assign higher weights to each vertex. In order to compute the mean curvature at each vertex v, the principal curvatures $C_{\min}(v)$ and $C_{\max}(v)$ (Cohen-Steiner and Morvan, 2003) are calculated as the minimum and maximum curving degrees of the surface $\mathcal{S}_i$. Then, the mean surface curvature C at each vertex v is defined as :

$$C_v = \frac{1}{2}\left(C_{\min}(v) + C_{\max}(v).\right) \tag{6.2}$$

Hence, the mean curvature of surface $\mathcal{S}_i$ is computed as $\{C(1), C(2), ..., C(n)\}$, where n is the total number of vertices in the surface $\mathcal{S}_i$. The additional information is incorporated in the weighting of the nodes by computing the exponential of the mean curvature, and defining the diagonal node weighting matrix G_a as :

$$G_a = \mathcal{D}_a^{-1}\left(\exp\left(diag\left(C(1), C(2), ..., C(n)\right)\right)\right) \tag{6.3}$$

The effect of the curvature feature on the matching accuracy will be assessed in the results section.

6.3.2 Groupwise shape analysis

Preprocessing and surface representation

Let $\left\{I_i^A\right\}_{i=1,...,N_A}$ and $\left\{I_i^B\right\}_{i=1,...,N_B}$ be two separate sets of segmented binary maps of a particular subcortical structure, with N_A and N_B as the number of samples in each set, respectively. To extract smooth 3D triangulated surface meshes from input binary maps, the labeled datasets are first reoriented in the same image orientation and resampled to isotropic voxel sizes of $1 \times 1 \times 1 mm^3$. Then, the isosurfaces of the segmentation are extracted using the marching cube algorithm (Lorensen and Cline, 1987) to generate 3D surface meshes denoted as $\left\{\mathcal{M}_i^A\right\}_{i=1,...,N_A}$ and $\left\{\mathcal{M}_i^B\right\}_{i=1,...,N_B}$ for the two study groups.

The 3D triangulated surface meshes are then smoothed using mean curvature flow algorithm (Desbrun et al., 1999), in order to create the smoothed meshes $\left\{\mathcal{S}_i^A\right\}_{i=1,...,N_A}$ and $\left\{\mathcal{S}_i^B\right\}_{i=1,...,N_B}$.This smoothing step is an iterative process, which removes surface irregularities

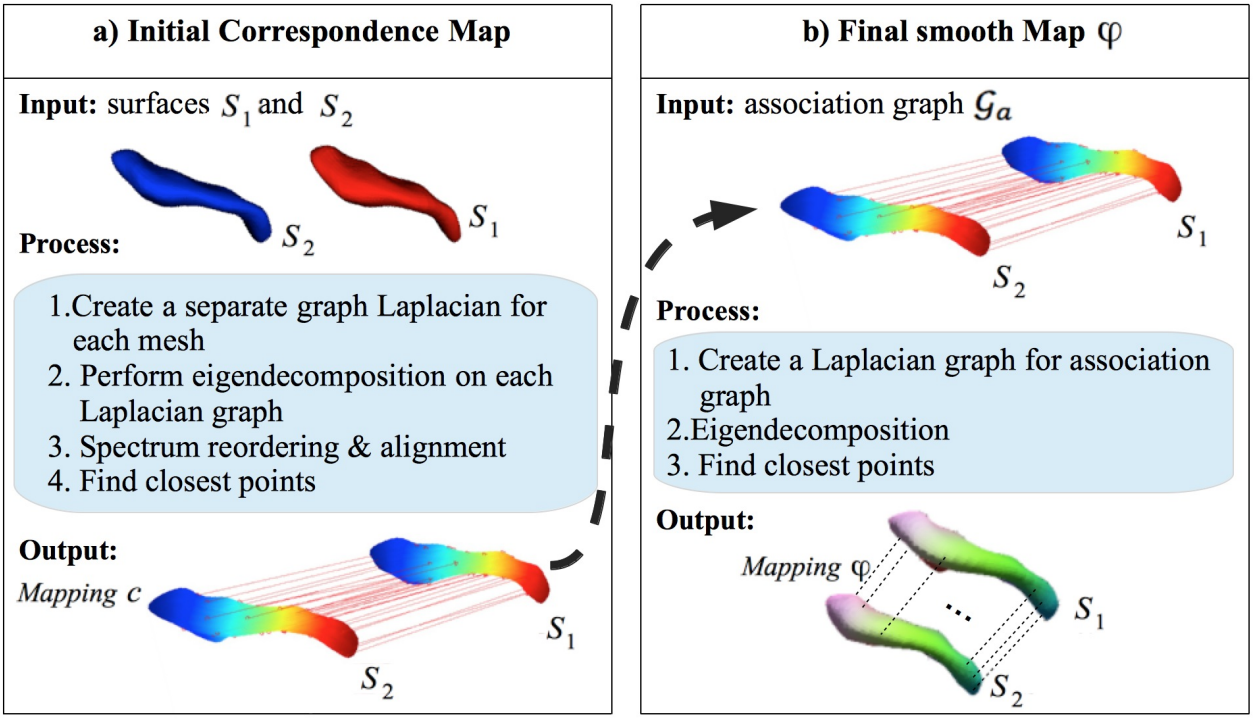

Figure 6.2 Surface matching between two surfaces. (a) Initial matching of two meshes. (b) Final correspondence mapping between two surfaces based on diffeomorphic spectral matching approach.

and improves the appearance of surfaces. Given a triangulated surface $\mathcal{M}_i$ and for each mesh vertex x, the mean curvature flow is computed using the following explicit vertex-updating scheme :

$$x_{new} \leftarrow x_{old} + \lambda H\left(x_{old}\right) \tag{6.4}$$

where the step-size λ is a small positive number. This parameter should be chosen small enough to keep the smoothing process stable. Here, $H\left(x_{old}\right)$ is a discrete approximation of the mean curvature vector at a mesh vertex x, which is defined as :

$$H\left(x_{old}\right) = \frac{1}{4\varnothing} \sum_i \left(\cot \alpha_i + \cot \beta_i\right)\left(Q_i - x_{old}\right) \tag{6.5}$$

where $\varnothing$ is the sum of the areas of the triangles surrounding x and Q_i are the neighbours of the vertex x_{old}. Here, α_i and β_i are the two angles opposite to the edge $Q_i x_{old}$. The process defined in Equation 6.4 is applied to every point of each triangulated surface $\mathcal{M}_i$ iteratively

to further smooth the mesh. High iterations produce smoother mesh, but it might cause the loss of fine surface details. Removing fine surface information could mislead a groupwise morphological study in capturing small shape differences. In this paper, the 3D surfaces are smoothed after five iterations. This is the least smoothing that is required to avoid failure in spectral matching process. The parameter λ is set to 1.0 as suggested in (Desbrun et al., 1999).

Reference surface and alignment

As a prerequisite for any shape analysis study, objects have to be normalized with respect to a reference coordinate frame. In order to define the reference surface $\mathcal{S}_r$, an arbitrary surface from the input dataset can be chosen randomly, and used as a reference mesh. Alternatively, an average template could be created in an iterative process and employed as a reference surface. In this study, these two different reference selection approaches are tested, in order to evaluate their impact on the performance of the proposed shape analysis framework.

The step-by-step procedure of the average reference computation is presented in Algorithm 1. This algorithm is based on the approach proposed by (Guimond et al., 2000), in which an average image was created by alternating between pairwise registrations and updates of the average image. The input to Algorithm 1 is the union of the two sets $\left\{\mathcal{S}_i^A\right\}_{i=1,\ldots,N_A}$ and $\left\{\mathcal{S}_i^B\right\}_{i=1,\ldots,N_B}$, which is defined as $\{\mathcal{S}_i\}_{i=1,\ldots,N_A+N_B}$. Starting from an initial reference surface (e.g., $\mathcal{S}_r = \mathcal{S}_1$), all other surfaces $\mathcal{S}_i$ are rigidly aligned to the selected reference mesh. This rigid alignment is performed using the ICP (iterative closest point) algorithm (Besl, 1992), which finds the optimal rigid transformation between each mesh and the reference $\mathcal{S}_r$. In the next step, the point-to-point mapping $\varphi_{i\to r}$ between each surface $\mathcal{S}_i$ and $\mathcal{S}_r$ is computed based on the spectral matching framework presented in Section 6.3.1. In the final step, the geometrical mean shape is estimated from all matched structures, and used as an updated reference shape. This process terminates when no more changes in $\mathcal{S}_r$ obtained or the maximum number of iterations is achieved. According to preliminary experiments, the maximum iteration value is set as 10.

Once the reference surface $\mathcal{S}_r$ is defined, using either random selection or average surface creation, all surfaces $\mathcal{S}_i$ are registered rigidly to $\mathcal{S}_r$. This global surface alignment between each surface $\mathcal{S}_i$ and reference surface $\mathcal{S}_r$ consists of rigid transformations.

Algorithm 2 Average template

Input : $N = (N_A + N_B)$ triangulated surfaces $\mathcal{S}_i$, and an initial reference surface (e.g., $\mathcal{S}_r = \mathcal{S}_1$)
repeat
    Align all surfaces $\mathcal{S}_i$ to $\mathcal{S}_r$ using rigid ICP
    Find point-to-point mapping $\varphi_{i \to r}$ between each surface $\mathcal{S}_i$ and $\mathcal{S}_r$
    Update reference $\mathcal{S}_r = \frac{1}{N} \sum_{i=1}^{N} (\mathcal{S}_i \circ \varphi_{i \to r})$
until No more changes in $\mathcal{S}_r$ obtained or the maximum number of iterations is reached
Output : Average template $\mathcal{S}_r$

Groupwise shape analysis

Given two sets of aligned surface meshes $\left\{\mathcal{S}_i^A\right\}_{i=1,\ldots,N_A}$ and $\left\{\mathcal{S}_i^B\right\}_{i=1,\ldots,N_B}$, the point-to-point correspondences between each surface and the reference $\mathcal{S}_r$ is established using the spectral matching approach presented in Section 6.3.1. Then, the mesh vertices of all surfaces are rearranged to have the consistent ordering across the populations. The resulting reconstructed meshes are denoted as $\left\{\mathcal{S}'^A_i\right\}_{i=1,\ldots,N_A}$ and $\left\{\mathcal{S}'^B_i\right\}_{i=1,\ldots,N_B}$ for the two study groups. The mean shapes $\mathcal{S}'^A_\mu$ and $\mathcal{S}'^B_\mu$ are computed by averaging the 3D coordinates of corresponding surface points across each group :

$$\mathcal{S}'^A_\mu = \frac{1}{N_A} \sum_{i=1}^{N_A} \mathcal{S}'^A_i \tag{6.6}$$

$$\mathcal{S}'^B_\mu = \frac{1}{N_B} \sum_{i=1}^{N_B} \mathcal{S}'^B_i \tag{6.7}$$

with $\varphi_{i \to r}$ the mapping from instance $\mathcal{S}_i$ to reference $\mathcal{S}_r$. The local shape differences between groups can be detected by computing a distance map between two mean shapes $\mathcal{S}'^A_\mu$ and $\mathcal{S}'^B_\mu$. This will provide the visual assessment of the location and magnitude of the differences between groups A and B. We use a standard, non-parametric Hotelling T^2 test (Pantazis et al., 2004) to check for significant group differences, with the null hypothesis that the two groups are drawn from the same distribution. The resulting raw p-values are then corrected for multiple comparisons by the false discovery rate (FDR) approach (Styner et al., 2006b).

The performance of the method is further evaluated by significant vertex ratio metric, which is estimated by computing the ratio of the number of statistically significant vertices over the total number of surface points of the mesh (Gao et al., 2014).

The global shape difference between two groups is computed by averaging the distances between the mean surfaces, which results in the mean absolute distance (MAD). The mean

absolute distance (MAD) attempts to estimate the average distance of surfaces ${\mathcal{S}'}_{\mu}^{A}$ and ${\mathcal{S}'}_{\mu}^{B}$ by projecting the vertices of the first surface on the second one (Gerig et al., 2001b). Moreover, the Hausdorff distance (Aspert et al., 2002) is calculated as the maximum distance between two mean shapes. This measure has high sensitivity to positional differences between two surfaces. In addition, Dice coefficient (Dice, 1945) is reported as a global measure, which indicates the amount of volume overlap between two mean shapes. The 3D Dice coefficient metric between two surfaces ${\mathcal{S}'}_{\mu}^{A}$ and ${\mathcal{S}'}_{\mu}^{B}$ is defined as the intersection divided by the mean volume of the two surfaces :

$$Dice\left({S'}_{\mu}^{A}, {S'}_{\mu}^{B}\right) = \frac{\left|{S'}_{\mu}^{A} \cap {S'}_{\mu}^{B}\right|}{\left(\frac{\left|{S'}_{\mu}^{A}\right| + \left|{S'}_{\mu}^{B}\right|}{2}\right)} \tag{6.8}$$

For identical surfaces, Dice coefficient achieves its maximum value of 1, with decreasing values indicating less volume overlap.

6.4 Results

In this section, we will first evaluate the accuracy of the proposed method under different configurations and initial conditions. Then, the performance of the shape analysis approach will be evaluated on different subcortical structures (hippocampus, putamen) from various neuroimaging datasets. Finally, the proposed methodology is applied on a clinical application of Alzheimer's disease. This disorder is one of the most widespread diseases in the elderly population, which gradually damages the brain regions including hippocampus. Here, we use our framework to quantify subcortical morphological changes in patients diagnosed with Alzheimer's and mild cognitive impairment.

6.4.1 Datasets

For accuracy and performance evaluation, two separate neuroimaging datasets were used. The first dataset includes putamen structures (PT dataset) and the second dataset consists of hippocampus shapes (HPC dataset).

The PT dataset includes 36 T1-weighted MR images from healthy controls. Subjects were recruited from a pediatric brain study (mean age 11, 24 males). Acquisition was performed on a 3.0 T MRI system (Philips Acheiva or Siemens) with an in-plane resolution of 256×256, slice thickness of 1 mm, and voxel size ranging between $1 \times 0.9677 \times 0.9677\ mm^3$ and $1 \times 1 \times 1\ mm^3$. In this dataset, the left putamen was segmented using FSL-FIRST automatic segmentation

toolbox (Patenaude et al., 2011a) and corrected by an experienced user. The segmented putamen structures in the dataset have been randomly separated into two groups to create two different groups A and B.

The HPC dataset contains 42 hippocampus shapes obtained from schizophrenic patients and matched healthy controls (mean age 32, all male gender) (Styner et al., 2004). The hippocampi were manually segmented from IR-Prepped SPGR (Inversion Recovery-Prepared Spoiled Gradient Echo) data segmented originally at $0.9375 \times 0.9375 \times 1.5\ mm^3$ resolution. In the HPC dataset, all cases were randomized and group association was performed to create two different groups (group A and group B). The SPHARM-PDM toolbox developers prepared this dataset at UNC Neuro Image Analysis Laboratory (see www.nitrc.org/projects/spharm-pdm), as part of the public UNC Shape Tool distribution for shape analysis studies. Since the HPC dataset was provided by SPHARM-PDM software developers, it is relevant to assess the performance of the proposed shape analysis method compared to the SPHARM-PDM approach on this dataset.

In order to validate the proposed framework on clinical applications, a popular brain imaging dataset in Alzheimer's disease, namely the Alzheimer's disease Neuroimaging Initiative (ADNI) was used. Capturing the structural morphometry have always been a target of interest in Alzheimer's disease studies, since evaluating the structural changes could provide a clue for early detection of the pathology. The ADNI database (adni.loni.usc.edu) was launched in 2003 as a public-private partnership, led by Principal Investigator Michael W. Weiner, MD. The primary goal of ADNI has been to test whether serial magnetic resonance imaging (MRI), positron emission tomography (PET), other biological markers, and clinical and neuropsychological assessment can be combined to measure the progression of mild cognitive impairment (MCI) and early Alzheimer's disease (AD). For up-to-date information, see www.adni-info.org. The database of ADNI consists of cross-sectional and longitudinal data including 1.5 or 3.0 T structural MR images. The detailed description of the MRI protocol of ADNI is provided in (Jack Jr et al., 2008). For this study, a subset of screening 1.5 T MR images is used including 47 normal controls (NC), 47 AD patients, and 47 individuals with MCI. The three groups are matched approximately by age and gender (NC with mean age of 76.7 ± 5.4, 23 males; AD with mean age of 77.4 ± 7.2, 21 males; and MCI with mean age of 75.0 ± 6.9, 28 males). For the purpose of reproducibility, the list of the study participants' identifiers is provided in the Supplementary material. Contributors of ADNI performed additional post-processing steps on MR images to correct certain image artifacts and to enhance standardization across sites and platforms. The post-processing steps include gradient nonlinearity correction (Jovicich et al., 2006), intensity inhomogeneity correction (Jack Jr et al., 2008), bias field correction (Sled et al., 1998), and phantom-based geometrical scaling to

remove calibration errors (Gunter et al., 2006). Here, we use these processed images. Left and right hippocampi were segmented using FSL-FIRST automatic segmentation software package (Patenaude et al., 2011a) and visual inspection was performed on the output binary masks to ensure the quality of the automatic segmentation.

6.4.2 Validation methodology

The proposed framework was first tested under different configurations using both PT and HPC datasets. The minimum number of spectral coordinates, which is required for having a stable output, was determined. Then, the impact of curvature features and different reference surfaces on the accuracy of the proposed framework was tested. In each case, mean absolute distance (MAD) measure, along with Hausdorff distance (Aspert et al., 2002) and Dice coefficient (Dice, 1945) was computed to assess the group differences between mean shape A and B. To evaluate the accuracy of the proposed framework, the performance of the spectral approach under different configurations was compared with a state-of-the-art method used for groupwise analysis of anatomical shapes, namely SPHARM-PDM (Styner et al., 2006b). The maximum spherical harmonics degree of the SPHARM-PDM method is set to 15 for putamen structures and 12 for hippocampus shapes.

Once the configuration of the proposed framework was completed, the proposed framework was validated on PT and HPC subcortical datasets. In these experiments, both local and global group differences were analyzed and compared to SPHARM-PDM. Finally, the proposed methodology was applied for quantifying hippocampal morphological variations in Alzheimer's disease (AD). Hippocampal morphometry have been increasingly used in the AD research in the perspective of early detection of the pathology and future treatments. Here, the proposed framework was applied for detecting the morphological changes in individuals with Alzheimer's disease, in order to verify the accuracy of the spectral based shape analysis approach in the statistical studies of this clinical application.

6.4.3 Framework configurations

Number of spectral coordinates

The number of eigenvectors used to model surfaces in the spectral domain has an impact on the accuracy of the established surface correspondences in the spectral matching process. In this experiment, we examine the effect of the number of eigenvectors used as spectral coordinates on the groupwise shape analysis output. The eigendecomposition process is performed twice in the spectral matching approach : once for generating the initial map c, and

once for establishing the final map φ (see Section 6.3.1). As mentioned in Section 6.3.1, the first k eigenvectors associated with the smaller non-zero eigenvalues are extracted as spectral coordinates. The rationale for this choice is that the eigenvectors associated with the lower non-zero eigenvalues represent coarse intrinsic geometric properties of a shape (i.e., depicting the global shape model). However, the question remains how many eigenvectors is enough to represent the surfaces in the initial step, as well as the association graph G_a in the final process.

Here, we apply our shape analysis framework on both PT and HPC datasets with varying number of eigenvectors, and evaluate the framework output by measuring the mean absolute distance between two groups A and B. In this experiment, 10 separate study groups A and B are created from each dataset, and the average mean absolute distance is reported under varying number of eigenvectors (Figure 6.3). This experiment demonstrates that the framework output becomes stable at $k = 3$ for PT dataset and $k = 4$ for HPC dataset, and gains no further significant changes beyond these values. The difference in the sufficient numbers of eigenvectors between two datasets is due to the higher complexity of hippocampus structures compared to putamen surfaces. Thus, more eigenvectors are required to model hippocampus surfaces. Therefore, we consider $k_{initial} = k_{final} = 3$ for PT, and $k_{initial} = k_{final} = 4$ for HPC dataset as the number of eigenvectors for the remainder of the experiments.

Incorporating curvature feature

In this section, the impact of integrating additional features on the performance of the spectral groupwise approach is first evaluated to understand the value of surface curvature in the matching process. Then, the robustness of the subcortical surface matching process, both with and without additional features, is assessed by applying synthetic deformations to the surfaces.

As mentioned previously in Section 6.3.1, one can include additional information in the spectral matching process, by establishing a meaningful node weight for each vertex. Here, we compute the exponential of the mean curvature at each vertex (Equation 6.3), and use the combination of curvature and spectral coordinates for surface matching.

In order to evaluate the performance improvement after incorporating additional information, 10 separate subsets are created from 36 putamen structures of PT dataset. Each subset includes 10 different surfaces, i.e., five surfaces are considered as the member of the study group A and the rest are marked as group B. The proposed shape analysis framework is then applied on each subset with and without curvature features. In addition, the accuracy of the two implementation of the shape analysis framework is compared with the state-of-the-art

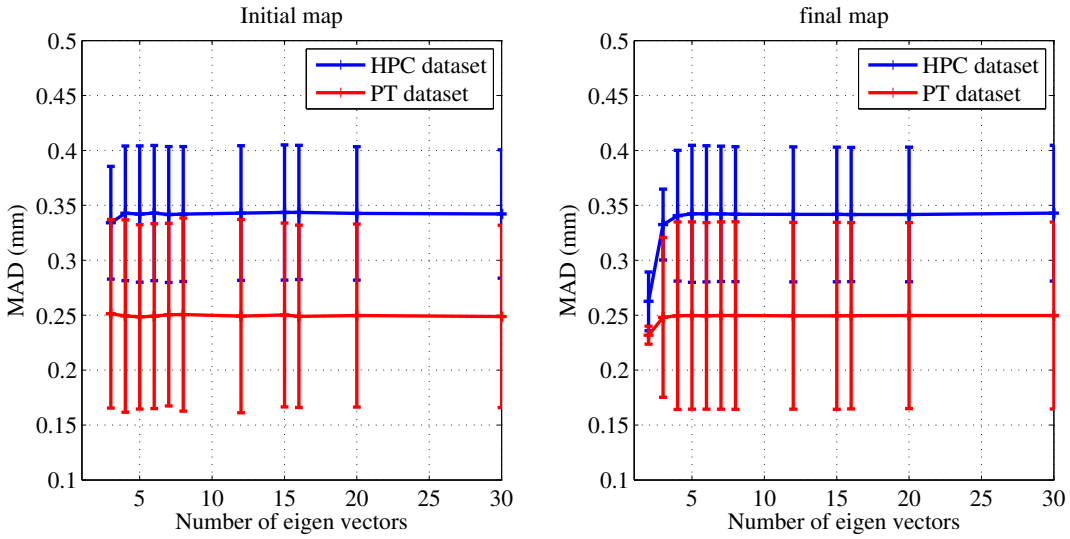

Figure 6.3 Performance of the shape analysis framework under varying number of eigenvectors used as spectral coordinates. Left : average mean absolute distance obtained for different number of eigenvectors in creating the initial map. Right : average mean absolute distance computed for different number of eigenvectors in creating the final map. The framework result becomes stable with three eigenvectors for PT dataset and four eigenvectors for HPC dataset.

groupwise shape analysis method, SPHARM-PDM (Styner et al., 2006b). Table 6.1 provides the average Dice coefficient, Hausdorff distance, and mean absolute distance in 10 separate subsets. Comparing our framework to SPHARM-PDM approach revealed that the groupwise shape analysis is more accurate using curvature features ($MAD = 0.25 \pm 0.09\ mm$) rather than using the spectral coordinate alone ($MAD = 0.37 \pm 0.14\ mm$).

We then tested the proposed shape analysis pipeline on the HPC dataset with and without curvature features, in order to investigate the influence of incorporating additional features. The extracted group differences show that the groupwise shape analysis integrated with curvature features ($Dice = 0.93, Hausd.Dist. = 1.16\ mm$, $MAD = 0.25 \pm 0.23\ mm$) is more accurate rather than using the spectral coordinate alone ($Dice = 0.70, Hausd.Dist. = 2.56\ mm$, $MAD = 0.95 \pm 0.57\ mm$). Hence, we can conclude that adding mean curvature has a significant positive effect on the framework's precision, when matching the hippocampus structures.

Now, we evaluate the accuracy of the subcortical surface matching process with and without additional features by testing for robustness to synthetic deformations on the PT dataset. To achieve this, we synthetically deform putamen surfaces, and match each putamen structure to

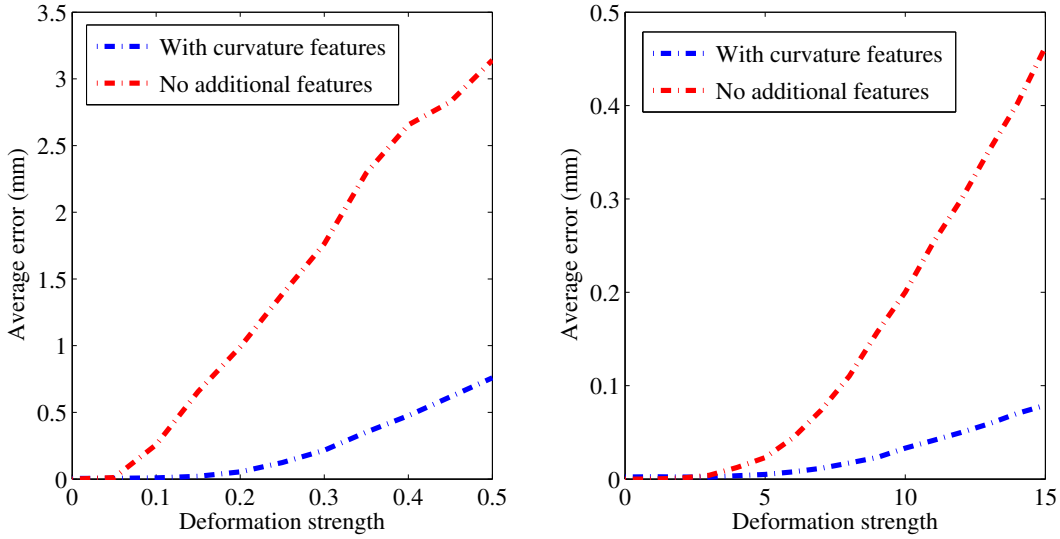

Figure 6.4 Testing the robustness of the spectral matching approach with respect to added deformations. Left : deformation on z direction, simulating surface compression ; Right : radial distortion. The average error at each deformation is shown for two separate implementations of the spectral approach, one with and another without incorporating additional features (curvature). This shows that using additional features improves the precision of the surface matching.

its deformed instance. Since the vertex indexing remains the same, we are able to establish a ground truth for correspondence maps. Thus, we measure the average distance between the locations of corresponding points found with spectral matching and the real locations of corresponding points defined by the ground truth.

Here, each vertex $x = (X, Y, Z)$ of the surface $\mathcal{S}_i$ is deformed by applying the transformation $Z' = (1 + \alpha)\, Z$. This deformation provides surface compression with out changing the topology of the mesh. All 36 putamen surfaces are deformed by varying α in the range of $[0, 0.4]$. Figure 6.4 left shows the accuracy of the surface matching with and without additional curvature features. At maximal deformation ($\alpha = 0.4$), the spectral matching method achieves an average error of 0.47 ± 0.10 mm with curvature features, and 2.65 ± 0.87 mm without extra information. In the next experiment, a radial distortion of $X' = X + \beta(X^2 + Y^2)^2 / \max\left((X^2 + Y^2)^2\right)$ is applied to each vertex $x = (X, Y, Z)$ of all 36 putamen surfaces. This deformation simulates a drastic change in a surface shape, while preserving the mesh topology. The controlling parameter β is varied in the range of $[0, 15]$ and the surface matching accuracy is assessed as shown in Figure 6.4 right. These experiment show the performance of the point-to-point spectral matching under synthetic deformation and indicates

Table 6.1 Shape differences between mean shape A and mean shape B with and without incorporating curvature features. The average Dice coefficient, Hausdorff distance and MAD are reported on 10 subsets of PT dataset. p-values of t-test between the spectral method and SPHARM-PDM framework are also shown. Spectral method without additional features produces significantly different results compared to SPHARM-PDM, while spectral framework integrated with curvature features generates similar results to the spherical method.

	Spectral method				**SPHARM-PDM**
	No additional features		**With additional features**		
Dice Coefficient	0.93±0.02	p = 0.02	0.94±0.02	p = 0.03	0.95±0.02
Hausd. Dist. (mm)	**2.08**±0.90	p <0.01	**1.15**±0.47	p = 0.18	**1.04**±0.34
MAD (mm)	**0.37**±0.14	p = 0.03	**0.25**±0.09	p = 0.64	**0.25**±0.09

that using additional curvature features enhances the surface matching accuracy.

Reference surface selection

In this section, we verify that the proposed shape analysis approach is unbiased to the choice of the reference surface within a study group. To this end, an arbitrary initial reference is selected as one of the surfaces in the PT dataset. Then, all surfaces are matched to this reference surface and shape analysis is conducted to estimate group differences. We performed 36 separate tests by iteratively selecting a new putamen surface as reference shape and computing the average mean distance in multiple runs (see Table 6.2). The average mean difference for the whole dataset is 0.14 ± 0.005 mm. In order to further examine the impact of reference surface on the shape analysis accuracy, in the next experiment, an average template is created in an iterative process, as described in Section 6.3.2. This template is applied as a reference surface in a shape analysis study on PT dataset, yielding a MAD of 0.14 ± 0.12 mm (see Table 6.2). These results suggest that the method produces near identical shape differences even by varying the choice of the initial reference. Therefore, if reducing the computational time is important in a study, it is possible to choose one of the input surfaces as a reference surface, instead of creating an average template.

Table 6.2 Shape differences between mean shape A and mean shape B. The average Dice coefficient, Hausdorff distance and MAD are reported for 36 separate runs by choosing 36 different initial references. In addition, Dice coefficient, Hausdorff distance and MAD are listed for a shape analysis test using average template as a reference surface.

	Different initial references ($n = 36$)	**Average template**
Dice Coefficient	0.97 ± 0.001	0.97
Hausd. Dist. (mm)	0.83 ± 0.12	0.83
MAD (mm)	0.14 ± 0.005	0.14 ± 0.12

6.4.4 Accuracy on subcortical shapes

In this section, we validate the performance of our proposed methodology on localizing structural morphologies across populations. The spectral based shape analysis framework is applied on both PT and HPC datasets to detect shape differences between groups A and B in each dataset. The performance of our spectral-based framework is compared with the state-of-the-art groupwise shape analysis method, SPHARM-PDM (Styner et al., 2006b).

For putamen shapes, the local group differences produced by both methods are illustrated in Figure 6.5, which shows that both methods capture similar shape differences. However, no significant difference is found after applying statistical analysis (see vertex ratio in Table 6.3). Since PT dataset includes healthy control subjects, detecting no significant differences between two groups was expected. The Dice coefficients between A and B ($Dice = 0.97$) and the mean absolute distances ($MAD = 0.14 \pm 0.11$ mm in spectral framework, and $MAD = 0.14 \pm 0.12$ mm in SPHARM-PDM) were the same for both methods (see Table 6.3). Also, the Hausdorff distances were 0.87 mm and 0.74 mm for spectral-based method and SPHARM-PDM, respectively. In order to further verify the accuracy of the proposed framework in comparing two groups of healthy subjects, we perform another experiment, in which the proposed pipeline is applied on different randomly separated datasets (i.e., five study group pairs, where each group contain 18 random putamen structures). The significant vertex ratio is computed on all five separate tests, which results in an average vertex ratio of zero. This experiment shows that the proposed method is working well by not detecting any significant shape variations between two healthy groups.

For hippocampus shapes, the location and magnitude of group differences is consistent between two methods (see Fig. 6). The p-values maps show a strong significance in tail region for both methods, while the head region does not show the same significant difference. On one hand, the subjects in HPC dataset are randomly divided into two groups A and B, thus we are not able to compare the pattern of hippocampal deformation with the one reported

Table 6.3 Evaluation of shape differences between mean shape A and mean shape B obtained with spectral method and SPHARM-PDM for the two datasets (HPC and PT). Results are compared using the Dice coefficient, the Hausdorff distance (Hausd. Dist.), the mean absolute distance (MAD), and significant vertex ratio.

	Hippocampus (HPC)		**Putamen (PT)**	
	Spectral Method	**SPHARM-PDM**	**Spectral Method**	**SPHARM-PDM**
Dice Coefficient	0.93	0.92	0.97	0.97
Hausd. Dist. (mm)	1.16	1.12	0.87	0.74
MAD (mm)	0.25 ± 0.23	0.28 ± 0.23	0.14 ± 0.11	0.14 ± 0.12
Vertex Ratio	0.16	0.23	0	0

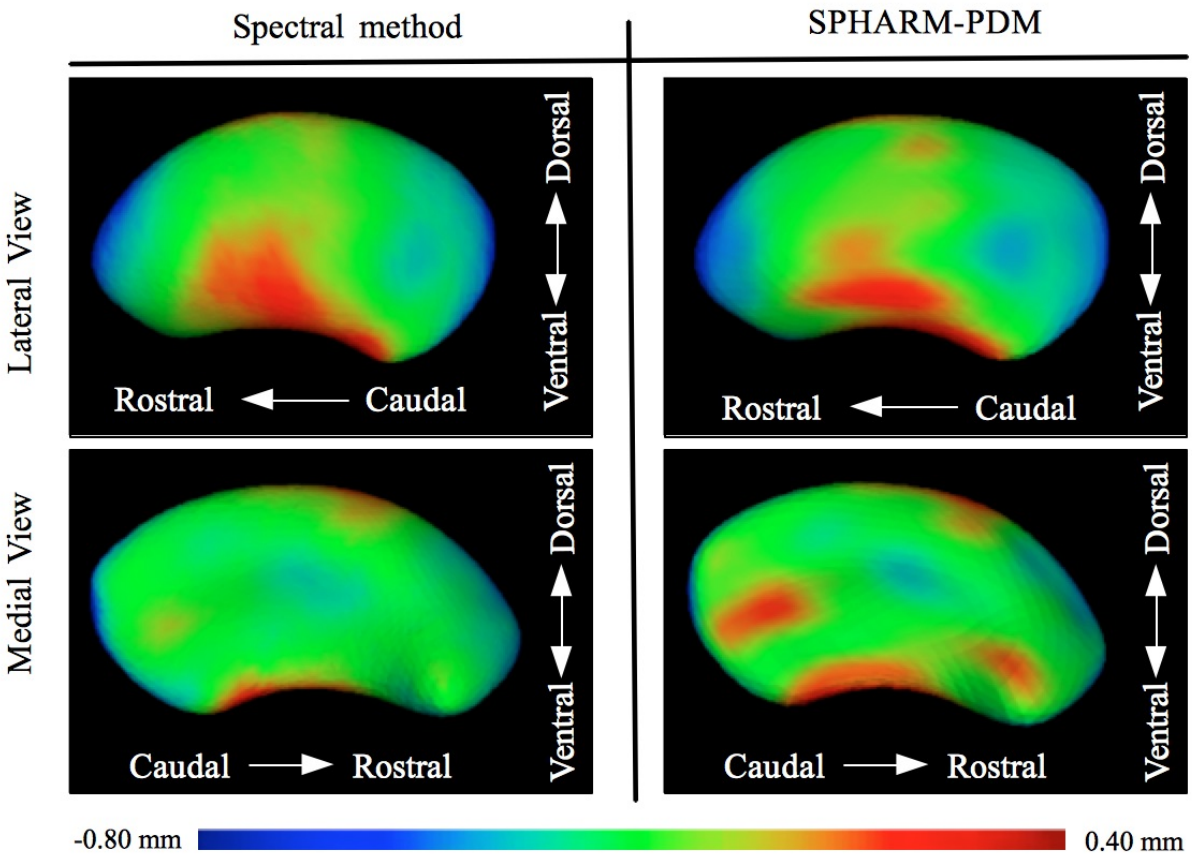

Figure 6.5 Putamen shape analysis. Distance maps were computed using the proposed spectral method on the left and SPHARM-PDM on the right. The resulting distance maps are shown in lateral and medial views. Statistical analysis showed that none of the captured group differences were significant.

in previous studies on Schizophrenia. On the other hand, inconsistency between groupwise shape analysis approaches have been reported in the literature (Gao et al., 2014; Styner et al., 2007). This might be due to the use of different strategies in extracting surface meshes and establishing surface correspondences between methods. The global shape differences show considerable agreement between the spectral framework ($Dice = 0.93$, $Hausd.Dist. = 1.16$ mm, $MAD = 0.25 \pm 0.23$ mm) and SPHARM-PDM ($Dice = 0.92$, $Hausd.Dist. = 1.12$ mm, $MAD = 0.28 \pm 0.23$ mm) (see Table 6.3). In general the two methods are consistent in global group difference measures and distance maps, although they show a small difference in p-value maps.

The computational time of both methods was measured on a 3.2 GHz Core i5 computer with 32GB of RAM. The computational cost of spectral method (PT : 5 min, HPC : 54 min)

is significantly lower than SPHARM-PDM (PT : 14 *min*, HPC : 242 *min* (or 4 *hours*)), especially for more complex shapes, like the hippocampus. This significant speed advantage was achieved without using parallel programing. These results suggest that the proposed spectral framework not only produces similar groupwise shape differences as SPHARM-PDM, it also has a clear speed advantage.

6.4.5 Application to Alzheimer's disease

Alzheimer's disease (AD) (Du et al., 2001) is the most common form of dementia in the elderly population. There is evidence that the neuropathological changes in AD damages the hippocampus structure, which is a brain region crucial to various cognitive functions (Du et al., 2001; Cho et al., 2011). Mild cognitive impairment (MCI) (Petersen et al., 1999) is considered as a transition state between normal aging and dementia. The cognitive deficits in MCI patients are not as severe as those seen in people with AD. However, MCI has a 10-fold risk of a transition to early Alzheimer's disease (Petersen et al., 1999). According to neuroanatomical studies, MCI patients have shown hippocampal deformation compared with healthy elderly people (Du et al., 2001; Kim et al., 2014). Here, our groupwise shape analysis is applied on the ADNI dataset including 47 AD patients, 47 individuals with MCI, and 47 matched normal controls (NC). The shape variation of left and right hippocampi was studied between AD and NC, as well as MCI and NC. To correct for head size differences across populations, each hippocampi surface was scaled by the individual's total intracranial volume. The total intracranial volumes were collected from ADNI database (adni.loni.usc.edu).

Figure 6.7 (a) and (b) show shape variations between AD and normal controls for the left and right hippocampi produced by spectral and SPHARM-PDM methods. In both methods, hippocampal surfaces of AD patients show inward local deformity mainly in lateral zones (CA1) and inferior-medial zones (subiculum), which is consistent with findings from previous studies (Wang et al., 2006; Cho et al., 2011; Kim et al., 2014). Table 6.4 shows the global

Table 6.4 Evaluation of shape differences between AD and control groups obtained with spectral method and SPHARM-PDM for the left and right hippocampus. Results are compared using the Dice coefficient, the Hausdorff distance (Hausd. Dist.), the mean absolute distance (MAD), and significant vertex ratio.

	Left Hippocampus		**Right Hippocampus**	
	Spectral Method	**SPHARM-PDM**	**Spectral Method**	**SPHARM-PDM**
Dice Coefficient	0.85	0.86	0.86	0.86
Hausd. Dist. (mm)	1.49	1.50	1.39	1.50
MAD (mm)	0.58 ± 0.26	0.55 ± 0.28	0.52 ± 0.29	0.55 ± 0.28
Vertex Ratio	0.45	0.40	0.46	0.45

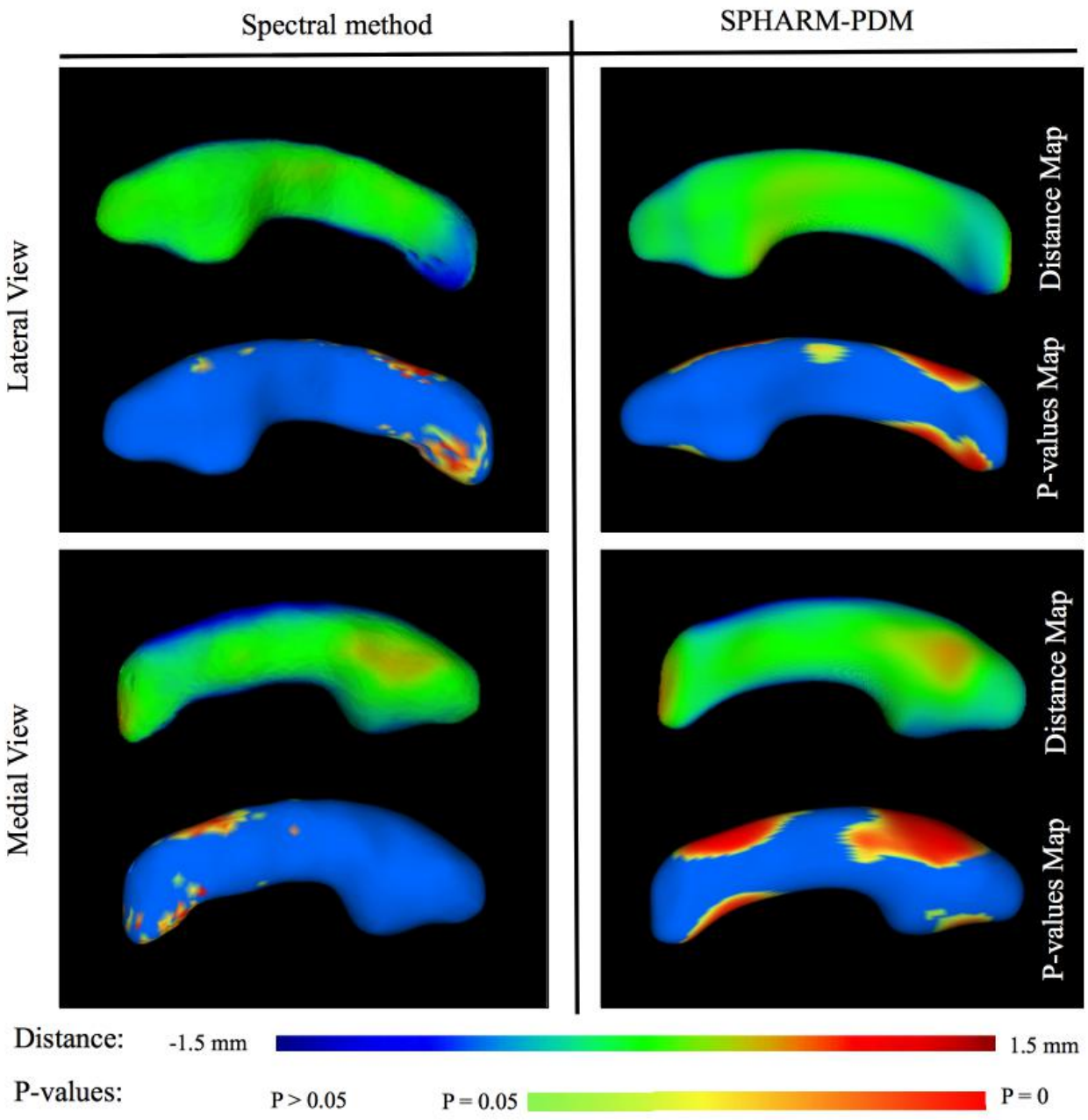

Figure 6.6 Hippocampus shape analysis. Distance maps are computed using spectral method and SPHARM-PDM. The resulting distance maps are shown in lateral and medial views. The respective FDR-corrected p-value maps are shown below distance maps.

shape differences between the spectral framework (Left hippocampi : $MAD = 0.58 \pm 0.26$ mm, Right hippocampi : $MAD = 0.55 \pm 0.29$ mm) and SPHARM-PDM (Left hippocampi : $MAD = 0.52 \pm 0.28$ mm, Right hippocampi : $MAD = 0.55 \pm 0.28$ mm). The p-values maps are almost similar between the two methods, however in general both methods limit the

shape changes to CA1 and subiculum. In addition, the ratio of the statistically significant vertices over the total number of surface points shows agreement between both methods.

The result of the same comparison performed between MCI patients and normal controls is shown in Figure 6.8 and Table 6.5. The distance maps produced by both methods are almost similar, while the p-value maps do not agree. Indeed, the spectral matching approach found significant inward variation in CA1 and subiculum regions of left and right hippocampi, however no significant region was captured by SPHARM-PDM. The amount of vertex ratio is interestingly different between spectral approach (Left hippocampi = 0.17 and Right hippocampi = 0.19) and SPHARM-PDM (Left hippocampi and Right hippocampi = 0). However, since there is no ground truth for the clinical datasets and the previous neuroanatomical studies on these pathologies used different input samples, it is unclear which method can be considered as the gold-standard. However, both methods provided almost the same global regional differences (Dice, Hausd. Dist., MAD) and similar distance maps. In addition both methods are in line with the previous neuroanatomical studies (Xie et al., 2013; Kim et al., 2014), which reported capturing weaker group differences between MCI and normal individuals rather than AD and normal controls.

6.5 Discussion

In this work, a new framework for groupwise shape analysis of subcortical structures, such as the hippocampus or putamen, is proposed in order to detect regional morphological alterations of subcortical structures from patients with neurological conditions, such as schizophrenia and Alzheimer's. The proposed method extracts the 3D meshes from input binary maps using the Marching cubes algorithm, which is one of the most popular 3D modeling algorithms in medical visualization. Since this approach was not able to generate high quality smoothed surfaces out of subcortical structures, the mean curvature flow algorithm was employed to smoothen the 3D surface meshes. Mean curvature flow smoothes a surface mesh by

Table 6.5 Evaluation of shape differences between MCI and control groups obtained with spectral method and SPHARM-PDM for the left and right hippocampus. Results are compared using the Dice coefficient, the Hausdorff distance (Hausd. Dist.), the mean absolute distance (MAD), and significant vertex ratio.

	Left Hippocampus		**Right Hippocampus**	
	Spectral Method	**SPHARM-PDM**	**Spectral Method**	**SPHARM-PDM**
Dice Coefficient	0.95	0.95	0.95	0.95
Hausd. Dist. (mm)	1.1	1.0	1.17	1.64
MAD (mm)	0.20 ± 0.18	0.21 ± 0.21	0.20 ± 0.20	0.24 ± 0.24
Vertex Ratio	0.17	0	0.19	0

moving the surface nodes along the normal direction and achieves the best smoothing result with respect to the geometric information of the surface. In the next step, all surfaces are rigidly registered to a reference surface and mean curvature is computed at each node of all surfaces. Once all shapes are globally aligned, the spectral matching approach as proposed in (Lombaert et al., 2013a,b) is applied in order to match each surface to the reference mesh. The proposed pipeline then creates two mean shapes as the geometric mean of all surfaces in each study group and a standard non-parametric permutation test is applied at every vertex point to detect significant local group differences. The framework terminates by applying various metrics in order to assess local and global shape differences across populations. As suggested by the authors of the spectral matching approach (Lombaert et al., 2013a,b), adding extra features, such as texture information, anatomical information, or landmark positions could lead to a better surface correspondence. For instance, in the case of matching cortical surfaces, the technique in (Lombaert et al., 2013b) proposed to use sulcal depth as additional feature, which provides information about the depth of the cerebral cortex. Therefore, the choice of additional features and assessing the effect of incorporating them into the matching process depends completely on the type of structures under study. In this work, we included the exponential of the mean curvature features in the node weights of the Laplacian matrix (Equation 6.1), since it intrinsically describes the local shape information of a 3D surface, without being too application specific. Experimental analysis in Section 6.4.3 revealed that embedding this additional feature significantly improves the matching accuracy to a greater extent. For instance, adding mean curvature has a significant positive effect on point correspondence performance, when matching hippocampus shapes. However, this feature is not crucial for analyzing putamen shapes. Hence, one might conclude that incorporating curvature features has more relevance to evaluate complex structures. In order to verify the performance of the proposed approach, the robustness of the shape analysis framework was evaluated using two reference selection approaches. According to these experiments, the use of an average reference shape gave slightly better results than using a single reference shape. However, the differences between average and randomly selected initial shape was not noticeable, indicating that the proposed framework is not significantly sensitive to this initial choice. Therefore, since computing an average reference is time-consuming, it is preferable to choose an arbitrary reference surface from input surfaces if the computational time is a critical issue in a particular study. A series of experiments were conducted in this study to analyze the performance of the proposed groupwise shape analysis approach. According to these experiments, the proposed group analysis framework and the state-of-the-art method SPHARM-PDM have considerable agreement in most of the cases. However, from a computational perspective, the proposed spectral method has a clear speed advantage over

the spherical harmonics based method. This speed advantage becomes more noticeable for more complex structures, such as for example analyzing a complex shape like the hippocampus, with a fourfold decrease in time compared to SPHARM-PDM. According to the experiments, the total running time of SPHARM-PDM could be reduced, by employing lower number of spherical harmonic coefficients. For instance, groupwise shape analysis on HPC dataset took on average 5.5 hours, when the structures were represented by 15 spherical coefficients, compared to 4 hours when 12 spherical coefficients were used. The problem is that the sufficient number of spherical coefficients must be provided in order to obtain an appropriate representation of a structure. In this paper, the number of spherical harmonic descriptions has been chosen in the range of 12 to 15, according to SPHARM-PDM software manual (www.nitrc.org/ projects/spharm-pdm) (Styner et al., 2006b). Aside from the consistency in the group distance maps produced by the two shape analysis methods, spectral and SPHARM-PDM methods, the generated p-value maps did not agree in some experiments. This type of inconsistency, which have been previously reported in the literature (Gao et al., 2014; Styner et al., 2007), mainly comes from the specific surface representation used by each method. A method like SPHARM-PDM generates smooth surfaces based on spherical harmonics, while our approach keeps the original meshes and applies only a slight smoothing process to remove surface irregularities. Severe smoothing can cause a method to miss small surface deformations in a groupwise morphological study. This might be the reason why SPHARM-PDM does not capture any region of group differences in the comparison between MCI and healthy controls. Another reason for inconsistency in capturing significant groupwise variations is the choice of surface correspondences across populations. This influence seems to be higher in studies with lower number of samples, especially when there is large shape variability due to the high age range and gender differences. Therefore, using relatively higher number of samples in the input populations, could reduce the inconsistency in groupwise morphological frameworks. Since there is no ground truth for the clinical datasets, it is not clear which one of the two methods (spectral group analysis or SPHARM-PDM) are more accurate. Nonetheless, one should keep in mind that both methods produce similar distance maps and close global group differences, which shows that the two methods are consistent in general. In addition, both methods did not detect any significant shape variations when the two groups of controls were used as inputs. This indicates that the two methods are working well. As an application, the proposed framework was applied on the ADNI dataset including AD, MCI, and normal controls. In previous neuroimaging studies, it has been reported that subjects with AD and MCI could be discriminated from healthy subjects by examining the pattern of hippocampal surface variations (Du et al., 2001; Cho et al., 2011; Petersen et al., 1999; Kim et al., 2014; Wang et al., 2006; Xie et al., 2013). Hippocampal atrophy begins

in lateral zones (CA1) and spreads to inferior-medial zones (subiculum) (Xie et al., 2013). The superior zones including CA2-4 and Gyrus Dentatus are preserved (Xie et al., 2013). We validated our scheme through a statistical shape analysis on hippocampal surface deformity in ADNI dataset, by demonstrating a consistency with previous clinical findings. These results suggest that the proposed spectral-based shape analysis framework could allow for quantitative assessment of variations in subcortical structures, associated with a neurological disorder, which leads to the better understanding of a pathology.

An important issue in any surface-based shape analysis approach is the reliance on the segmentation accuracy. This step has a crucial impact on a shape analysis pipeline, since its quality could affect the accuracy of the detected shape variations. The segmentation process becomes more challenging, when we attempt to capture slight group differences across a population, since small shape variations have greater chances of being lost in a segmentation process. In this paper, we used an openly-available automatic segmentation tool (FSL-FIRST (Patenaude et al., 2011a)) for segmenting structures in PT and ADNI datasets. However, in order to ensure about the quality of the structural delineations, we asked a trained expert user to correct the segmentations. These corrected labels were then used as an input in the proposed shape analysis framework. As future work, it would be helpful to incorporate a more accurate segmentation process in the pipeline, which is able to correctly define the boundary of each structure and extract smoothed meshes directly from MR images.

In summary, the proposed groupwise morphological framework with its methods for surface extraction, smoothing, matching, and statistical analysis is novel, and produced comparable results to the state-of-the-art algorithm, while being faster. This paper was the first work that integrated curvature-based spectral matching in to a groupwise shape analysis pipeline. Experimental analysis on real clinical dataset even showed that the extracted group differences were in line with the findings in other clinical studies. This paper proposed an alternative to the current state-of-the-art groupwise shape analysis framework and provides a new pipeline for future clinical studies.

6.6 Conclusions

In this paper, a new groupwise shape analysis framework is proposed for subcortical surfaces based on spectral matching theory. This spectral matching process is able to establish reliable correspondences between different surface meshes and may help in the investigation of groupwise structural differences between two study groups. From a clinical perspective, the proposed method can contribute to the diagnosis of subcortical shape variations in different pathologies, like Alzheimer's disease.

One important future direction of the proposed framework is to extend the available approach for diagnosis of different pathologies, which cause morphological variations in subcortical structures. This could be done by modeling the existing shape variations in patients using a classification approach, and try to distinguish the pathological subjects from normal individuals. Such a framework would become a complementary technique to other available diagnosis approaches, which are currently used for identifying different diseases. However, this kind of diagnosis framework requires incorporating larger datasets to achieve high and stable classification accuracy.

Acknowledgements

Funding was provided by the Canada Research Chairs and from the CHU Sainte-Justine Research Center. Hippocampus dataset (HPC) was provided by M. Styner and coworkers, UNC Neuro Image Analysis Laboratory, as part of the public UNC Shape Tool distribution and the original data acquisition was funded by the Stanley Foundation. ADNI data collection and sharing for this project was funded by the Alzheimer's Disease Neuroimaging Initiative (ADNI) (National Institutes of Health Grant U01 AG024904) and DOD ADNI (Department of Defense award number W81XWH-12-2-0012). ADNI is funded by the National Institute on Aging, the National Institute of Biomedical Imaging and Bioengineering, and through generous contributions from the following : AbbVie, Alzheimer's Association ; Alzheimer's Drug Discovery Foundation ; Araclon Biotech ; BioClinica, Inc. ; Biogen ; Bristol-Myers Squibb Company ; CereSpir, Inc. ; Eisai Inc. ; Elan Pharmaceuticals, Inc. ; Eli Lilly and Company ; EuroImmun ; F. Hoffmann-La Roche Ltd and its affiliated company Genentech, Inc. ; Fujirebio ; GE Healthcare ; IXICO Ltd. ; Janssen Alzheimer Immunotherapy Research & Development, LLC. ; Johnson & Johnson Pharmaceutical Research & Development LLC. ; Lumosity ; Lundbeck ; Merck & Co., Inc. ; Meso Scale Diagnostics, LLC. ; NeuroRx Research ; Neurotrack Technologies ; Novartis Pharmaceuticals Corporation ; Pfizer Inc. ; Piramal Imaging ; Servier ; Takeda Pharmaceutical Company ; and Transition Therapeutics. The Canadian Institutes of Health Research is providing funds to support ADNI clinical sites in Canada. Private sector contributions are facilitated by the Foundation for the National Institutes of Health (www.fnih.org). The grantee organization is the Northern California Institute for Research and Education, and the study is coordinated by the Alzheimer's Disease Cooperative Study at the University of California, San Diego. ADNI data are disseminated by the Laboratory for Neuro Imaging at the University of Southern California.

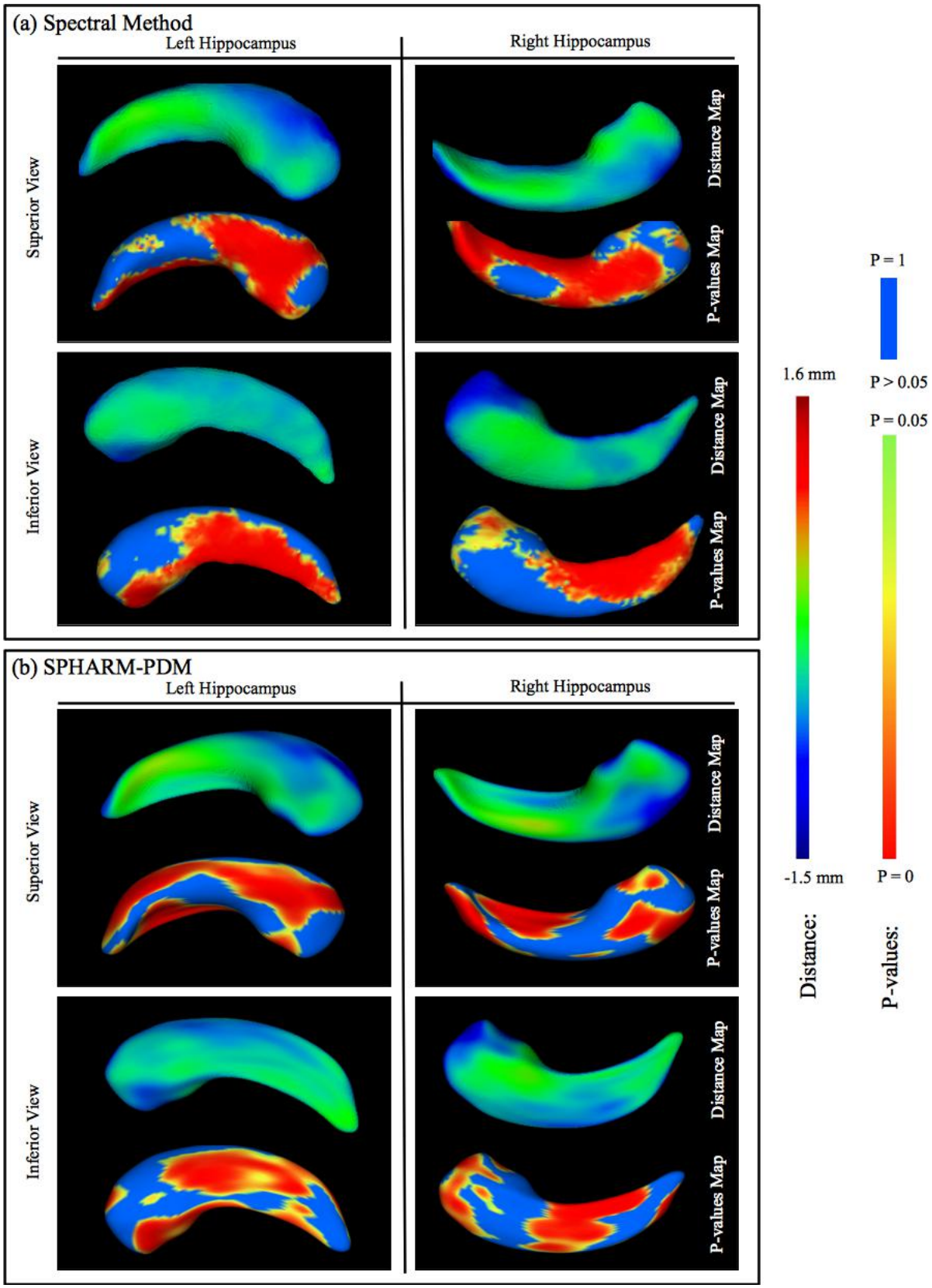

Figure 6.7 Left and right hippocampal shape deformations in AD patients compared with normal controls. Distance maps are computed along with the respective FDR-corrected p-values maps using spectral method (a) and SPHARM-PDM (b).

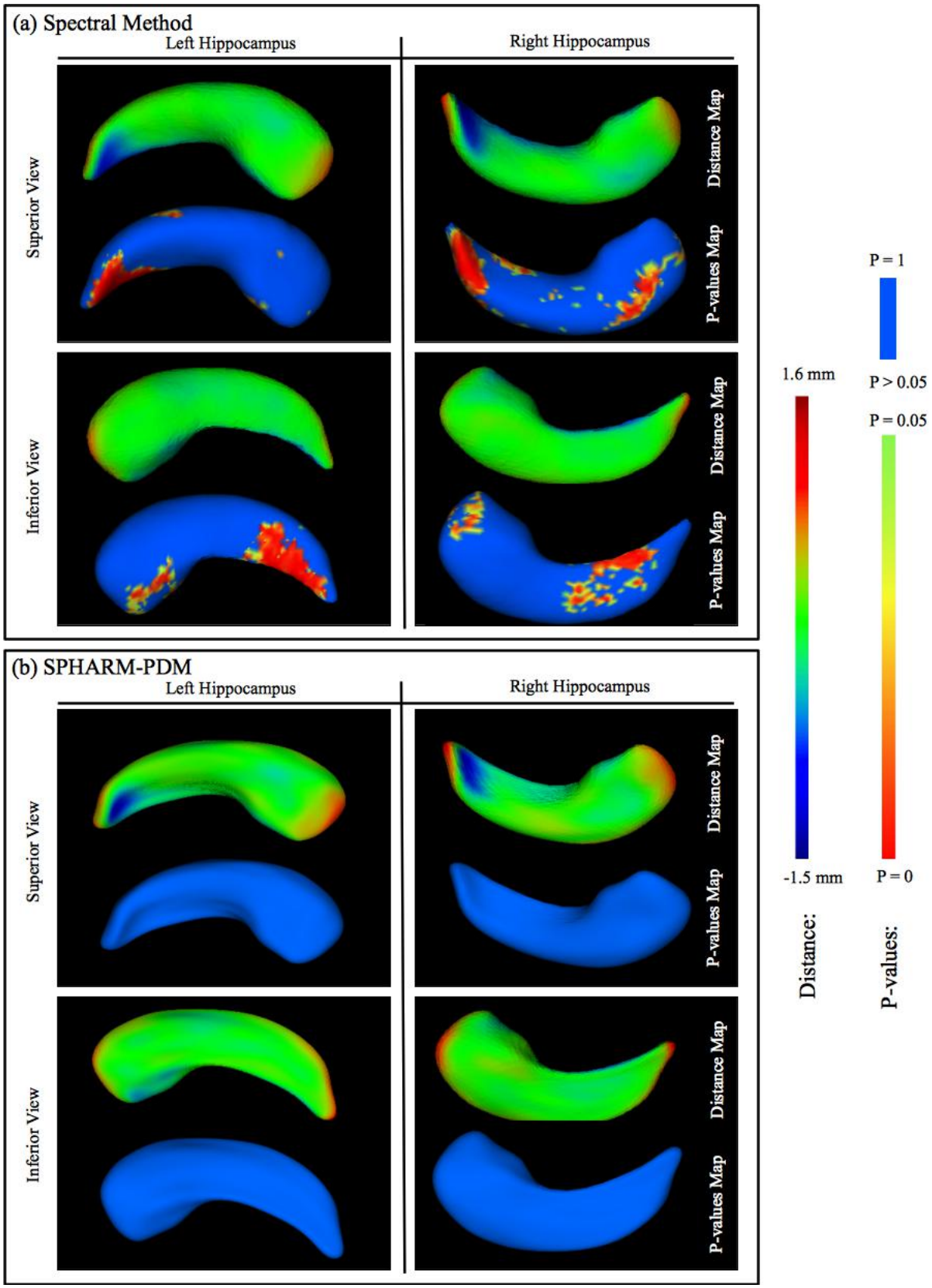

Figure 6.8 Left and right hippocampal shape deformations in MCI patients compared with normal controls. Distance maps are computed along with the respective FDR-corrected p-values maps using spectral method (a) and SPHARM-PDM (b).

CHAPTER 7 ARTICLE 3 : SUB-CORTICAL BRAIN MORPHOMETRY AND ITS RELATIONSHIP WITH COGNITION IN ROLANDIC EPILEPSY

Contribution of the first author in preparation and writing this paper is evaluated as 90%. This article has been submitted to the journal of Epilepsy Research on October 2016.

Remarks : This paper contains a study on children with benign epilepsy with centrotemporal spikes (BECTS). In this paper the morphological alterations in sub-cortical structures are investigated with respect to the side of the epilepsy focus. In addition, the association between sub-cortical morphometry and cognitive performances are evaluated. The results confirm the existence of structural changes in children with BECTS, as well as the correlation between morphological alterations and cognition.

Sub-cortical brain morphometry and its relationship with cognition in rolandic epilepsy

Mahsa Shakeri[a,b], Alexandre N. Datta[c], Domitille Malfait[b,d], Nadine Oser[c], Laurent Létourneau-Guillon[e], Philippe Major[b,f], Myriam Srour[g], Alan Tucholka[b,h], Samuel Kadoury[a,b], Sarah Lippé[b,d]

[a]Polytechnique Montréal, Department of Computer and Software Engineering, Montreal, Quebec, Canada

[b]CHU Sainte-Justine, Montreal, Quebec, Canada

[c]University of Basel Children's Hospital, Basel, Switzerland

[d] University of Montreal, Department of Psychology, Montreal, Quebec, Canada

[e] Notre-Dame Hospital, Department of Radiology, Montreal, Quebec, Canada

[f] University of Montreal, Department of Neuroscience, Montreal, Quebec, Canada

[g]McGill University, Division of Paediatric Neurology, Montreal, QC, Canada

[h] Barcelona Beta Brain Research Center, Pasqual Maragall Foundation, Barcelona, Spain

7.1 Abstract

Purpose : Rolandic epilepsy (RE), also called benign epilepsy with centrotemporal spikes (BECTS) is the most common childhood epilepsy syndrome. RE is associated with cognitive difficulties, which can affect children's quality of life. The underlying causes of these cognitive impairments are unclear. The objective of this prospective study is to investigate sub-cortical morphological alterations in RE children with left, right, or bilateral hemispheric focus and its association with cognition.

Methods : Participants include 41 children with rolandic epilepsy and 38 healthy controls (age 8–14 years), recruited from CHU Sainte-Justine Montreal Children Hospital ($N = 40$) and Basel's Children Hospital ($N = 39$). Quantitative volumetric assessment of putamen and caudate structures was performed on T1-weighted MR scans along with the morphological analysis to test for differences between patients and controls. These analysis were performed considering the side of epilepsy focus in all participants. Correlations were investigated between the sub-cortical morphometry and cognitive indices such as intelligence quotient (IQ), verbal comprehension index (VCI), perceptual reasoning index (PRI), working memory index (WMI), and processing speed index (PSI).

Results : Children with bilateral BECTS showed statistically significant volume reduction in right caudate ($p < .05$), while no statistically significant putamen volumetric changes were detected in BECTS participants compared to normal controls. According to a spectral-based groupwise shape analysis, regional alterations were found in both putamen and caudate structures of children with BECTS. In particular, children with left BECTS showed significant outward local deformity in left putamen and individuals with bilateral BECTS showed inward local group differences in both right putamen and right caudate. The correlation assessment showed positive association between the volume of the left caudate and cognitive indices in the group containing all BECTS participants. Negative correlation was found between putamen sub-regional shape alterations and cognition in individuals with right BECTS and in all BECTS participants. Negative associations between caudate sub-regional morphologies and cognitive indices were detected in both left and bilateral cohorts.

Significance : We have confirmed putamen and caudate shape alterations in children with BECTS. However, our results further suggest that variations in sub-cortical shape affect cognitive functions. Importantly, we have demonstrated that shape alterations and their relation with cognition depend on the side of epilepsy focus. Our results point to different syndromic entities in the BECTS population.

Keywords Benign epilepsy with centrotemporal spikes (BECTS), Rolandic Epilepsy (RE),

Brain morphometry, Neuropsychological assessment.

7.2 Introduction

Rolandic epilepsy (RE), also called benign epilepsy with centro-temporal spikes (BECTS), is the most common benign childhood focal epileptic syndrome (Kramer et al., 1998; Wirrell and Hamiwka, 2006), which occurs in children aged from three to 13 years old (Panayiotopoulos et al., 2008).

BECTS typically show cognitive deficits in language, verbal learning, attention, and executive function (Metz-Lutz and Filippini, 2006; Weglage et al., 1997), which affect children's quality of life (Malfait, 2011). Some studies on sub-cortical structures have shown atypical functional networks for language processes in BECTS (Datta et al., 2013; Malfait et al., 2015). Of special interest, the putamen and caudate have been shown to particularly engage in language cognitive tasks in BECTS, possibly reflecting a compensatory network (Malfait et al., 2015).

Recent studies on sub-cortical structures in BECTS have shown putamen volume enlargement (Garcia-Ramos et al., 2015a; Lin et al., 2012). Furthermore, Lin et al. (Lin et al., 2012) found shape changes in both putamen and caudate. They also reported a connection between putamen volume and cognitive performances on a complementary executive function test. Neither Garcia et al. (Garcia-Ramos et al., 2015a) nor Lin et al. (Lin et al., 2012) considered the side of epilepsy focus of the participants in their analysis, which could affect their findings. Among other available studies, few have considered the side of epileptic focus in detecting brain developmental impairment and finding the association between these morphological differences and cognition (Boxerman et al., 2007; Gelisse et al., 2003; Lundberg et al., 1999). These studies lacked a sufficient control group, due to including control participants with other pathologies, e.g., migraines (Boxerman et al., 2007) or not using any control cohort (Gelisse et al., 2003; Lundberg et al., 1999).

Given neurocognitive differences among children with BECTS and normal controls and the involvement of striatum in low and high order cognitive functions (MacDonald et al., 2014), the question is whether sub-cortical morphometric alterations explain variations in cognition. In fact, despite the various studies on neurodevelopmental etiology in BECTS, no research study has assessed the underlying structural shape alterations and its relation with cognition. Recent advancements in neuroimaging field have enabled subtle analysis of morphological differences between children with left, right, or bilateral BECTS and healthy controls. In this study, we use MR imaging and statistical morphological analysis to detect putamen and caudate changes in children with left, right, or bilateral BECTS compared to age and

gender matched healthy individuals. In addition, we investigate the association of sub-cortical volumetric and shape differences with cognitive indices.

7.3 Methods

7.3.1 Participants

Demographic characteristics of participants are shown in Table 7.1. Forty-one patients with BECTS (mean age 10.34 ± 1.73 years ; range 7.4 years–14 years ; 13 girls) were recruited from CHU Sainte-Justine Montreal Children Hospital ($N = 20$) and Basel's Children Hospital ($N = 21$). For all epileptic participants the EEG analysis was performed to locate the seizure focus. EEG characteristics of patients were according to the latest abnormal EEG. The epileptic focus was located in the left hemisphere for 13 patients and in the right centro-temporal areas for 18 patients. Nine children showed bilateral activation in both hemispheres. For one subject the information about the side of epilepsy focus was not available.

Thirty-eight healthy children (mean age 11.18 ± 1.72 years ; range 8.1 year–14.8 years ; 13 girls) were included as healthy controls ($N = 20$ from CHU Sainte-Justine Montreal Children Hospital and $N = 18$ from Basel's Children Hospital). Exclusion criteria were any epileptiform discharges on EEG or any personal or family history of epilepsy or developmental delay. All participants and their parents gave written informed consent prior to study participation. The ethics, scientific, and administrative committee of CHU Sainte-Justine Montreal Children Hospital and Basel's Children Hospital approved this study.

We created an age, gender, and IQ matched control cohort corresponding to each epileptic group (i.e.,13 L-BECTS, 18 R-BECTS, 9 B-BECTS, 41 BECTS) and used these matched control groups in all analysis.

Table 7.1 Demographic characteristics of participants.

	NC	**BECTS**
N	38	41
Age (years)	11.18±1.72	10.34±1.73
Gender (F/M)	13/25	13/28
Age at onset	–	7.59±1.77
AED (yes/no) [a]	–	26/15

[a] AED, antiepileptic drug(s).

7.3.2 Neuropsychological tests

To test cognitive performance, all participants underwent a comprehensive neuropsychological examination. Intelligence was assessed with the Wechsler Intelligence Scale (WISC IV (Wechsler, 2005)), which includes four scales : verbal comprehension index (VCI), perceptual reasoning index (PRI), working memory index (WMI), and processing speed index (PSI).

7.3.3 MRI acquisition

MR data from CHU Sainte-Justine Montreal Children Hospital were obtained on a 3.0-T Philips Achieva (Philips Healthcare, Best, The Netherlands). The participants ($N = 40$) underwent a T1-weighted structural scan (voxels = 1 mm isotropic, TR = 8.1 ms, TE = 3.7 ms, flip angle = 8°, FOV = 248 mm, slice thickness = 1 mm, slices = 160, direction = sagittal, in-plane resolution = 256×256). Data from Basel's Children Hospital were acquired using a 3.0-T Siemens MagnetomVERIO (Siemens Healthcare, Erlangen, Germany) MRI system. The imaging protocol of the participants ($N = 39$) included T1-weighted MRI scan (voxels = 1 mm isotropic, TR = 2000 ms, TE = 3.37 ms, flip angle = 8°, FOV = 256 mm, slice thickness = 1 mm, slices = 176, direction = sagittal, in-plane resolution = 256×256).

7.3.4 MRI Processing

Brain Extraction Tool (BET) (Smith et al., 2004) is used for skull stripping. We performed the standard preprocessing of intensity normalization, and histogram matching using Medical Image Processing, Analysis, and Visualization tool (MIPAV version 1.0) [1]. For histogram adaptation, we performed matching to the histogram of the first image in the dataset as reference. Putamen and caudate sub-cortical structures are automatically extracted using FSL-FIRST segmentation tool from FMRI Software Library (FSL) (Patenaude et al., 2011a). FIRST is a model-based tool, which uses a template created from manually segmented images, with sub-cortical labels parameterized as surface meshes. A Bayesian Active Appearance Model (AAM) is also utilized to define the boundary of each sub-cortical mesh precisely (Patenaude et al., 2011a). Recent studies have shown that the accuracy of the FIRST segmentation tool can reach up to 88% (Nugent et al., 2013). The output of the FIRST segmentation framework is a $3D$ binary mask, that will later be converted to $3D$ triangulated mesh model for volumetric and morphometry analysis.

1. http ://mipav.cit.nih.gov/

7.3.5 Morphological analysis

Volumetric analysis For volumetric analysis, the sub-cortical structure's volume in each subject is computed by counting the number of voxels within the region of segmentation. The volumetric differences between patients with BECTS and healthy controls are assessed using a student t-test. Differences are considered statistically significant at $p < 0.05$.

Groupwise shape analysis Sub-cortical shape analysis is performed using a recently proposed spectral-based statistical shape analysis framework for sub-cortical structures (Shakeri et al., 2016c). The spectral-based method extracts smoothed $3D$ triangulated surface meshes from segmented images, and establishes surface correspondences among the population of surfaces. Mean curvature features are incorporated in the matching process, to improve the accuracy of the resulting surface matching. Then, the group-wise shape analysis between two study groups (i.e., epileptic and healthy controls) is performed by creating two mean shapes as the geometric mean of all matched surfaces in each group, followed by a distance map computation between these mean surfaces. The sub-cortical surface shape analysis between children with BECTS and healthy controls are assessed using total intracranial volume as covariate to compensate for head size differences across participants, as suggested by Styner et al. (Styner et al., 2006a). Total intracranial volume is calculated using Freesurfer's software package (Fischl et al., 2002) by summing the volumes of gray matter, white matter, and CSF. To verify for statistically significant shape differences, a non-parametric permutation testing scheme is applied, followed by an FDR correction for multiple comparisons.

Sub-regional shape morphometry In addition to group-wise analysis of the entire structure, we propose to compute the subregional shape differences to a common template for each participant. This will produce a representation of the local morphological information for each individual, which could be used for further analysis, e.g. a study on correlation between structural morphology and cognition. Computing regional subdivisions are common in local shape analysis studies (Styner et al., 2007). Most of the time these subdivisions are done manually and based on landmarks, which is time consuming and not reproducible. Here, we first create an average template mesh out of a separate group of 10 healthy individuals using the spectral reference surface creation method suggested by Shakeri et al. (Shakeri et al., 2016c). Since we are studying putamen and caudate structures (both left and right), we would need to create four separate templates. Then, we compute three regional subdivisions on each template surface and propagate the sub-regions to the structures of all the individuals in our dataset. The three sub-regions are defined with equal size by drawing the planes orthogonal to the medial

axis of the template. The sub-regions include the rostral (1st sub-region), medial dorsal (2nd sub-region), and caudal (3rd sub-region) part of each structure. The motivation behind this subdivision was that when we checked the sub-cortical local changes in the dataset, these sub-regions typically showed distinct alterations across population. Once the regional subdivisions are defined on each surface, the mean distance from each mesh to the template is computed per sub-region. The significant mean differences are used as a representation of local shape deformation of structures in each sub-region.

7.3.6 Cognitive correlations

Structural volume and sub-regional shape differences were correlated with cognitive indices : intelligence quotient (IQ), verbal comprehension index (VCI), perceptual reasoning index (PRI), working memory index (WMI), and processing speed index (PSI). Pearson correlation analysis was performed using standard statistical software (SPSS version 22, IBM, New York, NY, U.S.A.), with significance threshold set to $p < 0.05$.

7.4 Results

7.4.1 Subject characteristics

The mean age at seizure onset in children with BECTS was 7.59 ± 1.77 years (range, 2.67–11.40 years). No group differences in age, sex, or total brain volume were detected among the L-BECTS, R-BECTS, B-BECTS, BECTS, and normal control (NC) groups. With regards to combining participants from two sites (CHU Sainte-Justine Montreal Children Hospital and Basel's Children Hospital), we did not find any statistically significant differences between two datasets by comparing the shape and volume of sub-cortical structures in healthy individuals. In addition, we included a balanced number of individuals from each site in each cohort (L-BECTS, R-BECTS, B-BECTS, BECTS, and NC) to eliminate the effect of using separate scanners on our analysis, as previously suggested (Takao et al., 2014).

The neuropsychological results are shown in Table 7.2 with mean and standard deviation of patients and healthy controls. The cognitive performances of epileptic patients and controls were compared using an un-paired t-test with a significant threshold of $p = 0.05$. No significant group differences were found between patients with BECTS and healthy subjects, with the exception of working memory score (WMI) in children with right BECTS.

Table 7.2 Neuropsychological results in epileptic patients and healthy controls. The values are reported as $Mean(std)$.

Group	IQ	VCI	PRI	WMI	PSI
L-BECTS	105.1(18.9)	103.6(16.5)	111.8(16.2)	102.8(16.5)	101.1(16.8)
R-BECTS	99.8(12.5)	100.3(11.7)	102.1(14.7)	95.6(10.3) [a]	96.0(13.4)
B-BECTS	96.5(13.9)	94.0(9.7)	99.7(19.3)	100.4(11.1)	94.1(10.9)
BECTS	100.8(15.1)	99.9(13.3)	104.7(16.7)	99.1(12.9)	97.2(14.1)
NC	106.2(7.6)	104.3(10.3)	108.7(10.9)	103.8(8.8)	100.8(11.1)

[a] Significant difference (p=0.03) to normal controls.

7.4.2 Sub-cortical volumetric and shape analysis

Children with bilateral BECTS showed statistically significant volume reduction in right caudate compared to matched healthy controls (B-BECTS $= 3556 \pm 534mm$, controls $= 4069 \pm 479mm$, $p = .048$). No significant caudate volumetric changes were detected in other BECTS group (See Table 1 in Appendix F). In addition, putamen volumetric analysis did not find any significant differences between children with BECTS and matched healthy individuals (See Table 2 in Appendix F). However, children with bilateral BECTS showed near significant putaminal volumetric alterations (p = .07 in left putamen and p = .06 in right putamen).

Figures 7.1 and 7.2 show shape variations between children with BECTS and matched normal controls for the putamen and caudate structures using spectral group-wise shape analysis. Individuals with left BECTS (L-BECTS) showed a large area of significant outward local deformity in left putamen, and small area of hypertrophy in the right caudate. Children with bilateral BECTS (B-BECTS) showed inward local group differences in both left and right putamen, as well as atrophy in the right caudate. The combined BECTS participant group showed outward deformity in both left and right caudate. In order to further analyze the significant local shape changes, new p-value maps were computed after FDR correction for multiple comparisons. Results showed that the rostral part of the left putamen in L-BECTS and the lateral caudal area of the right putamen in B-BECTS remained significant, as well as the dorsal and caudal part of the right caudate for B-BECTS.

7.4.3 Relationship with cognitive outcomes

Association between sub-cortical volume and cognitive indices was investigated for each group. The left caudate in the cohort containing all BECTS participants showed positive correlation with both IQ ($r = .35, p = .03$) and PRI ($r = .34, p = .03$). No significant correlations were found for caudate volume in the other groups. Also, investigating correlation

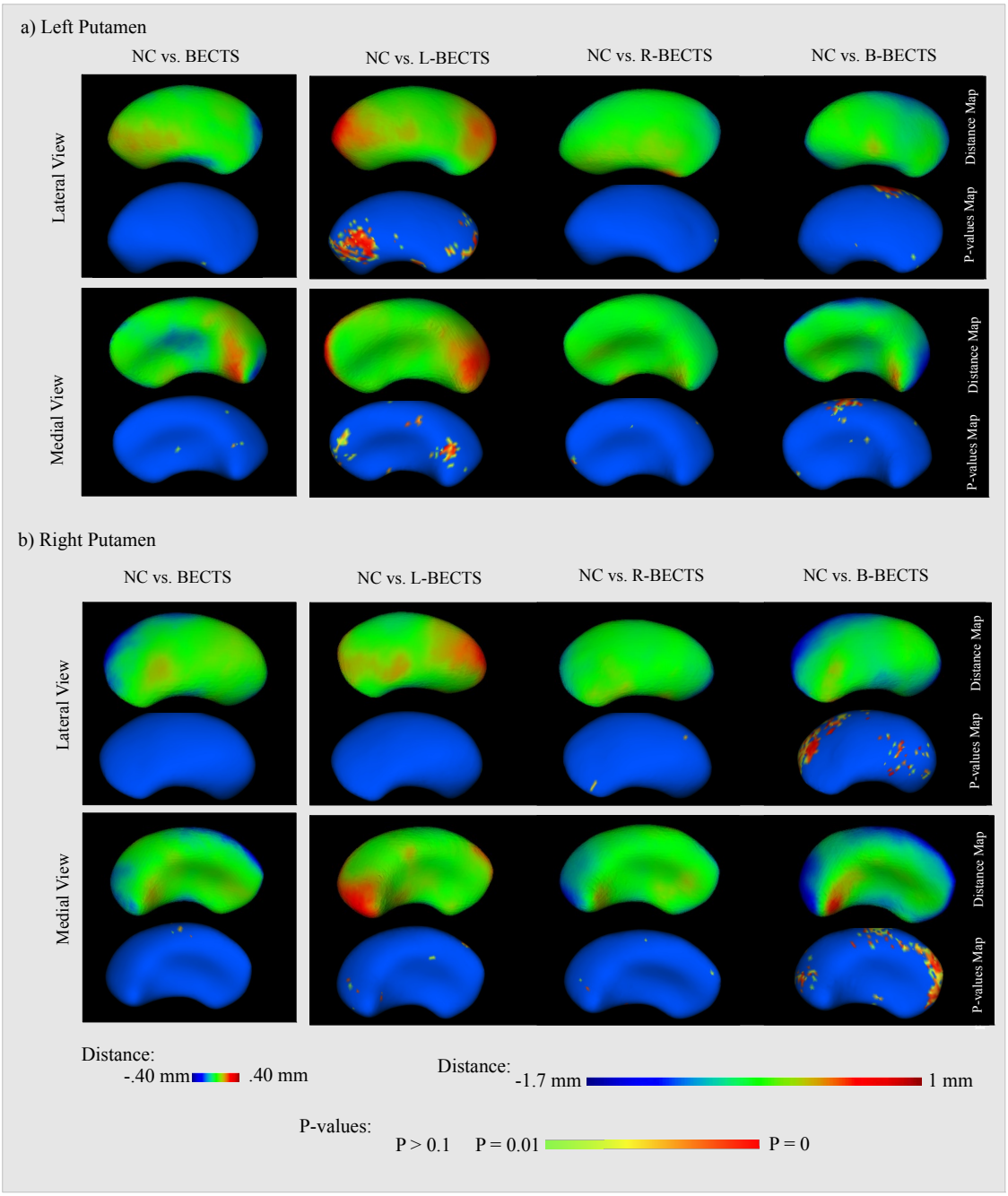

Figure 7.1 Putamen group-wise shape analysis. The resulting vertex-to-vertex distance maps are shown in lateral and medial views. The respective p-value maps are shown below distance maps (best viewed in colour).

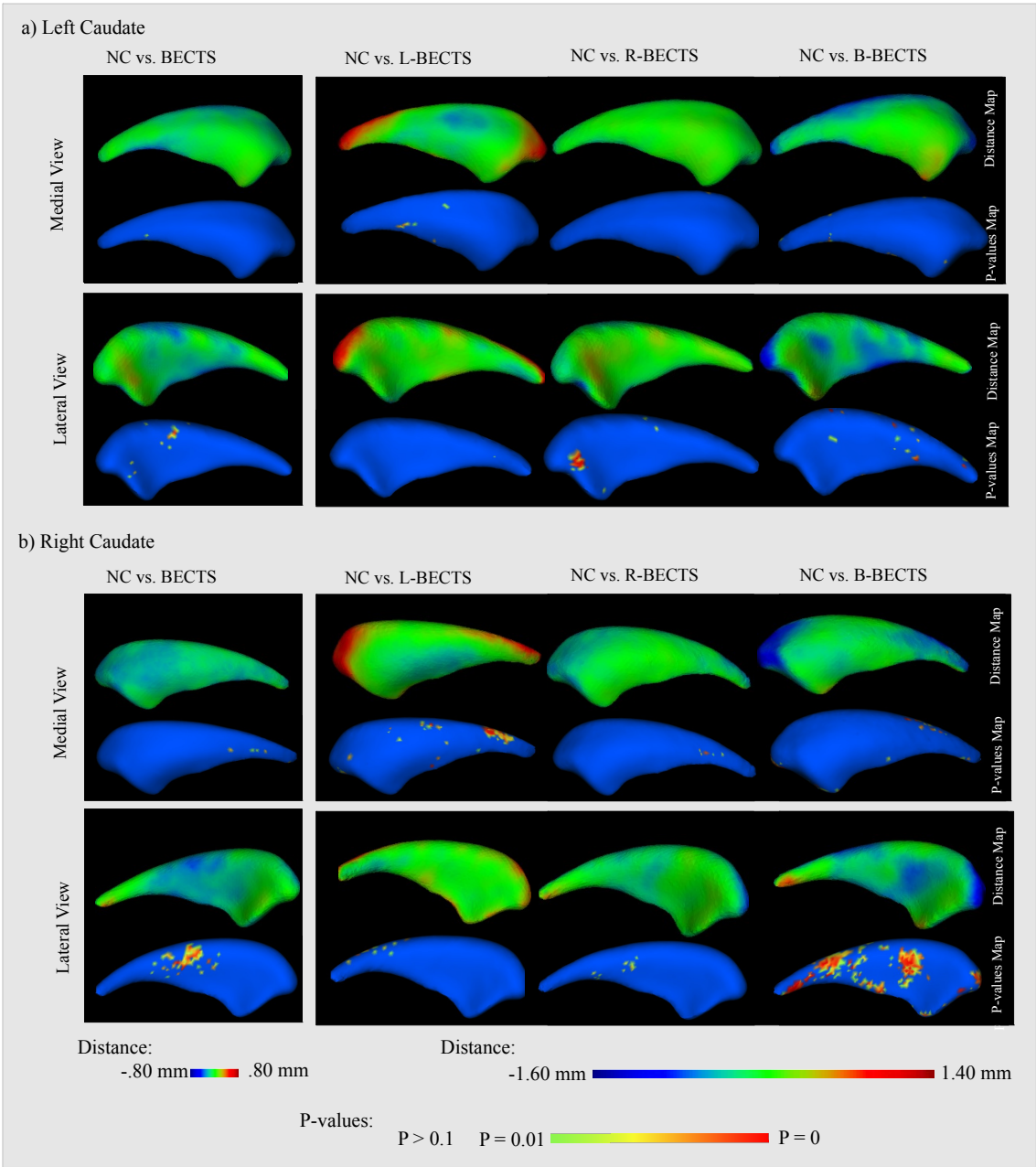

Figure 7.2 Caudate group-wise shape analysis. The resulting vertex-to-vertex distance maps are shown in lateral and medial views. The respective p-value maps are shown below distance maps (best viewed in colour).

between putamen volume and cognitive indices did not detect any significant link in either BECTS participants or healthy individuals.

In order to find the correlation between structural local shape changes and cognition, first sub-regional shape differences to a template were computed for each participant, as described in Section 7.3.5. Then, the correlation between the sub-regional shape differences and cognitive indices were computed per group as reported in Table 7.3 and Table 7.4. A strong negative correlation was found between right putamen and VCI in the medial dorsal area of R-BECTS. In addition, B-BECTS showed a strong association between caudal part of the right caudate and WMI. Some moderate links also existed between left and right putamen sub-regions and cognition in both R-BECTS and BECTS group, as well as between right caudate and cognitive indices in L-BECTS.

7.5 Discussion

In this work we investigated the morphological alterations in BECTS's sub-cortical structures and their relation to cognitive indices. This study aimed to better understand the underlying structure's morphology potentially responsible for cognitive compensatory phenomenon in BECTS, for the putamen and caudate in particular. Furthermore, we aimed at revealing the role of the side of epileptic focus on the structure to cognition link in left vs. right vs. bilateral BECTS.

In this study, children with B-BECTS showed statistically significant volume reduction in right caudate. Positive correlation between the volume of the left caudate and cognitive indices were found in the group containing all BECTS participants, which is consistent with the volume reduction reported in Table 1 of the Supplementary materials and the inward local deformity depicted in Figure 7.2. Meaning that the larger the caudate volume is in the BECTS, the higher the cognitive performance will be.

Left putamen in L-BECTS showed significant shape alterations, as well as right putamen and right caudate in B-BECTS. In children with R-BECTS and in the group including all BECTS participants, negative correlation were found between sub-regional putamen shape differences to a template and cognitive indices. Furthermore, participants with L-BECTS and B-BECTS showed negative correlation between the posterior area of the caudate and cognition. These results confirm that variations in putamen and caudate shape in BECTS are associated with reduced cognitive performance.

Table 7.3 Correlation between local putamen difference magnitude and neuropsychological results. The values are Pearson correlations reported for left (L) and right (R) putamen's sub-regions.

Putamen region	IQ		VCI		PRI		WMI		PSI	
	L	R	L	R	L	R	L	R	L	R
Region 1										
L-BECTS	.25	.02	-.18	-.20	.33	.12	.41	.29	.29	.22
R-BECTS	.06	-.12	.11	-.36	-.07	-.06	.05	-.47	.25	-.21
B-BECTS	.23	.40	.27	.35	-.44	.08	-.39	-.62	-.06	-.14
BECTS	.14	.15	-.05	-.11	-.13	.01	.09	-.05	.15	-.03
NC	.29	.01	.21	-.02	-.01	.13	.37	.16	.05	-.24
Region 2										
L-BECTS	.17	.06	-.01	-.03	.06	.22	.18	.05	.22	.19
R-BECTS	-.36	**-.56** [a]	**-.51** [a]	**-.70** [b]	**-.57** [a]	-.43	**-.54** [a]	-.3	.01	-.06
B-BECTS	-.38	.20	.18	.31	-.56	.52	-.63	.23	-.57	.41
BECTS	-.17	-.09	-.21	-.27	**-.41** [a]	-.07	-.29	-.11	-.04	.04
NC	-.27	.09	-.39	.11	.06	-16	.17	.14	-.31	.04
Region 3										
L-BECTS	.18	.25	.07	-.03	-.07	.15	.52	.57	.26	.40
R-BECTS	-.35	-.04	**-.57** [a]	-.14	-.46	-.02	-.09	-.33	-.21	-.15
B-BECTS	-.15	.15	.20	.49	-.08	.51	-.37	-.31	-.25	.02
BECTS	-.01	.13	-.09	-.11	-.17	.02	-.14	.05	-.01	.03
NC	-.05	-.06	.12	.06	-.21	-.20	.26	-.08	-.26	.03

[a] $P - values < 0.05$.
[b] $P - values < 0.005$.

Table 7.4 Correlation between local caudate difference magnitude and neuropsychological results. The values are pearson correlations reported for left (L) and right (R) caudate's sub-regions.

Caudate region	IQ		VCI		PRI		WMI		PSI	
	L	R	L	R	L	R	L	R	L	R
Region 1										
L-BECTS	-.12	.02	-.60	-.20	-.36	-.18	.05	.14	.10	.18
R-BECTS	.25	.19	.06	.19	.09	.1	.13	.04	-.08	-.33
B-BECTS	-.15	.07	-.01	-.08	.35	.01	-.29	.13	-.12	.24
BECTS	.09	.14	-.04	.08	.09	.17	.14	.25	.01	-.01
NC	.05	-.09	-.02	-.08	-.04	-.11	.32	.16	.02	-.09
Region 2										
L-BECTS	.10	-.20	.18	-.39	.14	.08	.02	-.08	-.21	-.18
R-BECTS	.33	-.06	.31	.05	.19	-.14	.23	-.12	.03	-.11
B-BECTS	.51	.10	.47	-.23	.19	.22	-.21	-.12	.31	.09
BECTS	.23	.03	.14	-.07	.21	.16	.24	.18	.07	.01
NC	-.12	-.12	-.04	-.08	-.07	-.20	.05	.20	-.13	-.10
Region 3										
L-BECTS	.03	-.35	.05	**-.57** [a]	-.20	-.05	.08	-.24	.10	-.35
R-BECTS	.25	.10	.09	.07	.18	.06	.06	-.07	.24	-.18
B-BECTS	.25	-.35	.23	.12	.07	-.44	-.01	**-.66** [a]	.26	-.58
BECTS	.18	-.01	.09	.06	.05	.06	.10	.04	.17	-.14
NC	-.06	-.14	.22	-.27	-.27	-.01	-.08	.02	-.13	.08

[a] $P - values < 0.05$.

7.5.1 Morphology analysis

Sub-cortical alterations have been reported in previous studies. Lin et al. (Lin et al., 2012) found putamen volume and shape hypertrophy, as well as caudate shape enlargement in BECTS. They reported that the putamen volume enlargement was associated with better cognitive performance compared to controls. In a recent longitudinal study on putamen structure, Garcia-Ramos et al. (Garcia-Ramos et al., 2015a) reported that children with BECTS demonstrated atypical volumetric changes in the putamen. In another study on sub-cortical structures, Kim et al. (Kim et al., 2015) found hypertrophy in putamen volume in BECTS participants. All these studies used patients with newly diagnosed BECTS and combined participants with different side of the epileptic focus, while the current study used participants with longer epilepsy duration (7 years) and aimed at revealing the role of epileptic focus in structural volume and shape alterations. Our experimental analysis found caudate volume reduction in B-BECTS, while no significant putamen volumetric differences were detected between left, right, bilateral-BECTS and controls. On the other hand, group-wise spectral-based shape analysis found subtle local shape differences, specially in left putamen of L-BECTS and right putamen and right caudate of B-BECTS. This meant that the differences in sub-cortical structure across subjects were focal and not distributed throughout the whole volume, thus the global volume measure was not able to detect those differences. These results showed the importance of local shape analysis based methods compared to the global volumetric tests for revealing subtle group differences in BECTS.

7.5.2 Correlation analysis

Volumetric analyses of the left caudate nucleus in all BECTS was positively associated with total IQ. This result is similar to MacDonald et al.'s study (MacDonald et al., 2014) of a large sample of neurotypical children, confirming the general role of striatum in global cognition. In a further analysis, the distance of each subject to a template was calculated and the correlations between local shape variations of three sub-regions and cognitive indices were computed. Negative correlations were found in putamen for the R-BECTS and the combined BECTS group, as well as the negative association in caudate for L-BECTS and B-BECTS for the dorsal region of the right caudate, supporting existing studies on caudate cognitive specific involvement (Robinson et al., 2012). As expected, the negative association showed that the more distinct the subjects were from the template, the lower the cognitive skills were, pointing to the fact that both reduction and enlargement in local volumes may interfere with cognitive performance. We found specific results according to the side of epileptic focus. This reveals the importance of performing separate analyses for each epilepsy focus in BECTS.

Nevertheless, the cognitive performance alterations associated with shape variations in the BECTS population did not respect the right/left hemispheric cognition specialization typically found in neurotypical individuals. This may further support studies revealing abnormal lateralization of cognitive functions in this population (Datta et al., 2013).

7.5.3 Limitations of the study

This study was a cross-sectional study with a number of limitations. The number of participants of the B-BECTS (nine cases) was limited. This might lead to not being able to handle inter-subject variability in this group. However, the total amount of participants (41 BECTS and 38 NC) is enviable in this study.

7.6 Conclusions

In this study, we assessed the underlying structural morphology potentially involved in the cognitive compensatory mechanisms in BECTS. In addition, we investigated the role of the localization of the epilepsy foci in correlation between structural morphology and cognitive indices in left vs. right vs. bilateral BECTS. Experiments revealed that shape alterations exist in left putamen of left BECTS and right putamen and caudate of bilateral BECTS. Correlation study showed negative correlation between cognition and sub-regional shape changes. Our results suggest possible altered brain maturation in this population and confirm that subtle brain morphological differences in BECTS are involved in their cognitive functioning. One important future direction is to perform a longitudinal follow-up on these children to investigate if the neurodevelopmental alterations related to lateralization persist over years and how these neurodevelopmental changes affect cognitive impairments in BECTS.

Acknowledgements

Funding was provided by the Canada Research Chairs, the CHU Sainte-Justine Research Center, Savoy Foundation, CIHR Catalyst Grant (#133354), and the Basel's Children Hospital. We thank all the children and families, who participated in this study.

CHAPTER 8 GENERAL DISCUSSION

The general methodology in this thesis established three research objectives that led to several original tools and frameworks for sub-cortical brain morphology analysis in benign epilepsy with centrotemporal spikes (BECTS). Firstly, an automated framework was developed in order to segment sub-cortical structures on a group of MR images, secondly, a new approach for investigating statistical groupwise shape analysis on sub-cortical structures was designed, and thirdly, a clinical study on BECTS revealed morphological alterations in epileptic children with left, right, or bilateral hemispheric focus and its association with cognition. The development of these new tools will be discussed in this chapter.

Our proposed coregistration-cosegmentation method can benefit from segmentation priors (probability maps) and produce results which are close to those generated using ground truth. In our method, the segmentation results are a by-product of the co-registration, where context labels are used to improve registration performance. We have shown that, by using accurate segmentation priors (e.g., CNN based segmentation maps) we can obtain such results close to the ground truth. More importantly, we also showed that by using less accurate priors (e.g., those learned using RF), we also obtain good results after coregistration-cosegmentation, especially in terms of Hausdorff and contour mean distances. This is due to our formulation, which includes a novel energy term that enables any prior to help during registration. Our proposed method may be used in combination with weak priors learned from weak annotations from non-radiologists, requiring less time to produce sub-optimal segmentation masks, yet delivering good results. Our further experiments have demonstrated that the proposed CNN-based coregistration-cosegmentation method produces better results compared to the state-of-the-art i.e., Freesurfer (Fischl et al., 2002) and FSL-FIRST (Patenaude et al., 2011a), for three sub-cortical structures. Freesurfer has shown higher segmentation accuracy on caudate structure, which might be due to the limitation of the designed 2D CNN in detecting the fine tail of the caudate structure.

In the developed segmentation method in Chapter 5, we apply two supervised classifiers (CNN and RF) to obtain prior semantic segmentations. Both of these approaches require manual annotations on a sub-set of a dataset to compute segmentation priors on the remaining volumes in the set. An extension to the current method would be to employ an unsupervised clustering method to extract segmentation priors. An approach starting with a bounding box around a structure, and maybe a user input drawing a line inside the structure would guide the unsupervised clustering approach toward the more accurate segmentation priors.

The proposed coregistration-cosegmentation method has considerable advantages over standard multi-atlas segmentation methods. Given a set of images, we compute the semantic segmentation probability maps once, and then segment all the volumes simultaneously. Therefore, if numerous ground-truth masks were to be used for the registration step, our method benefits from substantial computational gains, as complexity depends only on the number of input volumes we want to segment. Another difference is that, in classical multi-atlas segmentation approaches only appearance features are used to compute the deformation fields during the registration process, while no prior on the target image is available. We exploit more sophisticated features on all volumes to drive the co-registration process. These show that our novel method would be an important improvement to the current available automatic multi-atlas brain segmentation tools for MR images.

The developed coregistration-cosegmentation method applies the majority voting strategy to combine the semantic priors and compute the final segmentation on each MR volume. The accuracy of the proposed method could be further improved by exploiting a more sophisticated and intelligent label fusion approach. For instance, a strategy similar to the joint label fusion technique (Wang et al., 2013) that explicitly considers correlations among atlases would be effective.

Another possible improvement on the current segmentation method would be to repeat the whole coregistration-cosegmentation process multiple times. At each iteration, the initial semantic priors are replaced by the final segmentation of all images that have been created in the previous run. This way, every coregistration-cosegmentation run employs more accurate prior information that could lead to segmentations of higher quality.

The segmented sub-cortical structures on MR images are extracted as 3D surface meshes in our shape analysis framework. Then, the smoothed surfaces are matched using a spectral-based algorithm across a population of healthy and pathological meshes. The significant local group differences is finally produced as the output of the groupwise shape analysis framework. Our method incorporates mean curvature features in the spectral matching graph, since it intrinsically describes the local shape information of a 3D surface. Experimental analysis revealed that embedding this additional feature significantly improves the spectral surface matching accuracy. However, incorporating curvature features had more relevance to evaluate complex structures, such as hippocampus shapes rather than simple ones, like putamen. As an application, the features extracted from hippocampus surfaces matched by spectral method used in classification of Alzheimer's disease, which led to promising results.

A comparison of the proposed spectral-based shape analysis method with available groupwise shape analysis approaches (e.g., SPHARM-PDM (Styner et al., 2006a)) showed that

the proposed framework has considerable agreement with state-of-the-art methods, while being faster. This speed advantage becomes more noticeable for more complex structures, such as hippocampus shapes, with a fourfold decrease in computation time compared to SPHARM-PDM. These results suggest that the developed spectral-based shape analysis framework could allow for quantitative assessment of sub-cortical variations, associated with a neurological disorder, which leads to the better understanding of a pathology.

One limitation of the proposed shape analysis framework is that the accuracy of the segmentation process and the quality of the extracted 3D surface meshes could directly impact the final shape analysis results. Therefore, one possible future extension of the proposed methodology would be to combine the proposed segmentation and shape analysis framework, where 3D surface meshes are created during the segmentation process. This can be done by modelling the anatomical boundaries of structures using statistical shape models, and incorporating the anatomical shape consistency component as an additional term in the registration cost function. Therefore, both the surface extraction and refinement are performed during the segmentation process, with respect to the surface meshes of all other images in the set.

The morphological alterations in BECTS's brain have been investigated using the proposed groupwise sub-cortical shape analysis framework. Also, the association between the detected alterations and neuropsychological tests have been studied in depth. Previous studies have reported sub-cortical volumetric (Lin et al., 2012; Garcia-Ramos et al., 2015a; Kim et al., 2015) and shape alterations (Lin et al., 2012) in BECTS compared to controls. However, all these available studies used newly onset BECTS and combined participants with different sides of the epileptic focus, whereas our study used participants with longer epilepsy duration and aimed at revealing the role of epileptic focus in sub-cortical volume and shape alterations.

According to our experiments, significant volume reduction was detected in the right caudate of children with bilateral BECTS. However, no significant caudate volumetric changes were detected in other groups. Putamen volumetric analysis did not find any statistically significant differences between left, right, bilateral-BECTS and controls. On the other hand, spectral-based shape analysis showed significant shape alterations of left putamen in left BECTS, as well as significant local deformity of both right putamen and right caudate in bilateral BECTS. These analysis showed that the structural alterations in BECTS were spread throughout the surface, such that they were not detectable by global volumetric measures. This reveals the importance of local shape analysis methods compared to global volumetric tests in capturing slight morphological alterations in sub-cortical structures.

In another analysis, the distance of each subject to a surface template was calculated and

correlations between sub-regional shape variations and cognition ware computed. Negative correlations were detected for the right BECTS and the combined BECTS group in putamen structure. In addition, the caudate of children with bilateral and left BECTS showed negative association with cognitive indices. These results were expected, showing the fact that the further away the participants' sub-cortical structures were from the template, the lower the cognitive skills were.

Here, we divided each structure into three sub-regions and computed the mean shape distances to a template. This approach provides the three mean distance value for each subregion that were used in a correlation analysis. A more precise approach would be to compute distances to the template on all vertices of all structures, and then compute the correlation with cognition in a vertexwise manner. In this way, we could visualize the correlation between local shape alterations and cognitive indices in $3D$ sub-cortical structures.

In the current clinical cross-sectional study, we used a limited number of participants per group with epilepsy spanning of seven years. It would be interesting to increase patients recruitment in order to create separate groups for each age range. This would provide a better understanding of the neurodevelopmental alterations in children with BECTS with respect to normal aging in controls. The present study can be further extended by performing a longitudinal follow-up on the available cohort to verify if the neuroanatomical alterations and their correlation with cognition will remain over the years.

Although it is preferred to recruit all MRI scans from one site, in our clinical study we combined the MR scans from two separate sites (CHU Sainte-Justine Montreal Children Hospital and Basel's Children Hospital) to increase the statistical power on conducting evaluations of neuroanatomical alterations. Multi-center studies could introduce a between-center variance component, which might complicates the interpretation of the results. To eliminate the multi-scanner effect, we balanced the ratio of the cases to controls across the two scanners. In addition, we verified the existence of any sub-cortical shape or volume differences between normal subjects scanned by the two scanners, where no significant differences were detected.

From a global perspective, the new methods proposed in this thesis actually close a loop between a) the automatic segmentation tool developed in Chapter 5, which defines the boundary of sub-cortical structures in a prior-based coregistration and cosegmentation process, b) the statistical groupwise shape analysis tool, developed in Chapter 6, that extracts 3D surface meshes from binary segmentation maps and captures local shape alterations in sub-cortical regions, and c) the clinical study, presented in Chapter 7, that revealed the association between BECTS's brain morphological alterations and cognitive tests with respect to the side

of seizure focus.

CHAPTER 9 CONCLUSION AND RECOMMENDATIONS

This thesis addresses the general problem of sub-cortical morphological analysis in children with benign epilepsy with centrotemporal spikes (BECTS). The literature review presented in Chapter 3 highlighted the challenges of automatic segmentation and morphological analysis techniques, and also revealed the current limitations of the state-of-the-art. During this thesis, a set of tools were developed in order to analyze the sub-cortical brain morphometry in BECTS participants. More precisely, the methodology in Chapter 5 proposed a new automated framework for segmenting sub-cortical structures in a coregistration and cosegmentation process based on learned priors. In a second step presented in Chapter 6, a new spectral-based statistical groupwise morphological analysis approach was developed, that enabled capturing subtle local shape variations across two populations of surface meshes. In a third step in Chapter 7, a clinical study assessed the association between sub-cortical morphological alterations in BECTS and cognitive functions with respect to the side of seizure focus. The main findings and contributions from these research objectives were discussed in Chapter 8.

The next sections mention the contributions of the thesis, current limitations, and main recommendations for future work.

9.1 Advancement of knowledge

In this thesis we propose several contributions for the purpose of brain morphological analysis in BECTS. The first one (presented in Chapter 5) incorporates prior information to the standard graph based registration process. This approach demonstrates that semantic and context specific information can boost the registration algorithms by further improving the accuracy of the results. Our proposed approach shows how prior information about the anatomical structures of a given set of images, can be integrated within the energy function of a discrete population registration algorithm. We seek at performing joint registration-segmentation of the input images, while exploiting context information provided by pre-trained classifiers. We performed our experiments using both reliable (learned by Convolutional Neural Networks) and weak (learned by random forests) priors. Our analysis showed that accurate segmentation priors can produce close results to the ground truth. More importantly, we showed that less accurate priors would also lead to acceptable results after performing coregistration-cosegmentation process. The second contribution (presented in Chapter 6), proposed a novel groupwise morphological framework with its specific way of surface extraction, smoothing,

matching, and statistical analysis, and produced comparable results to state-of-the-art algorithms, while being faster. This work was the first one that integrated curvature-based spectral matching in to a groupwise subcortical shape analysis pipeline. Experimental analysis on real clinical datasets showed that the extracted group differences were concordant with the findings in other studies. The third contribution (discussed in Chapter 7) presents a clinical study on investigating morphological alterations and their relation with cognitive indices in BECTS. This study aimed to better understand the structural morphology that could potentially be responsible for cognitive compensatory phenomenon in BECTS, the putamen and caudate in particular. Furthermore, the experiments revealed the role of structural epilepsy lateralization with respect to cognition in left vs. right vs. bilateral BECTS.

9.2 Limits and constraints

Notwithstanding the advantages of each individual contribution with their identified extents, there are general limitations to this work.

In our coregistration and cosegmentation framework, we approximated the high-order problem through a pairwise formulation. However, simultaneously modeling high-order interactions and recovering all deformations with one-shot optimization would be the ideal approach for this problem. In addition, our framework uses prior probability maps in the energy formulation, and according to our experiments using more accurate classifiers will improve the registration results. However, it is preferable to further boost the registration performance, in order to get similar results to the ground truth when either reliable or weak priors are utilized.

As mentioned in the thesis, our groupwise shape analysis framework is based on spectral representation of surfaces. The spectral method assumes that the meshes being matched represent complete structures, that is the topology is equivalent across surfaces. Therefore, the proposed tool is not currently adopted to handle large structural deformations caused by severe neurological disorders, which may change the topology of a surface.

The presented clinical study on BECTS was a cross-sectional study with a number of limitations. For instance, the number of participants per group was limited, specially the number of bilateral BECTS (nine individuals). This might lead to an under-representation of inter-subject variability. However, the total amount of participants (41 BECTS and 38 NC) was enviable in this work.

9.3 Recommendations

To conclude this work, we present the major recommendations, which give the main lines and main research questions for future work.

Recommendation 1 : An interesting future direction is to use high-order graphs and inference methods adapted to our segmentation problem. Although the power of expression of graphical models grows together with their complexity, different types of high-order models can be efficiently optimized (Komodakis and Paragios, 2009; Dokania and Kumar, 2015). In Section D.2 we formulate prior based coregistration and cosegmentation as a high-order problem, which is then approximated through a pairwise formulation. More accurate results could be obtained if proper high-order inference adapted to the particular type of energy would be used. Accordingly, dual decomposition methods (Komodakis and Paragios, 2009), allowing efficient one-shot optimization could be considered as an alternative solution.

Recommendation 2 : Using accurate classifiers in energy function efficiently improves the registration results. This raises a number of questions. How can prior information be used to further enhance registration accuracy ? Can we benefit from the results of the coregistration-cosegmentation process to boost the classifiers used to create the initial priors ? One possible solution might be to introduce an additional term in the energy function of the deformable registration . This term could penalize the deformations that lead to disagreement between the estimated segmentation (priors) and the warped segmentation mask (the results of the coregistration). In this way the circuit between coregistration and label fusion will be closed, since it allows segmentation to influence the registration step.

Recommendation 3 : The spectral method used in the groupwise shape analysis framework in this thesis did not address the problem of using severely deformed surfaces with significant changes of the organ topology. How can spectral matching method handle these kinds of data ? One simple solution is to take advantage of user interactions to provide additional information for matching surfaces. For instance, a user could indicate the approximate pairs of corresponding points. The computation of eigenmodes could take into consideration such user inputs.

Recommendation 4 : The detected morphological variations in subcortical structures could be used for classifying unseen MR examinations into healthy and pathological BECTS individuals. For instance, the significant vertex ratio could be computed in different regional subdivisions between each surface and a reference mesh. Then, the computed significant vertex ratios along with other global features, e.g., the total surface volume, would be used to define a feature descriptor. A classifier, such as a Support Vector Machine (SVM), could be

designed to define the decision boundaries distinguishing healthy subjects from pathological patients. However, this kind of framework requires incorporating larger datasets of BECTS participants to achieve high and stable classification accuracy.

Recommendation 5 : One important future direction is to perform a longitudinal follow-up on these BECTS participants to investigate whether the neurodevelopmental alterations related to epilepsy lateralization persist over years. In addition, a longitudinal study could reveal that how sub-cortical morphological changes affect cognitive functions in children with BECTS.

REFERENCES

S. Alchatzidis, A. Sotiras, et N. Paragios, “Discrete multi atlas segmentation using agreement constraints”, dans *BMVC*, 2014.

P. Aljabar, R. a. Heckemann, a. Hammers, J. V. Hajnal, et D. Rueckert, “Multi-atlas based segmentation of brain images : atlas selection and its effect on accuracy.” *NeuroImage*, vol. 46, no. 3, pp. 726–38, jul 2009. DOI : 10.1016/j.neuroimage.2009.02.018. En ligne : http://www.ncbi.nlm.nih.gov/pubmed/19245840

P. Aljabar, R. Wolz, L. Srinivasan, S. J. Counsell, M. A. Rutherford, A. D. Edwards, J. V. Hajnal, et D. Rueckert, “A combined manifold learning analysis of shape and appearance to characterize neonatal brain development”, *IEEE Transactions on Medical Imaging*, vol. 30, no. 12, pp. 2072–2086, 2011.

S. Allassonnière, “Toward a coherent statistical framework for dense deformable template estimation”, *Royal Statistical Society*, vol. 69, no. 1, pp. 3–29, 2007.

P. Andersen, R. Morris, D. Amaral, T. Bliss, et J. O’ Keefe, *The Hippocampus Book*. Oxford University Press, 5 2009. DOI : 10.1093/acprof:oso/9780195100273.001.0001

B. a. Ardekani, S. Guckemus, A. Bachman, M. J. Hoptman, M. Wojtaszek, et J. Nierenberg, “Quantitative comparison of algorithms for inter-subject registration of 3D volumetric brain MRI scans.” *Journal of neuroscience methods*, vol. 142, no. 1, pp. 67–76, mar 2005. DOI : 10.1016/j.jneumeth.2004.07.014. En ligne : http://www.ncbi.nlm.nih.gov/pubmed/15652618

X. Artaechevarria, A. Munoz-Barrutia, et C. Ortiz-de Solorzano, “Combination strategies in multi-atlas image segmentation : application to brain MR data.” *IEEE transactions on medical imaging*, vol. 28, no. 8, pp. 1266–77, aug 2009. DOI : 10.1109/TMI.2009.2014372. En ligne : http://www.ncbi.nlm.nih.gov/pubmed/19228554

Y. Arzhaeva, E. V. Rikxoort, et B. V. Ginneken, “Automated segmentation of caudate nucleus in MR brain images with voxel classification”, dans *3D Segmentation In The Clinic : A Grand Challenge*, 2007, pp. 65–72.

J. Ashburner et K. J. Friston, “Voxel-based morphometry–the methods.” *NeuroImage*, vol. 11, no. 6 Pt 1, pp. 805–21, jun 2000. DOI : 10.1006/nimg.2000.0582. En ligne :

http://www.ncbi.nlm.nih.gov/pubmed/10860804

A. J. Asman et B. a. Landman, "Non-local statistical label fusion for multi-atlas segmentation." *Medical image analysis*, vol. 17, no. 2, pp. 194–208, feb 2013. DOI : 10.1016/j.media.2012.10.002. En ligne : http://www.pubmedcentral.nih.gov/articlerender.fcgi?artid=3648421{&}tool=pmcentrez{&}rendertype=abstract

N. Aspert, D. Santa-Cruz, et T. Ebrahimi, "MESH : measuring errors between surfaces using the Hausdorff distance", dans *Proceedings of the IEEE International Conference on Multimedia and Expo*, 2002, pp. 705–708. DOI : 10.1109/ICME.2002.1035879. En ligne : http://ieeexplore.ieee.org/lpdocs/epic03/wrapper.htm?arnumber=1035879

B. B. Avants, C. L. Epstein, M. Grossman, et J. C. Gee, "Symmetric diffeomorphic image registration with cross-correlation : evaluating automated labeling of elderly and neurodegenerative brain." *Medical image analysis*, vol. 12, no. 1, pp. 26–41, feb 2008. DOI : 10.1016/j.media.2007.06.004. En ligne : http://www.pubmedcentral.nih.gov/articlerender.fcgi?artid=2276735{&}tool=pmcentrez{&}rendertype=abstract

B. B. Avants, P. Yushkevich, J. Pluta, D. Minkoff, M. Korczykowski, J. Detre, et J. C. Gee, "The optimal template effect in hippocampus studies of diseased populations." *NeuroImage*, vol. 49, no. 3, pp. 2457–66, feb 2010. DOI : 10.1016/j.neuroimage.2009.09.062. En ligne : http://www.pubmedcentral.nih.gov/articlerender.fcgi?artid=2818274{&}tool=pmcentrez{&}rendertype=abstract

K. Babalola et T. Cootes, "Groupwise registration of richly labelled images", *Medical Image Analysis and Understanding*, 2006.

C. Baillard, P. Hellier, et C. Barillot, "Segmentation of brain 3D MR images using level sets and dense", vol. 5, pp. 185–194, 2001.

L. Bain, K. Jedrziewski, M. Morrison-Bogorad *et al.*, "Healthy brain aging : A meeting report from the Sylvan M. Cohen Annual Retreat of the University of Pennsylvania Institute on Aging", *Alzheimers Dementia*, vol. 4, pp. 443–446, 2008.

B. Bali, L. L. Kull, L. J. Strug, T. Clarke, P. L. Murphy, C. I. Akman, D. A. Greenberg, et D. K. Pal, "Autosomal dominant inheritance of centrotemporal sharp waves in rolandic epilepsy families", *Epilepsia*, vol. 48, no. 12, pp. 2266–2272, 2007. DOI : 10.1111/j.1528-1167.2007.01221.x

M. F. Beg, M. I. Miller, A. Trouve, et L. Younes, "Computing Large Deformation Metric

Mappings via Geodesic Flows of Diffeomorphisms", *International journal of computer vision*, vol. 61, no. 2, pp. 139–157, 2005.

Y. Bengio, "Learning deep architectures for ai", *Found. Trends Mach. Learn.*, vol. 2, no. 1, pp. 1–127, Jan. 2009. DOI : 10.1561/2200000006. En ligne : http://dx.doi.org/10.1561/2200000006

J. P. Besl, "A method for registration of 3D shapes", *IEEE transactions on pattern analysis and machine intelligence*, vol. 14, no. 2, pp. 239–256, 1992.

K. K. Bhatia, J. V. Hajnal, B. K. Puri, A. D. Edwards, et D. Rueckert, "Consistent groupwise non-rigid registration for atlas construction", dans *ISBI*, 2004.

C. M. Bishop, *Neural Networks for Pattern Recognition*. New York, NY, USA : Oxford University Press, Inc., 1995.

S. Bouix, J. C. Pruessner, D. Louis Collins, et K. Siddiqi, "Hippocampal shape analysis using medial surfaces." *NeuroImage*, vol. 25, no. 4, pp. 1077–89, may 2005. DOI : 10.1016/j.neuroimage.2004.12.051. En ligne : http://www.ncbi.nlm.nih.gov/pubmed/15850726

J. L. Boxerman, K. Hawash, B. Bhavna, Clarke Tara, R. Jeffrey, et D. K. Pal, "Is Rolandic Epilepsy Associated With Abnormal Findings On Cranial MRI ?" *Epilepsy research*, vol. 75, no. 212, pp. 180–185, 2007.

Y. Boykov, O. Veksler, et R. Zabih, "Fast approximate energy minimization via graph cuts", *PAMI*, 2001.

S. M. Brambati, K. P. Rankin, J. Narvid, W. W. Seeley, D. Dean, H. J. Rosen, B. L. Miller, J. Ashburner, et M. L. Gorno-Tempini, "Atrophy progression in semantic dementia with asymmetric temporal involvement : a tensor-based morphometry study." *Neurobiology of aging*, vol. 30, no. 1, pp. 103–11, jan 2009. DOI : 10.1016/j.neurobiolaging.2007.05.014. En ligne : http://www.pubmedcentral.nih.gov/articlerender.fcgi?artid=2643844{&}tool=pmcentrez{&}rendertype=abstract

A. D. Brébisson et G. Montana, "Deep neural networks for anatomical brain segmentation", dans *CVPR Bioimage Computing Workshop*, 2015.

G. Capovilla, A. Berg, J. Cross, S. Moshe, F. Vigevano, P. Wolf, et G. Avanzini, "Conceptual dichotomies in classifying epilepsies : Partial versus generalized and idiopathic versus symptomatic", *Epilepsia*, 2009.

J. Cates, P. T. Fletcher, M. Styner, et H. C. Hazlett, “Particle-Based Shape Analysis of Multi-Object Complexes”, *Medical image computing and computer-assisted intervention*, vol. 11, no. 1, pp. 477–485, 2009.

M. M. Chakravarty, P. Steadman, M. C. van Eede, R. D. Calcott, V. Gu, P. Shaw, A. Raznahan, D. L. Collins, et J. P. Lerch, “Performing label-fusion-based segmentation using multiple automatically generated templates”, *Human Brain Mapping*, vol. 34, no. 10, pp. 2635–2654, 2013. DOI : 10.1002/hbm.22092

S.-C. Chan et W.-T. Lee, “Benign epilepsy in children.” *Journal of the Formosan Medical Association = Taiwan yi zhi*, vol. 110, no. 3, pp. 134–44, mar 2011. DOI : 10.1016/S0929-6646(11)60023-5. En ligne : http://www.ncbi.nlm.nih.gov/pubmed/21497276

L. Chen, G. Papandreou, I. Kokkinos, K. Murphy, et A. Yuille, “Semantic image segmentation with deep convolutional nets and fully connected crfs”, *arXiv preprint arXiv :1412.7062*, 2014.

X. W. Chen et X. Lin, “Big data deep learning : Challenges and perspectives”, *IEEE Access*, vol. 2, pp. 514–525, 2014. DOI : 10.1109/ACCESS.2014.2325029

Y. Cho, J. K. Seong, S. Y. Shin, Y. Jeong, J. H. Kim, A. Qiu, K. Im, J. M. Lee, et D. L. Na, “A multi-resolution scheme for distortion-minimizing mapping between human subcortical structures based on geodesic construction on Riemannian manifolds”, *NeuroImage*, vol. 57, no. 4, pp. 1376–1392, 2011. DOI : 10.1016/j.neuroimage.2011.05.066. En ligne : http://dx.doi.org/10.1016/j.neuroimage.2011.05.066

G. E. Christensen et H. J. Johnson, “Consistent image registration.” *IEEE transactions on medical imaging*, vol. 20, no. 7, pp. 568–82, jul 2001. DOI : 10.1109/42.932742. En ligne : http://www.ncbi.nlm.nih.gov/pubmed/12814574

Y. Chudasama et T. Robbins, “Functions of frontostriatal systems in cognition : Comparative neuropsychopharmacological studies in rats, monkeys and humans”, *Biological Psychology*, 2006.

M. K. Chung, K. J. Worsley, T. Paus, C. Cherif, D. L. Collins, J. N. Giedd, J. L. Rapoport, et a. C. Evans, “A unified statistical approach to deformation-based morphometry.” *NeuroImage*, vol. 14, no. 3, pp. 595–606, sep 2001. DOI : 10.1006/nimg.2001.0862. En ligne : http://www.ncbi.nlm.nih.gov/pubmed/11506533

M. K. Chung, K. J. Worsley, B. M. Nacewicz, K. M. Dalton, et R. J. Davidson, "General multivariate linear modeling of surface shapes using SurfStat", *NeuroImage*, vol. 53, no. 2, pp. 491–505, 2010. DOI : 10.1016/j.neuroimage.2010.06.032. En ligne : http://dx.doi.org/10.1016/j.neuroimage.2010.06.032

M. Chupin, a. R. Mukuna-Bantumbakulu, D. Hasboun, E. Bardinet, S. Baillet, S. Kinkingnéhun, L. Lemieux, B. Dubois, et L. Garnero, "Anatomically constrained region deformation for the automated segmentation of the hippocampus and the amygdala : Method and validation on controls and patients with Alzheimer's disease." *NeuroImage*, vol. 34, no. 3, pp. 996–1019, feb 2007. DOI : 10.1016/j.neuroimage.2006.10.035. En ligne : http://www.ncbi.nlm.nih.gov/pubmed/17178234

M. Chupin, A. Hammers, R. S. Liu, O. Colliot, J. Burdett, E. Bardinet, J. S. Duncan, L. Garnero, et L. Lemieux, "Automatic segmentation of the hippocampus and the amygdala driven by hybrid constraints : method and validation", *Neuroimage*, vol. 46, no. 3, pp. 749–761, 2009.

D. Cohen-Steiner et J.-M. Morvan, "Restricted delaunay triangulations and normal cycle", dans *Proceedings of the nineteenth conference on Computational geometry - SCG '03*. New York, New York, USA : ACM Press, 2003, pp. 312–321. DOI : 10.1145/777837.777839. En ligne : http://portal.acm.org/citation.cfm?doid=777792.777839

D. L. Collins, C. J. Holmes, T. M. Peters, et A. C. Evans, "Automatic 3 ?D model ?based neuroanatomical segmentation", *Human brain mapping*, vol. 3, no. 3, pp. 190–208, 1995.

D. Collins et A. C. Evans, "ANIMAL :validation and applications of nonlinear registration based segmentation", *International Journal of Pattern Recognition and Artificial Intelligence*, vol. 11, pp. 1271–1294, 1997.

A. Connolly, E. Northcott, et D. Cairns, "Quality of life of children with Benign Rolandic Epilepsy", *Pediatric neurology*, vol. 35, pp. 240–245, 2006.

T. F. Cootes, C. J. Taylor, D. H. Cooper, et J. Graham, "Active shape models-Their training and application", *Computer vision and image understanding*, vol. 61, no. 1, pp. 38–59, 1995.

T. F. Cootes, G. J. Edwards, et C. J. Taylor, "Active appearance models", *H. Burkhardt and B. Neumann Eds*, vol. 2, pp. 484–498, 1998. En ligne : http://medcontent.metapress.com/index/A65RM03P4874243N.pdf

P. Coupé, S. F. Eskildsen, J. V. Manjón, V. S. Fonov, et D. L. Collins,

"Simultaneous segmentation and grading of anatomical structures for patient's classification : application to Alzheimer's disease." *NeuroImage*, vol. 59, no. 4, pp. 3736–47, feb 2012. DOI : 10.1016/j.neuroimage.2011.10.080. En ligne : http://www.ncbi.nlm.nih.gov/pubmed/22094645

W. R. Crum, R. I. Scahill, et N. C. Fox, "Automated hippocampal segmentation by regional fluid registration of serial MRI : validation and application in Alzheimer's disease." *NeuroImage*, vol. 13, no. 5, pp. 847–55, may 2001. DOI : 10.1006/nimg.2001.0744. En ligne : http://www.ncbi.nlm.nih.gov/pubmed/11304081

J. Csernansky, S. Joshi, L. Wang, J. Haller, M. Gado, J. Miller, U. Grenander, et M. Miller, "Hippocampal morphometry in schizophrenia by high dimensional brain mapping", *Proceedings of the National Academy of Sciences of the United States of America*, vol. 95, no. 19, pp. 11 406–11 411, 1998.

J. Csernansky, L. Wang, D. Jones, D. Rastogi-Cruz, J. A. Posener, G. Heydebrand, P. Miller, et M. I. Miller, "Hippocampal deformities in schizophrenia characterized by high dimensional brain mapping", *American Journal of Psychiatriy*, vol. 159, no. 12, pp. 2000–2006, 2002.

J. Danielsson et F. Petermann, "Cognitive deficits in children with benign rolandic epilepsy of childhood or rolandic discharges : a study of children between 4 and 7 years of age with and without seizures compared with healthy controls." *Epilepsy & Behavior*, vol. 16, pp. 646–51, 2009.

A. N. Datta, N. Oser, F. Bauder, O. Maier, F. Martin, G. P. Ramelli, M. Steinlin, P. Weber, et I. K. Penner, "Cognitive impairment and cortical reorganization in children with benign epilepsy with centrotemporal spikes", *Epilepsia*, vol. 54, no. 3, pp. 487–494, 2013. DOI : 10.1111/epi.12067

C. Davatzikos, Y. Fan, X. Wu, D. Shen, et S. Resnick, "Alzheimer's disease via pattern classification of mri." *Neurobiology of aging*, vol. 29, no. 4, pp. 514–523, 2008.

B. M. Dawant, S. L. Hartmann, J. P. Thirion, F. Maes, D. Vandermeulen, et P. Demaerel, "Automatic 3-D segmentation of internal structures of the head in MR images using a combination of similarity and free-form transformations : Part I, Methodology and validation on normal subjects." *IEEE transactions on medical imaging*, vol. 18, no. 10, pp. 909–16, oct 1999. En ligne : http://www.ncbi.nlm.nih.gov/pubmed/10628950

M. Desbrun, M. Meyer, P. Schr, et A. H. Barr, "Implicit Fairing of Irregular Meshes using Diffusion and Curvature Flow", dans *SIGGRAPH*, 1999, pp. 317–324.

L. R. Dice, “Measures of the amount of ecologic association between species”, *Ecology*, vol. 26, no. 3, 1945.

P. K. Dokania et M. P. Kumar, “Parsimonious Labeling”, dans *ICCV 2015*, 2015.

H. Doose, B. Brigger-Heuer, et B. Neubauer, “Children with focal sharp waves : Clinical and genetic aspects”, *Epilepsia*, vol. 38, no. 7, pp. 788–796, 1997. DOI : 10.1111/j.1528-1157.1997.tb01466.x

A. T. Du, N. Schuff, D. Amend, M. P. Laakso, Y. Y. Hsu, W. J. Jagust, K. Yaffe, J. H. Kramer, B. Reed, D. Norman, H. C. Chui, et M. W. Weiner, “Magnetic resonance imaging of the entorhinal cortex and hippocampus in mild cognitive impairment and Alzheimer’s disease.” *Journal of neurology, neurosurgery, and psychiatry*, vol. 71, no. 4, pp. 441–447, 2001. DOI : 10.1136/jnnp.71.4.441

S. Duchesne, J. Pruessner, et D. Collins, “Appearance-based segmentation of medial temporal lobe structures”, *NeuroImage*, vol. 17, no. 2, pp. 515 – 531, 2002. DOI : http://dx.doi.org/10.1006/nimg.2002.1188

B. Fischl, D. H. Salat, E. Busa, M. Albert, M. Dieterich, C. Haselgrove, A. Van Der Kouwe, R. Killiany, D. Kennedy, S. Klaveness *et al.*, “Whole brain segmentation : automated labeling of neuroanatomical structures in the human brain”, *Neuron*, vol. 33, no. 3, pp. 341–355, 2002.

Y. Gao, T. Riklin-Raviv, et S. Bouix, “Shape analysis, a field in need of careful validation.” *Human brain mapping*, vol. 35, no. 10, pp. 4965–78, oct 2014. DOI : 10.1002/hbm.22525. En ligne : http://www.ncbi.nlm.nih.gov/pubmed/24753006

C. Garcia-Ramos, D. C. Jackson, J. J. Lin, K. Dabbs, J. E. Jones, D. A. Hsu, C. E. Stafstrom, L. Zawadzki, M. Seidenberg, V. Prabhakaran, et B. P. Hermann, “Cognition and brain development in children with benign epilepsy with centrotemporal spikes”, *Epilepsia*, vol. 56, no. 10, pp. 1615–1622, 2015. DOI : 10.1111/epi.13125

——, “Cognition and brain development in children with benign epilepsy with centrotemporal spikes”, *Epilepsia*, vol. 56, no. 10, pp. 1615–1622, 2015. DOI : 10.1111/epi.13125

P. Gelisse, D. Corda, C. Raybaud, C. Dravet, M. Bureau, et P. Genton, “Abnormal neuroimaging in patients with benign epilepsy with centrotemporal spikes”, *Epilepsia*, vol. 44, no. 3, pp. 372–378, 2003. DOI : 10.1046/j.1528-1157.2003.17902.x

J. Genizi, S. Shamay-Tsoory, E. Shahar, S. Yaniv, et J. Aharon-Perez, “Impaired Social

Behavior in Children With Benign Childhood Epilepsy With Centrotemporal Spikes", *J Child Neurol*, vol. 27, no. 2, pp. 156–61, 2012.

G. Gerig, M. Jomier, et M. Chakos, "Valmet : A new validation tool for assessing and improving 3D object segmentation", dans *Medical Image Computing and Computer-Assisted Intervention MICCAI 2001*, 2001, pp. 516–523.

G. Gerig, M. Styner, M. E. Shenton, et J. A. Lieberman, "Shape versus Size : Improved understanding of the Morphology of Brain Structures", dans *4th International Conference on Medical Image Computing and Computer Assisted Intervention, LNCS 2208*, 2001, pp. 24–32.

a. Ghanei, H. Soltanian-Zadeh, et J. P. Windham, "Segmentation of the hippocampus from brain MRI using deformable contours." *Computerized medical imaging and graphics : the official journal of the Computerized Medical Imaging Society*, vol. 22, no. 3, pp. 203–16, 1998. En ligne : `http://www.ncbi.nlm.nih.gov/pubmed/9740038`

B. Glocker, A. Sotiras, N. Komodakis, et N. Paragios, "Deformable medical image registration : setting the state of the art with discrete methods." *Annu Rev Biomed Eng*, 2011.

H. Goldberg-Stern, O. Gonen, M. Sadeh, S. Kivity, A. Shuper, et D. Inbar, "Neuropsychological aspects of benign childhood epilepsy with centrotemporal spikes", *Seizure*, vol. 19, no. 1, pp. 12 – 16, 2010. DOI : `http://dx.doi.org/10.1016/j.seizure.2009.10.004`

C. D. Good, I. S. Johnsrude, J. Ashburner, R. N. Henson, K. J. Friston, et R. S. Frackowiak, "A voxel-based morphometric study of ageing in 465 normal adult human brains." *NeuroImage*, vol. 14, no. 1 Pt 1, pp. 21–36, jul 2001. DOI : `10.1006/nimg.2001.0786`. En ligne : `http://www.ncbi.nlm.nih.gov/pubmed/11525331`

M. Goryawala et et al., "Inclusion of neuropsychological scores in atrophy models improves diagnostic classification of alzheimer's disease and mild cognitive impairment." *Computational Intelligence and Neuroscience*, 2015.

S. Gouttard, M. Styner, S. Joshi, R. G. Smith, H. Cody Hazlett, et G. Gerig, "Subcortical Structure Segmentation using Probabilistic Atlas Priors", dans *SPIE Medical Imaging*, J. P. W. Pluim et J. M. Reinhardt, éds., vol. 6512, mar 2007. DOI : `10.1117/12.708626`. En ligne : `http://proceedings.spiedigitallibrary.org/proceeding.aspx?articleid=1299623`

L. J. Grady et J. R. Polimeni, *Discrete Calculus*, 2010.

A. Guimond, J. Meunier, et J. P. Thirion, “Average Brain Models : A Convergence Study”, *Computer Vision and Image Understanding*, vol. 77, no. 2, pp. 192–210, 2000.

J. Gunter, M. Bernstein, B. Borowski, J. Felmlee, D. Blezek, R. Mallozzi, J. Levy, N. Schuff, et J. C. Jack, “Validation Testing of the MRI Calibration Phantom for the Alzheimer's Disease Neuroimaging Initiative Study”, dans *Proceedings 14th Scientific Meeting, International Society for Magnetic Resonance in Medicine*, 2006.

Y. Guo, G. Wu, L. A. Commander, S. Szary, V. Jewells, W. Lin, et D. Shen, *Segmenting Hippocampus from Infant Brains by Sparse Patch Matching with Deep-Learned Features*. Cham : Springer International Publishing, 2014, pp. 308–315.

A. Hammers, R. Allom, M. J. Koepp, S. L. Free, R. Myers, L. Lemieux, T. N. Mitchell, D. J. Brooks, et J. S. Duncan, “Three-dimensional maximum probability atlas of the human brain, with particular reference to the temporal lobe.” *Human brain mapping*, vol. 19, no. 4, pp. 224–47, aug 2003. DOI : 10.1002/hbm.10123. En ligne : http://www.ncbi.nlm.nih.gov/pubmed/12874777

M. Harandi, C. Sanderson *et al.*, “Graph embedding discriminant analysis on grassmannian manifolds for improved image set matching”, dans *CVPR*, 2011, p. 2705.

S. L. Hartmann, M. H. Parks, P. R. Martin, et B. M. Dawant, “Automatic 3-D segmentation of internal structures of the head in MR images using a combination of similarity and free-form transformations : Part II, validation on severely atrophied brains.” *IEEE transactions on medical imaging*, vol. 18, no. 10, pp. 917–26, oct 1999. DOI : 10.1109/42.811273. En ligne : http://www.ncbi.nlm.nih.gov/pubmed/10628951

R. S. Hastings, R. V. Parsey, M. A. Oquendo, V. Arango, et J. J. Mann, “Volumetric analysis of the prefrontal cortex, amygdala, and hippocampus in major depression.” *Neuropsychopharmacology : official publication of the American College of Neuropsychopharmacology*, vol. 29, no. 5, pp. 952–9, may 2004. DOI : 10.1038/sj.npp.1300371. En ligne : http://www.ncbi.nlm.nih.gov/pubmed/14997169

R. a. Heckemann, J. V. Hajnal, P. Aljabar, D. Rueckert, et A. Hammers, “Automatic anatomical brain MRI segmentation combining label propagation and decision fusion.” *NeuroImage*, vol. 33, no. 1, pp. 115–26, oct 2006. DOI : 10.1016/j.neuroimage.2006.05.061. En ligne : http://www.ncbi.nlm.nih.gov/pubmed/16860573

R. A. Heckemann, S. Keihaninejad, P. Aljabar, D. Rueckert, J. V. Hajnal, et A. Hammers, “Improving intersubject image registration using tissue-class information benefits robustness

and accuracy of multi-atlas based anatomical segmentation", *NeuroImage*, 2010.

J. Heijbel, S. Blom, et M. Rasmuson, "Benign epilepsy of childhood with centrotemporal eeg foci : A genetic study", *Epilepsia*, vol. 16, no. 2, pp. 285–293, 1975. DOI : 10.1111/j.1528-1157.1975.tb06059.x. En ligne : http://dx.doi.org/10.1111/j.1528-1157.1975.tb06059.x

T. Heimann et H.-P. Meinzer, "Statistical shape models for 3D medical image segmentation : a review." *Medical image analysis*, vol. 13, no. 4, pp. 543–63, aug 2009. DOI : 10.1016/j.media.2009.05.004. En ligne : http://www.ncbi.nlm.nih.gov/pubmed/19525140

B. Hermann, J. Jones, R. Sheth, C. Dow, M. Koehn, et M. Seidenberg, "Children with new-onset epilepsy : Neuropsychological status and brain structure", *Brain*, vol. 129, no. 10, pp. 2609–2619, 2006. DOI : 10.1093/brain/awl196

G. E. Hinton et R. R. Salakhutdinov, "Reducing the dimensionality of data with neural networks", *Science*, vol. 313, no. 5786, pp. 504–507, 2006. DOI : 10.1126/science.1127647. En ligne : http://science.sciencemag.org/content/313/5786/504

R. E. Hogan, K. E. Mark, L. Wang, S. Joshi, M. I. Miller, et R. D. Bucholz, "Mesial Temporal Sclerosis and Temporal Lobe Epilepsy : MR Imaging Segmentation of the Hippocampus in Five Patients", *Radiology*, vol. 216, no. 1, pp. 291–297, 2000.

S. Hu et D. L. Collins, "Joint level-set shape modeling and appearance modeling for brain structure segmentation", *NeuroImage*, vol. 36, no. 3, pp. 672 – 683, 2007. DOI : http://dx.doi.org/10.1016/j.neuroimage.2006.12.048

J. E. Iglesias, C. Y. Liu, P. M. Thompson, et Z. Tu, "Robust brain extraction across datasets and comparison with publicly available methods", *IEEE Transactions on Medical Imaging*, vol. 30, no. 9, pp. 1617–1634, Sept 2011. DOI : 10.1109/TMI.2011.2138152

J. E. Iglesias et M. R. Sabuncu, "Multi-atlas segmentation of biomedical images : A survey", *Medical Image Analysis*, vol. 24, no. 1, pp. 205 – 219, 2015.

I. Isgum, M. Staring, A. Rutten, M. Prokop, M. a. Viergever, et B. van Ginneken, "Multi-atlas-based segmentation with local decision fusion–application to cardiac and aortic segmentation in CT scans." *IEEE transactions on medical imaging*, vol. 28, no. 7, pp. 1000–10, jul 2009. DOI : 10.1109/TMI.2008.2011480. En ligne : http://www.ncbi.nlm.nih.gov/pubmed/19131298

C. R. Jack Jr, M. A. Bernstein, N. C. Fox, P. Thompson, G. Alexander, D. Harvey, B. Borowski, P. J. Britson, J. L. Whitwell, C. Ward, A. M. Dale, J. P. Felmlee, J. L. Gunter, D. L. G. Hill, R. Killiany, N. Schuff, S. Fox-bosetti, C. Lin, C. Studholme, S. Charles, G. Krueger, H. a. Ward, et G. J. Metzger, "The Alzheimer's Disease Neuroimaging Initiative (ADNI) : MRI Methods", *Journal of Magnetic Resonance*, vol. 27, no. 4, pp. 685–691, 2008. DOI : 10.1002/jmri.21049.The

S. Joshi, B. Davis, M. Jomier, et G. Gerig, "Unbiased diffeomorphic atlas construction for computational anatomy." *NeuroImage*, vol. 23 Suppl 1, no. June 2004, pp. S151–60, jan 2004. DOI : 10.1016/j.neuroimage.2004.07.068. En ligne : http://www.ncbi.nlm.nih.gov/pubmed/15501084

S. Joshi, S. Pizer, S. Member, P. T. Fletcher, P. Yushkevich, A. Thall, S. Member, et J. S. Marron, "Multiscale Deformable Model Segmentation and Statistical Shape Analysis Using Medial Descriptions", *IEEE transaction on medical imaging*, vol. 21, no. 5, pp. 538–550, 2002.

J. Jovicich, S. Czanner, D. Greve, E. Haley, A. Van Der Kouwe, R. Gollub, D. Kennedy, F. Schmitt, G. Brown, J. MacFall, B. Fischl, et A. Dale, "Reliability in multi-site structural MRI studies : Effects of gradient non-linearity correction on phantom and human data", *NeuroImage*, vol. 30, no. 2, pp. 436–443, 2006. DOI : 10.1016/j.neuroimage.2005.09.046

G. Jurkevičienė, M. Endzinienė, I. Laukienė, V. Šaferis, D. Rastenytė, S. Plioplys, et N. Vaičienė-Magistris, "Association of language dysfunction and age of onset of benign epilepsy with centrotemporal spikes in children", *European Journal of Paediatric Neurology*, vol. 16, no. 6, pp. 653 – 661, 2012. DOI : http://dx.doi.org/10.1016/j.ejpn.2012.03.011

H. Kanemura, S. Hata, K. Aoyagi, K. Sugita, et M. Aihara, "Serial changes of prefrontal lobe growth in the patients with benign childhood epilepsy with centrotemporal spikes presenting with cognitive impairments/behavioral problems." *Brain & development*, vol. 33, no. 2, pp. 106–13, feb 2011. DOI : 10.1016/j.braindev.2010.03.005. En ligne : http://www.ncbi.nlm.nih.gov/pubmed/20381984

a. Kelemen, G. Székely, et G. Gerig, "Elastic model-based segmentation of 3-D neuroradiological data sets." *IEEE transactions on medical imaging*, vol. 18, no. 10, pp. 828–39, oct 1999. DOI : 10.1109/42.811260. En ligne : http://www.ncbi.nlm.nih.gov/pubmed/10628943

A. R. Khan, L. Wang, et M. F. Beg, “FreeSurfer-initiated fully-automated subcortical brain segmentation in MRI using Large Deformation Diffeomorphic Metric Mapping.” *NeuroImage*, vol. 41, no. 3, pp. 735–46, jul 2008. DOI : 10.1016/j.neuroimage.2008.03.024. En ligne : http://www.pubmedcentral.nih.gov/articlerender.fcgi?artid=2905149{&}tool=pmcentrez{&}rendertype=abstract

E.-H. Kim, M.-S. Yum, W.-H. Shim, H.-K. Yoon, Y.-J. Lee, et T.-S. Ko, “Structural abnormalities in benign childhood epilepsy with centrotemporal spikes (BCECTS).” *Seizure*, vol. 27, pp. 40–6, 2015. DOI : 10.1016/j.seizure.2015.02.027. En ligne : http://www.ncbi.nlm.nih.gov/pubmed/25891925

H. Kim, “Advanced Morphometry Of Mesiotemporal Structures In Temporal Lobe Epilepsy”, *Ph.D. dissertation, McGill University*, 2012.

J. Kim, M. D. C. Valdes-Hernandez, N. a. Royle, et J. Park, “Hippocampal Shape modeling based on a Progressive Template Surface Deformation and Its Verification”, *IEEE Transactions on Medical Imaging*, vol. 34, no. 6, pp. 1242–1261, 2014. DOI : 10.1109/TMI.2014.2382581. En ligne : http://ieeexplore.ieee.org/lpdocs/epic03/wrapper.htm?arnumber=6990617

D. P. Kingma et M. Welling, “Auto-encoding variational bayes”, dans *International Conference on Learning Representations (ICLR)*, 2013. En ligne : http://arxiv.org/abs/1312.6114

A. Klein, J. Andersson, B. a. Ardekani, J. Ashburner, B. Avants, M.-C. Chiang, G. E. Christensen, D. L. Collins, J. Gee, P. Hellier, J. H. Song, M. Jenkinson, C. Lepage, D. Rueckert, P. Thompson, T. Vercauteren, R. P. Woods, J. J. Mann, et R. V. Parsey, “Evaluation of 14 nonlinear deformation algorithms applied to human brain MRI registration.” *NeuroImage*, vol. 46, no. 3, pp. 786–802, jul 2009. DOI : 10.1016/j.neuroimage.2008.12.037. En ligne : http://www.pubmedcentral.nih.gov/articlerender.fcgi?artid=2747506{&}tool=pmcentrez{&}rendertype=abstract

J. Klemencic, J. P. W. Pluim, M. A. Viergever, H. G. Schnack, et V. Valencic, “Non-Rigid Registration Based Active Appearance Models for 3D Medical Image Segmentation”, *Journal of Imaging Science and Technology*, vol. 2, pp. 166–171, 2004.

N. Komodakis et N. Paragios, “Beyond Pairwise Energies : Efficient Optimization for Higher-order MRFs”, dans *Computer Vision and Pattern Recognition, CVPR 2009*, 2009, pp. 2985–2992.

N. Komodakis, G. Tziritas, et N. Paragios, “Performance vs computational efficiency for optimizing single and dynamic mrfs : Setting the state of the art with primal-dual strategies”, *Computer Vision and Image Understanding*, 2008.

C. Konrad, T. Ukas, C. Nebel, V. Arolt, a. W. Toga, et K. L. Narr, “Defining the human hippocampus in cerebral magnetic resonance images–an overview of current segmentation protocols.” *NeuroImage*, vol. 47, no. 4, pp. 1185–95, oct 2009. DOI : 10.1016/j.neuroimage.2009.05.019. En ligne : http://www.pubmedcentral.nih.gov/articlerender.fcgi?artid=3299307{&}tool=pmcentrez{&}rendertype=abstract

U. Kramer, Y. Nevo, M. Y. Neufeld, A. Fatal, Y. Leitner, et S. Harel, “Epidemiology of epilepsy in childhood : A cohort of 440 consecutive patients”, *Pediatric Neurology*, vol. 18, no. 1, pp. 46 – 50, 1998. DOI : http://dx.doi.org/10.1016/S0887-8994(97)00154-9

A. Krizhevsky, I. Sutskever, G. E. Hinton, et A. Krizhevsky, “Imagenet classification with deep convolutional neural networks”, dans *Advances in Neural Information Processing Systems (NIPS ’12)*, 2012, p. 1097 ?1105.

A. Krizhevsky, I. Sutskever, et G. Hinton, “Imagenet classification with deep convolutional neural networks”, dans *NIPS*, 2012.

Y. LeCun, L. Bottou, Y. Bengio, et P. Haffner, “Gradient-based learning applied to document recognition”, *Proceedings of the IEEE*, 1998.

A. D. Leow, I. Yanovsky, M.-C. Chiang, A. D. Lee, A. D. Klunder, A. Lu, J. T. Becker, S. W. Davis, A. W. Toga, et P. M. Thompson, “Statistical properties of jacobian maps and the realization of unbiased large-deformation nonlinear image registration”, *IEEE Transactions on Medical Imaging*, vol. 26, no. 6, pp. 822–832, 2007.

Y. Li, Y. Wang, G. Wu, F. Shi, L. Zhou, W. Lin, D. Shen, A. D. N. Initiative *et al.*, “Discriminant analysis of longitudinal cortical thickness changes in alzheimer’s disease using dynamic and network features”, *Neurobiology of aging*, vol. 33, no. 2, pp. 427–e15, 2012.

A. Liasis, D. E. Bamiou, S. Boyd, et A. Towell, “Evidence for a neurophysiologic auditory deficit in children with benign epilepsy with centro-temporal spikes”, *Journal of Neural Transmission*, vol. 113, no. 7, pp. 939–949, 2006. DOI : 10.1007/s00702-005-0357-6

J. J. Lin, J. D. Riley, D. A. Hsu, C. E. Stafstrom, K. Dabbs, T. Becker, M. Seidenberg, et B. P. Hermann, “Striatal hypertrophy and its cognitive effects in new-onset benign epilepsy with centrotemporal spikes.” *Epilepsia*, vol. 53, no. 4, pp. 677–85, apr 2012. DOI :

10.1111/j.1528-1167.2012.03422.x. En ligne : http://www.pubmedcentral.nih.gov/articlerender.fcgi?artid=3321058{&}tool=pmcentrez{&}rendertype=abstract

S. Lindgren, M. Kihlgren, L. Melin, C. Croona, S. Lundberg, et O. Eeg-Olofsson, "Development of cognitive functions in children with rolandic epilepsy", *Epilepsy Behav*, vol. 5, pp. 903–910, 2004.

H. Lombaert, L. Grady, J. R. Polimeni, et F. Cheriet, "Fast Brain Matching with Spectral Correspondence", dans *Information Processing in Medical Imaging*, 2011, pp. 660–673.

——, "FOCUSR : feature oriented correspondence using spectral regularization–a method for precise surface matching." *IEEE transactions on pattern analysis and machine intelligence*, vol. 35, no. 9, pp. 2143–60, sep 2013. DOI : 15A24E1C-FA85-48DC-A556-C6526C479AB2. En ligne : http://www.ncbi.nlm.nih.gov/pubmed/23868776

H. Lombaert, J. Sporring, et K. Siddiqi, "Diffeomorphic Spectral Matching of Cortical Surfaces", dans *Information Processing in Medical Imaging*. Springer Berlin Heidelberg, 2013, pp. 376–389.

H. Lombaert, A. Criminisi, et N. Ayache, *Spectral Forests : Learning of Surface Data, Application to Cortical Parcellation*. Cham : Springer International Publishing, 2015, pp. 547–555.

J. Long, E. Shelhamer, et T. Darrell, "Fully convolutional networks for semantic segmentation", *CVPR*, 2015.

W. E. Lorensen et H. E. Cline, "Marching cubes : A high resolution 3D surface construction algorithm", dans *SIGGRAPH '87 Proceedings of the 14th annual conference on Computer graphics and interactive techniques*, 1987, pp. 163–169.

D. V. Losifescu, M. E. Shenton, S. K. Warfield, R. Kikinis, J. Dengler, F. A. Jolesz, et R. W. Mccarley, "An Automated Registration Algorithm for Measuring", *NeuroImage*, vol. 25, no. 6, pp. 13–25, 1997.

S. Lundberg, O. Eeg-Olofsson, R. Raininko, et K. E. Eeg-Olofsson, "Hippocampal asymmetries and white matter abnormalities on mri in benign childhood epilepsy with centrotemporal spikes", *Epilepsia*, vol. 40, no. 12, pp. 1808–1815, 1999. DOI : 10.1111/j.1528-1157.1999.tb01603.x

C. Luo, Y. Zhang, W. Cao, Y. Huang, F. Yang, J. Wang, S. Tu, X. Wang, D. Yao, et by Cheng, “Altered Structural and Functional Feature of Striato - Cortical Circuit In Benign Epilepsy with Centrotemporal Spikes”, *International Journal of Neural Systems*, vol. 25, no. 6, 2015. DOI : 10.1142/S0129065715500276

P. A. MacDonald, H. Ganjavi, D. L. Collins, A. C. Evans, et S. Karama, “Investigating the relation between striatal volume and iq”, *Brain Imaging and Behavior*, vol. 8, no. 1, pp. 52–59, 2014. DOI : 10.1007/s11682-013-9242-3. En ligne : http://dx.doi.org/10.1007/s11682-013-9242-3

R. Maglietta, N. Amoroso, M. Boccardi, S. Bruno, A. Chincarini, G. B. Frisoni, P. Inglese, A. Redolfi, S. Tangaro, A. Tateo, et R. Bellotti, “Automated hippocampal segmentation in 3D MRI using random undersampling with boosting algorithm”, *Pattern Analysis and Applications*, vol. 19, no. 2, pp. 579–591, 2016. DOI : 10.1007/s10044-015-0492-0. En ligne : "http://dx.doi.org/10.1007/s10044-015-0492-0

D. Malfait, A. Tucholka, S. Mendizabal, J. Tremblay, C. Poulin, M. Oskoui, M. Srour, L. Carmant, P. Major, et S. Lippé, “FMRI brain response during sentence reading comprehension in children with benign epilepsy with centro-temporal spikes”, *Epilepsy Research*, vol. 117, pp. 42–51, 2015. DOI : 10.1016/j.eplepsyres.2015.08.009. En ligne : http://dx.doi.org/10.1016/j.eplepsyres.2015.08.009

D. Malfait, “Troubles cognitifs et comportementaux chez l’enfant ayant une épilepsie bénigne à pointes centro-temporales”, *Revista Neuropsicologia Latinoamericana*, vol. 3, no. 1, pp. 47–57, 2011. DOI : 10.5579/rnl.2011.0055

S. Marsland et C. Twining, “Constructing diffeomorphic representations of non-rigid registrations of medical images”, *IEEE transaction on medical imaging*, vol. 23, no. 8, pp. 1006–1020, 2004.

T. McInerney, G. Hamarneh, M. Shenton, et D. Terzopoulos, “Deformable organisms for automatic medical image analysis.” *Medical image analysis*, vol. 6, no. 3, pp. 251–66, sep 2002. En ligne : http://www.pubmedcentral.nih.gov/articlerender.fcgi?artid=2845173{&}tool=pmcentrez{&}rendertype=abstract

M.-N. Metz-Lutz et M. Filippini, “Neuropsychological findings in rolandic epilepsy and landau-kleffner syndrome”, *Epilepsia*, vol. 47, pp. 71–75, 2006. DOI : 10.1111/j.1528-1167.2006.00695.x

D. Mietchen et C. Gaser, “Computational morphometry for detecting changes in brain structure due to development, aging, learning, disease and evolution.” *Frontiers in neuroinformatics*, vol. 3, no. August, p. 25, jan 2009. DOI : 10.3389/neuro.11.025.2009. En ligne : http://www.pubmedcentral.nih.gov/articlerender.fcgi?artid=2729663{&}tool=pmcentrez{&}rendertype=abstract

M. I. Miller, G. E. Christensen, Y. Amit, et U. Grenander, “Mathematical textbook of deformable neuroanatomies.” *Proceedings of the National Academy of Sciences of the United States of America*, vol. 90, no. 24, pp. 11 944–8, dec 1993. En ligne : http://www.pubmedcentral.nih.gov/articlerender.fcgi?artid=48101{&}tool=pmcentrez{&}rendertype=abstract

P. Moeskops, M. A. Viergever, A. M. Mendrik, L. S. de Vries, M. J. N. L. Benders, et I. Isgum, “Automatic Segmentation of MR Brain Images With a Convolutional Neural Network”, *IEEE Transactions on Medical Imaging*, vol. 35, no. 5, pp. 1252–1261, 2016. DOI : 10.1109/TMI.2016.2548501. En ligne : http://ieeexplore.ieee.org/lpdocs/epic03/wrapper.htm?arnumber=7444155

C. Monjauze, L. Tuller, C. Hommet, M.-A. Barthez, et A. Khomsi, “Language in benign childhood epilepsy with centro-temporal spikes abbreviated form : Rolandic epilepsy and language”, *Brain and Language*, vol. 92, no. 3, pp. 300 – 308, 2005. DOI : http://dx.doi.org/10.1016/j.bandl.2004.07.001. En ligne : http://www.sciencedirect.com/science/article/pii/S0093934X04002135

C. Monjauze, H. Broadbent, S. G. Boyd, B. G. R. Neville, et T. Baldeweg, “Language deficits and altered hemispheric lateralization in young people in remission from bects”, *Epilepsia*, vol. 52, no. 8, pp. e79–e83, 2011. DOI : 10.1111/j.1528-1167.2011.03105.x

J. H. Morra, Z. Tu, L. G. Apostolova, A. E. Green, A. W. Toga, et P. M. Thompson, “Comparison of AdaBoost and support vector machines for detecting Alzheimer’s disease through automated hippocampal segmentation.” *IEEE transactions on medical imaging*, vol. 29, no. 1, pp. 30–43, jan 2010. DOI : 10.1109/TMI.2009.2021941. En ligne : http://www.pubmedcentral.nih.gov/articlerender.fcgi?artid=2805054{&}tool=pmcentrez{&}rendertype=abstract

A. Myronenko, X. Song, et A. C. Miguel, “Non-rigid point set registration :Coherent Point Drift”, *IEEE Trans. Pattern Anal. Mach. Intell.*, vol. 32, pp. 2262–2275, 12 2009.

A. Myronenko, X. Song, et A. C.-p. Miguel, “Non-rigid point set registration : Coherent

Point Drift", *IEEE Transactions on Pattern Analysis and Machine Intelligence*, vol. 32, no. 12, pp. 2262–2275, 2009.

D. Nain, S. Haker, A. Bobick, et A. Tannenbaum, "Multiscale 3-D shape representation and segmentation using spherical wavelets." *IEEE transactions on medical imaging*, vol. 26, no. 4, pp. 598–618, apr 2007. DOI : 10.1109/TMI.2007.893284. En ligne : http://www.pubmedcentral.nih.gov/articlerender.fcgi?artid=3660982{&}tool=pmcentrez{&}rendertype=abstract

B. Neubauer, B. Fiedler, B. Himmelein, F. Kampfer, U. Lassker, G. Schwabe, I. Spanier, D. Tams, C. Bretscher, K. Moldenhauer, G. Kurlemann, S. Weise, K. Tedroff, O. Eeg-Olofsson, W. C, et S. U., "Centrotemporal spikes in families with rolandic epilepsy : linkage to chromosome 15q14", *Neurology*, vol. 51, no. 6, pp. 1608–1612, 1998.

M. J. Nitzken, M. F. Casanova, M. D. G. Gimel, T. Inanc, J. M. Zurada, L. Fellow, et A. Elbaz, "Shape Analysis of Human Brain : A Brief Survey", *IEEE Journal of Biomedical and Health Informatics*, vol. 18, no. 4, pp. 1337–1354, 2014. DOI : 10.1109/JBHI.2014.2298139

E. Northcott, A. Connolly, et A. Berroya, "The neuropsychological and language profile of children with benign rolandic epilepsy." *Epilepsia*, vol. 46, pp. 924–930, 2005.

——, "Memory and phonological awareness in children with Benign Rolandic Epilepsy compared to a matched control group", *Epilepsy research*, vol. 75, pp. 57–62, 2007.

A. C. Nugent, D. a. Luckenbaugh, S. E. Wood, W. Bogers, C. a. Zarate, et W. C. Drevets, "Automated subcortical segmentation using FIRST : test-retest reliability, interscanner reliability, and comparison to manual segmentation." *Human brain mapping*, vol. 34, no. 9, pp. 2313–29, sep 2013. DOI : 10.1002/hbm.22068. En ligne : http://www.ncbi.nlm.nih.gov/pubmed/22815187

D. Ong, M. Walterfang, G. S. Malhi, M. Styner, D. Velakoulis, et P. Christos, "Size and shape of the caudate nucleus in individuals with bipolar affective disorder", *Australian and New Zealand Journal of Psychiatry*, vol. 46, no. 4, pp. 340–351, 2012. DOI : 10.1016/j.biotechadv.2011.08.021.Secreted

G. M. Overvliet, A. P. Aldenkamp, S. Klinkenberg, J. S. H. Vles, et J. Hendriksen, "Impaired language performance as a precursor or consequence of Rolandic epilepsy ?" *Journal of the Neurological Sciences*, vol. 304, no. 1-2, pp. 71–74, 2011. DOI : 10.1016/j.jns.2011.02.009

C. P. Panayiotopoulos, M. Michael, S. Sanders, T. Valeta, et M. Koutroumanidis, “Benign childhood focal epilepsies : assessment of established and newly recognized syndromes”, *Brain*, vol. 131, no. 9, pp. 2264–2286, 2008. DOI : 10.1093/brain/awn162

C. Panayiotopoulos, “Brain Imaging in the Diagnosis and Management of Epilepsies”, dans *The Epilepsies : Seizures, Syndromes and Management.* Bladon Medical Publishing, 2005.

B. Paniaguaa, L. Bompard, J. Cates, R. Whitaker, M. Datar, C. VAchet, et M. Styner, “Combined SPHARM-PDM and entropy-based particle systems shape analysis framework”, dans *SPIE Conference 8317 Progress in Biomedical Optics and Imaging*, vol. 1, 2012, pp. 1–10. DOI : 10.1117/12.911228.Combined

D. Pantazis, R. M. Leahy, T. E. Nichols, et M. Styner, “Statistical Surface-Based Morphometry Using A Non-Parametric Approach”, dans *International Symposium on Biomedical Imaging (ISBI)*, 2004, pp. 1283–1286.

H. R. Pardoe, A. T. Berg, J. S. Archer, R. K. Fulbright, et G. D. Jackson, “A neurodevelopmental basis for BECTS : evidence from structural MRI.” *Epilepsy research*, vol. 105, no. 1-2, pp. 133–9, jul 2013. DOI : 10.1016/j.eplepsyres.2012.11.008. En ligne : http://www.pubmedcentral.nih.gov/articlerender.fcgi?artid=3669634{&}tool=pmcentrez{&}rendertype=abstract

S. Parisot, H. Duffau, S. Chemouny, et N. Paragios, “Joint tumor segmentation and dense deformable registration of brain mr images”, dans *MICCAI*, 2012.

B. Patenaude, S. M. Smith, K. D. N., et M. Jenkinson, “A bayesian model of shape and appearance for subcortical brain segmentation”, *NeuroImage*, 2011.

B. Patenaude, S. M. Smith, D. N. Kennedy, et M. Jenkinson, “A bayesian model of shape and appearance for subcortical brain segmentation”, *Neuroimage*, vol. 56, no. 3, pp. 907–922, 2011.

F. Perkins, J. Breier, et M. McManis, “Benign rolandic epilepsy - perhaps not so benign : use of magnetic source imaging as a predictor of outcome”, *J Child Neurol*, vol. 23, pp. 389–393, 2008.

R. Petersen, G. Smith, S. Waring, R. Ivnik, E. Tangalos, et E. Kokmen, “Mild cognitive impairment : clinical characterization and outcome”, *Arch. Neurol*, vol. 56, no. 3, pp. 303 – 308, 1999.

P. Piccinelli, R. Borgatti, et A. Aldini, “Academic performance in children with rolandic epilepsy”, *Dev Med Child Neurol*, vol. 50, pp. 353–356, 2008.

F. Pinton, B. Ducot, J. Motte, A. Arbués, C. Barondiot, M. Barthez, Y. Chaix, R. Cheminal, M. Livet, M. Penniello, S. Peudenier, A. de Saint-Martin, et C. Billard, “Cognitive functions in children with benign childhood epilepsy with centrotemporal spikes (bects).” *Epileptic Disorder*, vol. 8, no. 1, pp. 11–23, 2006.

A. Pitiot, H. Delingette, P. M. Thompson, et N. Ayache, “Expert knowledge-guided segmentation system for brain MRI.” *NeuroImage*, vol. 23 Suppl 1, pp. S85–96, jan 2004. DOI : 10.1016/j.neuroimage.2004.07.040. En ligne : http://www.ncbi.nlm.nih.gov/pubmed/15501103

S. M. Pizer, P. T. Fletcher, S. Joshi, A. Thall, J. Z. Chen, Y. Fridman, D. S. Fritsch, G. Gash, J. M. Glotzer, M. R. Jiroutek, C. Lu, K. E. Muller, G. Tracton, P. Yushkevich, et E. L. Chaney, “Deformable M-Reps for 3D Medical Image Segmentation.” *International journal of computer vision*, vol. 55, no. 2-3, pp. 85–106, nov 2003. En ligne : http://www.pubmedcentral.nih.gov/articlerender.fcgi?artid=3697155{&}tool=pmcentrez{&}rendertype=abstract

S. Powell, V. A. Magnotta, H. Johnson, V. K. Jammalamadaka, N. C. Andreasen, et R. Pierson, “Registration and Machine Learning Based Automated Segmentation of Subcortical and Cerebellar Brain Structures Stephanie”, *NeuroImage*, vol. 39, no. 1, pp. 238–247, 2009.

A. Prasoon, K. Petersen, C. Igel, F. Lauze, E. Dam, et M. Nielsen, “Deep feature learning for knee cartilage segmentation using a triplanar convolutional neural network”, dans *MICCAI*, 2013.

N. A. Ranginwala, L. S. Hynan, M. F. Weiner, et C. L. I. White, “Clinical criteria for the diagnosis of alzheimer disease : Still good after all these years”, *The American Journal of Geriatric Psychiatry*, vol. 16, no. 5, pp. 384 – 388, 2008. DOI : http://dx.doi.org/10.1097/JGP.0b013e3181629971. En ligne : http://www.sciencedirect.com/science/article/pii/S1064748112606058

E. M. Reinthaler, D. Lal, S. Lebon, M. S. Hildebrand, H.-H. M. Dahl, B. M. Regan, M. Feucht, H. SteinbÖck, B. Neophytou, G. M. Ronen, L. Roche, U. Gruber-Sedlmayr, J. Geldner, E. Haberlandt, P. Hoffmann, S. Herms, C. Gieger, M. Waldenberger, A. Franke, M. Wittig, S. Schoch, A. J. Becker, A. Hahn, K. Männik, M. R. Toliat, G. Winterer, T. 16p11.2 European Consortium, H. Lerche, P. Nürnberg, H. Mefford, I. E. Scheffer, S. F.

Berkovic, J. S. Beckmann, T. E. C. The EPICURE Consortium, T. Sander, S. Jacquemont, A. Reymond, F. Zimprich, et B. A. Neubauer, "16p11.2 600 kb duplications confer risk for typical and atypical rolandic epilepsy", *Human Molecular Genetics*, vol. 23, no. 22, pp. 6069–6080, 2014. DOI : 10.1093/hmg/ddu306

D. Riva, C. Vago, S. Franceschetti, C. Pantaleoni, S. D'Arrigo, T. Granata, et S. Bulgheroni, "Intellectual and language findings and their relationship to {EEG} characteristics in benign childhood epilepsy with centrotemporal spikes", *Epilepsy & Behavior*, vol. 10, no. 2, pp. 278 – 285, 2007. DOI : http://dx.doi.org/10.1016/j.yebeh.2006.12.003

J. L. Robinson, A. R. Laird, D. C. Glahn, J. Blangero, M. K. Sanghera, L. Pessoa, P. M. Fox, A. Uecker, G. Friehs, K. A. Young, J. L. Griffin, W. R. Lovallo, et P. T. Fox, "The functional connectivity of the human caudate : An application of meta-analytic connectivity modeling with behavioral filtering", *NeuroImage*, vol. 60, no. 1, pp. 117 – 129, 2012. DOI : http://dx.doi.org/10.1016/j.neuroimage.2011.12.010. En ligne : http://www.sciencedirect.com/science/article/pii/S1053811911014121

T. Rohlfing, "Image similarity and tissue overlaps as surrogates for image registration accuracy : Widely used but unreliable", *IEEE Transactions on Medical Imaging*, 2012.

——, "Image similarity and tissue overlaps as surrogates for image registration accuracy : Widely used but unreliable", *IEEE Transactions on Medical Imaging*, 2012.

T. Rohlfing, R. Brandt, R. Menzel, et C. R. Maurer, "Evaluation of atlas selection strategies for atlas-based image segmentation with application to confocal microscopy images of bee brains." *NeuroImage*, vol. 21, no. 4, pp. 1428–42, apr 2004. DOI : 10.1016/j.neuroimage.2003.11.010. En ligne : http://www.ncbi.nlm.nih.gov/pubmed/15050568

S. Roweis et L. Saul, "Nonlinear dimensionality reduction by locally linear embedding", *Science*, vol. 290, pp. 2323–6, 2000.

D. Rueckert, L. Sonoda, C. Hayes, D. Hill, M. Leach, et D. Hawkes, "Nonrigid registration using free-form deformations : application to breast mr images", *IEEE TMI*, 1999.

D. Rueckert, A. F. Frangi, A. Member, et J. A. Schnabel, "Automatic Construction of 3-D Statistical Deformation Models of the Brain Using Nonrigid Registration", *IEEE transaction on medical imaging*, vol. 22, no. 8, pp. 1014–1025, 2003.

M. R. Sabuncu, B. T. T. Yeo, K. Van Leemput, B. Fischl, et P. Gol-

land, “A generative model for image segmentation based on label fusion.” *IEEE transactions on medical imaging*, vol. 29, no. 10, pp. 1714–29, oct 2010. DOI : 10.1109/TMI.2010.2050897. En ligne : http://www.pubmedcentral.nih.gov/articlerender.fcgi?artid=3268159{&}tool=pmcentrez{&}rendertype=abstract

D. Sarco, K. Boyer, S. Lundy-Krigbaum, M. Takeoka, F. Jensen, M. Gregas, et D. Waber, “Benign rolandic epileptiform discharges are associated with mood and behavior problems.” *Epilepsy Behav*, vol. 22, pp. 298–303, 2011.

R. Sarkis, E. Wyllie, R. C. Burgess, et T. Loddenkemper, “Neuroimaging findings in children with benign focal epileptiform discharges.” *Epilepsy research*, vol. 90, no. 1-2, pp. 91–8, jun 2010. DOI : 10.1016/j.eplepsyres.2010.03.012. En ligne : http://www.ncbi.nlm.nih.gov/pubmed/20418066

D. Schomer et F. Lopes da Silva, *Niedermeyer’s Electroencephalography : Basic Principles, Clinical Applications, and Related Fields*. Lippincott Williams & Wilkins, 2010.

M. Shakeri, H. Lombaert, S. Lippé, et S. Kadoury, “Groupwise shape analysis of the hippocampus using spectral matching”, dans *Progress in Biomedical Optics and Imaging - Proceedings of SPIE*, vol. 9034, 2014. DOI : 10.1117/12.2043615

M. Shakeri, H. Lombaert, et S. Kadoury, *Classification of Alzheimer’s Disease Using Discriminant Manifolds of Hippocampus Shapes*. Cham : Springer International Publishing, 2015, pp. 65–73.

M. Shakeri, E. Ferrante, S. Tsogkas, S. Lippé, S. Kadoury, I. Kokkinos, et N. Paragios, *Prior-based Coregistration and Cosegmentation*, 2016.

M. Shakeri, H. Lombaert, A. N. Datta, N. Oser, L. Létourneau-Guillon, L. V. Lapointe, F. Martin, D. Malfait, A. Tucholka, S. Lippé, et S. Kadoury, “Statistical shape analysis of subcortical structures using spectral matching”, *Computerized Medical Imaging and Graphics*, vol. 52, pp. 58 – 71, 2016. DOI : http://dx.doi.org/10.1016/j.compmedimag.2016.03.001. En ligne : http://www.sciencedirect.com/science/article/pii/S0895611116300179

M. Shakeri, H. Lombaert, S. Tripathi, et S. Kadoury, “Deep spectral-based shape features for alzheimer’s disease classification”, dans *Workshop on Spectral and Shape Analysis in Medical Imaging (SESAMI 2016), Held in Conjunction with MICCAI 2016, Athens, Greece, October 12, 2016*, 2016.

M. Shakeri, S. Tsogkas, E. Ferrante, S. Lippé, S. Kadoury, N. Paragios, et I. Kokkinos, “Sub-cortical brain structure segmentation using f-cnn’s”, dans *13th IEEE International Symposium on Biomedical Imaging, ISBI 2016, Prague, Czech Republic, April 13-16, 2016*, 2016, pp. 269–272. DOI : 10.1109/ISBI.2016.7493261. En ligne : http://dx.doi.org/10.1109/ISBI.2016.7493261

D. Shen, E. H. Herskovits, et C. Davatzikos, “An adaptive-focus statistical shape model for segmentation and shape modeling of 3-D brain structures.” *IEEE transactions on medical imaging*, vol. 20, no. 4, pp. 257–70, apr 2001. DOI : 10.1109/42.921475. En ligne : http://www.ncbi.nlm.nih.gov/pubmed/11370893

D. Shen, S. Moffat, S. M. Resnick, et C. Davatzikos, “Measuring size and shape of the hippocampus in MR images using a deformable shape model.” *NeuroImage*, vol. 15, no. 2, pp. 422–34, feb 2002. DOI : 10.1006/nimg.2001.0987. En ligne : http://www.ncbi.nlm.nih.gov/pubmed/11798276

K. Shen, P. Bourgeat, J. Fripp, F. Mériaudeau, D. Ames, K. a. Ellis, C. L. Masters, V. L. Villemagne, C. C. Rowe, et O. Salvado, “Supervised Method to Build an Atlas Database for Multi-atlas Segmentation-propagation”, dans *SPIE Medical Imaging*, N. Karssemeijer et R. M. Summers, éds., vol. 7624, mar 2010, pp. 76 241N–76 241N–8. DOI : 10.1117/12.844048. En ligne : http://proceedings.spiedigitallibrary.org/proceeding.aspx?articleid=1340093

L. Shen, J. Ford, F. Makedon, et A. Saykin, “Hippocampal shape analysis : surface-based representation and classification Li”, *SPIE Medical Imaging*, pp. 253–264, may 2003. DOI : 10.1117/12.480851. En ligne : http://proceedings.spiedigitallibrary.org/proceeding.aspx?articleid=758055

L. Shen, H. Farid, et M. A. McPeake, “Modeling three-dimensional morphological structures using spherical harmonics”, *Evolution*, vol. 63, no. 4, pp. 1003–1016, 2009. DOI : 10.1111/j.1558-5646.2008.00557.x.MODELING

R. D. Sheth, A. R. Gutierrez, et R. Jack, E, “Rolandic Epilepsy and Cortical Dysplasia : MRI Correlation of Epileptiform Discharges”, *Pediatric neurology*, vol. 17, no. 2, pp. 177–179, 1997.

F. Shi, B. Liu, Y. Zhou, C. Yu, et T. Jiang, “Hippocampal volume and asymmetry in mild cognitive impairment and Alzheimer’s disease : Meta-analyses of MRI studies.”

Hippocampus, vol. 19, no. 11, pp. 1055–64, nov 2009. DOI : 10.1002/hipo.20573. En ligne : http://www.ncbi.nlm.nih.gov/pubmed/19309039

W. D. Shields et O. C. Snead, "Benign epilepsy with centrotemporal spikes." *Epilepsia*, vol. 50 Suppl 8, pp. 10–5, sep 2009. DOI : 10.1111/j.1528-1167.2009.02229.x. En ligne : http://www.ncbi.nlm.nih.gov/pubmed/19702727

H. C. Shin, M. R. Orton, D. J. Collins, S. J. Doran, et M. O. Leach, "Stacked autoencoders for unsupervised feature learning and multiple organ detection in a pilot study using 4d patient data", *IEEE Transactions on Pattern Analysis and Machine Intelligence*, vol. 35, no. 8, pp. 1930–1943, Aug 2013. DOI : 10.1109/TPAMI.2012.277

J. G. Sled, A. P. Zijdenbos, et A. C. Evans, "A nonparametric method for automatic correction of intensity nonuniformity in MRI data." *IEEE transactions on medical imaging*, vol. 17, no. 1, pp. 87–97, 1998. DOI : 10.1109/42.668698

S. M. Smith, M. Jenkinson, M. W. Woolrich, C. F. Beckmann, T. E. Behrens, H. Johansen-Berg, P. R. Bannister, M. D. Luca, I. Drobnjak, D. E. Flitney, R. K. Niazy, J. Saunders, J. Vickers, Y. Zhang, N. D. Stefano, J. M. Brady, et P. M. Matthews, "Advances in functional and structural {MR} image analysis and implementation as {FSL}", *NeuroImage*, vol. 23, Supplement 1, pp. S208 – S219, 2004, mathematics in Brain Imaging. DOI : http://dx.doi.org/10.1016/j.neuroimage.2004.07.051. En ligne : http://www.sciencedirect.com/science/article/pii/S1053811904003933

A. Sotiras, N. Komodakis, B. Glocker, J.-F. Deux, et N. Paragios, "Graphical models and deformable diffeomorphic population registration using global and local metrics", 2009.

L. H. Staib et J. S. Duncan, "Model-based deformable surface finding for medical images." *IEEE transactions on medical imaging*, vol. 15, no. 5, pp. 720–31, jan 1996. DOI : 10.1109/42.538949. En ligne : http://www.ncbi.nlm.nih.gov/pubmed/18215953

S. Standring, *Gray's anatomy : the anatomical basis of clinical practice*. New York : Elsevier Limited, 2016.

L. J. Strug, T. Clarke, T. Chiang, M. Chien, Z. Baskurt, W. Li, R. Dorfman, B. Bali, E. Wirrell, S. L. Kugler, D. E. Mandelbaum, S. M. Wolf, P. McGoldrick, H. Hardison, E. J. Novotny, J. Ju, D. A. Greenberg, J. J. Russo, et D. K. Pal, "Centrotemporal sharp wave EEG trait in rolandic epilepsy maps to Elongator Protein Complex 4 (ELP4)", *Eur J Hum Genet*, vol. 17, no. 9, pp. 1171–1181, jan 2009.

M. Styner, G. Gerig, J. Lieberman, D. Jones, et D. Weinberger, “Statistical shape analysis of neuroanatomical structures based on medial models”, *Medical image analysis*, vol. 7, pp. 207–220, 2003.

M. Styner, I. Oguz, et S. Xu, “Framework for the statistical shape analysis of brain structures using SPHARM-PDM”, *Insight Journal*, no. 1071, pp. 242–250, 2006. En ligne : http://www.ncbi.nlm.nih.gov/pmc/articles/PMC3062073/

M. Styner, J. A. Lieberman, D. Pantazis, et G. Gerig, “Boundary and medial shape analysis of the hippocampus in schizophrenia.” *Medical image analysis*, vol. 8, no. 3, pp. 197–203, 2004. DOI : 10.1016/j.media.2004.06.004. En ligne : http://www.ncbi.nlm.nih.gov/pubmed/15450215

M. Styner, J. A. Lieberman, R. K. Mcclure, D. R. Weinberger, D. W. Jones, et G. Gerig, “Morphometric analysis of lateral ventricles in schizophrenia and healthy controls regarding genetic and disease-specific factors”, *Proceedings of the National Academy of Sciences*, vol. 102, no. 13, pp. 4872–4877, 2005.

M. Styner, I. Oguz, S. Xu, C. Brechb, D. Pantazis, et G. Gerig, “Statistical Shape Analysis of Brain Structures using SPHARM-PDM”, *Miccai 2006 Opensource workshop*, pp. 1–7, 2006.

M. Styner, S. Xu, M. El-sayed, G. Gerig, C. Science, N. Carolina, et C. Hill, “Correspondence Evaluation in Local Shape Analysis and Structural Subdivision”, dans *2007 IEEE International Symposium on Biomedical Imaging : From Nano to Macro*, 2007, pp. 1192–1195.

H.-I. Suk et D. Shen, *Deep Learning-Based Feature Representation for AD/MCI Classification*. Berlin, Heidelberg : Springer Berlin Heidelberg, 2013, pp. 583–590.

G. Székely, a. Kelemen, C. Brechbühler, et G. Gerig, “Segmentation of 2-D and 3-D objects from MRI volume data using constrained elastic deformations of flexible Fourier contour and surface models.” *Medical image analysis*, vol. 1, no. 1, pp. 19–34, mar 1996. En ligne : http://www.ncbi.nlm.nih.gov/pubmed/9873919

N. Tajbakhsh, J. Y. Shin, S. R. Gurudu, R. T. Hurst, C. B. Kendall, M. B. Gotway, et J. Liang, “Convolutional neural networks for medical image analysis : Full training or fine tuning ?” *IEEE Transactions on Medical Imaging*, vol. 35, no. 5, pp. 1299–1312, May 2016. DOI : 10.1109/TMI.2016.2535302

H. Takao, N. Hayashi, et K. Ohtomo, “Effects of study design in multi-scanner voxel-based morphometry studies”, *NeuroImage*, vol. 84, pp. 133–140, 2014. DOI : 10.1016/j.neuroimage.2013.08.046. En ligne : http://dx.doi.org/10.1016/j.neuroimage.2013.08.046

T. B. Terriberry, J. N. Damon, S. M. Pizer, S. C. Joshi, et G. Gerig, “Population-Based Fitting of Medial Shape Models with Correspondence Optimization”, *Information Processing in Medical Imaging, IPMI 2007*, vol. 20, pp. 700–712, 2007.

A. Tsai, A. Yezzi, W. Wells, C. Tempany, D. Tucker, A. Fan, W. E. Grimson, et A. Willsky, “A shape-based approach to the segmentation of medical imagery using level sets.” *IEEE transactions on medical imaging*, vol. 22, no. 2, pp. 137–54, feb 2003. DOI : 10.1109/TMI.2002.808355. En ligne : http://www.ncbi.nlm.nih.gov/pubmed/12715991

A. Tsai, W. Wells, C. Tempany, E. Grimson, et A. Willsky, “Mutual information in coupled multi-shape model for medical image segmentation”, *Medical Image Analysis*, 2004.

N. J. Tustison, B. B. Avants, P. A. Cook, Y. Zheng, A. Egan, P. A. Yushkevich, et J. C. Gee, “N4itk : Improved n3 bias correction”, *IEEE Transactions on Medical Imaging*, vol. 29, no. 6, pp. 1310–1320, June 2010. DOI : 10.1109/TMI.2010.2046908

J. Vannest, J. R. Tenney, R. Gelineau-Morel, T. Maloney, et T. A. Glauser, “Cognitive and behavioral outcomes in benign childhood epilepsy with centrotemporal spikes”, *Epilepsy and Behavior*, vol. 45, pp. 85–91, 2015. DOI : 10.1016/j.yebeh.2015.01.041

D. F. Vears, M.-H. Tsai, L. G. Sadleir, B. E. Grinton, L. M. Lillywhite, P. W. Carney, A. Simon Harvey, S. F. Berkovic, et I. E. Scheffer, “Clinical genetic studies in benign childhood epilepsy with centrotemporal spikes”, *Epilepsia*, vol. 53, no. 2, pp. 319–324, 2012. DOI : 10.1111/j.1528-1167.2011.03368.x

A. Vedaldi et K. Lenc, “Matconvnet-convolutional neural networks for matlab”, *arXiv preprint arXiv :1412.4564*, 2014.

A. Verrotti, G. Latini, D. Trotta, R. Giannuzzi, R. Cutarella, G. Morgese, et F. Chiarelli, “Typical and atypical rolandic epilepsy in childhood : a follow-up study.” *Pediatric neurology*, vol. 26, no. 1, pp. 26–9, jan 2002. En ligne : http://www.ncbi.nlm.nih.gov/pubmed/11814731

P. Visser, F. Verhey, P. Hofman, P. Scheltens, et J. Jolles, “Medial temporal lobe atrophy predicts alzheimer’s disease in patients with minor cognitive impairment”, *Journal of*

Neurology, Neurosurgery & Psychiatry, vol. 72, no. 4, pp. 491–497, 2002.

U. Vovk, F. Pernus, et B. Likar, "A review of methods for correction of intensity inhomogeneity in mri", *IEEE Transactions on Medical Imaging*, vol. 26, no. 3, pp. 405–421, March 2007. DOI : 10.1109/TMI.2006.891486

S. Völkl-Kernstock, S. Bauch-Prater, E. Ponocny-Seliger, et M. Feucht, "Speech and school performance in children with benign partial epilepsy with centrotemporal spikes (bcects)", *Seizure*, vol. 18, no. 5, pp. 320 – 326, 2009. DOI : http://dx.doi.org/10.1016/j.seizure.2008.11.011

C. Wachinger et M. Reuter, "Domain Adaptation for Alzheimer's Disease Diagnostics", *Neuroimage*, vol. 139, pp. 470–479, 2016. DOI : 10.1016/j.neuroimage.2016.05.053

H. Wang, J. wook Suh, J. Pluta, M. Altinay, et P. Yushkevich, "Optimal Weights for Multi-Atlas Label Fusion", *medical imaging*, vol. 22, pp. 73–84, 2011.

H. Wang, j. w. Suh, S. R. Das, J. Pluta, C. Craige, et P. a. Yushkevich, "Multi-Atlas Segmentation with Joint Label Fusion", *IEEE transactions on pattern analysis and machine intelligence*, 2013.

L. Wang, J. P. Miller, M. H. Gado, D. W. McKeel, M. Rothermich, M. I. Miller, J. C. Morris, et J. G. Csernansky, "Abnormalities of hippocampal surface structure in very mild dementia of the Alzheimer type", *NeuroImage*, vol. 30, pp. 52–60, 2006. DOI : 10.1016/j.neuroimage.2005.09.017

S. K. Warfield, K. H. Zou, et W. M. Wells, "Simultaneous truth and performance level estimation (STAPLE) : an algorithm for the validation of image segmentation." *IEEE transactions on medical imaging*, vol. 23, no. 7, pp. 903–21, jul 2004. DOI : 10.1109/TMI.2004.828354. En ligne : http://www.pubmedcentral.nih.gov/articlerender.fcgi?artid=1283110{&}tool=pmcentrez{&}rendertype=abstract

D. Wechsler, *WISC-IV Echelle d'Intelligence de Wechsler pour Enfants et Adolescents*. ECPA, Les Editions du Centre de Psychologie Appliquee, 2005.

J. Weglage, A. Demsky, M. Pietsch, et G. Kurlemann, "Neuropsychological, intellectual, and behavioral findings in patients with centrotemporal spikes with and without seizures", *Developmental medicine and child neurology*, vol. 39, pp. 646–651, 1997.

M. Wilke, R. a. Kowatch, M. P. DelBello, N. P. Mills, et S. K. Holland, "Voxel-based morphometry in adolescents with bipolar disorder : first results." *Psychiatry research*, vol.

131, no. 1, pp. 57–69, may 2004. DOI : 10.1016/j.pscychresns.2004.01.004. En ligne : http://www.ncbi.nlm.nih.gov/pubmed/15246455

E. C. Wirrell et L. D. Hamiwka, "Do children with benign rolandic epilepsy have a higher prevalence of migraine than those with other partial epilepsies or nonepilepsy controls ?" *Epilepsia*, vol. 47, no. 10, pp. 1674–1681, 2006. DOI : 10.1111/j.1528-1167.2006.00639.x

R. Wolz, P. Aljabar, J. V. Hajnal, A. Hammers, et D. Rueckert, "LEAP : learning embeddings for atlas propagation." *NeuroImage*, vol. 49, no. 2, pp. 1316–25, jan 2010. DOI : 10.1016/j.neuroimage.2009.09.069. En ligne : http://www.pubmedcentral.nih.gov/articlerender.fcgi?artid=3068618{&}tool=pmcentrez{&}rendertype=abstract

M. Wu, C. Rosano, P. Lopez-Garcia, C. S. Carter, et H. J. Aizenstein, "Optimum template selection for atlas-based segmentation." *NeuroImage*, vol. 34, no. 4, pp. 1612–8, feb 2007. DOI : 10.1016/j.neuroimage.2006.07.050. En ligne : http://www.ncbi.nlm.nih.gov/pubmed/17188896

B. Wyman, D. Harvey, K. Crawford, M. Bernstein, O. Carmichael, P. Cole, P. Crane, C. Decarli, N. Fox, J. Gunter, D. Hill, R. Killiany, C. Pachai, A. Schwarz, N. Schuff, M. Senjem, J. Suhy, P. Thompson, M. Weiner, et C. Jack, "Standardization of analysis sets for reporting results from adni mri data", *Alzheimer's and Dementia*, vol. 9, no. 3, pp. 332–337, 2013. DOI : 10.1016/j.jalz.2012.06.004

B. T. Wyman, D. J. Harvey, K. Crawford, M. A. Bernstein, O. Carmichael, P. E. Cole, P. K. Crane, C. DeCarli, N. C. Fox, J. L. Gunter *et al.*, "Standardization of analysis sets for reporting results from adni mri data", *Alzheimer's Dementia*, vol. 9, no. 3, pp. 332–337, 2013.

J. Xie, E. Fletcher, B. Singh, et O. Carmichael, "Robust measurement of individual localized changes to the aging hippocampus." *Computer vision and image understanding : CVIU*, vol. 117, no. 9, pp. 1128–1137, sep 2013. DOI : 10.1016/j.cviu.2012.12.007. En ligne : http://www.pubmedcentral.nih.gov/articlerender.fcgi?artid=4130487{&}tool=pmcentrez{&}rendertype=abstract

J. Xu, L. Xiang, Q. Liu, H. Gilmore, J. Wu, J. Tang, et A. Madabhushi, "Stacked sparse autoencoder (ssae) for nuclei detection on breast cancer histopathology images", *IEEE Transactions on Medical Imaging*, vol. 35, no. 1, pp. 119–130, Jan 2016. DOI : 10.1109/TMI.2015.2458702

J. Yang et J. S. Duncan, “3D image segmentation of deformable objects with joint shape-intensity prior models using level sets”, *Medical image analysis*, vol. 8, no. 3, pp. 285–294, 2004. DOI : 10.1016/j.media.2004.06.008.3D

W. Zhang, R. Li, H. Deng, L. Wang, W. Lin, S. Ji, et D. Shen, “Deep convolutional neural networks for multi-modality isointense infant brain image segmentation”, *NeuroImage*, vol. 108, pp. 214 – 224, 2015. DOI : http://dx.doi.org/10.1016/j.neuroimage.2014.12.061. En ligne : http://www.sciencedirect.com/science/article/pii/S1053811914010660

G. Zhao, X. Wang, Y. Niu, L. Tan, , et S.-X. Zhang, “Segmenting brain tissues from chinese visible human dataset by deep-learned features with stacked autoencoder”, *BioMed Research International*, vol. 2016, pp. 1–12, 2016.

Z. Zhao, S. R. Aylward, et E. K. Teoh, “A novel 3D partitioned active shape model for segmentation of brain MR images.” *Medical image computing and computer-assisted intervention : MICCAI ... International Conference on Medical Image Computing and Computer-Assisted Intervention*, vol. 8, no. Pt 1, pp. 221–8, jan 2005. En ligne : http://www.ncbi.nlm.nih.gov/pubmed/16685849

D. Zikic, B. Glocker, et a. Criminisi, “Encoding atlases by randomized classification forests for efficient multi-atlas label propagation”, *Medical Image Analysis*, vol. 18, no. 8, pp. 1262–1273, 2014. DOI : 10.1016/j.media.2014.06.010. En ligne : http://dx.doi.org/10.1016/j.media.2014.06.010

ANNEXE A ARTICLE 4 : SUB-CORTICAL BRAIN STRUCTURE SEGMENTATION USING F-CNN'S

*Mahsa Shakeri[2,4], *Stavros Tsogkas[1], Enzo Ferrante[1], Sarah Lippe[3,4], Samuel Kadoury[2,4], Nikos Paragios[1], Iasonas Kokkinos[1]

[1]CVN, CentraleSupelec, Inria, Universite Paris-Saclay, [2] Polytechnique Montreal, [3] University of Montreal, [4] Sainte-Justine Hospital Research Center

Presentation

This appendix presents the article "Sub-cortical brain structure segmentation using F-CNN's" (Shakeri et al., 2016b) published in 13th IEEE International Symposium on Biomedical Imaging, ISBI 2016, held in Prague, Czech Republic, in April 2016. The objective of this article is to present an automatic sub-cortical segmentation algorithm using Fully Convolutional Neural Networks and Markov Random Field (MRF).

abstract

In this paper we propose a deep learning approach for segmenting sub-cortical structures of the human brain in Magnetic Resonance (MR) image data. We draw inspiration from a state-of-the-art Fully-Convolutional Neural Network (F-CNN) architecture for semantic segmentation of objects in natural images, and adapt it to our task. Unlike previous CNN-based methods that operate on image patches, our model is applied on a full blown 2D image, without any alignment or registration steps at testing time. We further improve segmentation results by interpreting the CNN output as potentials of a Markov Random Field (MRF), whose topology corresponds to a volumetric grid. Alpha-expansion is used to perform approximate inference imposing spatial volumetric homogeneity to the CNN priors. We compare the performance of the proposed pipeline with a similar system using Random Forest-based priors, as well as state-of-art segmentation algorithms, and show promising results on two different brain MRI datasets.

keywords Convolutional neural networks, semantic segmentation, Markov Random Fields, sub-cortical structures, Magnetic Resonance Imaging

A.1 Introduction

Image segmentation is a fundamental process in several medical applications. Diagnosis, treatment, planning and monitoring, as well as pathology characterization, benefit from accurate

segmentation. In this paper we are interested in brain sub-cortical structures located at the frontostriatal system. Previous studies have shown the involvement of the frontostriatal structures in different neurodegenerative and neuropsychiatric disorders, including schizophrenia, Alzheimer's disease, attention deficit, and subtypes of epilepsy (Chudasama and Robbins, 2006). Segmenting these parts of the brain enables a physician to extract various volumetric and morphological indicators, facilitating the quantitative analysis and characterization of several neurological diseases and their evolution.

In the past few years, deep learning techniques, and particularly Convolutional Neural Networks (CNNs), have rapidly become the tool of choice for tackling challenging computer vision tasks. CNNs were popularized by Lecun, after delivering state-of-art results on handwritten digit recognition (LeCun et al., 1998). However, they fell out of favor in the following years, mostly due to hardware and training data limitations. Nowadays, the availability of large-scale datasets (e.g. ImageNet), powerful GPUs and appropriate software libraries, have rekindled the interest in deep learning and have made it possible to harness their power. Krizhevsky et al. (Krizhevsky et al., 2012b) published results demonstrating clear superiority of deep architectures over hand-crafted features or shallow networks, for the task of image classification. Since then, CNNs have helped set new performance records for many other tasks; object detection, texture recognition and object semantic segmentation just to name a few.

Our work is similar in spirit to (Prasoon et al., 2013), but with some notable differences. In (Prasoon et al., 2013) the authors train one CNN for each of the three orthogonal views of MRI scans, for knee cartilage segmentation, with the loss being computed on the concatenated outputs of the three networks. The inputs to each CNN are 28×28 image patches and the output is a softmax probability of the central pixel belonging to the tibial articular cartilage. In contrast, our method operates on full 2D image slices, exploiting context information to accurately segment regions of interest in the brain. In addition, we use *fully convolutional* CNNs (Long et al., 2015) to construct dense segmentation maps for the whole image, instead of classifying individual patches. Furthermore, our method handles multiple class labels instead of delivering a foreground-background segmentation, and it does that efficiently, performing a single forward pass in $5ms$.

CNNs are characterized by large receptive fields that allow us to exploit context information across the spatial plane. Processing 2D slices individually, however, means that we remain agnostic to *3D context* which is important, since we are dealing with volumetric data. The obvious approach of operating directly on the 3D volume instead of 2D slices, would drastically reduce the amount of data available for training, making our system prone to overfitting,

while increasing its computational requirements. Alternatively, we construct a Markov Random Field on top of the CNN output in order to impose volumetric homogeneity to the final results. The CNN scores are considered as unary potentials of a multi-label energy minimization problem, where spatial homogeneity is propagated through the pair-wise relations of a 6-neighborhood grid. For inference we choose the popular alpha-expansion technique that leads to guaranteed optimality bounds for the type of energies we define (Boykov et al., 2001).

A.2 Using CNNs for Semantic Segmentation

Our network is inspired by the Deeplab architecture that was recently proposed for semantic segmentation of objects (Chen et al., 2014). Due to limited space, we refer the reader to (Chen et al., 2014) for details. One obvious and straightforward choice for adapting the Deeplab network to our task, would be to simply fine-tune the last three convolutional layers that replace their fully connected counterparts in the VGG-16 network, while initializing the rest of the weights to the VGG-16 values. This is a common approach when adapting an already existing architecture to a new task, but given the very different nature of natural RGB images and MR image data (RGB vs. grayscale, varying vs. black background), we decided to train a fully convolutional network from scratch.

Training a deep network from scratch presents us with some challenges. Medical image datasets tend to be smaller than natural image datasets, and segmentation annotations are generally hard to obtain. In our case, we only have a few 3D scans at our disposal, which increases the risk of overfitting. In addition, the repeated pooling and sub-sampling steps that are applied in the input images as it flows through a CNN network, decrease the output resolution, making it difficult to detect and segment finer structures in the human brain. To address these challenges, we make a series of design choices for our network : first, we opt for a shallower network, composed of five pairs of convolutional/max pooling layers. We sub-sample the input only for the first two max-pooling layers, and keep a stride of 1 for the remaining layers, introducing holes, as in (Chen et al., 2014). This allows us to keep increasing the effective receptive field of filters, without further reducing the resolution of the output response maps. For a 256×256 input image, the total sub-sampling factor of the network is 4, resulting in a $64 \times 64 \times L$ array, where L is the number of class labels. A $1-$pixel stride is used for all convolutional layers and 0.5 activation probability for all dropout layers. The complete list of layers and important parameters is given in Table A.1. At test time, a 2D image is fed to the network and the output is a three-dimensional array of probability maps (one for each class), obtained via a softmax operation. To obtain a brain segmentation at this stage, we simply resize the output to the input image dimensions using bilinear interpolation

and assign at each pixel the label with the highest probability. However, we still need to impose volumetric homogeneity to the solution. We propose to do it using Markov Random Fields.

A.2.1 Multi-label segmentation using CNN-based priors

For every slice of a 3D image, the output of the proposed CNN is a softmax map that indicates the probability of every pixel to be part of a given brain structure $l \in \mathcal{L}$ (label). We consider the volume $P_i^{\text{CNN}}(l) : \mathcal{L} \rightarrow [0, 1]$ formed by the stacked CNN output slices, as a prior of the brain 3D structures, where i indicated a voxel from the original image.

Let $\mathcal{G} = \langle \mathcal{V}, \mathcal{E} \rangle$ be a graph representing a Markov Random Field, where nodes in $\mathcal{V}$ are variables (voxels) and $\mathcal{E}$ is a standard 6-neighborhood system defining a 3D grid. Variables $i \in \mathcal{V}$ can take labels l_i from a labelspace $\mathcal{L}$. A labeling $\mathcal{S} = \{l_i \mid i \in \mathcal{V}\}$ assigns one label to every variable. We define the energy $E(\mathcal{S})$ which consists of unary potentials V_i and pair-wise potentials V_{ij} such that it is minimum when $\mathcal{S}$ corresponds to the best possible labeling.

Unary terms are defined as $V_i(l_i) = -\log(P_i^{\text{CNN}}(l_i))$, and they assign low energy to high probability values. Pair-wise terms encode the spatial homogeneity constraint by simply encouraging neighbor variables to take the same semantic label. In order to align the segmentation boundaries with intensity edges, we made this term inversely proportional to the difference of the intensity I_i and I_j associated to the given voxels. The pair-wise formulation is $V_{i,j}(l_i, l_j) = w_{ij}.[l_i \neq \ l_j]$ where $w_{ij} = \exp\left(-\frac{|(I_i - I_j)|^2}{2\sigma^2}\right)$. Finally, the energy minimization problem is defined as :

$$\mathcal{S}^* = \operatorname{argmin} E(\mathcal{S}) = \operatorname{argmin} \sum_{i \in \mathcal{V}} V_i(l_i) + \lambda \sum_{(i,j) \in \mathcal{E}} V_{i,j}(l_i, l_j). \tag{A.1}$$

$\mathcal{S}^*$ represents the optimal label assignment. Note that this energy is a metric in the space of labels $\mathcal{L}$; thus, it is guaranteed that using alpha-expansion technique we can find a solution $\hat{\mathcal{S}}$ whose energy lies within a factor of 2 with respect to the optimal energy (i.e. $E(\hat{\mathcal{S}}) \leq 2.E(\mathcal{S}^*)$). Alpha-expansion is a well known move-making technique to perform approximate inference using graph cuts, that has shown to be accurate in a broad range of vision problems. We refer the reader to (Boykov et al., 2001) for a complete discussion on energy minimization using alpha-expansion.

Table A.1 Layers used in our architecture. All convolutional layers have a stride of one pixel ; a hole stride of "1" means that we introduce no holes.

Block	conv kernel	# filters	hole stride	pool kernel	pool stride	dropout
1	7×7	64	1	3×3	2	no
2	5×5	128	1	3×3	2	no
3	3×3	256	2	3×3	1	yes
4	3×3	512	2	3×3	1	yes
5	3×3	512	2	3×3	1	yes
6	4×4	1024	4	no pooling		yes
7	1×1	39	1	no pooling		no

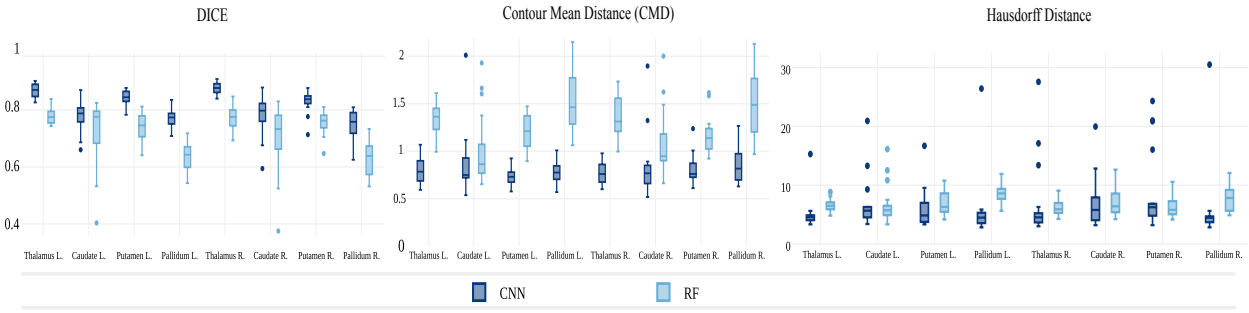

Figure A.1 Average Dice coefficient, Hausdorff distance, and contour mean distance on eight subcortical structures of IBSR dataset. The proposed CNN-based method outperforms the RF-based approach (better viewed in color and magnified).

A.3 Experiments and Discussion

We used the proposed method to segment a group of sub-cortical structures located at the frontostriatal network, including thalamus, caudate, putamen and pallidum. We evaluated our approach on two brain MRI datasets.

The first one is a publicly available dataset provided by the Internet Brain Segmentation Repository (IBSR) (Rohlfing, 2012a). It contains 18 labeled 3D T1-weighted MR scans with slice thickness of around 1.3 mm. In this work we use the subset of 8 primarily subcortical labels, including left and right thalamus, caudate, putamen, and pallidum. The second dataset is obtained from a Rolandic Epilepsy (RE) study, including 17 children with epilepsy and 18 matched healthy individuals. For each participant, T1-weighted magnetic resonance images (MRI) were acquired with a 3 T scanner (Philips Acheiva) with an in-plane resolution of 256×256 and slice thickness of 1 mm. The left and right putamen structures were manually

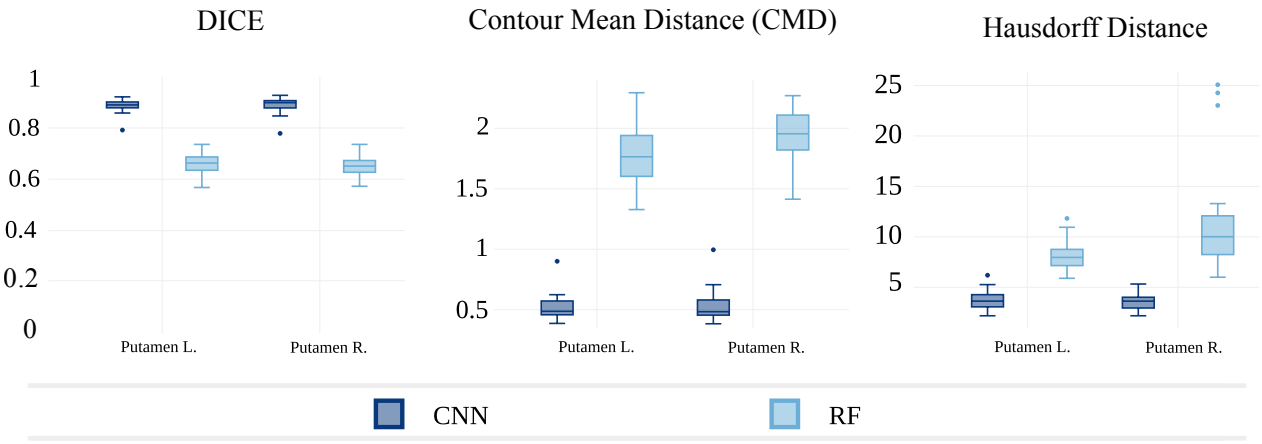

Figure A.2 The average Dice coefficient, Hausdorff distance, and contour mean distance on left and right putamen structure of RE dataset. The proposed CNN-based method generates more accurate segmentation results compared to the RF-based approach (better viewed in color and magnified).

annotated by an experienced user. For both datasets, we process volumes slice by slice, after resizing them to 256×256 pixels. We treat these 2D slices as individual grayscale images to train our CNN.

In the first experiment, we compare the performance of our segmentation method using CNN priors, with an approach based on Random Forest priors, where the same MRF refinement is applied. The RF-based per-voxel likelihoods are computed in the same way as (Alchatzidis et al., 2014). Then, the RF probability maps are considered as the unary potentials of a Markov Random Field and alpha-expansion is used to compute the most likely label for each voxel, as explained in Section A.2.1. Figure A.1 and Figure A.2 show the average Dice coefficient, Hausdorff distance, and contour mean distance between output segmentations and the ground truth for different structures. These results show that the CNN-based approach achieves higher Dice compared to RF-based method, while producing lower Hausdorff and contour mean distance.

In the second experiment, we compare the accuracy of our proposed method with two publicly available state-of-the-art automatic segmentation toolboxes, Freesurfer (Fischl et al., 2002), and FSL-FIRST (Patenaude et al., 2011a). In Table A.2, we report the average Dice coefficient for the left and right structures; these results show that our method provides better segmentations compared to the state-of-the-art for three sub-cortical structures in both IBSR and RE dataset. However, Freesurfer results in better segmentation for caudate in the IBSR dataset which could be attributed to the limitation of CNN in capturing thin tail areas

of the caudate structures. In Figure A.3 we show qualitative results.

A.3.1 CNN Training and Evaluation Details

The input to our network is a single 2D slice from a 3D MRI scan, along with the corresponding label map. We apply data augmentation to avoid overfitting : we use horizontally flipped and translated versions of the input images by 5, 10, 15, 20 pixels, across the x/y axes. Other transformations, such as rotation, could be considered as well. The MR image data are centered and the background always takes zero values, so we do not perform mean image subtraction as is usually the case.

In the case of IBSR, we split the available data into three sets. Each time, we use two of the sets as training data (approximately $100K$ training samples) and the third set as test data. One of the training data volumes is left out and used as validation data. Similarly, we split RE into two subsets of equal size, using one for training and one for testing, each time. We train on both datasets for 35 epochs starting with a learning rate of 0.01 and dropping it at a logarithmic rate until 0.0001. For training, we use standard SGD with a momentum of 0.9 and a softmax loss. For all our experiments we used MATLAB and the deep learning library MatConvNet (Vedaldi and Lenc, 2014). Code, computed probability maps, and more results can be found at `https://github.com/tsogkas/brainseg`.

We also experimented with CNNs trained on 2D slices from the other two views (sagittal and coronal) but the resulting models performed poorly. The problem is rooted in the inherent symmetry of some brain structures and the fact that the CNN is evaluated on individual slices, ignoring 3D structure. For instance, when processing slices across sagittal view, the right and left putamen appear at roughly the same positions in the image. They are also very similar in terms of shape and appearance, which fools the system into assigning the same label to both regions. This simple example demonstrates the need for richer priors that take into account the full volume structure to assign class labels.

A.4 Conclusion

In this paper, we proposed a deep learning framework for segmenting frontostriatal subcortical structures in MR images of the human brain. We trained a fully convolutional neural network for segmentation of 2D slices and treated the output probability maps as a proxy for the respective voxel likelihoods. We further improved segmentation results by using the CNN outputs as potentials of a Markov Random Field (MRF) to impose spatial volumetric homogeneity. Our experiments show that the proposed method outperforms approaches based

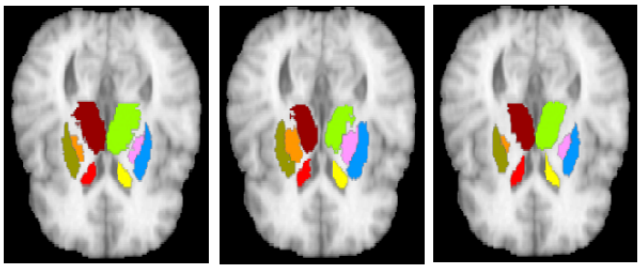

Figure A.3 2D slice segmentation (IBSR). **Left :** Groundtruth. **Middle :** RF-based results. **Right :** CNN-based results.

on other learned priors, as well as state-of-the-art segmentation methods. However, we also note some limitations : the current model is not able to accurately capture thin tail areas of the caudate structures. Second, symmetric structures confound the CNN training process when considering views which are parallel to the plane of symmetry. Third, graph-based methods have to be used to impose volumetric consistency since training is done on 2D slices. Different network layouts, taking account of volumetric structure can possibly help overcome these limitations.

Table A.2 The average Dice coefficient of the three methods on different brain structures. Values are reported as the average of the left and right structures.

	Proposed	Freesurfer	FSL
IBSR-Thalamus	**0.87**	0.86	0.85
IBSR-Caudate	0.78	**0.82**	0.68
IBSR-Putamen	**0.83**	0.81	0.81
IBSR-Pallidum	**0.75**	0.71	0.73
RE-Putamen	**0.89**	0.74	0.88

ANNEXE B ARTICLE 5 : GROUPWISE SHAPE ANALYSIS OF THE HIPPOCAMPUS USING SPECTRAL MATCHING

Mahsa Shakeri[a,b], Hervé Lombaert[c], Sarah Lippe[b,d], Samuel Kadoury[a,b]

[a] MEDICAL, Polytechnique Montreal, [b] CHU Sainte-Justine Hospital Research Center,
[c]Centre for Intelligent Machines, McGill University, [d] University of Montreal

Presentation

This appendix presents the article "Groupwise shape analysis of the hippocampus using spectral matching" (Shakeri et al., 2014) published in Biomedical Optics and Imaging Proceedings of SPIE 2014, held in San Diego, California, in February 2014. The objective of this article is to present a spectral-based group-wise shape analysis to detect morphological changes in sub-cortical structures.

abstract

The hippocampus is a prominent subcortical feature of interest in many neuroscience studies. Its subtle morphological changes often predicate illnesses, including Alzheimer's, schizophrenia or epilepsy. The precise location of structural differences requires a reliable correspondence between shapes across a population. In this paper, we propose an automated method for groupwise hippocampal shape analysis based on a spectral decomposition of a group of shapes to solve the correspondence problem between sets of meshes. The framework generates diffeomorphic correspondence maps across a population, which enables us to create a mean shape. Morphological changes are then located between two groups of subjects. The performance of the proposed method was evaluated on a dataset of 42 hippocampus shapes and compared with a state-of-the-art structural shape analysis approach, using spherical harmonics. Difference maps between mean shapes of two test groups demonstrates that the two approaches showed results with insignificant differences, while Gaussian curvature measures calculated between matched vertices showed a better fit and reduced variability with spectral matching.

Keywords : hippocampus, groupwise shape analysis, correspondence, spectral matching

B.1 Introduction

The hippocampus is the main target of deformation in many neurodegenerative diseases (Andersen et al., 2009). Extracting its morphological characteristics is an important and

challenging problem in medical image analysis. Early morphological studies on the hippocampus were based on volumetric analysis, which had the advantage of simplicity (Hastings et al., 2004; Shi et al., 2009). However, structural changes at specific locations were not accurately detected using volumetric frameworks. Thus, hippocampal shape analysis has emerged as a way of evaluating morphology location and magnitude in the brain anatomy.

Several works have proposed hippocampal shape analysis via deformable registration to a template, where population-wise comparisons are performed by analyzing the individual deformable transformations (Csernansky et al., 1998, 2002). Another type of shape analysis method is based on medial surface descriptions, which allows for the quantification of local positional changes by assessing morphological variation of the skeleton extracted from a given object (Bouix et al., 2005; Joshi et al., 2002). Besides these, some methods use spherical harmonics description combined with Point Distribution Models (PDM) to discover structural differences across a population (Shen et al., 2003; Styner et al., 2006a). However, these surface-based frameworks depend on establishing vertex correspondence across subjects, which are prone to inter-subject variability and are more adapted to sphere-like shapes.

SPHARM-PDM is a popular groupwise shape analysis method based on spherical harmonic combined with point distribution models. This method solves the correspondence problem by the alignment of the spherical parametrization using a first order ellipsoid (Styner et al., 2006a). In this method the spherical description of surface meshes is sampled into triangulated surfaces via icosahedron subdivision. These surfaces are then spatially aligned using rigid Procrustes alignment. However, as this method establishes correspondence on simplified spherical models of surfaces, it is restricted to surfaces with spherical topology and is computationally expensive. In this work we propose an alternative groupwise hippocampal shape analysis approach based on spectral matching in which the correspondence maps are computed using a new surface matching approach presented in (Lombaert et al., 2013b). In spectral matching relationships are modeled as graphs and an eigendecomposition of these graphs enables us to match similar features. The objective of this work is to investigate whether a shape analysis method based on spectral matching could produce similar shape geometries on hippocampus and identify groupwise differences to SPHARM-PDM method.

B.2 Method

The inputs to the proposed method include two groups of hippocampus meshes. Our framework establishes correspondences across surface points for each group using spectral matching and creates two mean shapes as outputs. The workflow for the procedure is illustrated in Figure B.1

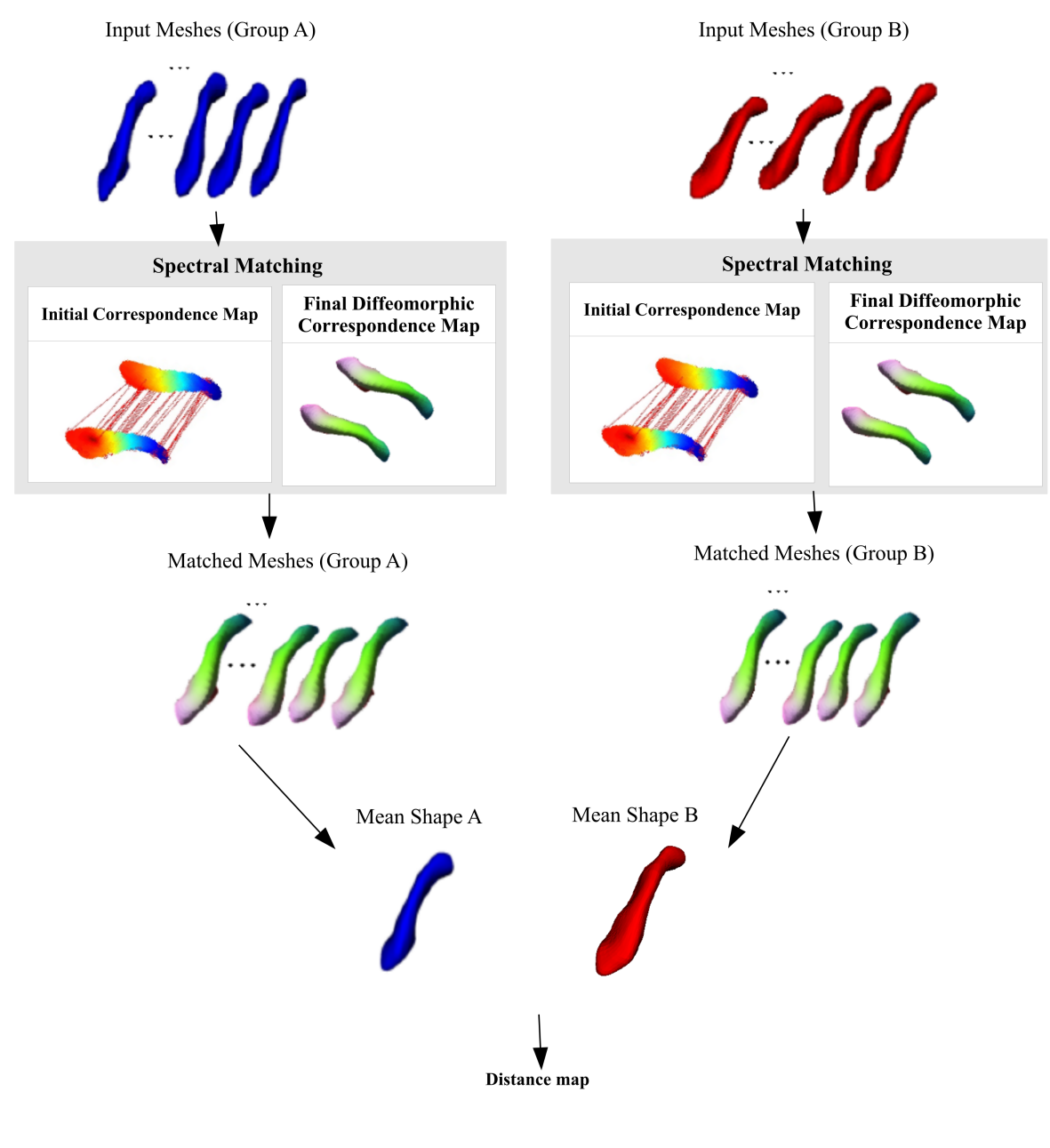

Figure B.1 Hippocampal shape analysis between two groups of subjects (group A and B) using spectral matching. At first, an initial reference image is selected randomly in each group ($A^{(0)}$ and $B^{(0)}$ in top row). Then, all vertices of all meshes are mapped to the reference image using the spectral matching algorithm (second and third rows). Finally, the mean surface of each group is created (bottom row).

In the proposed method, an initial reference is randomly selected and all vertices of all other surfaces are matched to the reference image. A spectral matching approach presented in (Lombaert et al., 2013b) is used to find the correspondence between each mesh and the selected reference image. This approach is able to provide a diffeomorphic correspondence map between two surfaces. Before applying this method, a preliminary correspondence map has to be generated between two meshes. We used a conventional spectral matching method presented in (Lombaert et al., 2013a) to compute this initial correspondence map. In Section B.2.1, the spectral method for matching two surface meshes is briefly described. Section B.2.2 presents the groupwise hipppocampal shape analysis approach, in which the vertex correspondence between meshes is established using the spectral matching method described in Section B.2.1.

B.2.1 Matching two surfaces using spectral matching

Given two surface meshes $S^{(1)}$ and $S^{(2)}$, the matching between these two shapes is conducted in a two-step process (Figure B.2.a and b). At first, we build the graph $g^{(i)} = \left\{V^{(i)}, E^{(i))}\right\}$ from the set of vertices and edges of each surface $S^{(i)}$. Then, the weighted adjacency matrix $W^{(i)}$ is defined in terms of node affinities. The diagonal node degree matrix $D^{(i)}$ is determined as the sum of all point affinities. The general Laplacian operator on a graph $g^{(i)}$ is formulated with $L^{(i)} = G^{-1}\left(D^{(i)} - W^{(i)}\right)$ where G is a diagonal node weighting matrix ($G = D^{(i)}$). The eigendecomposition of each graph's Laplacian matrix $L^{(i)}$ reveals its spectral components. After reordering the spectral components by finding the optimal permutation of components between the pair of meshes, regularization is performed by matching the spectral embeddings. The correspondence map c between each pair of vertices on $S^{(1)}$ and $S^{(2)}$ is established with a simple nearest-neighbor search between spectral representation of and . An overview of the procedure of finding the correspondence map c is shown in Figure B.2.a.

In the next step, the final map (diffeomorphic match) between two surfaces $S^{(1)}$ and $S^{(2)}$ is obtained as shown in Figure B.2.b. In this procedure, an association graph $g_a = \{V_{1,2}, E_{1,2,c}\}$ is defined as the union of the set of vertices and edges of two surfaces $S^{(1)}$ and $S^{(2)}$ with an initial set of correspondence links c between both surfaces. The spectral decomposition of this unique association graph creates a shared set of eigenvectors that enables a direct mapping $\varphi_{1\to 2}$ between two meshes (see (Lombaert et al., 2013b) for more details).

B.2.2 Morphological Analysis

Let $\{S^i\}_{i=0,\ldots,n}$ be a set of $n+1$ surface meshes. We would like to compute the mean shape $\bar{S}$ as the geometric mean of all surface meshes in the set. For that purpose, at first an

initial reference mesh $S^{(0)}$ is selected randomly. Then, all vertices of all meshes $S^{(i)}$ are matched to the reference mesh $S^{(0)}$, using the spectral mapping $\{\varphi_{i\to 0}\}_{i=0,\ldots,n}$ described in Section B.2.1. In the next step, the mean surface $\bar{S}$ is defined by averaging the 3D coordinates of corresponding surface points across the group. The position of point on mean surface $\bar{x_j}$ is defined as follows :

$$\bar{x_j} = \frac{1}{n+1}\sum_{i=1}^{n} x'^{(i)}_j \tag{B.1}$$

Where $x'^{(i)}_j$ is the interpolated position of point i on surface $S^{(i)}$ computed using the mapping $\varphi_{i\to 0}$.

By applying the proposed approach to two groups of surface meshes (A and B) and obtaining a mean shape for both groups (Figure B.1), the local shape differences between groups can be detected by computing a difference map between two mean shapes after registering them together.

B.3 Results

To evaluate the performance of the proposed spectral matching method, we used a dataset of 42 hippocampus shapes obtained from schizophrenic patients (Styner et al., 2004). The hippocampi were segmented from IR-Prepped SPGR (Inversion Recovery-Prepared Spoiled Gradient Echo) data segmented originally at $0.9375x0.9375x1.5mm$ resolution as part of an adult schizophrenia study (mean age 32, all male gender). All cases have been fully randomized and group association has been performed to create two different groups (group A and group B) with 21 subjects (42 subjects in total). We compared the performance of the spectral matching approach with a state-of-the-art method used for groupwise analysis of anatomical shapes, namely SPHARM-PDM (Styner et al., 2006a).

We generated mean shapes, for both groups of subjects, using our spectral groupwise framework and SPHARM-PDM. The distance maps between the mean shapes produced by both methods are illustrated in Figure B.3. Dice volume difference measures, Hausdorff distance, and average absolute distance between the mean shapes of group A and B are listed in Table B.1. These results suggest that the proposed spectral framework produces similar groupwise shape differences as SPHARM-PDM.

Figure B.4 presents the comparison between mean shapes computed using spectral matching and SPHARM-PDM. The Dice coefficient, Hausdorff distance, and average absolute distance

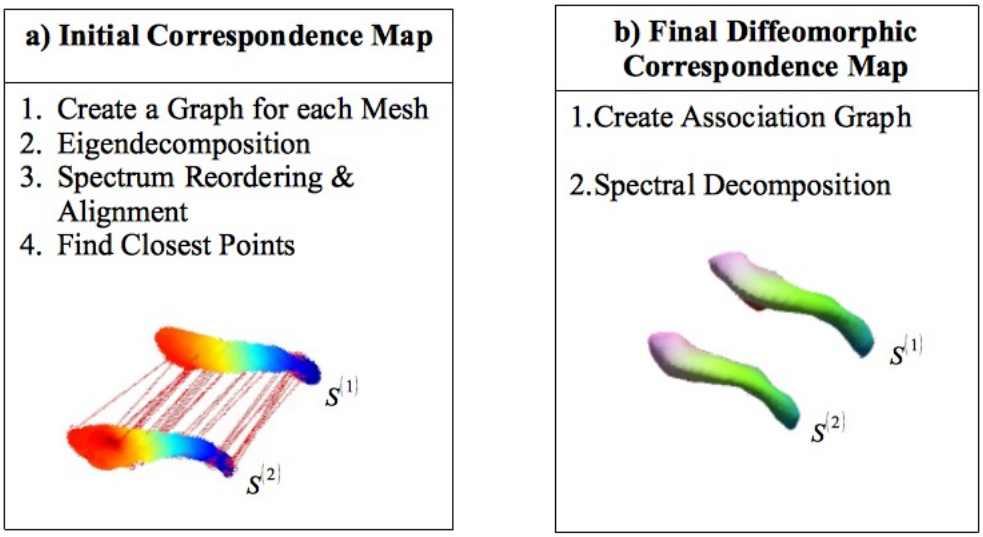

Figure B.2 (a) Initial matching of two meshes using the algorithm proposed in Lombaert et al. (2013a). (b) Final correspondence mapping between two surfaces based on diffeomorphic spectral matching approach in (Lombaert et al., 2013b).

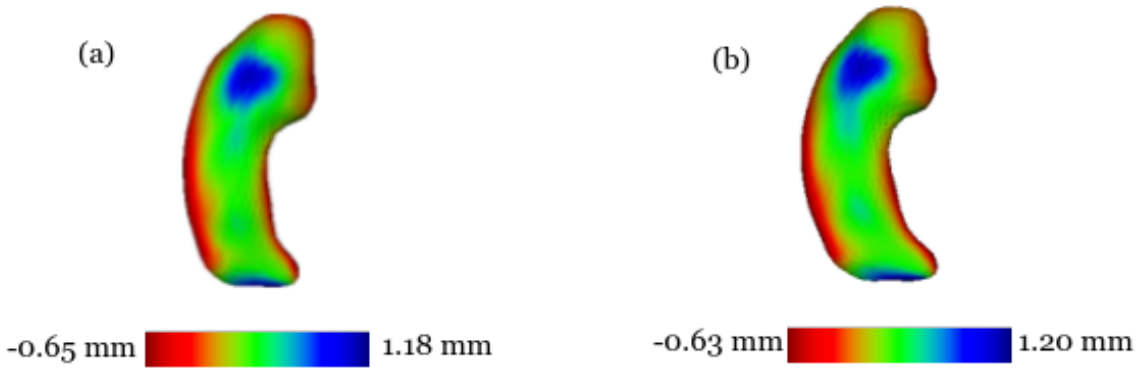

Figure B.3 (a) Distance map between group A and B using SPHARM-PDM. (b) Distance map between group A and B with spectral matching. The proposed framework based on spectral matching yield similar results as the state-of-the-art method.

Table B.1 Shape differences between mean shape A and mean shape B.

	Spectral Matching	**SPHARM-PDM**
Dice Coefficient	0.92	0.92
Hausdorff Distance (mm)	1.20	1.18
Mean Absolute Distance (mm)	0.03 ± 0.39	0.03 ± 0.38

are reported in Table B.2. This shows that our method yields similar accuracy than the method based on spherical harmonics .

In order to assess the variability in curvature between matched vertices in spectral matching and in SPHARM-PDM, the gaussian curvature was computed at each vertex of all meshes in the dataset. We computed the minimum, maximum, mean, and the standard deviation across all correspondent vertices, and obtained the average metrics for vertices (Table B.3). These show that the measures are similar between both approaches. More importantly, the spectral matching approach shows a lower standard deviation compared to SPHARM-PDM, indicated lesser variability in the curvature measure for matched vertices.

In the final experiment, the Euclidean distance was computed between all correspondent vertices using both spectral matching and SPHARM-PDM. The minimum, maximum, mean, and the standard deviation across all matched vertices are reported in Table B.4. These results show that the distances between matched vertices are similar in both methods.

B.4 Discussion

In this work, a new approach for groupwise hippocampal shape analysis is proposed in order to detect regional alterations of hippocampal morphology in neurological conditions such as schizophrenia and epilepsy. The proposed scheme finds diffeomorphic correspondences among a population of surfaces in the spectral domain. This enables us to create a mean shape and locate the morphological changes between two groups of healthy and pathological subjects.

In this paper the performance of the proposed approach was compared with a state-of-the-art method, namely SPHARM-PDM (Styner et al., 2006a). Looking at the distance maps between mean shapes created using spectral matching and SPHARM-PDM methods, we find that both methods yield differences which are statistically insignificant. In addition to distance maps, the accuracy of the obtained mean shapes using spectral matching was evaluated using the Dice volume difference measure. According to the reported Dice coefficient, there is almost a perfect overlap between the mean shapes computed using spectral matching and SPHARM-PDM.

Table B.2 Shape differences obtained with spectral matching and SPHARM-PDM.

	Spectral Matching	**SPHARM-PDM**
Dice Coefficient	0.99	0.98
Hausdorff Distance (mm)	0.29	0.36
Mean Absolute Distance (mm)	0.0028 ± 0.0459	0.0031 ± 0.0636

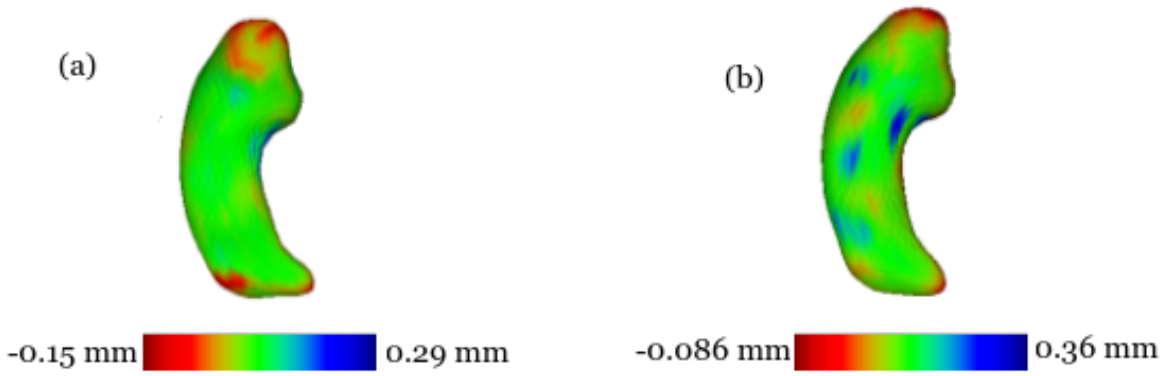

Figure B.4 (a) Difference map for mean shape A. (b) Difference map for mean shape B. There is a small difference between mean shapes computed using spectral matching and SPHARM-PDM.

Table B.3 Curvature measures computed with spectral matching and SPHARM-PDM

	Group A		Group B	
	Spectral Matching	**SPHARM-PDM**	**Spectral Matching**	**SPHARM-PDM**
Max curvature	5.34×10^{-4}	5.46×10^{-4}	5.47×10^{-4}	5.5×10^{-4}
Min curvature	2.9×10^{-4}	2.89×10^{-4}	2.51×10^{-4}	2.42×10^{-4}
Mean curvature	4.14×10^{-4}	4.16×10^{-4}	3.90×10^{-4}	3.95×10^{-5}
Std curvature	6.54×10^{-5}	6.89×10^{-5}	7.55×10^{-5}	8.05×10^{-5}

Table B.4 Distance measures obtained with spectral matching and SPHARM-PDM

	Group A		Group B	
	Spectral Matching	**SPHARM-PDM**	**Spectral Matching**	**SPHARM-PDM**
Max distance (mm)	2.61	2.53	3.24	2.91
Min distance (mm)	0.43	0.43	0.57	0.62
Mean distance (mm)	1.36	1.37	1.58	1.61
Std distance (mm)	0.57	0.56	0.66	0.62

In order to indicate the variability of correspondent vertices, we computed curvature measures at each vertex of all meshes in the dataset. Comparing curvature measures obtained from both spectral matching and SPHARM-PDM method, shows that the matched vertices have close variability in both methods. However, the average standard deviation of curvature measure for spectral method is lower compared to SPHARM-PDM, which indicates the reduced variability and better fit of matched vertices in spectral method.

In order to achieve higher accuracy in surface matching, additional information (e.g., texture, anatomical information, or landmark positions) can be incorporated in extended spectral representation. These additional information which can be embedded as weights in graph nodes and as extra coordinates lead to little computational expenses in the mapping part of our framework. Further improvements of the method lies in enhancing the quality of input meshes. The number of vertices, the quality of triangulation, and the smoothing level of the meshes are the effective factors that play an important role in the accuracy of the result. The more accurate the input surface meshes are, the more valid the result of hippocampal shape analysis would be. Therefore, further work seek to incorporate additional features to help improve the matching, and to propose a strategy to provide proper input surfaces.

B.5 Conclusions

In this paper, a new approach for groupwise hippocampal shape analysis based on spectral matching is described. Our proposed scheme finds diffeomorphic correspondences among a population of surfaces in the spectral domain which could be an alternative to the current hippocampal morphometry analysis methods. The performance of the proposed approach was compared with the SPHARM-PDM method (Styner et al., 2006a). According to the experiments, the two methods showed results with insignificant differences. In order to improve the accuracy of our groupwise hippocampal shape analysis approach, we need to incorporate additional information in spectral matching, as well as enhancing the quality of input meshes.

ANNEXE C ARTICLE 6 : CLASSIFICATION OF ALZHEIMER'S DISEASE USING DISCRIMINANT MANIFOLDS OF HIPPOCAMPUS SHAPES

Mahsa Shakeri[1,2], Hervé Lombaert[3], Samuel Kadoury[1,2]

[1] MEDICAL, Polytechnique Montreal, Montréal, Québec, Canada,[2] CHU Sainte-Justine Hospital Research Center, [3]Inria Sophia-Antipolis Méditerranée, Asclepios Team, Sophia-Antipolis, France,

Presentation

This appendix presents the article "Classification of Alzheimer's Disease using Discriminant Manifolds of Hippocampus Shapes" (Shakeri et al., 2015) published in Proceedings of the First International Machine Learning Meets Medical Imaging Workshop (MLMMI), Held in Conjunction with ICML 2015, Lille, France, July 11, 2015. The objective of this article is to describe the morphometric variations of the hippocampus in a discriminant nonlinear graph embedding with Grassmannian manifolds to detect the presence of Alzheimer's disease.

abstract

Neurodegenerative pathologies, such as Alzheimer's disease, are linked with morphological alterations of subcortical structures which can be assessed from medical imaging and biological data. Recent advances in machine learning have helped to improve classification and prognosis rates. We present here a classification framework for Alzheimer's disease which extracts triangulated surface meshes from segmented binary maps in MRI, and establishes reliable point-to-point correspondences among a population of hippocampus 3D surfaces using their spectral representation. Morphological changes between groups are detected using a manifold learning algorithm based on Grassmannian kernels in order to assess similarity between shape topology in control normals and patients. A second manifold using discriminant embeddings is then generated to maximize the class separability between three clinical groups recognized in dementia. We test the method to classify 47 subjects with Alzheimer's Disease (AD), 47 with mild cognitive impairment (MCI) and 47 healthy controls enrolled in a clinical study. Classification rates compare favorably to standard classification methods based on SVM and traditional manifold learning methods evaluated on the same database.

C.1 Introduction

Alzheimer's disease (AD) is the most common form of dementia, with an incidence that doubles every five years after the age of 65 (Bain et al., 2008). As life expectancy increases,

the number of AD patients increases accordingly, which causes a heavy socioeconomic burden. It is expected that treatment decisions will greatly benefit from diagnostic and prognostic tools that identify individuals likely to progress to dementia sooner. This is especially important in individuals with mild cognitive impairment (MCI), who present a conversion rate of approximately 15% per year. Towards this end, neuroimaging datasets for AD including magnetic resonance imaging (MRI) and other types of biomarkers have shown considerable promise to detect longitudinal changes in subjects scanned repeatedly over time (Wyman et al., 2013a), by offering rich information on the patient's morphometric and anatomical profiles. Their use stems from the premise that longitudinal changes may be more reproducible and more precisely measured with MRI and other parameters such as in clinical scores, cerebrospinal fluid (CSF), or proteomic assessments.

A number of studies reported structural changes in the hippocampus, parahippocampal gyrus, cingulate, and other brain regions in both MCI and AD patients (Visser et al., 2002). Other studies have used intensity information to discriminate elderly normal controls (NC) with patients inflicted with AD or mild cognitive impairment (MCI), based on T1-weighted MRI (Li et al., 2012). Previous machine learning algorithms using MRI were based on traditional morphometric measures, such as subcortical volume or shape descriptors of brain structures (Chupin et al., 2009) and their change over time (Leow et al., 2007). These were based on finding a low-dimensional representation of complex and high-dimensional data using principal component analysis (PCA) and multidimensional scaling (MDS). However these methods are typically linear, making it easy to transform data from image space into the learned subspace, but lacks the ability to process irregular or abnormal structures, which tend to follow non-linear patterns of variation. To cope with this limitation, manifold learning methods on the other hand tend to better model highly non-linear data, such as from neuroimaging datasets (Aljabar et al., 2011). Recently, discriminant embeddings exploit within and between-class similarities to establish correspondences between disparate data, thereby offering a more accurate relationship of subtile structural alterations in AD.

The objective of this study is to propose a classifier which distinguishes NC subjects from patients with MCI and patients afflicted with AD. First, segmented hippocampus shapes from MRI are matched between each other using a spectral representation of the 3D mesh surface of the sub-cortical surface in order to have one-to-one vertex correspondences between hippocampus shapes throughout a population. Once a training set of hippocampus shapes is created for three clinical relevant groups (NC, MCI, AD), a discriminant manifold based on Grassmannian kernels is trained to maximize the separation between these three groups and

improve the classification accuracy for any unseen MRI, which can be processed by mapping the segmented hippocampus onto the trained manifold. Th main contribution of this paper is to develop a hippocamus classification approach based on their spectral representation which is classified in the Grassmannian space.

C.2 Methods

C.2.1 Hippocampus shape alignment

In the first step, segmented binary masks obtained from diagnostic T1-weighted MRI are processed to the same image orientation and isotropic voxel sizes, and then converted into 3D triangulated surfaces using the marching cube algorithm. A Gaussian smoothing process is subsequently applied on each surface in order to remove surface irregularities. Then, a reference surface is defined in an iterative process, and all triangulated surfaces are aligned to this reference using a rigid registration algorithm. In order to establish the point-to-point correspondences across all surfaces, each mesh is matched to a randomly selected reference surface using a spectral matching algorithm as proposed in (Lombaert et al., 2013b).

The matching between two surfaces S_i and S_j of the hippocampus from two separate subjects is conducted in a two-step process. In the first step, an initial transformation is calculated between the two surfaces, followed by a second step to establish a smooth map between the two meshes based on a diffeomorphic mapping (Lombaert et al., 2013b). First, the spectrums of the meshes S_i and S_j are computed according to spectral representation theory. Meshes are described by their principal eigenmodes following an eigendecomposition of their respective Laplacian matrix L. In order to add robustness to the feature matching process, the mean curvature at each point of the mesh defined as $C(i) = 0.5 * (C_{min} + C_{max})$ are calculated, where the principal curvatures C_{min} and C_{max} are estimated as the minimum and maximum curving degrees of a mesh S, respectively. Hence, the mean curvature of C is computed as $\{C(1), C(2), \cdots, C(n)\}$, where n is the number vertices. We incorporate these features in the weighting of the nodes of the spectral graph $\mathcal{G}$ by computing the exponential of the mean curvature, and defining the graph Laplacian as $\tilde{L} = \mathcal{G}L$, where

$$\mathcal{G} = P^{-1}(\exp(diag(\{C(1), C(2), \cdots, C(n)\})))^{-1} \tag{C.1}$$

and P is the diagonal node degree matrix integrating distance weights. Once meshes are described in the spectral domain, the first e eigenvectors associated with non-zero eigenvalues are chosen to define the spectral representations $\tilde{S}_i$ and $\tilde{S}_j$. After reordering and sign adjust-

ment (Lombaert et al., 2013a) of the resulting spectrums $\tilde{S}_i$ and $\tilde{S}_j$, we perform non-rigid alignment of the spectral coordinates using Coherent Point Drift (CPD) (Myronenko et al., 2009b). The CPD approach finds a continuous transformation between the surfaces $\tilde{S}_i$ and $\tilde{S}_j$ in the spectral domain. Once the two spectral representations are aligned, the point-by-point correspondences between two meshes could be directly established in the Euclidean space, such that the two closest points in the spectral domain are considered as corresponding points in the Euclidean space. Thus, the correspondence map c between S_i and S_j is established with a simple nearest-neighbor search in spectral domain.

It was shown in (Lombaert et al., 2013b) that incorporating extra features might create discontinuities in the correspondence map c. As a solution, a diffeomorphic matching is applied to find the final map between two shapes. This is obtained by defining an association graph composed of the set of vertices and edges, based on the initial set of correspondence links. The graph Laplacian operator is applied on the resulting graph, followed by a spectral decomposition to produce a shared set of eigenvectors, from which the first and last eigenvalues are used to obtain one-to-one vertex correspondences between the mesh vertices. This procedure is repeated for all training meshes in the three groups of the database, with (1) normal controls, (2) MCI patients and (3) AD patients.

C.2.2 Learning the discriminant Grassmannian manifold

Manifold learning algorithms are based on the premise that data are often of artificially high dimension and can be embedded in a lower dimensional space. However the presence of outliers and multi-class information can on the other hand affect the discrimination and/or generalization ability of the manifold. We propose to learn the optimal separation between three classes (1) normal controls, (2) MCI patients and (3) AD patients, by using a discriminant graph-embedding based on Grassmannian manifolds for the classification problem initially proposed in (Harandi et al., 2011). Each sample mesh surface S, which vertices has been rearranged using the alignment method in 2.1, can be viewed as the set of low-dimensional m subspaces of $\mathbb{R}^n$ on a Grassmannian manifold and represented by orthonormal matrices, each with a size of $n \times m$, with n the higher dimensionality of vertices defined earlier. Two points on a Grassmannian manifold are equivalent if one can be mapped into the other one by a $m \times m$ orthogonal matrix. In this work, similarity between two surfaces (S_i, S_j) on the manifold is measured as a combination of projection and canonical correlation Grassmannian kernels $\mathbb{K}_{i,j}$ defined in the Hilbert Space. By describing different features of the hippocampus shape with each kernel, $\mathbb{K}_{i,j}$ can improve discriminatory accuracy between shapes.

In order to effectively discover the low-dimensional embedding, it is necessary to maintain the local structure of the data in the new embedding. The structure $G = (\boldsymbol{V}, \boldsymbol{W})$ is an undirected similarity graph, with a collection of nodes $\boldsymbol{V}$ connected by edges, and the symmetric matrix $\boldsymbol{W}$ with elements describing the relationships between the nodes. The diagonal matrix $\boldsymbol{D}$ and the Laplacian matrix $\boldsymbol{L}$ are defined as $\boldsymbol{L} = \boldsymbol{D} - \boldsymbol{W}$, with $\boldsymbol{D}(i,i) = \sum_{j \neq i} \boldsymbol{W}_{ij} \forall i$. Here, N labelled points $\mathbb{S} = \{(S_i, c_i)\}_{i=1}^{N}$ are generated from the underlying manifold $\mathcal{M}$, where c_i denotes the label (NC, MCI or AD). The task at hand is to maximize a measure of discriminatory power by mapping the underlying data into a vector space, while preserving similarities between data points in the high-dimensional space. Discriminant graph-embedding based on locally linear embedding (LLE) (Roweis and Saul, 2000) uses graph-preserving criterions to maintain these similarities, which are included in a sparse and symmetric $N \times N$ matrix, denoted as M.

Within and between similarity graphs : In our work, the geometrical structure of $\mathcal{M}$ can be modeled by building a within-class similarity graph $\boldsymbol{W}_w$ for hippocampus of same group and a between-class similarity graph $\boldsymbol{W}_b$, to separate hippocampus from the three classes. When constructing the discriminant LLE graph, elements are partitioned into $\boldsymbol{W}_w$ and $\boldsymbol{W}_b$ classes. The intrinsic graph G is first created by assigning edges only to samples of the same class (ex : MCI). The local reconstruction coefficient matrix $M(i,j)$ is obtained by minimizing :

$$\min_{M} \sum_{j \in \mathcal{N}_w(i)} \|S_i - M(i,j) S_j\|^2 \quad \sum_{j \in \mathcal{N}_w(i)} M(i,j) = 1 \;\; \forall i \tag{C.2}$$

with $\mathcal{N}_w(i)$ as the neighborhood of size k_1, within the same region as point i (e.g. hippocampus from MCI patient). Each sample is therefore reconstructed only from 3D meshes of the same clinical group. The local reconstruction coefficients are incorporated in the within-class similarity graph, such that the matrix $\boldsymbol{W}_w$ is defined as :

$$W_w(i,j) = \begin{cases} (M + M^T - M^T M)_{ij}, & \text{if } \; S_i \in \mathcal{N}_w(S_j) \text{ or } x_j \in \mathcal{N}_w(S_i) \\ 0, & \text{otherwise.} \end{cases} \tag{C.3}$$

Conversely, the between-class similarity matrix $\boldsymbol{W}_b$ depicts the statistical properties to be avoided in the optimization process and used as a high-order constraint. Distances between healthy and pathological samples are computed as :

$$W_b(i,j) = \begin{cases} 1/k_2, & \text{if } S_i \in \mathcal{N}_b(S_j) \text{ or } S_j \in \mathcal{N}_b(S_i) \\ 0, & \text{otherwise} \end{cases} \tag{C.4}$$

with $\mathcal{N}_b$ containing k_2 neighbors having different class labels from the ith sample. The objective is to transform points to a new manifold $\mathcal{M}$ of dimensionality d, i.e. $S_i \rightarrow y_i$, by mapping connected samples from the same group in $\boldsymbol{W}_w$ as close as possible to the class cluster, while moving NC, MCI and AD meshes of $\boldsymbol{W}_b$ as far away from one another. This results in optimizing the objective functions :

$$f_1 = \min \frac{1}{2} \sum_{i,j} (y_i - y_j)^2 W_w(i,j) \qquad f_2 = \max \frac{1}{2} \sum_{i,j} (y_i - y_j)^2 W_b(i,j) \tag{C.5}$$

Supervised manifold learning : The optimal projection matrix, mapping new points to the manifold, is obtained by simultaneously maximizing class separability and preserving interclass manifold property, as described by the objective functions in Eq.(C.5). Assuming points on the manifold are known as similarity measures given by the Grassmannian kernel $\mathbb{K}_{i,j}$, a linear solution can be defined, i.e., $y_i = (\langle \alpha_1, S_i \rangle, \ldots, \langle \alpha_r, S_i \rangle)^T$ for the r largest eigenvectors with $\alpha_i = \sum_{j=1}^{N} a_{ij} S_j$. Defining the coefficient $\boldsymbol{A}_l = (a_{l1}, \ldots, a_{lN})^T$ and kernel $\boldsymbol{K}_i = (k_{i1}, \ldots, k_{iN})^T$ vectors, the output can be described as $y_i = \langle \alpha_l, S_i \rangle = \boldsymbol{A}_l^T \boldsymbol{K}_i$. By replacing the linear solution in the minimization and maximization of the between- and within-class graphs, the optimal projection matrix $\mathbb{A}$ is acquired from the optimization of the function as proposed in (Harandi et al., 2011). The proposed algorithm uses the points on the Grassmannian manifold implicitly (i.e., via measuring similarities through a kernel) to obtain a mapping $\mathbb{A}$. The matrix maximizes a quotient similar to discriminant analysis, while retaining the overall geometrical structure. Hence for any new segmented surface mesh S_q, a manifold representation can be obtained using the kernel function based on S_q and mapping $\mathbb{A}$.

C.3 Experiments and results

We used the Alzheimer's Disease Neuroimaging Initiative (ADNI) database with 1.5 or 3.0 T structural MR images (adni.loni.usc.edu). For this study, a subset of baseline 1.5 T MR images is used including 47 normal controls (NC), 47 AD patients, and 47 individuals with MCI. The three groups are matched approximately by age and gender (NC with a mean age of 76.7 ± 5.4, 23 male ; AD with a mean age of 77.4 ± 7.2, 21 males ; MCI with a mean age

of 75.0 ± 6.9, 28 males). Additional post-processing steps were performed on the MR images to correct certain image artifacts and to enhance standardization across sites and platforms. The post-processing steps include gradient non-linearity correction, intensity inhomogeneity correction, bias field correction, and phantom-based geometrical scaling to remove calibration errors. Here, we use these processed images. Left and right hippocampi were segmented using FSL-FIRST automatic segmentation (Patenaude et al., 2011b) and visual inspection was performed on the output binary masks to ensure the quality of the segmentation. Fig. C.1 shows the shape differences in the left and right hippocampus between NC, MCI and AD.

The optimal size was found at $k_1 = 7$ for within-class neighborhoods ($\mathcal{N}_w$), and $k_2 = 4$ for between-class neighborhoods ($\mathcal{N}_b$). The optimal manifold dimensionality was set at $d = 5$, when the trend of the nonlinear residual reconstruction error curve stabilized for the entire training set. Fig. C.2 shows the resulting manifold with embedded hippocampus shapes which can be clearly identified into three separate groups, due to the discriminative nature of the framework. Table C.1 presents accuracy, sensitivity and specificity results for SVM (nonlinear RBF kernel), LLE and the proposed method between three clinically relevant pairs of diagnostic groups (NC/AD, NC/MCI, MCI/AD). The classifier performance was obtained by repeating 100 times a random selection of samples, using 75% of the data for training and 25% for testing in each run. Results show a significant improvement using the discriminant manifold embedding compared to standard approaches. It also illustrates that increased accuracy can be achieved using the discriminant embedding with combined kernel ($\alpha_1 = 1, \alpha_2 = 5$), which suggests the benefit of extracting complementary features from the dataset for classification purposes compared to different types of classification models (SVM, LLE).

C.4 Conclusion

Our main contribution consists in describing morphometric variations of the hippocampus in a discriminant nonlinear graph embedding with Grassmannian manifolds to detect the presence of Alzheimer's disease. A spectral matching process based on the eigendecomposition of the Laplacian matrix of hippocampus shapes extracted from a dataset of MRI images enabled to establish one-to-one correspondences in mesh vertices. This is critical to construct a reliable training set of sub-cortical shapes from various pathological groups and normal controls. A manifold embedding including intrinsic and penalty graphs measuring similarity within clinical relevant groups and between NC, MCI and AD patients, respectively, was trained to differentiate between the different hippocampus shapes. A combination of canonical

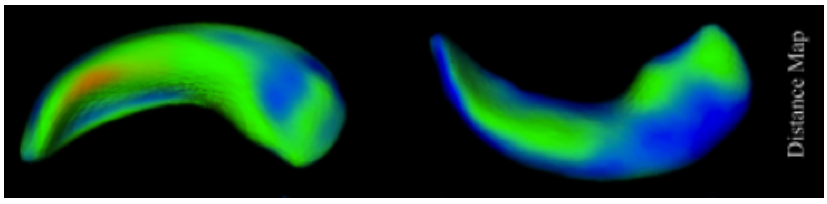

(a)

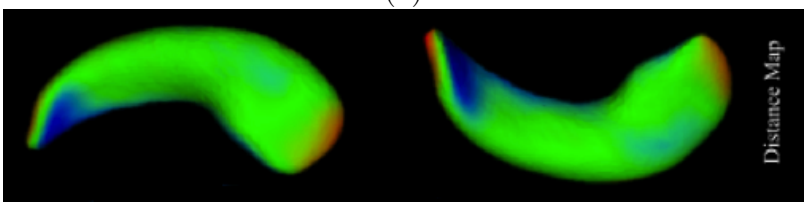

(b)

Figure C.1 (a) Distance maps of left and right hippocampal shape deformations in AD patients compared with normal controls. (b) Distance maps of left and right hippocampal shape deformations in MCI patients compared with normal controls.

Table C.1 Classification results for the classification of NC, MCI and AD patients from segmented hippocampal regions. We compare a standard SVM classification approach, with a single LLE method and the proposed discriminant LLE method.

	NC/AD			NC/MCI			MCI/AD			All groups		
	SVM	LLE	**DLLE**	SVM	LLE	**DLLE**	SVM	LLE	**DLLE**	SVM	LLE	**DLLE**
Sensitivity tp/(tp+fn)	0.75	0.84	**0.90**	0.58	0.61	**0.69**	0.50	0.57	**0.60**	0.61	0.67	**0.73**
Specificity tn/(tn+fp)	0.69	0.77	**0.85**	0.62	0.70	**0.77**	0.57	0.61	**0.67**	0.62	0.69	**0.77**
Overall accuracy	0.72	0.79	**0.88**	0.60	0.65	**0.72**	0.54	0.58	**0.65**	0.62	0.67	**0.74**

correlation kernels creates a secondary manifold to simplify the deviation estimation from normality, improving detection of pathology compared to standard LLE. Experiments show the need of nonlinear embedding of the learning data, and the relevance of the proposed method for stratifying different stages of dementia progression. In the context of Alzheimer's disease, the method can improve for the early detection of the disease with promising classification rates based on ground-truth knowledge. Future work will compare results to volumetric measurements and improve the deviation metric using high-order tensorization and investigate into fully automated hippocampus segmentation, as it can affect the precision of the spectral correspondence process.

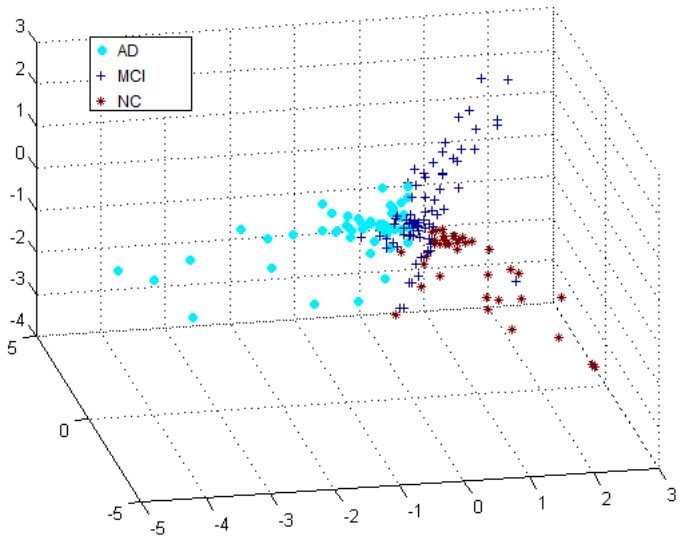

Figure C.2 Resulting manifold embedding with low-dimensional coordinates of samples points taken from the NC, MCI and AD groups.

ANNEXE D ARTICLE 7 : DEEP SPECTRAL-BASED SHAPE FEATURES FOR ALZHEIMER'S DISEASE CLASSIFICATION

Mahsa Shakeri[1,2], Herve Lombaert[3], Shashank Tripathi[1], Samuel Kadoury[1,2]

[1] MEDICAL, Polytechnique Montreal, Montréal, Québec, Canada,[2] CHU Sainte-Justine Hospital Research Center, [3]Inria Sophia-Antipolis, France,

Presentation

This appendix presents the article "Deep spectral-based shape features for Alzheimer's Disease classification" (Shakeri et al., 2016d) accepted in Workshop on Spectral and Shape Analysis in Medical Imaging (SESAMI 2016), Held in Conjunction with MICCAI 2016, Athens, Greece, October 12, 2016. The objective of this article is to apply a deep learning variational auto-encoder on the spectral representation of the vertex coordinates of surface meshes to learn the low dimensional features. This method simultaneously trains a multi-layer perceptrons using softmax activation to classify Alzheimer's patients from normal subjects.

abstract Alzheimer's disease (AD) and mild cognitive impairment (MCI) are the most prevalent neurodegenerative brain diseases in elderly population. Recent studies on medical imaging and biological data have shown morphological alterations of subcortical structures in patients with these pathologies. In this work, we take advantage of these structural deformations for classification purposes. First, triangulated surface meshes are extracted from segmented hippocampus structures in MRI and point-to-point correspondences are established among population of surfaces using a spectral matching method. Then, a deep learning variational auto-encoder is applied on the vertex coordinates of the mesh models to learn the low dimensional feature representation. A multi-layer perceptrons using softmax activation is trained simultaneously to classify Alzheimer's patients from normal subjects. Experiments on ADNI dataset demonstrate the potential of the proposed method in classification of normal individuals from early MCI (EMCI), late MCI (LMCI), and AD subjects with classification rates outperforming standard SVM based approach.

keywords classification, spectral matching, variational autoencoder, Alzheimer's disease.

D.1 Introduction

Alzheimer's disease (AD) is characterized by progressive impairment of cognitive and memory functions in elderly population. Considering its worldwide prevalence, early diagnosis of this

disease might have a huge impact on the overall well-being of the population, and the burden to caregivers, as well as the associated financial costs to the world's health system. Studies reported that AD can be diagnosed by clinical assessments in most of the cases (Ranginwala et al., 2008), while by the time the patient is diagnosed the disease progression may have deteriorated. Therefore, early diagnosis of this neuropathology is of special interest.

Mild cognitive impairment (MCI) is considered as a transition state between normal aging and dementia (Petersen et al., 1999). The cognitive deficits in MCI patients are not as severe as those seen in individuals with AD. However, studies have suggested that about $10 - 12\%$ of subjects with MCI progress to AD per year (Petersen et al., 1999). Therefore, these individuals with milder degrees of cognitive and functional impairment than AD patients are particularly interesting subjects, since biomarker manifestation could potentially be different at such an early stage of the disease.

Studies have shown that the neuropathological changes in AD and MCI affect the hippocampus structure, which is a brain region crucial to various cognitive functions (Du et al., 2001). Neuroimaging datasets for AD including magnetic resonance imaging (MRI) and other types of biomarkers have shown considerable promise to detect longitudinal changes in subjects (Wyman et al., 2013b), by offering rich information on the patients morphometric and anatomical profiles. Their use stems from the premise that morphological changes may be more reproducible and more precisely measured with MRI than other parameters such as clinical scores, cerebrospinal fluid (CSF), or proteomic assessments.

Recent advances in medical imaging and classification techniques have led to a better discrimination between Alzheimer's disease and healthy aging. Because of the high dimensionality of medical image, various dimensionality reduction approaches have been developed to facilitate and enhance classification accuracy. A simple method is principal components analysis (PCA) (Davatzikos et al., 2008), which finds the directions of greatest variance in the dataset and represents each data point by its coordinates along each of these directions. A nonlinear generalization of PCA is multi-layer autoencoders (AE) (Bengio, 2009), which is a feedforward neural network to encode the input into a more compact from and reconstruct the input with the learned representation. Among available AE architectures, the deep variational autoencoder (VAE) (Kingma and Welling, 2013) method has recently become popular in computer vision due to its capability to learn a manifold without the assumption of linearity in addition to its generative property.

With respect to surface representation, recent studies have shown the advantage of spectral shape description compared to Euclidean surface representation (Lombaert et al., 2013a,b, 2015). The use of eigenvalues have led to interesting results for AD classification in (Wachin-

ger and Reuter, 2016), where Laplace-Beltrami spectrum on the intrinsic geometry of the structural meshes was computed to define the shape descriptors.The spectral coordinates, which were derived from the Laplacian eigenfunctions of shapes have been used in (Lombaert et al., 2015) to parametrize surfaces explicitly. The authors applied a Random Decision Forest classifier on spectral representation of surfaces and achieved a significant improvement on cortical parcellations. Also, in (Lombaert et al., 2013a) and Lombaert et al. (2013b), the eigendecomposion of the surfaces in the spectral domain were used to provide pointwise information on meshes and establish accurate point-to-point correspondences across surfaces.

In this work, we present a surface-based classification technique based on classification of spectral features using variational stacked auto-encoders. We first extract 3D surface meshes of hippocampus structures from segmented binary MR images. Then, the point-to-point surface correspondences is established across populations (NC, AD, EMCI, LMCI) using a spectral matching approach. In spectral based shape matching approach, relationships are modeled as graphs and an eigendecomposition on these graphs enables us to match similar features. Once the matched surfaces are created, the vertex coordinates are used as shape feature descriptors. Then, variational autoencoder (VAE) obtains the non-linear low-dimensional embedding of the shape features. A multi-layer perceptron (MLP) classifier is simultaneously trained to model the non-linear decision boundaries between classes.

The work follows on the prior work of (Suk and Shen, 2013), which used a Stacked Auto-Encoder (SAE) to discover the latent representation from the grey matter (GM) tissue densities and voxel intensities. Unlike Suk et al. (Suk and Shen, 2013), which selects intensity and volume based features from MRI and PET modalities, we create the feature descriptors from matched hippocampi surfaces extracted from MRI. Moreover, instead of training a separate classifier on the low dimensional features as in (Suk and Shen, 2013), we add a softmax multi-layer perceptron on top of our variational autoencoder network to obtain both dimensionality reduction and the classification output at the same time.

The rest of the paper is organized as follows. In Section D.2, we present the morphological feature extraction method using spectral shape matching, as well as the feature representation and classification method based on variational autoencoder and multi-layer perceptron. Section D.3 includes the description of the dataset, experiments and discussion. Our conclusions are presented in Section D.4, along with envisioned future research directions.

D.2 Methodology

Given MR images along with their corresponding hippocampus segmentations (produced manually or automatically), we first extract features from MRI as explained in Section 2.1. Then, we use a deep variational autoencoder (VAE) to learn a latent feature representation from the low-level features and train a multi-layer perceptron (MLP) for classification purposes in Section 2.2.

D.2.1 Shape feature extraction using spectral matching

Given a reference surface mesh S_r and a population of n surfaces $\{S_i\}_{i=1..n}$, the spectral matching between each surface meshe S_i and S_r is done in a two step process. First, an initial map is calculated between the two surfaces (Lombaert et al., 2013a). This initial map is then used in the second step to establish a smooth map between the two meshes (Lombaert et al., 2013b).

Here, we consider vertices and neighbouring points in each surface mesh as nodes and edges of a graph. Then a laplacian graph is created for each surface graph from the set of vertices and edges of each mesh. The general Laplacian operator L_i (Grady and Polimeni, 2010) is defined on each surface as following :

$$L_i = G_i^{-1} (D_i - W_i) \tag{D.1}$$

where W_i is the weighted adjacency matrix, which is created based on a distance between connected nodes. The term D_i is a diagonal matrix, in which the elements are set by the degree of vertices. G_i is a node weighting matrix created based on the mean curvature at each node as described in (Shakeri et al., 2016c).

The eigendecomposition of Laplacian matrix L_i provides its spectral components. After reordering the spectral components by finding the optimal permutation of components between the pair of meshes, regularization is performed by matching the spectral embeddings. The correspondence initial map c between each pair of vertices on S_i and S_r is established with a simple nearest-neighbour search between their spectral representations.

In the next step, given initial map c, the final smooth map between two surfaces S_i and S_r is obtained. In this process, an association graph is defined as the union of the set of vertices and edges of two surfaces with an initial set of correspondence links c between both surfaces. Then, a Laplacian matrix is created for the association graph, and the spectral decomposition

is computed to produce a shared set of eigenvectors that enables a direct mapping between two meshes S_i and S_r.

Once all 3D meshes are matched to the reference, the vertices of all surfaces are rearranged to create the new reconstructed meshes with consistent vertex ordering. Now, the shape descriptor x_i will be created for the surface S_i as a vector of (X, Y, Z) coordinate of all vertices.

D.2.2 Feature learning and classification

In this work we use a deep learning-based feature representation method to improve the classification accuracy. Here, we take inspiration from the variational autoencoder network, which learns the low-dimensional manifold without the linearity assumption and has a generative model. In this section, we explain the proposed network architecture, which is a combination of a variational autoencoder network (VAE) and a softmax multi-layer perceptron (MLP). The combined VAE-MLP network architecture is shown in Figure D.1.

Deep variational autoencoder and MLP classifier :

Auto-encoders are a type of deep neural networks structurally defined by input, hidden, and output layers. Given the input data $x \in R^D$ defined from the spectral representation of mesh shapes, an auto-encoder maps it to a latent representation $z \in R^d$ (encoding), which could be used for unsupervised learning or for feature extraction. The representation z from the hidden layer is then mapped back to a vector $y \in R^D$ (decoding), which approximately reconstructs the input vector x. The hidden layer in the middle, i.e., z, can be constrained to be a bottleneck to learn compact representations of the input data.

Variational autoencoder (VAE) assumes that data is generated by a directed graphical model with a latent variable z. VAE uses the encoder network to map the input x into the continuous latent variables $(q_\phi(z|x))$ and uses decoder network to map latent variables to reconstructed data $(p_\theta(x|z))$, where ϕ and θ are the parameters of the encoder (recognition model) and decoder (generative model), respectively.

The lower bound VAE loss function of the variational autoencoder for individual datapoint x_i has the following form :

$$L_{VAE}(\theta, \phi; x_i) = -D_{KL}\left(q_\phi\left(z|x_i\right)||p_\theta\left(z\right)\right) + E_{q_\phi(z|x_i)}\left[\log p_\theta\left(x_i|z\right)\right] \tag{D.2}$$

The first component is the regularization term, which is the KL divergence of the approximate

posterior from the prior, while the second term is the expected reconstruction error. As shown in (Kingma and Welling, 2013), we assume both $p_\theta(z)$ and $q_\phi(z|x_i)$ as Gaussian. Given J as the dimensionality of z and K as the number of samples per datapoint, the resulting estimator for x_i will be as follows :

$$L_{VAE}(\theta, \phi; x_i) = -\frac{1}{2}\sum_{j=1}^{J}\left(1 + \log\left(\sigma_j^2\right) - \mu_j^2 - \sigma_j^2\right) + \frac{1}{K}\sum_{k=1}^{K}\log p_\theta\left(x_i|z_{i,k}\right) \tag{D.3}$$

where, $z_{i,k} = \mu_i + \sigma_i \odot \epsilon_k$ and $\epsilon_k \sim N(0, I)$.

Here, μ and σ can be computed using the deterministic encoder network. The reconstruction (decoding) term of $\log p_\theta\left(x_i|z_{i,k}\right)$ could be set as a bernoulli cross-entropy loss function.

The low dimensional features $z_i = \mu_i + \sigma_i$ from the latent layer are fed to an MLP classifier for solving the classification problem. For the last layer, we use the cross entropy loss function and the softmax activation function, which is standard for classification problems (Bishop, 1995). The softmax function ensures that the network outputs are all between zero and one, and that they sum to one on every time step. Therefore, they can be interpreted as the posterior probabilities, given all the inputs up to the current one. We set the number of units in the classification output layer to be equal to the number of classes of interest (i.e., two).

The network architecture :

Annotated medical image datasets tend to be small and generally hard to obtain. This increases the risk of network overfitting in medical applications. Therefore, we make a series of design choices for our network to avoid overfitting. Our network includes L_2 regularization at each layer to penalize the squared magnitude of all parameters directly in the objective function. That is, for every weight w in the network, we add the term $\frac{1}{2}\lambda w^2$ to the cost function, where λ is the regularization strength.

We also add a drop out layer with the probability of 0.5 after each dense layer. During training, dropout is implemented by only keeping a neurone active with some probability p, or setting it to zero otherwise. Network weights are set based on the uniform initialization scaled by the square root of the number of inputs.

We train the network for 100 epochs with batch size of 28 starting with a learning rate of 0.00001 and dropping it at a logarithmic rate to 0.000001. For the deep learning library, we use Keras and Theano. We determine the number of hidden units based on the classification results. The optimal structure of the network is shown in Figure D.1.

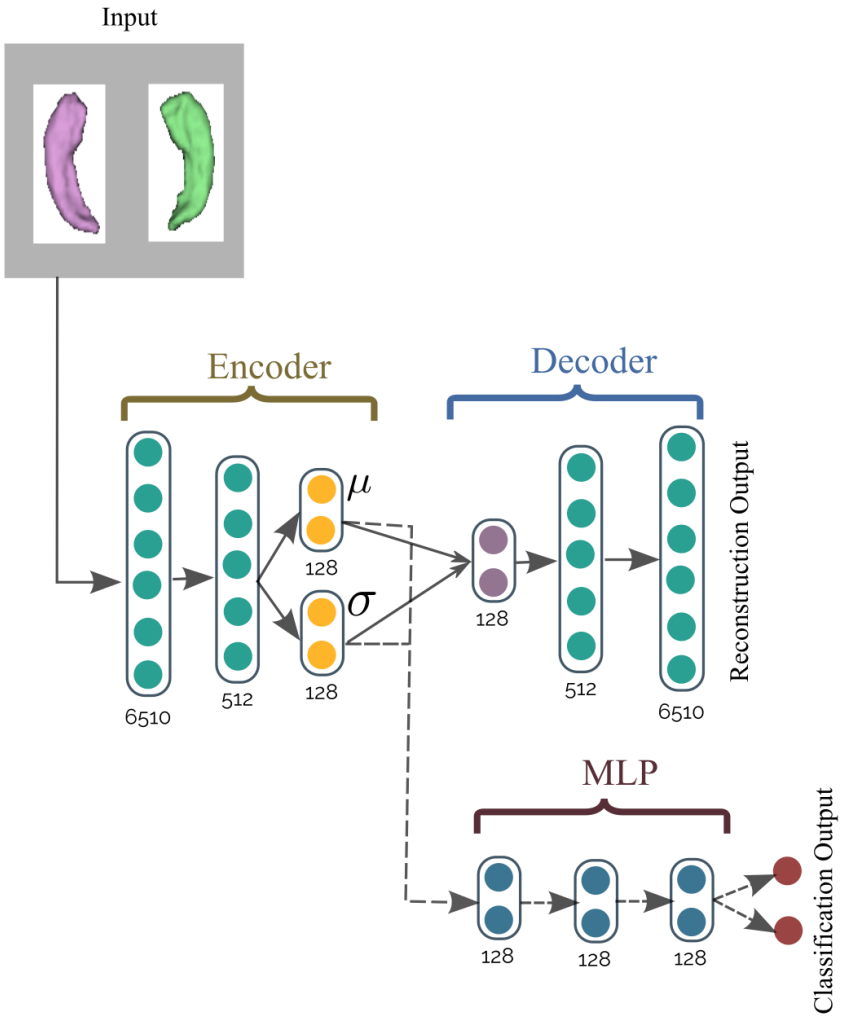

Figure D.1 The architecture of our proposed network. The numbers mentioned under each layer correspond to the layer's dimension.

D.3 Experiments

We evaluate the performance of our approach on a popular brain imaging dataset in Alzheimer's disease, namely the Alzheimer's Disease Neuroimaging Initiative (ADNI). The ADNI database (adni.loni.usc.edu) was launched in 2003 as a public-private partnership, led by Principal Investigator Michael W. Weiner, MD. The primary goal of ADNI has been to test whether serial magnetic resonance imaging (MRI), positron emission tomography (PET), other biological markers, and clinical and neuropsychological assessment can be combined to measure the progression of mild cognitive impairment (MCI) and early Alzheimer's disease (AD). For up-to-date information, see www.adni-info.org. The database of ADNI consists of cross-sectional and longitudinal data including 1.5 or 3.0 T structural MR images. The

detailed description of the MRI protocol of ADNI is provided in (Jack Jr et al., 2008).

For this study, a subset of latest 1.5 T MR images is used including 150 normal controls (NC), 90 AD patients, 160 early MCI (EMCI), and 160 individuals with late MCI (LMCI). ADNI performed additional post-processing steps on MR images to correct certain image artifacts and to enhance standardization across sites and platforms (Jack Jr et al., 2008). The post-processing steps include gradient non-linearity correction, intensity inhomogeneity correction, bias field correction, and phantom-based geometrical scaling to remove calibration errors. In this work, we use these processed images. Here, hippocampi was segmented using FSL-FIRST automatic segmentation software package (Patenaude et al., 2011a) and visual inspection was performed on the output binary masks to ensure the quality of the automatic segmentation.

Here we consider six binary classification problems : AD vs. NC, NC vs. EMCI, NC vs. LMCI, AD vs. EMCI, AD vs. LMCI, and EMCI vs. LMCI. We consider 20% of data for test and the rest for train. Each time 20% of train set is left out and used for validation.The whole process is repeated five times for unbiased evaluation. The regularization strength λ is set as 0.05 based on experimental results.

We tested different network architectures and realized that going deeper than the proposed model in Figure D.1 would not help improving the classification accuracy, however the dimensionality of the hidden and the latent unit had direct effect on the classification performance.

In the analysis of the results, the performance of the classifier are measured by its sensitivity (SE), specificity (SP) and accuracy (AC). Sensitivity, which is the ability of the classifier to correctly identify positive results, is defined as TP/(TP+FN). Specificity refers to the ability to correctly identify negative results and is formulated as TN/(FP+ TN). Accuracy is defined as (TP+ TN)/(TP+TN+FN+FP).

As baseline, we train a linear Support Vector Machines (SVM) on the same dataset after applying principle components analysis (PCA) for dimensionality reduction. The features are extracted from 3D surface meshes after applying spectral matching in the same way as our

Table D.1 Comparison of the classification accuracy (AC%), sensitivity (SE%), and specificity (SP%) with a baseline method using the same spectral-based shape feature descriptor. The proposed method achieved higher accuracy in most of the cases.

	NC/AD			NC/EMCI			NC/LMCI			AD/EMCI			AD/LMCI			EMCI/LMCI		
	AC	SE	SP	AC	SE	SP	AC	SE	SP	AC	SE	SP	AC	SE	SP	AC	SE	SP
Baseline	80	70	86	55	52	58	**63**	**56**	**75**	76	65	71	63	58	66	51	50	52
Proposed	**84**	**73**	**89**	**56**	**52**	**60**	59	52	64	**81**	**70**	**82**	**67**	**58**	**73**	**63**	**62**	**66**

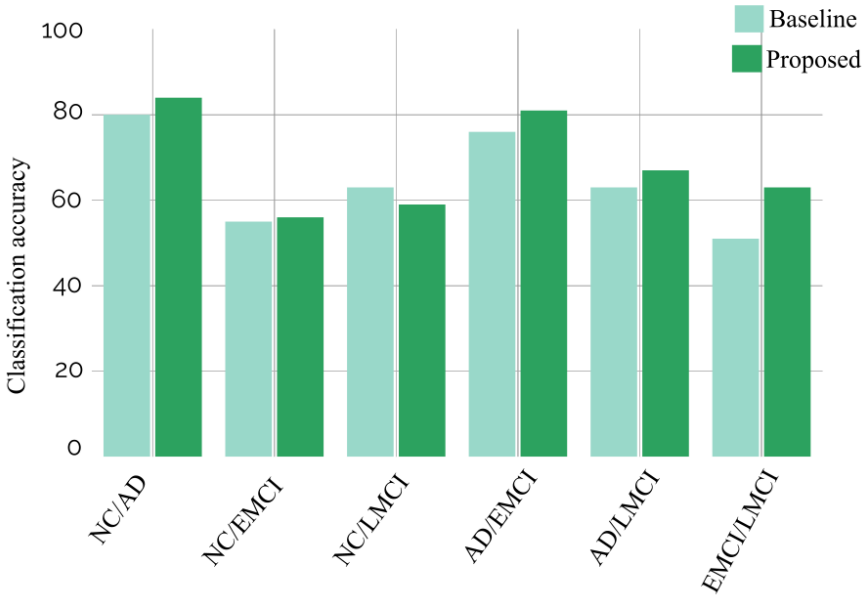

Figure D.2 Comparison of the classification accuracy with a baseline approach using the same spectral-based shape feature representation. The VAE-based method achieved higher accuracy in most of the cases.

proposed method. The classification accuracy for the proposed and the baseline methods is illustrated in Figure D.2. We summarize the classification accuracy along with the sensitivity (SE), and specificity (SP) measures in Table D.1.

These results show that our method produces higher accuracy in most of the cases. As expected, the best classification accuracies are those obtained for groups, which are well separated diagnostically. For instance, 84% and 81% for the classification of NC versus AD and EMCI versus AD, respectively. The computational time of both methods is around 60 *sec* for training on 300 surfaces and less than 5 *ms* for testing on one surface.

In addition, the obtained results is comparable to the previously proposed approaches that have used MRI based features. For instance, Suk et al. (Suk and Shen, 2013) and Goryawala et al. (Goryawala and et al., 2015) found the accuracy of 85% and 84%, respectively for the classification of NC versus AD. These method have also included additional information from PET modality or neuropsychological test to improve the classification performance. One future direction of our proposed approach would be to include a combination of informative features to reach a higher accuracy.

D.4 Conclusions

In this paper we have proposed a deep learning method based on a spectral feature representation using hippocampus morphology for the classification of Alzheimer's Disease. The morphological features were extracted as 3D surface meshes from MR image and spectral matching process was used to establish point-to-point correspondences in mesh vertices. A variational autoencoder was trained to find the latent feature representation from hippocampus morphological variations. A softmax classifier was applied to differentiate between NC, EMCI, LMCI, and AD.

Experimental evaluation on the ADNI dataset demonstrates the effectiveness of our approach especially in classifying AD vs. NC and AD vs. EMCI. This work shows the importance of the VAE-based morphological feature representation in improving the diagnosis accuracy in different stages of dementia. Future research directions include adding other informative features, such as cognitive information and multimodal data (e.g., PET) to increase the classification accuracy.

Acknowledgements

Funding was provided by the Canada Research Chairs and from the CHU Sainte-Justine Hospital's Research Center, Montreal, Canada. ADNI data collection and sharing for this project was funded by the Alzheimer's Disease Neuroimaging Initiative (ADNI) (National Institutes of Health Grant U01 AG024904) and DOD ADNI (Department of Defense award number W81XWH-12-2-0012). ADNI is funded by the National Institute on Aging, the National Institute of Biomedical Imaging and Bioengineering, and through generous contributions from the following : AbbVie, Alzheimer's Association ; Alzheimer's Drug Discovery Foundation ; Araclon Biotech ; BioClinica, Inc. ; Biogen ; Bristol-Myers Squibb Company ; CereSpir, Inc. ; Eisai Inc. ; Elan Pharmaceuticals, Inc. ; Eli Lilly and Company ; EuroImmun ; F. Hoffmann-La Roche Ltd and its affiliated company Genentech, Inc. ; Fujirebio ; GE Healthcare ; IXICO Ltd. ; Janssen Alzheimer Immunotherapy Research & Development, LLC. ; Johnson & Johnson Pharmaceutical Research & Development LLC. ; Lumosity ; Lundbeck ; Merck & Co., Inc. ; Meso Scale Diagnostics, LLC. ; NeuroRx Research ; Neurotrack Technologies ; Novartis Pharmaceuticals Corporation ; Pfizer Inc. ; Piramal Imaging ; Servier ; Takeda Pharmaceutical Company ; and Transition Therapeutics. The Canadian Institutes of Health Research is providing funds to support ADNI clinical sites in Canada. Private sector contributions are facilitated by the Foundation for the National Institutes of Health (www.fnih.org). The grantee organization is the Northern California Institute for Research and Education, and

the study is coordinated by the Alzheimer's Disease Cooperative Study at the University of California, San Diego. ADNI data are disseminated by the Laboratory for Neuro Imaging at the University of Southern California.

ANNEXE E SUPPLEMENTARY MATERIALS FOR CHAPTER 5

This section provides the supplementary materials for Chapter 5.

In this supplementary material we demonstrate results that were not included in the paper due to space constraints. Figures E.1-E.3 compare the six segmentation approaches described in the paper, in terms of average Dice coefficient (DC), Hausdorff distance (HD) and contour mean distance (CMD) respectively. We show results for the right side subcortical structures of IBSR dataset (Rohlfing, 2012b). Note that the subcortical structure symmetry is reflected on the trend of the results, which is very similar to the one observed in Figure 1 in the paper.

In Table E.1, we include some numerical results corresponding to the experiments reported in the main paper. As we can observe, when we use accurate priors (Coreg+CNN), we achieve results close to the ground truth after coregistration and segmentation in the majority of the cases. Moreover, when we use weak priors like (Coreg+RF), we improve the initial results given by the thresholded priors, especially in terms of CMD and HD. The significant differences between the proposed coregistration-cosegmentation method and the standard multi-atlas segmentation approach (Pairwise) is revealed using statistical t-test with a significant threshold of $p = 0.05$.

We also include, in Figure E.4, a diagram explaining the workflow of the co-registration and segmentation algorithm.

We compare the accuracy of our proposed CNN-based coregistration and cosegmentation method with our proposed deep CNN/MRF-based method (Appendix A), as well as the two publicly available state-of-the-art automatic segmentation toolboxes, Freesurfer (Fischl et al., 2002), and FSL-FIRST (Patenaude et al., 2011a). In Figure E.5, we report the average Dice coefficient for a group of sub-cortical structures on IBSR dataset. These results show that our coregistration-cosegmentation method provides better segmentations compared to the state-of-the-art for three sub-cortical structures. However, Freesurfer produces better segmentation for caudate, which could be due to the limitation of the designed CNN network in capturing thin tail areas of the caudate structures.

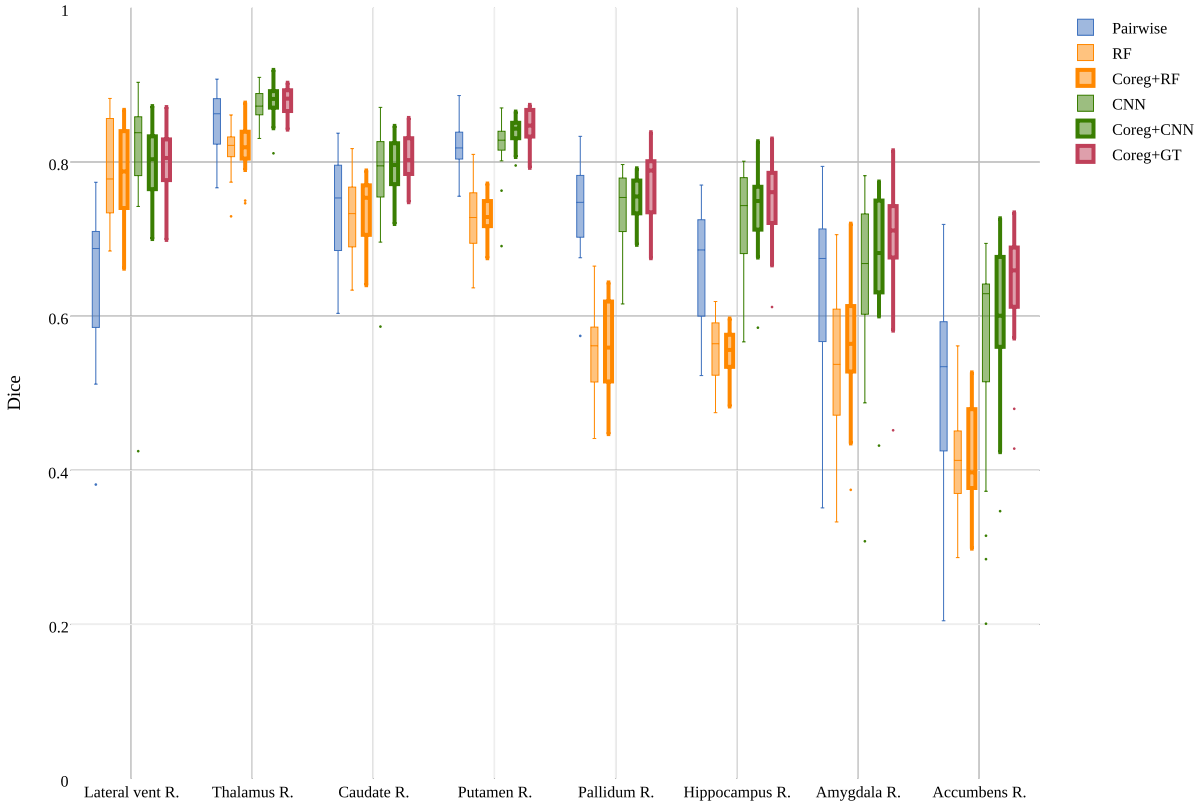

Figure E.1 Average Dice (DC) measure for right subcortical structures in IBSR (best viewed in color). **DC :** higher = better.

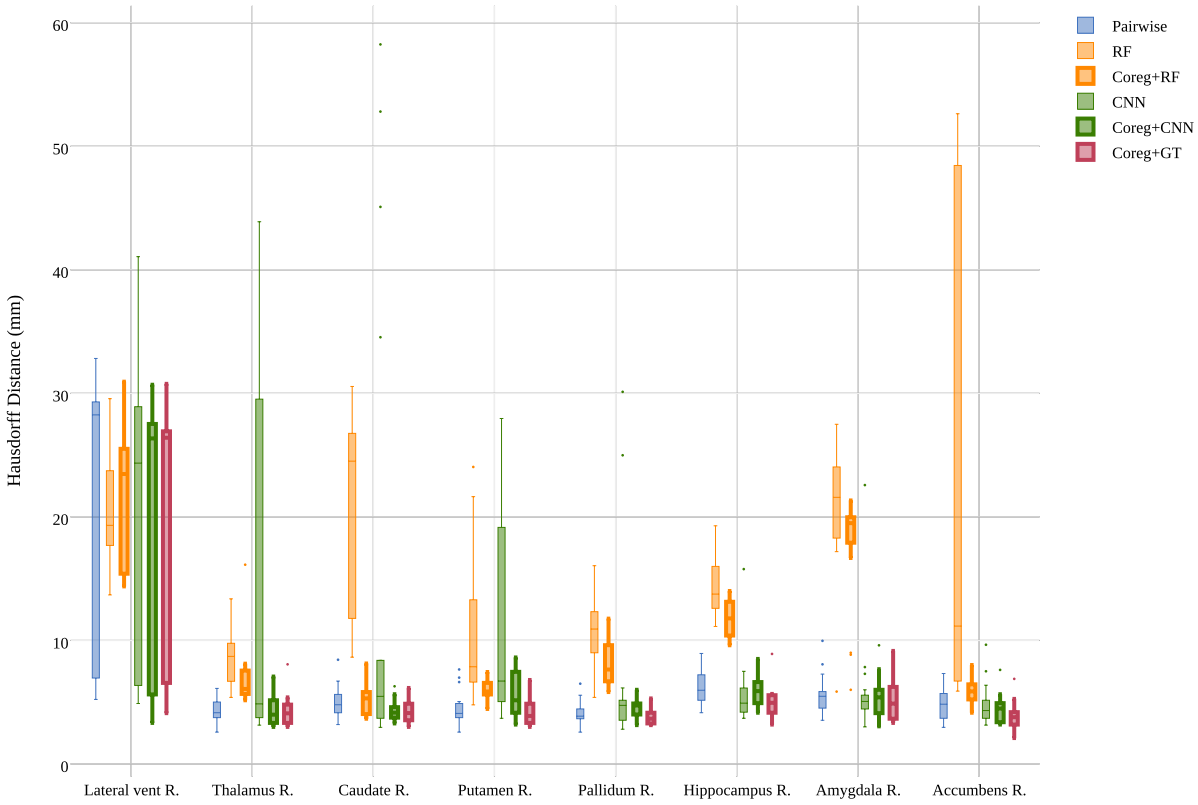

Figure E.2 Hausdorff distance (HD) for right subcortical structures in IBSR (best viewed in color). **HD :** lower = better.

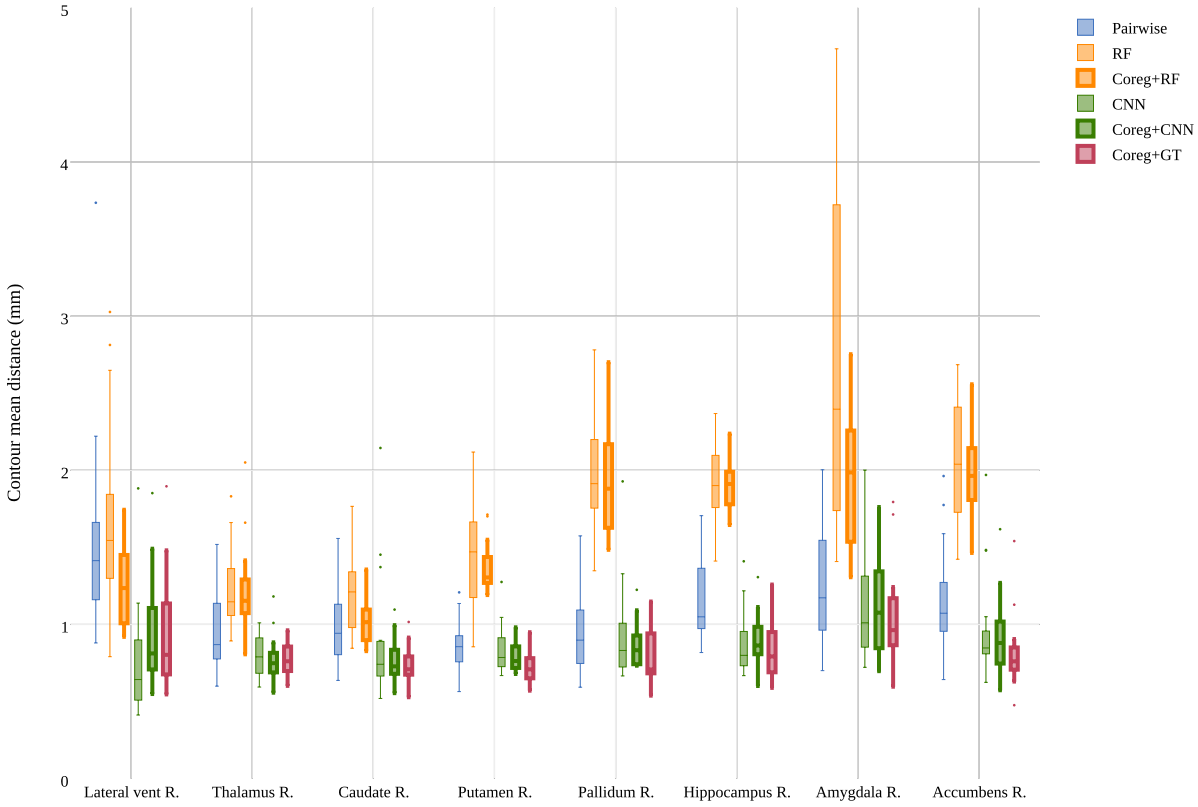

Figure E.3 Contour mean distance (CMD) for right subcortical structures in IBSR (best viewed in color). **CMD :** lower = better.

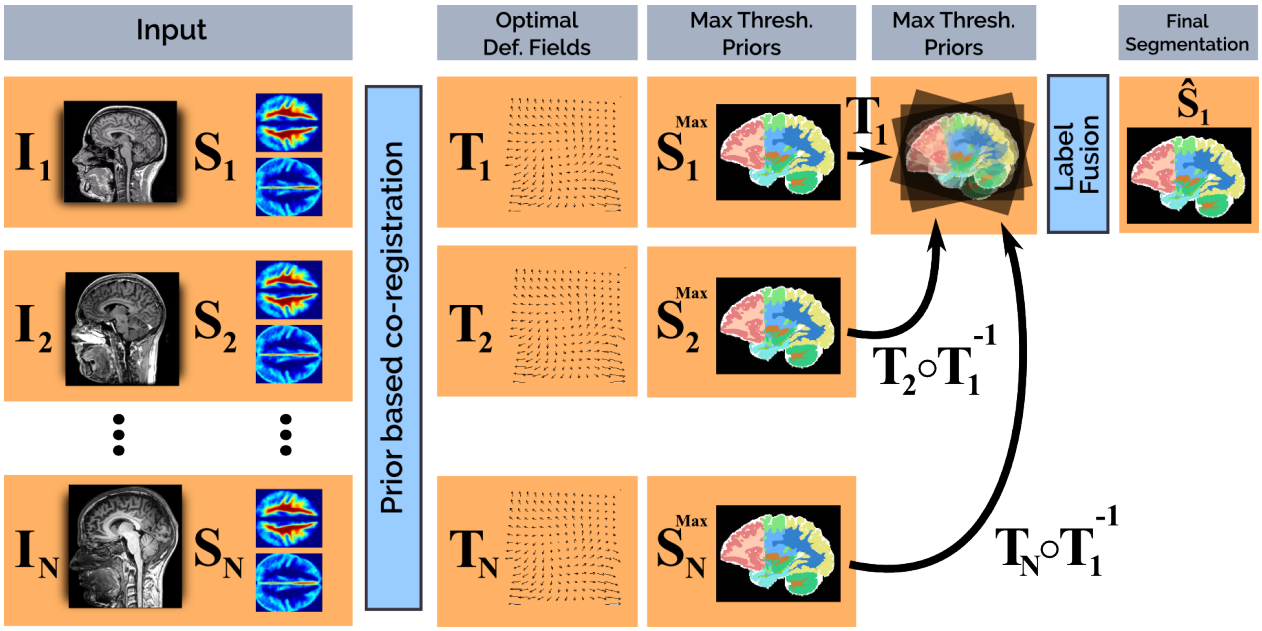

Figure E.4 Co-registration and segmentation workflow. The input consists of images I_i and their corresponding segmentation likelihoods S_i. After running the prior co-registration algorithm (which considers the priors in the energy formulation through the semantic consistency term), the optimal deformation fields are used to deform the *maximum-a-posteriori* of the segmentation likelihoods, which are considered as segmentation hypothesis. A label fusion strategy is then applied to generate the final segmentation mask. The example in this figure illustrates the process to generate the final segmentation for image I_1. The same strategy is followed to generate the rest of the segmentation.

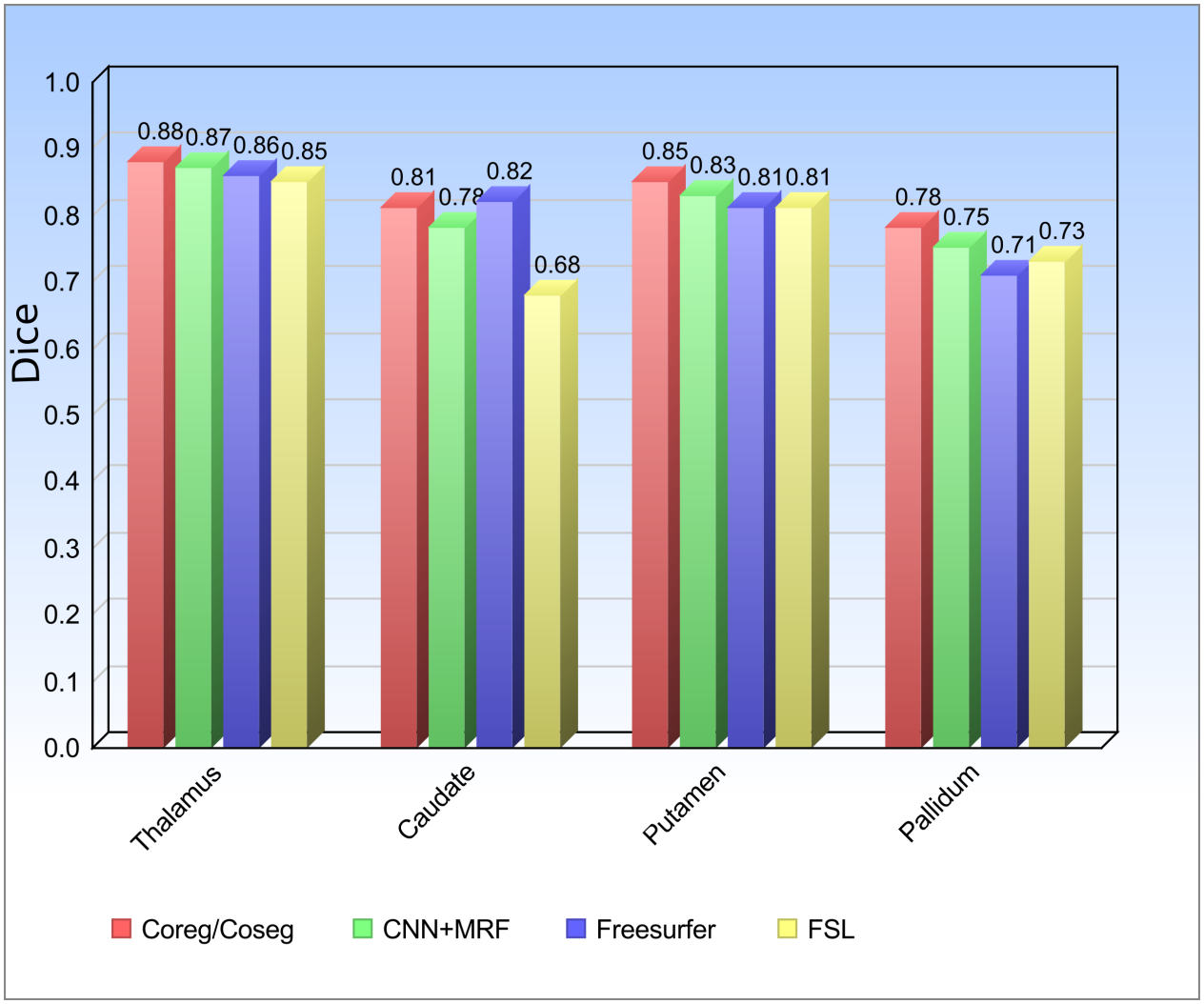

Figure E.5 Average Dice coefficient on a group of sub-cortical structures of IBSR dataset. Comparison of the coregistration and cosegmentation method (Coreg/Coseg; proposed in Chapter 5) with CNN segmentation approach (CNN+MRF; proposed in Appendix A), as well as two state-of-the-art automatic segmentation toolboxes, Freesurfer (Fischl et al., 2002), and FSL-FIRST (Patenaude et al., 2011a).

Table E.1 Comparison of the mean and standard deviation of the Dice coefficient, Hausdorff distance and contour mean distance on the IBSR and RE datasets, using the 6 different approaches discussed in the paper. We use bold face to denote the best results (excluding Coreg+GT which is the oracle). Significant differences between the proposed coregistration-cosegmentation method and the standard multi-atlas segmentation approach (Pairwise) is indicated by asterisk (*).

			Pairwise	**RF**	**Coreg+RF**	**CNN**	**Coreg+CNN**	**Coreg+GT**
IBSR	Dice	mean	0.70	0.64	0.65*	0.75	**0.76***	0.78*
		std	0.12	0.15	0.14	0.13	**0.10**	0.09
	CMD	mean	1.10	1.79	1.58*	0.87	**0.87***	0.81*
		std	0.37	0.68	0.46	0.26	**0.22**	0.21
	HD	mean	6.80	16.40	9.80*	9.70	**6.48**	6.09
		std	6.07	10.50	5.73	10.97	**5.66**	5.88
RE	Dice	mean	0.82	0.65	0.65	0.88	**0.88***	0.89*
		std	0.05	0.04	0.03	0.03	**0.02**	0.03
	CMD	mean	0.81	1.95	1.88*	**0.54**	0.58*	0.49*
		std	0.23	0.24	0.19	0.11	**0.09**	0.12
	HD	mean	**3.69**	11.71	7.70	4.93	4.18*	2.80*
		std	0.86	5.58	0.98	7.48	**0.83**	0.76

*P-values < 0.05.

ANNEXE F SUPPLEMENTARY MATERIALS FOR CHAPTER 7

This section provides the supplementary materials for Chapter 7.

Table F.1 Mean caudate volumetric difference (mm^3) between epileptic patients and healthy controls. The values are reported as $Mean(std)$.

Groups	Left Caudate		Right Caudate	
NC vs. L-BECTS	3806(488) vs. 3912(485)	p=.58	3853(395) vs. 4043(519)	p=.31
NC vs. R-BECTS	3942(535) vs. 3856(398)	p=.59	3866(585) vs. 4101(369)	p=.16
NC vs. B-BECTS	3888(515) vs. 3464(443)	p=.08	4069(479) vs. 3556(534)	**p=.048**
NC vs. BECTS	3905(537) vs. 3786(461)	p=.34	4028(410) vs. 3854(568)	p=.18

Table F.2 Mean putamen volumetric difference (mm^3) between epileptic patients and healthy controls. The values are reported as $Mean(std)$.

Groups	Left Putamen		Right putamen	
NC vs. L-BECTS	5221(609) vs. 5419(565)	p=.40	5264(649) vs. 5480(452)	p=.34
NC vs. R-BECTS	5330(508) vs. 5296(665)	p=.86	5492(465) vs. 5294(634)	p=.29
NC vs. B-BECTS	5353(482) vs. 4866(586)	p=.07	5410(469) vs. 4906(583)	p=.06
NC vs. BECTS	5224(527) vs. 5239(637)	p=.91	5341(547) vs. 5267(595)	p=.61